MULTISCALE SIMULATIONS OF POLYMER-MATRIX NANOCOMPOSITES

Georgios G. Vogiatzis

ΕΘΝΙΚΟ ΜΕΤΣΟΒΙΟ ΠΟΛΥΤΕΧΝΕΙΟ

ΣΧΟΛΗ ΧΗΜΙΚΩΝ ΜΗΧΑΝΙΚΩΝ

ΠΡΟΣΟΜΟΙΩΣΕΙΣ, ΣΕ ΠΟΛΛΕΣ ΚΛΙΜΑΚΕΣ ΜΗΚΟΥΣ ΚΑΙ ΧΡΟΝΟΥ, ΝΑΝΟΣΥΝΘΕΤΩΝ ΥΛΙΚΩΝ ΠΟΛΥΜΕΡΙΚΗΣ ΜΗΤΡΑΣ

MULTISCALE SIMULATIONS OF POLYMER-MATRIX NANOCOMPOSITES

Γεώργιος Γρ. Βογιατζής

Georgios G. Vogiatzis

Διδακτορική Διατριβή υποβληθείσα στη Σχολή Χημικών Μηχανικών
του Εθνικού Μετσόβιου Πολυτεχνείου για την απόκτηση του τίτλου του
Διδάκτορος του Εθνικού Μετσόβιου Πολυτεχνείου

Αθήνα, Ιανουάριος 2015

Thesis examination committee:

- **Professor Theodoros (Doros) Theodorou** (supervisor)
  School of Chemical Engineering,
  National Technical University of Athens

- **Professor Andreas Boudouvis** (member of the advisory committee)
  School of Chemical Engineering,
  National Technical University of Athens

- **Professor Constantinos Charitidis** (member of the advisory committee)
  School of Chemical Engineering,
  National Technical University of Athens

- **Professor Emeritus Polykarpos Pissis**
  School of Applied Mathematical and Physical Sciences,
  National Technical University of Athens

- **Professor Vlasis Mavrantzas**
  Department of Chemical Engineering,
  University of Patras

- **Assistant Professor Antonis Karantonis**
  School of Chemical Engineering,
  National Technical University of Athens

- **Associate Professor Markus Hütter**
  Department of Mechanical Engineering,
  Eindhoven University of Technology

«Η έγκριση της διδακτορικής διατριβής από την Ανώτατη Σχολή Χημικών
Μηχανικών του Ε. Μ. Πολυτεχνείου δεν υποδηλώνει αποδοχή
των γνωμών του συγγραφέα. (Ν. 5343/1932, Άρθρο 202)»

This dissertation is dedicated to
my parents, my grandparents and Froso
for their love, endless support and encouragement.

Contents

Acknowledgements

I would like to start by expressing my sincerest gratitude to my supervisor, *Professor Doros Theodorou*, the person who trusted me with this project and gave me the opportunity to work with him. He was always there for me, supporting me at all levels, scientific, moral and financial, motivating and inspiring me towards new routes. He has been a model scientist for me, with his brilliant thinking, passion for perfection and commitment to science. He was always urging me to take up new challenges in science, encouraging me to become an independent scientist. I really have no words to express my appreciation for him.

Secondly, I would like to thank *Professor Andreas Boudouvis* and *Professor Constantinos Charitidis* for being members of my thesis advisory committee and for their generous help and support at all levels. I would like to specially acknowledge the generous allocation of computer time on clusters of the School of Chemical Engineering of the National Technical University of Athens, thoroughly maintained by Professor Andreas Boudouvis and his collaborators.

Next, I would like to thank *Professor Polykarpos Pissis*, *Professor Vlasis Mavrantzas*, *Associate Professor Markus Hütter* and *Assistant Professor Antonis Karantonis* for closely following my work. We had very interesting discussions throughout these years, providing me with their useful scientific advice. Special thanks to Associate Professor Hütter and Professor Pissis for giving me the opportunity to visit their groups and develop an active collaboration with them.

Many of my past and present colleagues have been extremely helpful to me during my PhD and I am thankful for that. First of all I would like to thank the senior members of the Computational Materials Science and Engineering Group, *Dr. Grigorios Megariotis*, *Dr. Loukas Peristeras*, *Dr. Evangelos Voyiatzis*, *Dr. Georgios Boulougouris*, *Dr. Christos Tzoumanekas* and *Lecturer Georgios Papadopoulos* for their help during the first steps of my thesis and our active collaboration throughout its course. Moreover, I would like to thank *Assistant Professor Lambert van Breemen* for the very productive time we spent together, both in Athens and in Eindhoven. Despite the fact that we met in a project different than my PhD, he has been a great counselor for me. Last but not least, I would like to thank *Dr. Georgios Kritikos* for the very active and fruitful collaboration we had. Since a long time I have considered all of them not just as colleagues, but also as good friends.

I would like to thank my office-mates *Dr. Nikolaos Lempesis*, *Mr. Orestis Ziogos* and *Mr. Ioannis Mathioudakis*, who I shared my office with for about four years. I really had a great time working with them. At this point I should mention the interesting discussions I had with *Mr. Constantinos Koutsoumaris* and *Mr. Dimosthenis Georgopoulos* who kindly shared with me their experience on continuum theories and experimental studies, respectively.

Follows, many thanks to *Mr. Andreas Morphis*, *Ms. Ioulia Tzouvadaki*, *Mr. Ioannis Petsagkourakis*, *Ms. Xrysa Charitoglou*, *Mr. Andreas Gavrielides* and *Ms. Ariadni Boziki*. I had the pleasure to work with them in the framework of their Diploma and Master's theses and very much enjoyed it.

Very special thanks to my parents, *Grigorios* and *Maria* for their love, support and encouragement. They stood by me in difficult times and they always had a way of guiding me to make the right decisions. I would like to extend my special thanks to my grandmother *Margarita* and my grandparents *Georgios* and *Marianthi*, for their unconditional love. I would never have finished this work without their love and support.

Last but not least, I would like to thank my beloved girlfriend *Froso* for being by my side for more than six years. She has always been there when I needed to complain, laugh and just have someone to listen. I hope I will have the opportunity to make up for her endless patience during the hard time of my PhD.

A lot of people have stood by me during my PhD, to whom I am deeply indebted. I would like to single out my uncle, *Dr. Grigorios Ntokos* for being a role model for me. I spent a wonderful summer working by his side and discovering how everyday science makes people's lives better. A second person I would like to acknowledge is the good friend of mine, *Mr. Georgios Dertilis* for the great times and memories that we shared during our friendship.

As far as the the financial support of this thesis is concerned, I am deeply grateful to the Alexander S. Onassis Public Benefit Foundation for my doctoral scholarship, under contract number GZH 005/2011-2012. Part of this work was funded by the European Union through the projects NANOMODEL and COMPNANOCOMP under grant numbers 211778 and 295355, respectively. Part of the computational work was carried out under the HPC-EUROPA2 project (project number: 228398) with the support of the European Commission Capacities Area - Research Infrastructures Initiative and the PRACE-2IP project (FP7 RI-283493) resource Fionn based in Ireland at the Irish Centre for High-End Computing (ICHEC). Code development was greatly facilitated by using hardware donated by nVIDIA, through the nVIDIA Academic Partnership Program.

Summary

Polymer-matrix nanocomposites, i.e. nanoparticle-filled polymers, are just at their infancy of development, but offer huge potential for future applications and energy savings. The observation that, other things being equal, the effectiveness of the filler increases with an increase in surface to volume ratio has provided large impetus for a shift from micron- to nanosized filler particles. Therefore polymer-based nanocomposites are considered an important branch of the emerging field of nanotechnology.

A multiscale simulation strategy has been designed and applied to quantify the effects of incorporating fullerenes on the segmental motion of long-chain atactic polystyrene (PS), to predict the scattering curves from the grafted PS corona of silica particles dispersed in PS, and to estimate the storage and loss moduli of polyisoprene (PI). *Each level in our multiscale modeling framework is receiving input from more fundamental levels and is providing input to more coarse-grained ones, enabling a reliable prediction of structure-property relations from chemical constitution and composition with an absolute minimum of adjustable parameters.*

Four interconnected levels of representation have been developed for polymer nanocomposites:

(a) An atomistic one, where both nanoparticles and polymer chains are represented in terms of detailed atomistic force fields. Fullerenes (C_{60}) are dispersed in atactic PS matrix, and atomistic Molecular Dynamics (MD) simulations are undertaken to uncover details of packing and to quantify *segmental dynamics* and *local stresses*.

(b) A coarse-grained representation, in which each repeat unit is mapped onto a single "superatom", and each nanoparticle is viewed as a sphere interacting with the polymer superatoms and with other nanoparticles via Hamaker-type potentials. For PS the coarse-grained model utilizes the effective potential energy function already derived for the bulk melt via Iterative Boltzmann Inversion. Hamaker potentials are obtained by integration of the atomistic pair potentials invoked at the atomistic level of description, assuming uniform density of interacting sites. Equilibration of coarse-grained polymer-nanoparticle systems at all length scales is achieved via *connectivity-altering* Monte Carlo (MC) moves, which are particularly efficient for polymer matrices of high molar mass. These simulations are strategically important for generating *well-equilibrated starting configurations* for atomistic MD through *reverse-mapping*.

(c) A *Field Theory-inspired Monte Carlo (FTiMC)* level, where polymer chains are represented as freely jointed sequences of Kuhn segments. Nanoparticles (e.g. SiO_2) are again modeled as structureless spheres interacting with each other and with the Kuhn segments through Hamaker potentials. For polymer-polymer interactions, however, an effective energy function is used, which prevents large departures of the local polymer density from its value in the bulk melt everywhere in the system. This simulation methodology is capable of capturing structural features at length scales on the order of hundreds of nanometers. By randomly linking chains at the FTiMC representation level, initial configurations for network simulations of slip-spring models can be created.

(d) A slip-spring network representation where cross-links, entanglements and chain ends are the degrees of freedom of the polymeric matrix. From the thermodynamic point of view, the system under study is fully described by a *Helmholtz energy function* which accounts for the entropic springs connecting cross-links or entanglements, non-bonded interactions (derived from *any appropriate equation of state*, e.g. the Sanchez-Lacombe) and Hamaker interactions between nodal points - nanoparticles and nanoparticles - nanoparticles. Brownian simulations at this level, operating at the length scales of up to 1 μm and time scales up to 1 ms, account for changes in segmental mobility induced by the nanoparticles and track elementary events of *chain slippage across entanglements*, *chain entanglement* and *re-entanglement*.

Well-equilibrated melt configurations sampled by coarse grained MC were reverse-mapped to the atomistic level via a rigorous quasi Metropolis reconstruction. Our approach yields atomistic configurations exhibiting characteristics in *excellent agreement with experimental measurements*. The main goal of our atomistic simulation work, i.e., the study of PS-C_{60} dynamics at the segmental and local levels, has been accomplished by analyzing long MD trajectories of our well-equilibrated reverse-mapped structures. Our simulation results generally indicate that the addition of C_{60}s to PS leads to *slower segmental dynamics* (as estimated by characteristic times extracted from the decay of orientational time-autocorrelation functions of suitably chosen vectors), suggesting an *increase of the bulk* T_g *by about 1 K*, upon the addition of C_{60}s at a concentration of 1% by weight. This observation is in favorable agreement with differential scanning calorimetry measurements. We then employ a *space discretization* in order to study the effect of C_{60}s on *segmental dynamics at a local level*. Each fullerene serves as the center of a Voronoi cell, whose volume is determined by the neighboring fullerenes. Backbone carbons lying in every cell are tracked throughout the MD trajectory and their mean-square displacement is measured for the time they reside in the same cell. Overall mean-square displacement of backbone atoms is found to be smaller in the presence of fullerenes, than in bulk PS. However, atoms moving in smaller (more confined) Voronoi cells exhibit faster motion

than the atoms moving inside larger Voronoi cells. This can be correlated with the increased rotational diffusion of fullerenes, as the volume of the Voronoi cell becomes smaller. These observations drive us to envision *fullerenes as nanoscopic millstones*, forcing the polymeric chains to diffuse faster.

The structural features of *PS brushes grafted on spherical silica nanoparticles* immersed in PS are investigated by means of a MC methodology based on polymer mean field theory (FTiMC). The nanoparticle radii (either 8 or 13 nm) are held constant, while the grafting density and the lengths of grafted and matrix chains are varied systematically in a series of simulations. The profiles of polymer density around the particles are examined; based on them, the brush thickness of grafted chains is estimated and its scaling behavior is *compared against theoretical models and experimental findings*. In addition, *Small Angle Neutron Scattering (SANS) spectra* have been *predicted* both from single grafted chains and from the entire grafted corona. It is found that increasing both the grafting density and the grafted chain molar mass drastically alters the brush dimensions, affecting the wetting behavior of the polymeric brush. On the contrary, especially for particles dispersed in high molecular weight matrix, variation of the matrix chain length causes an almost imperceptible change of the density around the particle surface.

Finally, at the last level of modeling, an *equation of state - based* coarse-grained model for entangled melt and rubber simulations has been formulated and developed. Structural features of entangled melts have been found to be in good agreement with theoretical predictions. This model is parameterized by transferring information from the more detailed levels of modeling to it. The mean square-displacement of polymer beads and chain centers of mass as a function of time exhibits the regimes expected from reptation theory with contour length fluctuations and constraint release. The ultimate target of this level is to extract the shear relaxation modulus, $G\left(t\right)$, for nanocomposite polymer melts and rubbers. Results from applying the model to cis-1,4 polyisoprene melts are in favorable agreement with experiment, demonstrating the utility of the model and simulation approach in predicting linear viscoelastic properties from molecular constitution.

Περίληψη

Μία υπολογιστική μεθοδολογία προτυποποίησης και προσομοίωσης σε πολλές κλίμακες μήκους και χρόνου (multiscale modeling and simulation) σχεδιάσθηκε και υλοποιήθηκε για τη μελέτη νανοσύνθετων υλικών πολυμερικής μήτρας. Αναλυτικότερα, οι προσομοιώσεις εστιάζονται στην ποσοτικοποίηση της επίδρασης της διασποράς φουλερενίων στην τμηματική δυναμική ατακτικού πολυστυρενίου υψηλού μοριακού βάρους, στην πρόβλεψη των χαρακτηριστικών κλιμάκωσης του μεγέθους εμφυτευμένων αλυσίδων πολυστυρενίου σε σωματίδια πυριτίας τα οποία έχουν διασπαρεί σε μήτρα πολυστυρενίου, και στην εκτίμηση των μέτρων αποθήκευσης και απωλειών ενέργειας τήγματος πολυϊσοπρενίου.

Οι ιδιότητες ενός σύνθετου ετερογενούς υλικού εξαρτώνται από τις ιδιότητες των συστατικών υλικών και τη χαρακτηριστική κλίμακα μήκους της συνύπαρξής τους, καθώς και τις χημικές και μορφολογικές λεπτομέρειες της διασποράς. Ο όρος «νανοσύνθετο» χρησιμοποιείται για τα σύνθετα υλικά των οποίων η χαρακτηριστική κλίμακα μήκους της διεσπαρμένης φάσης είναι της τάξης των μερικών νανομέτρων (10^{-9}m). Ένα νανοσύνθετο υλικό διαφοροποιείται από ένα παραδοσιακό σύνθετο (με διασπορά στην κλίμακα μήκους των μικρομέτρων 10^{-6}m) ως προς: τη μεγάλη αριθμητική πυκνότητα σωματιδίων μέχρι και $\sim 10^{20}\mathrm{m}^{-3}$, την εκτεταμένη διαφασική επιφάνεια ανά όγκο νανοσωματιδίων $\sim 10^{7}\frac{\mathrm{cm}^2}{\mathrm{cm}^3}$, τη συσχέτιση και την αλληλεπίδραση σωματιδίου-σωματιδίου οι οποίες εμφανίζονται σε χαμηλές συγκεντρώσεις (μικρότερες από $0,1$ % v/v), τις μικρές αποστάσεις ανάμεσα στα διεσπαρμένα νανοσωματίδια (της τάξης των νανομέτρων) και τις συγκρίσιμες κλίμακες μήκους ανάμεσα στο μέγεθος του σωματιδίου, την απόσταση ανάμεσα στα νανοσωματίδια και το τυπικό μέγεθος του πολυμερούς, π.χ. τη μέση γυροσκοπική ακτίνα $\langle R_g \rangle \sim 10\,\mathrm{nm}$.

Ενώ είναι σήμερα ευρύτατα αποδεκτό ότι η προσθήκη νανοσωματιδίων σε μία πολυμερική μήτρα μπορεί να οδηγήσει σε δραστική βελτίωση των ιδιοτήτων του υλικού μήτρας, οι μηχανισμοί, μέσω των οποίων η προσθήκη νανοσωματιδίων επηρεάζει τις ιδιότητες του υλικού μήτρας, παραμένουν ακόμα άγνωστοι. Η κατανόηση και ποσοτική περιγραφή των σχέσεων σύστασης-δομής-ιδιοτήτων των νανοσύνθετων υλικών πολυμερικής μήτρας παραμένει ύψιστης σημασίας ζητούμενο. Η παρατήρηση ότι η αποτελεσματικότητα του υλικού που διασπείρεται αυξάνεται με αύξηση της εκτειθέμενης επιφάνειας ανά όγκο, έχει δώσει μεγάλη ώθηση για τη χρήση σωματιδίων με διαστάσεις στη νανοκλίμακα. Κάθε επίπεδο στην ιεραρχία μοντέλων που χρησιμοποιούμε λαμβάνει δεδομένα εισόδου από λεπτομερέστερα επίπεδα και δίνει δεδομένα εξόδου (παρατηρήσεις, μετρήσεις και παραμέτρους) σε πιο αδρά επίπεδα. Η διασύνδεση αυτή καθιστά αξιόπιστη την πρόβλεψη σχέσεων δομής-ιδιοτήτων από τη χημική σύσταση χρησιμοποιώντας τον ελάχιστο δυνατό αριθμό ελεύθερων παραμέτρων.

Τέσσερα διασυνδεδεμένα επίπεδα αναπαράστασης και προσομοίωσης αναπτύχθηκαν σε αυτή την εργασία για τα νανοσύνθετα υλικά πολυμερικής μήτρας:

(α) Ατομιστικό επίπεδο, όπου, τόσο τα νανοσωματίδια, όσο και οι πολυμερικές αλυσίδες αναπαρίστανται με λεπτομερή ατομιστικά δυναμικά αλληλεπίδρασης. Φουλερένια (C_{60}) διασπείρονται σε μήτρα ατακτικού πολυστυρενίου (polystyrene (PS)). Προσομοιώσεις Μοριακής Δυναμικής (Molecular Dynamics (MD)) αποκαλύπτουν λεπτομέρειες της τοπικής δομής, της τμηματικής δυναμικής (segmental dynamics) και των τοπικών τάσεων στο υλικό.

(β) Αδροποιημένο επίπεδο, όπου οι αλυσίδες πολυστυρενίου αναπαρίστανται ως αλληλουχίες δυάδων (dyads) οι οποίες αλληλεπιδρούν μεταξύ τους τόσο δεσμικά, όσο και μη δεσμικά. Το αδροποιημένο δυναμικό του πολυστυρενίου έχει προκύψει από επαναληπτική αντιστροφή κατά Boltzmann (Iterative Boltzmann Inversion (IBI)) των συναρτήσεων κατανομής ζευγών ολιγομερών του στυρενίου. Στο αδροποιημένο επίπεδο, τα φουλερένια θεωρούνται σφαιρικά κελύφη, τα οποία αλληλεπιδρούν με τα μονομερή του πολυστυρενίου, μέσω ενός δυναμικού το οποίο προκύπτει από την ολοκλήρωση κατά Hamaker των στοιχειωδών αλληλεπιδράσεων Lennard-Jones ανάμεσα στα συνιστώντα άτομα. Η εξισορρόπηση των τηγμάτων πραγματοποιείται χρησιμοποιώντας πανίσχυρες τεχνικές Monte Carlo (MC) μεταβολής της συνδετικότητας. Κατόπιν, πραγματοποιείται αποκατάσταση της ατομιστικής λεπτομέρειας, μέσω μίας διαδικασίας η οποία βασίζεται σε συνδυασμό τοπικών κινήσεων MC και σταδιακής ελαχιστοποίησης της δυναμικής ενέργειας της παραγόμενης απεικόνισης. Τελικά, η δυναμική των νανοσυνθέτων πολυστυρενίου εκτιμάται από τροχιές Μοριακής Δυναμικής στο ατομιστικό επίπεδο αναπαράστασης.

(γ) Μεσοσκοπικό επίπεδο, όπου οι διαμορφώσεις των πολυμερικών αλυσίδων εξελίσσονται μέσω προσομοίωσης Metropolis Monte Carlo, με τις αλληλεπιδράσεις μεταξύ τους να προκύπτουν από ένα συναρτησιακό της κατανομής πυκνότητας το οποίο είναι εμπνευσμένο από τη θεωρία μέσου πεδίου των πολυμερών (Field Theory-inspired Monte Carlo (FTiMC)). Οι πολυμερικές αλυσίδες δεν αλληλεπιδρούν άμεσα, αλλά όλες μαζί συμμετέχουν στις διακυμάνσεις πυκνότητας του τήγματος. Η προσέγγιση αυτή διατηρεί τα πλεονεκτήματα της θεωρίας πεδίου (μικρό υπολογιστικό κόστος, μεγάλες κλίμακες μήκους) αλλά είναι απαλλαγμένη από την προσέγγιση σαγματικού σημείου και ενδείκνυται για την αντιμετώπιση συστημάτων με περίπλοκες γεωμετρίες.

(δ) Επίπεδο δικτύου διαπλοκών, όπου οι πολυμερικές αλυσίδες έχουν αναχθεί σε ένα δίκτυο διαπλοκών, με σκοπό την πρόβλεψη ρεολογικών ιδιοτήτων τηγμάτων και ελαστομερών. Από θερμοδυναμική σκοπιά, το σύστημα χαρακτηρίζεται πλήρως από την ενέργεια Helmholtz η οποία περιλαμβάνει συνεισφορές από τα εντροπικά ελατήρια (τα οποία συνδέουν εσωτερικά τμήματα των αλυσίδων μεταξύ τους και με σταυροδεσμούς), μη δεσμικές αλληλεπιδράσεις (οι οποίες καθορίζονται από μία καταστατική εξίσωση, π.χ. την εξίσωση Sanchez-Lacombe) και αλληλεπιδράσεις τύπου Hamaker ανάμεσα σε τμήματα αλυσίδων και νανοσωματίδια και μεταξύ νανοσωματιδίων. Οι τροχιές των τμημάτων του πολυμερούς προκύπτουν από προσομοιώσεις δυναμικής κατά Brown σε αυτό το επίπεδο, ενώ η συνδετικότητα του δικτύου διαπλοκών μεταβάλλεται μέσω μίας μεθόδου κινητικής προσομοίωσης Monte Carlo (kinetic Monte Carlo (kMC)), η οποία θεωρεί στοιχειώδη συμβάντα ολίσθησης των διαπλοκών κατά μήκος του περιγράμματος των αλυσίδων, δημιουργίας και καταστροφής διαπλοκών.

Η προσομοίωση της δυναμικής νανοσύνθετων τηγμάτων πολυστυρενίου - φουλερενίων (σφαιρικών μορίων C_{60}) βασίζεται σε μία προσέγγιση δύο επιπέδων. Η εξισορρόπηση των τηγμάτων πραγματοποιείται σε αδροποιημένο επίπεδο, όπου κάθε κέντρο αλληλεπίδρασης αντιστοιχεί σε ένα μονομερές, χρησιμοποιώντας αποτελεσματικές τεχνικές MC μεταβολής της συνδετικότητας. Κατόπιν, πραγματοποιείται αποκατάσταση της ατομιστικής λεπτομέρειας, μέσω μίας διαδικασίας η οποία βασίζεται σε συνδυασμό τοπικών κινήσεων MC και σταδιακής ελαχιστοποίησης της δυναμικής ενέργειας της παραγόμενης απεικόνισης. Τελικά, η δυναμική των νανοσυνθέτων πολυστυρενίου εκτιμάται από τροχιές Μοριακής Δυναμικής (MD) στο ατομιστικό επίπεδο αναπαράστασης. Οι προσομοιώσεις προέβλεψαν ελαφρή επιβράδυνση της δυναμικής παρουσία φουλερενίων σε συγκέντρωση 1% κατά βάρος, στις περισσότερες θερμοκρασίες που εξετάσθηκαν. Κατά συνέπεια, επέρχεται μικρή αύξηση της θερμοκρασίας υαλώδους μετάπτωσης με την ενσωμάτωση των φουλερενίων στο σύστημα, πρόβλεψη η οποία επιβεβαιώνεται από τις διαθέσιμες πειραματικές μετρήσεις. Κατόπιν μελετάται η τοπική δυναμική, σε περιοχές του χώρου οι οποίες προκύπτουν από ψηφιδοποίηση του χωρίου της προσομοίωσης σε πολύεδρα Voronoi, τα οποία έχουν ως κέντρα τους τα μόρια C_{60}. Ο όγκος των πολύεδρων Voronoi χρησιμοποιείται ως εκτίμηση του βαθμού του χωρικού περιορισμού που επάγουν τα φουλερένια στο περιβάλλον τους. Τα αποτελέσματά μας δείχνουν ότι, ενώ κατά μέσο όρο επιβραδύνεται η μεταφορική κίνηση των ατόμων άνθρακα του σκελετού των πολυμερικών αλυσίδων, στην περίπτωση του νανοσυνθέτου η τοπική δυναμική χαρακτηρίζεται από ανομοιογένεια. Άτομα τα οποία βρίσκονται σε ισχυρά περιορισμένες περιοχές παρουσιάζουν ταχύτερη διάχυση σε σύγκριση με άτομα σε λιγότερο περιορισμένες. Κατόπιν, με κατάλληλη χρήση του θεωρήματος virial εκτιμώνται οι τάσεις σε ατομιστικό επίπεδο, όπου ιδιαίτερο ενδιαφέρον παρουσιάζουν οι κατανομές τους ανάλογα με το είδος του ατόμου. Τέλος, με κατάλληλη άθροιση, προκύπτουν οι τάσεις σε τοπικό επίπεδο.

Η τοπική δομή κοντά στην επιφάνεια σφαιρικών νανοσωματιδίων πυριτίας (SiO_2) μελετάται με χρήση της μεθοδολογίας προσομοιώσεων Monte Carlo εμπνευσμένων από τη θεωρία μέσου πεδίου, FTiMC. Η μελέτη εστιάζεται σε νανοσωματίδια τα οποία φέρουν εμφυτευμένες αλυσίδες πολυστυρενίου (PS) και είναι διεσπαρμένα σε μήτρα πολυστυρενίου. Στην ισορροπία πραγματοποιείται εκτίμηση του πάχους της πολυμερικής ψήκτρας των εμφυτευμένων αλυσίδων η οποία περιβάλλει το νανοσωματίδιο (grafted polymer brush). Η ακτίνα των νανοσωματιδίων (8 ή 13 nm) διατηρείται σταθερή, ενώ μεταβάλλονται συστηματικά η πυκνότητα εμφύτευσης και το μήκος των εμφυτευμένων και ελεύθερων αλυσίδων, σε μία σειρά προσομοιώσεων. Στην ισορροπία εξετάζονται οι ακτινικές κατανομές πυκνότητας του πολυμερούς γύρω από τα νανοσωματίδια και μελετάται η εξάρτηση του πάχους της πολυμερικής ψήκτρας από την πυκνότητα εμφύτευσης και το μοριακό βάρος. Τα αποτελέσματα των προσομοιώσεων βρίσκονται σε καλή συμφωνία, τόσο ως προς θεωρητικά μοντέλα, όσο και ως προς τις διαθέσιμες πειραματικές παρατηρήσεις. Το πάχος της πολυμερικής μήτρας αυξάνει με την πυκνότητα εμφύτευσης των αλυσίδων στην επιφάνεια του νανοσωματιδίου, καθώς αύξηση της πυκνότητας εμφύτευσης αναγκάζει τις εμφυτευμένες αλυσίδες να εκταθούν μακρύτερα από την επιφάνεια εμφύτευσης, αυξάνοντας επακόλουθα και το πάχος της πολυμερικής ψήκτρας. Το ίδιο παρατηρείται και με αύξηση του μήκους των εμφυτευμένων αλυσίδων, ενώ μεταβολή του μοριακού βάρους της περιβάλλουσας μήτρας επιφέρει ανεπαίσθητη μεταβολή της κατανομής πυκνότητας γύρω από την επιφάνεια του νανοσωματιδίου. Προσομοιώσεις σε αυτό το επίπεδο αναπαράστασης επιτρέπουν την άμεση πρόβλεψη περιθλασιογραφημάτων σκέδασης νετρονίων υπό μικρές γωνίες, Small Angle Neutron Scattering (SANS), από τις συντεταγμένες των αδροποιημένων τμημάτων πολυμερούς.

Στο τελευταίο επίπεδο προτυποποίησης αναπτύσσεται ένα θερμοδυναμικά συνεπές αδροποιημένο μοντέλο για τη δυναμική διαπλεγμένων τηγμάτων και ελαστομερών. Τα δομικά χαρακτηριστικά διαπλεγμένων τηγμάτων βρίσκονται σε καλή συμφωνία με τις θεωρητικές προβλέψεις. Επίσης, η δυναμική συμπεριφορά του μοντέλου περιγράφει καλά τα κύρια χαρακτηριστικά της δυναμικής των διαπλεγμένων τηγμάτων. Προβλέψεις του μέτρου χαλάρωσης διατμητικών τάσεων, $G(t)$, από προσομοιώσεις τηγμάτων cis-1,4 πολυϊσοπρενίου σε κατάσταση ισορροπίας οδηγούν σε πολύ ικανοποιητικά αποτελέσματα καταδεικνύοντας τη χρησιμότητα του μοντέλου στην πρόβλεψη των γραμμικών ιξωδοελαστικών ιδιοτήτων από τη μοριακή σύσταση.

List of Figures

List of Tables

Nomenclature

Symbols and Notation

Latin Symbols

A	Helmholtz energy, $A = U - TS$
A_{b}	Bonded contribution to the Helmholtz energy, defined by eq 5.2, page 154
A_{nb}	Nonbonded contribution to the Helmholtz energy in a slip-spring based network model, defined by eq 5.6, page 154
$\mathcal{A}$	Arbitrary property of a system
$\mathscr{A}$	Hamaker constant, defined by eq 4.8, page 119
$\mathcal{A}_{\mathrm{obs}}$	Macroscopically observable property, defined by eq 2.4, page 14
a_{lib}	Amplitude of the fast motions described by a mKWW expression , defined by eq 3.4, page 80
A_{pair}	Pairwise additive contribution to the Helmholtz energy, e.g. entropic spring, defined by eq 5.2, page 154
$A^{\mathrm{intra}}_{\mathrm{pair}}$	Pairwise additive Helmholtz energy of intramolecular strands in a slip-spring based network representation, defined by eq 5.4, page 154
$A^{\mathrm{sls}}_{\mathrm{pair}}$	Pairwise additive Helmholtz energy of intermolecular strands (slip-springs) in a slip-spring based network representation, defined by eq 5.5, page 154
a_{pp}	Tube diameter, page 41
a_{vol}	Helmholtz energy density (free energy per unit volume)
$\mathbf{b}_i$	Bond vector connecting particles $i - 1$ and i along a polymer chain, page 26

b_{K}	Kuhn length, page 34
c_1, c_2	Williams - Landel - Ferry (WLF) coefficients , defined by eq 3.7, page 83
$\mathcal{C}_{\mathbf{e}}$	Rotational correlation function of a vector **e** , defined by eq 3.10, page 89
C_∞	Flory's characteristic ratio at infinite chain length, defined by eq 2.81, page 34
C_N	Flory's characteristic ratio, defined by eq 2.80, page 34
$D_{\mathrm{cm}}^{\mathrm{Rouse}}$	Self-diffusivity of the center of mass of a chain, according to the Rouse model, defined by eq 2.107, page 40
E	Total energy, $E = \mathcal{V} + \mathcal{K}$
e	Vector describing the orientation of a solid body
$\mathbb{F}$	Deformation gradient tensor, defined by eq 2.29, page 21
$\boldsymbol{\mathcal{F}}_i$	Random force acting on atom i
$\mathbf{F}_i$	Force acting on atom i
G	Gibbs energy
$G^*(\omega)$	Complex modulus, defined by eq 2.45, page 25
$g_{\mathrm{cm}}(t)$	Mean-square displacement of the center of mass of a group of particles, as a function of time, defined by eq 2.105, page 39
G_{e}	Rubbery plateau modulus, page 44
$g_i(t)$	Mean-square displacement of the particle i, as a function of time, defined by eq 2.110, page 41
$G(t)$	Shear relaxation modulus, page 24
$G'(\omega)$	Storage modulus, defined by eq 2.43, page 25
$G''(\omega)$	Loss modulus, defined by eq 2.44, page 25
$\tilde{G}$	Reduced Gibbs energy used in an equation of state, e.g. the Sanchez Lacombe equation of state, page 46
h	Planck's constant, $h = 6.62606957 \times 10^{-34}$ $\mathrm{m^2 kg/s}$

h	Polymer brush thickness or height
$\mathcal{H}$	Hamiltonian
$\mathbf{H}$	Mobility tensor, page 37
$\mathcal{H}_{\mathrm{nb}}\left[\rho\left(\mathbf{r}\right)\right]$	Polymer nonbonded effective Hamiltonian in FTiMC formulation, defined by eq 4.2, page 117
$\mathcal{H}_{\mathrm{p}}\left[\rho\left(\mathbf{r}\right)\right]$	Nanoparticle - nanoparticle and nanoparticle - polymer nonbonded effective Hamiltonian in FTiMC formulation, defined by eq 4.4, page 117
$\mathbb{I}$	Unit tensor
k_{B}	Boltzmann's constant, $k_{\mathrm{B}} = 1.3806488 \times 10^{-23}$ $\mathrm{m^2 kg\, s^{-2} K^{-1}}$
$\mathcal{K}$	Kinetic energy
k_{diff}	Rate of the diffusion of a Rouse bead along the chain, defined by eq 5.34, page 163
k_{hopping}	Rate of an individual jump of the one end of a slip-spring, defined by eq 5.36, page 163
$\mathbf{k}$	A vector in reciprocal space
l	Bond length
L, L_x, L_y, L_z	Simulation box edge lengths
$\langle L \rangle$	Average contour length of the primitive path, defined by eq 2.114, page 42
L_{c}	Length between two consecutive cross-links along a chain, used in Appendix B , page 204
l_{sl}	Adjustable parameter which sets the length scale of a slip-spring, defined by eq 5.5, page 154
m	Mass of a particle
M_{e}	Number-average molar mass of an entanglement strand, page 41
M_{f}	Molar mass of free (matrix) chains
M_{g}	Molar mass of grafted chains

m_{monomer}	Molar mass of a monomer
M_{w}	Molar mass
N	Number of particles
n	Number of molecules (or polymeric chains)
$\mathcal{N}_{\mathrm{A}}$	Avogadro constant, $\mathcal{N}_{\mathrm{A}} = 6.02214129(27) \times 10^{23}$ mol^{-1}
N_{b}	Number of bonds along the backbone of a chain
N_{c}	Number of crosslinks per chain, used in Appendix B , page 201
n_{cands}	Number of candidates for a slip-spring to be attached to, defined by eq 5.37, page 166
$\bar{N}_{\mathrm{c}}$	Number of unique crosslinks per chain, used in Appendix B , page 201
N_{e}	Number of monomers in an entanglement strand
N_{dof}	Number of degrees of freedom
N_{f}	Chain length of matrix (free) chains
n_{f}	Number of free (not grafted to nanoparticles) polymeric chains present in the simulation box, page 116
N_{g}	Chain length of grafted chains
$n_{\mathrm{g},k}$	Number of polymeric chains grafted to nanoparticle k, page 116
N_{ij}	Number of Kuhn segments assigned to a strand connecting beads i and j
N_{inner}	Number of innermost atoms, on each side of the middle segment of a chain, page 86
N_{links}	Number of crosslinks randomly dispersed in the simulation box, used in Appendix B , page 201
n_{p}	Number of nanoparticles dispersed in the system, page 116
N_{sub}	Number of monomers or segments of a subchain
$\mathcal{O}$	Limiting behavior of a function (Landau notation)

P	Probability
p	Pressure, $p = -1/3\ \mathrm{Tr}(\boldsymbol{\tau})$ where $\boldsymbol{\tau}$ is the stress tensor
$P_1\left(t\right)$	Legendre polynomial of the first kind , defined by eq 3.6, page 81
$P_2\left(t\right)$	Legendre polynomial of the second kind, defined by eq 3.8, page 83
P_{accept}	Probability of accepting a trial move in the course of a Monte Carlo simulation , defined by eq 2.147, page 51
$\mathcal{P}\left(\mathbf{k}\right)$	Form factor of a single chain, defined by eq 4.17, page 136
$\mathbf{p}_i, \mathbf{p}_j$	Momentum vectors
p_i	Atomic-level hydrostatic pressure , defined by eq 3.13, page 93
$P_{\mathrm{L}}\left(L_{\mathrm{c}}\right)$	Distribution of lengths between consecutive crosslinks along a chain , defined by eq B.1, page 204
$p_{\mathrm{local}}\left(V_{\mathrm{ctrl}}\right)$	Local hydrostatic pressure of atoms residing in control volume $\left(V_{\mathrm{ctrl}}\right)$, defined by eq 3.16, page 99
$\tilde{p}$	Reduced pressure used in an equation of state, e.g. the Sanchez Lacombe equation of state, page 46
Q	Partition function
$\mathbf{q}_i, \mathbf{q}_j$	Generalized coordinates vectors
Q_{NpT}	Partition function in the isothermal-isobaric ensemble, defined by eq 2.19, page 18
Q_{NVE}	Partition function in the microcanonical ensemble, defined by eq 2.13, page 17
Q_{NVT}	Partition function in the isothermal ensemble, defined by eq 2.16, page 18
Q_{NVT}^{id}	Partition function of an ideal gas in the NVT ensemble, defined by eq 2.25, page 19
r	Distance between two particles
$\mathcal{R}$	Random displacement in a Brownian Dynamics (BD) scheme, defined by eq 2.158, page 55

$\mathbf{r}_{\mathrm{cm}}$	Position of the center of mass of a group of particles, defined by eq 2.50, page 27
$\mathbf{r}_{\mathrm{cm},k}$	Position of the center of mass of an entity k, e.g. a nanoparticle
$\mathbf{R}_{\mathrm{e}}$	End-to-end vector of a random walk or polymer chain, defined by eq 2.48, page 27
$R_{\mathrm{e},0}$	Unperturbed end-to-end distance
$\mathscr{R}$	Reference configuration, usually refers to an undeformed solid (for a thorough discussion, please see ref 74), page 21
R_{full}	Contour length of a chain (length at full extension), defined by eq 2.82, page 34
R_{g}^2	Squared radius of gyration, defined by eq 2.54, page 28
$\mathbf{r}_i, \mathbf{r}_j$	Position vectors
$\mathbf{r}_{ij}$	Separation vector between points i and j, $\mathbf{r}_{ij} = \mathbf{r}_j - \mathbf{r}_i$
S	Entropy
s	Contour length along a chain, $0 \leq s \leq 1$
$\mathcal{S}_N$	Fourier transform of the probability density of a random flight, defined by eq 2.59, page 29
$S_{\mathrm{g}}(\mathbf{k})$	Structure factor of the grafted corona, defined by eq 4.20, page 140
$S_{\mathrm{tot}}(\mathbf{k})$	Total structure factor, defined by eq 4.11, page 124
$\mathbf{S}$	Radius of gyration tensor, defined by eq 2.52, page 28
$\mathbf{s}_i$	Position vector of atom i in the frame of reference with origin at the center of mass of the chain, $\mathbf{s}_i = \mathbf{r}_i - \mathbf{r}_{\mathrm{cm}}$, defined by eq 2.51, page 28
S_x^2, S_y^2, S_z^2	Eigenvalues of the radius of gyration tensor, $\mathbf{S}$, defined by eq 2.53, page 28
T	Temperature
t	Time
T_{g}	Glass transition temperature, page 8
t_{obs}	Observation time

$\tilde{T}$	Reduced temperature used in an equation of state, e.g. the Sanchez Lacombe equation of state, page 46
$\mathbf{u}$	Displacement of a material point, defined by eq 2.30, page 21
$\mathbf{u}_{\mathrm{CH-CM}}$	A vector starting from the backbone CH united atom and ending at the center of mass of the phenyl ring of PS, page 81
$\mathbf{v}_i$	Velocity of the particle i
V	Volume
$\mathcal{V}_0$	Potential energy of a single configuration of an isolated ideal chain, page 26
$V_{\mathscr{R}}$	Volume at a reference (usually undeformed) state
$\mathcal{V}$	Potential energy
$V^{\mathrm{acc}}_{\mathrm{cell},k}$	Accessible volume of the cell k
V_{ctrl}	Control volume used for calculating a local stress tensor , defined by eq 3.15, page 99
V_i	Atomic volume of atom i
$\tilde{v}$	Reduced volume used in an equation of state, e.g. the Sanchez Lacombe equation of state, page 46
W	Probability density of a random variable
$w\left(\mathbf{b}_i\right)$	Distribution function that the displacement $\mathbf{b}_i$ along a random flight lies between $\mathbf{r}_i$ and $\mathbf{r}_i + \mathrm{d}\mathbf{r}_i$, page 29
$W_N\left(\mathbf{R}_\mathrm{e}\right)$	Probability density of finding the N-th segment of a chain or the particle of a random flight after N displacements at position $\mathbf{R}_\mathrm{e}$ with respect to its start, page 29
$\mathcal{Z}_0$	Configurational partition function of a single chain, defined by eq 2.46, page 26
$\mathcal{Z}_{\mathrm{FTiMC}}$	Partition function used in FTiMC simulations, defined by eq 4.1, page 116
$\mathcal{Z}_{NpT}$	Configurational integral in the NpT ensemble, defined by eq 2.126, page 46
$\mathcal{Z}_{NVT}$	Configurational integral in the NVT ensemble, defined by eq 2.24, page 19

Nomenclature

Greek Symbols

$\alpha_{\mathrm{attempt}}$	Radius of the sphere in which candidates for slip-spring creation can be found
α, β	Cartesian component indices
α_{p}	Radius of curvature of a surface, or radius of a spherical nanoparticle
α_{s}	Radius of a polymeric segment
β_{KWW}	Stretching exponent of the KWW expression , defined by eq 3.4, page 80
δ	Hildebrand's solubility parameter , defined by eq 3.3, page 75
$\boldsymbol{\epsilon}$, $\epsilon_{\alpha\beta}$	Engineering strain, defined by eq 2.35, page 23
$\boldsymbol{\epsilon}_{\mathrm{L}}$, $\epsilon_{\mathrm{L},\alpha\beta}$	Logarithmic or true strain, defined by eq 2.38, page 23
ε	Depth of the potential well of a Lennard-Jones potential
η	Viscosity
Γ	Point in phase space (set of coordinates and momenta corresponding to one microscopic state), page 14
γ	Total shear
$\dot{\gamma}$	Shear rate
κ_0	Strength of polymer mean-field interactions, connected to the isothermal compressiblity, defined by eq 4.3, page 117
κ_{T}	Isothermal compressibility
Λ	Thermal wavelength, defined by eq 2.26, page 20
$\lambda_{(\hat{\mathbf{n}})}$	Stretch ratio in the direction $\hat{\mathbf{n}}$, defined by eq 2.32, page 22
ν_{diff}	Pre-exponential factor of the rate of an individual jump of one end of a slip-spring
ϕ	Torsion angle (or azimuthal angle)
$\phi(\mathbf{r})$	Segment density
φ	Volume fraction

π	3.1415926 ...
ρ_{ens}	Probability density of an equilibrium ensemble
$\rho_{\mathrm{cell},k}$	Density of the cell k of a discretization grid
$\rho\left(\mathbf{r}\right)$	Local density at position **r**
ρ_{mol}	Molecular density, i.e. number of molecules (or polymeric chains) per unit volume
$\tilde{\rho}$	Reduced density used in an equation of state, e.g. the Sanchez Lacombe equation of state, page 46
$\boldsymbol{\sigma}, \sigma_{\alpha\beta}$	Instantaneous stress tensor
σ_{g}	Grafting density
$\widehat{\sigma}_{\mathrm{g}}$	Reduced grafting density, page 129
$\boldsymbol{\sigma}_i$	Atomic-level stress tensor of atom i
σ	Distance at which the Lennard-Jones potential becomes zero (collision diameter)
$\boldsymbol{\sigma}_{\mathrm{local}}$	Local stress tensor , defined by eq 3.15, page 99
$\boldsymbol{\tau}, \tau_{\alpha\beta}$	Thermodynamic or equilibrium stress tensor
τ_0	Kuhn segment relaxation time (Rouse model), defined by eq 2.101, page 38
τ_{c}	Segmental relaxation time , defined by eq 3.5, page 81
$\tau_{\mathrm{c,g}}$	Correlation time at the glass transition temperature, T_{g} , defined by eq 3.7, page 83
τ_{d}	Disentanglement or reptation time, page 43
τ_{e}	Relaxation time of an entanglement strand in the tube model, page 42
τ_{lib}	Characteristic time of fast liberations described by a mKWW expression , defined by eq 3.4, page 80
τ_{R}	Rotational relaxation time, obtained by the Rouse model, defined by eq 2.100, page 38

τ_{seg}	Segmental relaxation time of the KWW epxression , defined by eq 3.4, page 80
$\tau_{\text{vM},i}$	Atomic-level von Mises shear stress , defined by eq 3.14, page 94
τ_{υ}	Relaxation time of mode υ, page 38
θ	Polar angle
$\mathbf{\Omega}_k$	Orientation of entity k, e.g. Eulerian angles
Ω	Number of states of a system
ω	Angular frequency
υ	Mode index, page 38
ζ	Friction coefficient of a polymer segment in units of kg/s

Mathematical Notation

$\mathbf{A}, \mathbf{B}, ..., \mathbf{Z}, \mathbb{A}, \mathbb{B}, ..., \mathbb{Z}$	Vectors or tensors
$\mathscr{N}, \mathscr{O}, \mathscr{R}$	States of a system
$\langle \ldots \rangle_{\text{ens}}$	Ensemble average
$\langle \ldots \rangle_t$	Time average
$\binom{a}{b}$	Binomial coefficient, $\binom{a}{b} = \frac{a!}{b!(a-b)!}$ where $a!$ is the factorial of a
$\dot{(\cdot)}, \ddot{(\cdot)}, \ldots$	First (dx/dt), second, etc. time derivative
$\Delta \cdot$	Increment in a variable
$\delta(\cdot)$	Dirac delta function, in a heuristic definition, $\delta(x) = \begin{cases} +\infty, & x = 0 \\ 0, & x \neq 0 \end{cases}$ and $\int_{-\infty}^{\infty} \delta(x)\, \mathrm{d}x = 1$
$\delta_{\alpha\beta}$	Kronecker's delta $\delta_{\alpha\beta} = \begin{cases} 1, & \alpha = \beta \\ 0, & \alpha \neq \beta \end{cases}$
$\mathrm{d} \cdot / \mathrm{d}x$	Derivative with respect to x
$\partial / \partial \mathbf{x} \equiv \nabla_{\mathbf{x}}$	Gradient operator with respect to the vectorial quantity $\mathbf{x}$

$\left.\frac{\mathrm{d}\cdot}{\mathrm{d}x}\right\vert_{x=x_0}$	Derivative with respect to x at $x = x_0$
$\partial\cdot/\partial x$	Partial derivative with respect to x
$\left.\frac{\mathrm{d}\cdot}{\mathrm{d}x}\right)_{y_1,y_2,\ldots}$	Partial derivative with respect to x, while keeping y_1, y_2 , $\ldots$ constant
d·	Differential
$\mathcal{D}\mathbf{r}_i\left(\bullet\right)$	Functional integration over all possible conformations ("paths") of chain i.
$a!$	Factorial function, $a! = \prod_{j=1}^{a} j$
$\Gamma\left(x\right)$	Gamma function, defined via the Euler integral of the second kind: $\Gamma\left(x\right) = \int_0^\infty y^{x-1}e^{-y}\mathrm{d}y$ for $\mathrm{Re}\left(x\right) > 0$.
$H\left(x\right)$	Heaviside's unit step function, $H\left(x\right) = \begin{cases} 0, & x < 0 \\ 1 & x > 0 \end{cases}$
$\cdot_{i,j,\ldots}$	Enumeration of particles, molecules, etc.
$\cdot\wedge\cdot$	Logical conjuction operator, mostly used for describing connectivity
$\min\left(a, b\right)$	The lower of the two values a, b
$P(A\mid B)$	Conditional probability of event A given the event B
$\{\cdot,\cdot,\ldots,\cdot\}$	Set, i.e. a collection of distinct objects
$\otimes$	Tensor product
$\mathscr{A} \to \mathscr{B}$	Transition from the state $\mathscr{A}$ to the state $\mathscr{B}$
$\mathrm{Tr}\left(\cdot\right)$	Trace, i.e. the sum of the elements on the main diagonal of a square tensor
$\mathbb{A}^{\mathrm{T}}$	The transpose of matrix $\mathbb{A}$, formed by turning rows into columns and vice versa.

Abbreviations

BD Brownian Dynamics

CG coarse grained

GC-MC Coarse Grained Monte Carlo

CLF contour-length fluctuation

CPU central processing unit

CR constraint release

DFT Density Functional Theory

DPD Dissipative Particle Dynamics

DSC Differential Scanning Calorimetry

EoS Equation of State

FE Finite Elements

FTiMC Field Theory-inspired Monte Carlo

GPU graphics processing unit

IBI Iterative Boltzmann Inversion

kMC kinetic Monte Carlo

LAMMPS Large-scale Atomic/Molecular Massively Parallel Simulator

LD Langevin Dynamics

MC Monte Carlo

MD Molecular Dynamics

mKWW modified Kohlrausch - Williams - Watts

MSD mean-square displacement

NMR Nuclear Magnetic Resonance

PE Polyethylene

PI polyisoprene

PMF Potential of Mean Force

PNCs polymer-matrix nanocomposites

PP primitive path

PRISM Polymer Reference Interaction Site Model

PS polystyrene

SANS Small Angle Neutron Scattering

SCF Self Consistent Field

TST Transition State Theory

WLF Williams - Landel - Ferry

1 Introduction

In this short introductory chapter, the framework of the thesis is set. We will explain why polymer matrix nanocomposites is an interesting field to work on and why multiscale modeling is not a luxury but a necessity. Moreover, starting from experimental observations, we will pose the relevant *questions* which shape the present thesis.

1.1 Polymer-Matrix Nanocomposites

In the simplest sense, a *composite* is an object made up of two or more distinct parts. Within materials science and engineering, composite materials are put together from two or more components that remain distinct or separate within the final product. Composites can be found anywhere, being as simple as a matrix material that envelops a reinforcing material, like concrete surrounding steel bars, helping it prevent failure under tension. The *real challenge* is that the options for making a composite are almost limitless, but only a few combinations of materials will *combine synergistically*, and the design criteria may not be obvious. The observation that, other things being equal, the effectiveness of the filler increases with an increase in *surface to volume ratio* has provided large impetus to the shift from micron- to nanosized particles. With the appearance of synthetic methods that can produce nanometer sized fillers, resulting in an enormous increase of surface area, a new class of materials emerged, known as *polymer-matrix nanocomposites (PNCs)*, i.e., polymer hosts filled with nanoparticles, which possess properties that typically differ significantly from those of the pure polymer, even at low nanoparticle concentrations.[1,2]

Nanocomposite materials contain particles of size $\alpha_{\mathrm{p}} \sim 10$ nm, dispersed at a volume fraction, φ, often lower than 10^{-3} within a polymer matrix, are characterized by particle number densities of $\rho_{\mathrm{n}} = 3\varphi / \left(4\pi\alpha_{\mathrm{p}}^3\right) \approx 10^{20}$ m^{-3}, interfacial areas per unit volume of $3\varphi/\alpha_{\mathrm{p}} \approx 10^6$ m^{-1}, and interparticle spacings, $\rho_{\mathrm{n}}^{-1/3} - 2\alpha_{\mathrm{p}} \approx 10$ nm that are commensurate with the particle dimensions, $\alpha_{\rm p}$ and the radii of gyration of matrix chains, $R_{\rm g} \approx 10$ nm.

The practice of adding nanoscale filler particles to reinforce polymeric materials can be traced back to the early years of the composite industry, in the second half of the 19th century. Charles Goodyear, inventor of vulcanized rubber, attempted to prepare nanoparticle-toughened automobile tires by blending carbon black, zinc oxide, and/or magnesium sulfate particles with vulcanized rubber.[3] Another example was the clay-reinforced resin known as Bakelite that was introduced in the early 1900's as one of the first mass-produced polymer-nanoparticle composites and fundamentally transformed the nature of practical household materials.[4–7] Then, a long period of time passed till the early 1990s when it was first demonstrated that the thermal and mechanical properties of Nylon-6 were improved by the addition of a few percent (2-4 % w/w) mica-type layered silicates to the extent that it could be used in an automotive engine compartment.[8,9]

Even though some property improvements have been achieved in nanocomposites, nanoparticle dispersion is difficult to control, with both thermodynamic and kinetic processes playing significant roles. It has been demonstrated that dispersed spherical nanoparticles can yield a range of multifunctional behavior, including a viscosity decrease, reduction of thermal degradation, increased mechanical damping, enriched electrical and/or magnetic performance, and control of thermomechanical properties.[10–14] The tailor-made properties of these systems are very important to the manufacturing procedure, as they fully overcome many of the existing operational limitations. As a final product, a polymeric matrix enriched with dispersed particles may have better properties than the neat polymeric material and can be used in more demanding and novel applications. Therefore, an understanding and quantitative description of the physicochemical properties of these materials is of major importance for their successful production.

As part of this renewed interest in nanocomposites, researchers also began seeking design rules that would allow them to engineer materials that combine the desirable properties of nanoparticles and polymers. In light of the diversity of polymers and nanoparticles, the potential for use of PNCs is nearly limitless. The ensuing research revealed a number of key challenges in producing nanocomposites that exhibit a desired behavior. The greatest stumbling block to the large-scale production and commercialization of nanocomposites is the dearth of cost-effective methods for controlling the *dispersion of the nanoparticles* in polymeric hosts. The nanoscale particles typically aggregate, which negates any benefits associated with the nanoscopic dimension. PNCs generally possess nonequilibrium morphologies due to the complex interplay of enthalpic and entropic interactions leading to particle aggregation, particle bridging interactions, and phase separation at various length scales.[15,16] The second challenge is associated with understanding and predicting property enhancements of these materials, which are intimately connected to their morphology.

1.2 Multiscale Modeling

Understanding the fascinating and complex structure and dynamics of polymeric materials has been an ongoing challenge for many decades. From the point of view of molecular simulations, the spectrum of length and time scales associated with polymer melts of long chains poses a formidable challenge to studying the long-time dynamics.[17,18] The topological constraints arising from chain connectivity and uncrossability (entanglements) dominate intermediate and long-time relaxation[19] and transport phenomena when polymers become sufficiently long. Atomistic molecular simulations of dense phases of soft matter prove to be difficult for many systems across length and time scales of practical interest. Even coarse-grained particle-based simulation methods may not be applicable due to the lack of faithful descriptions of polymer-polymer and polymer-surface interactions. Since complex interactions between constituent phases at the atomic level ultimately manifest themselves in macroscopic properties, a large range of length and time scales must be addressed and a combination of modeling techniques is therefore required to simulate meaningfully the bulk-level behavior of nanocomposites.[20]

Soft condensed matter is a relatively new term describing a huge class of rather different materials such as colloids, polymers, membranes, complex molecular assemblies, complex fluids etc. Though these materials are rather different in their structures, there is one unifying aspect, which makes it very reasonable to treat such systems from a common point of view. Compared to "hard matter" the characteristic *energy density is much smaller*. While the typical energy of a chemical bond (C-C bond) is about 3×10^{-19} J $\approx 80k_\mathrm{B}T$ at room temperature of 300 K, the nonbonded interactions are of the order of $k_\mathrm{B}T$ and allow for strong density fluctuations even though the molecular connectivity is never affected (k_B is the Boltzmann's constant). To give a rough reasoning for this, we can compare the cohesive energy density, which gives a first estimate of the elastic constants, between a typical "hard matter" crystal to soft matter. The ratio between the two shows that polymeric systems are typically 100 to 10000 times softer than classical crystals. As a consequence the *average thermal energy* $k_\mathrm{B}T$ is not negligible for these systems any more, but rather *defines the essential energy scale*. This means that entropy, which typically is of the order of $k_\mathrm{B}T$ per degree of freedom, plays a crucial role. Especially in the case of macromolecules, this mainly means intramolecular entropy, which for a linear polymer of length N contributes to the free energy a term of order

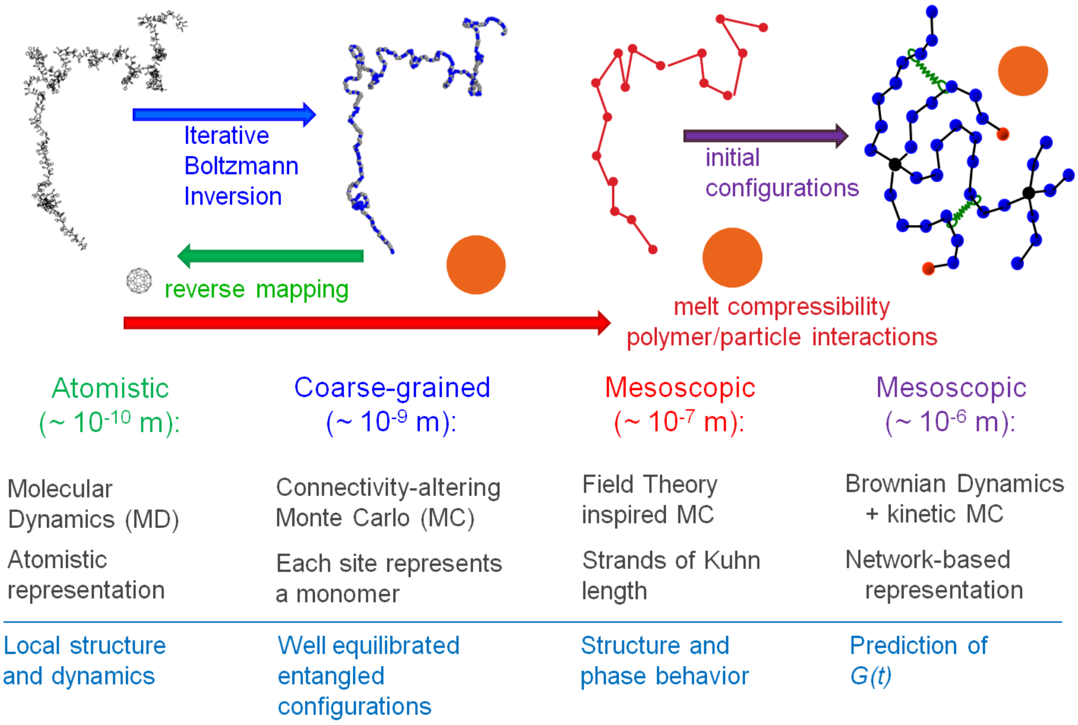

Figure 1.1: Levels of modeling developed in this thesis, connections between them, methods employed in each one and main simulation observables.

$Nk_\mathrm{B}T$, representing about 90% of the free energy of polymeric materials.[21] As an immediate consequence it is clear that typical quantum chemical electronic structure calculations (Hartree-Fock or Density Functional Theory (DFT)) which focus on obtaining the energy as a function of nuclear coordinates cannot be sufficient to characterize soft condensed matter and will even be less sufficient to properly predict/interpret macroscopic properties. These methods provide the solid molecular scale foundations for the multiscale modeling method discussed in this thesis. However, these methods are beyond the scope of our work.

1.2.1 Atomistic Molecular Dynamics (MD)

The stepping stone of our multiscale strategy (Figure 1.1) is atomistic MD (please refer to Section 2.4.1 on page 49 for a brief description). As accurate MD potentials are developed for a broad range of materials based on quantum chemistry calculations and with the increase of supercomputer performance, atomistic MD simulations have become a very powerful tool for analyzing the complex physical phenomena of polymeric materials, including dynamics, viscosity, shear thinning and α- and β-relaxations. However, as discussed above, entangled polymer systems are characterized by a wide range of spatial and temporal scales. It is still not feasible to perform atomistic MD simulations of highly entangled polymer chain systems, due to their large equilibration and relaxation times, long-range electrostatic interactions and tremendous number of atoms. The atomistic MD model for such a system, with a typical size of about a micrometer and a relaxation time on the scale of microseconds, would consist of billions of atoms and would require billions of time steps to run, which is obviously beyond the capability of the technique, even with the most sophisticated supercomputers available today.

1.2.2 Coarse Grained Monte Carlo (GC-MC)

A robust sampling of the configuration space of polymeric substances is a prerequisite for the reliable prediction of their physical properties. The constraints posed by atomistic MD simulations can be overcome by resorting to Monte Carlo (MC) simulations (please refer to Section 2.4.2 on page 51). Through the design of efficient unphysical moves, configurational sampling (Section 2.1.1/iii, page 15) can be dramatically enhanced. MC moves such as concerted rotation,[22] configurational bias,[23,24] and internal configurational bias[25] have thus successfully addressed the problem of equilibrating polymer systems of moderate chain lengths. However, even these moves prove incapable of providing equilibration when applied to long-chain polymer melts. A solution to that problem was given by the development and efficient implementation of a chain connectivity-altering MC move, end-bridging.[26,27] Using end-bridging, atomistic systems consisting of a large number of long chains, up to C_{1000}, have been simulated in full atomistic detail.[27] Despite its efficiency in equilibrating long-chain polymer melts, end-bridging cannot equilibrate monodisperse polymer melts; a finite degree of polydispersity is necessary for the move to operate. While this is not a drawback in modeling industrial polymers, which are typically polydisperse, an ability to equilibrate strictly monodisperse polymers is highly desirable for comparing against theory or model experimental systems. Morover, end-bridginig relies on the existence of chain ends, rendering itself inappropriate for dense phases of chains with nonlinear architectures. These limitations have been overcome by the introduction of Double Bridging (DB) and Intramolecular Double Rebridging (IDR).[28,29] The key innovation of those moves is the construction of two bridging trimers between two different chains, as far as the former is concerned, or along the same chain, as far as the latter move is concerned, thus preserving the initial chain lengths.

Even MC simulations using atomistic forcefields have not been extremely efficient, as Doxastakis et al. have shown.[30] The hard interactions between atoms reduce the acceptance rate of the moves. Thus, it is essential to resolve to parallel tempering techniques in order to allow motion of the system in its phase space.[31] For the second level of our simulation hierarchy, we follow the work of Spyriouni et al.,[32] combining connectivity-altering MC simulations with soft potentials obtained from Iterative Boltzmann Inversion (IBI) of atomistic polystyrene (PS) structures.[33] Following Milano and Müller-Plathe,[33] the coarse-grained model consists of sequences of superatoms centered on methylene carbons of two different types, according to the stereochemical kind of the dyad they belong to. The corresponding force-field contains bond stretching, bond angle bending and nonbonded terms. The intramolecular potentials (bond and angle) are based on sums of Gaussians. For the nonbonded part, numerical potentials are used.

Well equilibrated coarse-grained configurations can been reverse-mapped to atomistic ones, thus establishing the green link indicated in Figure 1.1. The reverse mapping procedure retains the tacticity which is implicit in the coarse-grained representation, while regrowing atomistic sites by a quasi-Metropolis procedure that avoids unphysical configurations. Subsequent potential energy minimizations and local MC moves allow the full relaxation of the system to a potential energy minimum. The positions of the atoms which served as the centers of the coarse-grained sites remain constant throughout the reverse-mapping, thus, preserving the long-length scale features, as those were equilibrated during the GC-MC simulations.

Coarse graining, MC equilibration, reverse-mapping and atomistic MD simulations of PS - C_{60} melts and glasses are presented in Chapter 3.

1.2.3 Mesoscopic Simulations

A major challenge in simulating realistic PNCs is that neither the length nor the time scales can be adequately treated by means of atomistic simulations alone, because of the extensive computational load. Until relatively recently, a somewhat neglected level of description in materials modeling has been the *mesoscopic* regime, lying between atomic (or super-atomic like) particles and Finite Elements (FE) representations of a continuum, and covering characteristic length scale of 10^{-8} m to 10^{-5} m. At this scale, the system is still too small to be regarded as a continuum, yet too large to be simulated efficiently using atomic models. In a more precise way, a *mesoscale* can be defined as an intermediate length scale at which the phenomena at the next level below (e.g. particle motions) can be regarded as having been equilibrated, and at which new phenomena emerge with their own characteristic time scales.

Among the several mesoscopic methods applied to the study of polymers, Self Consistent Field (SCF) theory has been a well-founded tool.[34] This method adopts a field-theoretic description of the polymeric fluids and makes a saddle-point (mean-field) approximation. An alternative to invoking the saddle-point approximation is performing a normal Metropolis MC simulation, with the potential energy of the system given by field-theoretic functionals. One of the first attempts has been made by Laradji et al.[35] for polymer brushes and then by Daoulas and

Müller[36] and Detcheverry et al.[37,38] for polymeric melts. The coordinates of all particles in the system are explicitly retained as degrees of freedom and evolve through MC moves. The term Field Theory-inspired Monte Carlo (FTiMC) tries to capture the essence of the method. We adapt this strategy to nanocomposite melts, where spherical particles (either bare or grafted) are dispersed in the polymeric matrix.

MC simulations inspired by the polymer mean field theory in order to study the structural features of PS - grafted silica nanoparticles are presented in Chapter 4.

Tracking the motion of mesoscopic particles requires the use of stochastic dynamics.[39] To this end, we provide initial configurations from FTiMC simulations to Brownian Dynamics (BD) simulations. Polymer beads are envisioned as moving through a viscous medium which consists of the remaining polymer. This picture is exactly the basis of the Rouse model for unentangled polymer dynamics (Section 2.3.4/i on page 36). By taking a step further, we introduce the effect of chain entanglement by considering entropic springs connecting beads of neighboring chains. The goal of this approach is to develop a consistent simulation implementation of the reptation theory (Section 2.3.4/v on page 41). Friction coefficients needed for treating the missing degrees of freedom are obtained by atomistic simulations, while conservative interactions between the beads are parameterized by an appropriate equation of state.

An equaton of state - based mesoscopic simulation strategy for the study of entangled polymer dynamics is presented in Chapter 5.

1.3 Motivation

PNCs have been an area of intense industrial and academic research for the past twenty years. Irrespectively of the measure employed - articles, patents, or funding - efforts in PNCs have been exponentially growing worldwide over the last ten years. PNCs represent a radical alternative to conventional filled polymers or polymer blends - a staple of the modern plastics industry. Considering the multitude of potential nanoparticles, polymeric resins, and applications, the field of PNCs is immense.[40]

Despite the unprecedented efforts placed on PNCs research there are still open questions which have not been definitely addressed yet. In the following we will summarize only a few of them, introducing the work carried out in this thesis.

1.3.1 Segmental Dynamics and the Glass Transition Temperature

When cooling a glass forming liquid, instead of freezing at a well defined temperature, one observes a huge increase of the viscosity which takes place continuously. Such glass formers can be either simple liquids or polymer liquids, and many features are similar in both regarding the glass transition. One defines the *glass transition temperature*, T_{g}, as the temperature at which the dominant relaxation time on the molecular scale (or monomeric scale in the case of polymers) reaches about ~ 100 s, which corresponds typically to a viscosity of 10^{12} Pa s in the case of simple liquids. Typically for such glass forming liquids, the viscosity increases by twelve orders of magnitude over a change of temperature of about 100 K down to T_g. The underlying mechanisms involved in this dramatic increase are still poorly understood.[41,42]

Experimental results on polymer dynamics and the glass transition in PNCs are not conclusive concerning the mechanism and the details of this modification. Increases or decreases in T_{g} by as much as 30 K[43] have been reported depending on polymer - nanoparticle interactions. Reduction of T_{g} has been reported in the case of weak interactions between filler and polymer.[44] In other cases the addition of nanoparticles causes no significant change to the glass transition of the polymer, presumably because effects causing increase and decrease of polymer mobility are present simultaneously and effectively canceling out each other.[45] Moreover, strong interactions between the filler particles and the polymer suppress crystallinity, yielding new segmental relaxation mechanisms in semicrystalline polymers, originating from polymer chains restricted between condensed crystal regions and the semi-bound polymer in an interfacial layer with strongly reduced mobility.[46]

Concerning the spatial extent of the T_{g}-shift, several studies[47,48] on PNCs show an increase of the glass transition temperature, suggesting that the mobility of the entire volume of the polymer is restricted by the presence of the nanoparticles. However, there are many experimental results suggesting that the restriction of chain mobility caused by the nanoparticles does not extend throughout the material but affects only the chains within a few nanometers of the filler surface.[49] The existence of such an interfacial layer seems relatively well-established in the case of silica-filled elastomers, however its exact nature is not well understood: experimental results have been described in terms of one or two distinct interfacial layers or a gradual change in dynamics with changing distance from the particle.

A detailed study of the (global and local) segmental dynamics and the glass transition of a PS-C_{60} melt is presented in Chapter 3.

1.3.2 Enhancing Nanoparticle Dispersion by Surface Grafting

One of the biggest challenges is the rational control of *filler clustering* or *aggregation*, which often adversely affects material properties. The idea of achieving a good, uniform nanoparticle dispersion state has been the focus of considerable research, especially because of its favorable impact on optical and some mechanical behavior of the resulting composites.[50,51] In the past few years, several research groups have modified the surface of nanoparticle fillers in an effort to improve their dispersion in a polymer matrix. A promising strategy for controlling the dispersion and morphology of PNCs is to graft polymer chains onto the nanoparticles to form a brush layer.[16] The free chain/brush interfacial interactions may be "tuned" by controlling grafting density, σ_{g}, the degrees of polymerization of the grafted chains, N_{g}, and of the polymer host, N_{f}, the nanoparticle size, α_{p}, and its shape. For example, if nanoparticles are grafted with chains compatible with the matrix polymer, filler dispersion is favored.[52–56] Motivated by this concept, experimentalists have synthesized nanometer sized particles with high surface grafting density.[54,57,58] At fixed polymer chemistry, when the molecular weight of matrix polymer is lower than that of grafted polymer, nanoparticles disperse. On the contrary, if the molecular weight of the matrix polymer is higher than that of the grafted polymer, nanoparticles are thought to aggregate.[54] Since both the matrix and the brush have the same chemical structure, the immiscibility for longer matrix chains is entropic in origin and attributable to the concept of "brush autophobicity".[52,59–63]

A detailed discussion on the scaling of grafted polymer layers and the contribution of this thesis to the understanding of this phenomenon is presented in Chapter 4.

1.3.3 Mechanical and Rheological Properties

The dispersion of micro- or nano-scale rigid particles within a polymer matrix often - but by no means always - produces an enhancement in the properties of these materials. As mentioned earlier, the most important application of this sort involves rigid inorganic particles (originally carbon black, later also silica) in a cross-linked elastomer matrix, where an improvement of mechanical properties is sought. This so-called *rubber reinforcement* is a complex phenomenon, which may involve an enhanced grip of tires on wet roads, an improved resistance to wear and abrasion, and an increase of tire's ultimate mechanical strength (toughness, tearing resistance).

There is a variety of phenomena seeking an explanation. For the purpose of this introduction we will focus on a subset of them. Under very small cyclic deformations, there is a linear viscoelastic regime characterized by a very significant increase (sometimes even by two orders of magnitude compared to the reference unfilled network) of the in-phase storage modulus, both under elongation and under shear.[64] At medium-to-large strains, filled elastomers exhibit a markedly non-linear response which is absent in unfilled elastomers ("Payne effect").[65] The degree of non-linearity increases strongly with particle loading. An order-of-magnitude drop in the modulus is often observed on going to 5–10 % deformation (under shear), bringing the asymptotic modulus of the filled systems much closer to that of the reference unfilled network.

Other related effects are commonly observed in filled elastomers. One is deformation hysteresis ("Mullins effect"): under cyclic deformation, the elastic modulus in the first cycle is higher than that in the following ones.[66] This points to some kind of "damage" of the material, which, however, is often reversible. The original properties can be recovered within a few hours, by high-temperature annealing of the sample. Secondly, fillers affect also the dissipative, out-of-phase components of the modulus. This is expected, since, probably, friction of the polymer chains against the filler surfaces, or of two particles against each other produces new energy dissipation mechanisms, which are absent in unfilled elastomers. Elastic and dissipative effects likely share a common origin. Finally, reinforcement effects have a remarkable temperature dependence. The small-strain (linear) modulus of filled rubbers decreases with temperature, pointing to important enthalpic effects. The situation is completely reversed compared to unfilled elastomers, where the modulus increases linearly with absolute temperature due to the entropic nature of rubber elasticity.

The first steps towards a model capable of predicting the non-linear rheology of reinforced rubbers is presented in Chapter 5.

1.4 Aim and Outline of the Thesis

The present thesis aims at developing novel modeling and simulation methodologies by linking the microscopic, mesoscopic and macroscopic levels in a *rigorously predictive* and *computationally tractable* way to address the structure and properties of *industrially highly relevant nanocomposite materials*. Starting from atomistic molecular simulations, parameters and functional relations derived from them will serve as an input for higher level modeling techniques, without using empirical, physically non-meaningful fitting parameters. Each modeling level should capture the correct physics behind the phenomena by receiving input from more fundamental levels and providing input to more coarse-grained ones. Between atomistic simulation and macroscopic mechanical response there are at least eight orders of magnitude on the length scale and seven orders of magnitude on the time scale to be bridged, and this has to be done without significant loss of relevant information, else there will be no predictive capability. Methods have been developed as general as possible, allowing their application to a wide class

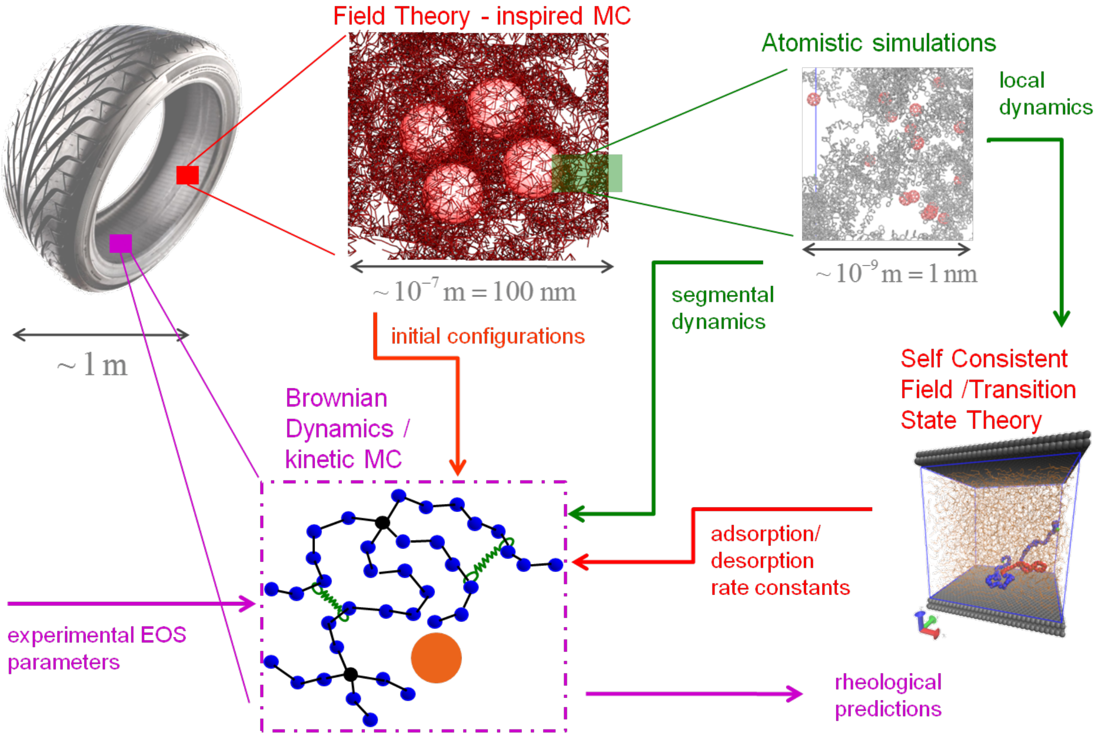

Figure 1.2: Our modeling hierarchy, as it can be applied to predicting the rheological behavior of cis-1,4 polyisoprene nanocomposite melts, which are used for the manufacturing of “green tires”.

of systems.

The quantitative relationships between composition (volume fraction, chemical constitution, shape and size of nanoparticles, chemical constitution and molar mass distribution of polymer matrix, areal density and molar mass distribution of grafted chains that may be present), processing conditions, degree of dispersion of the nanoparticles, dynamics of the matrix chains, and macroscopic properties are still elusive. Molecular simulation holds great promise as a means for understanding and predicting these relationships. This thesis hopes to contribute to the advance of the simulation field. In Figure 1.2, a unified simulation approach to the study of “green tires” is presented. Nanoparticle-filled elastomers constitute a promising route to reducing fuel consumption (and CO_2 emissions) in the automotive industry. The different levels of modeling (Figure 1.1), as well as the necessary interconnections between them, are drawn towards the estimation of the mechanical and rheological properties of silica-reinforced rubber.

In the following Chapter, a brief self-contained summary of statistical mechanics, continuum mechanics, polymer physics and molecular simulation concepts is provided. We limit ourselves to the absolute minimum of definitions and methods to be presented, trying not to sacrifice consistency and rigor. Chapter 2 contains the common background of all methods developed in the thesis. Subsequent chapters seek answers to specific *questions* regarding PNCs. In Chapter 3, the segmental dynamics and stresses of PS - C_{60} melts and glasses are thoroughly investigated. Despite the fact that we have not been able to explain the macroscopic viscosity reduction in terms of microscopic observables, several advances have been made towards an understanding of this phenomenon. In Chapter 4 the scaling of grafted polymer brushes is studied as a function of the molecular properties of the grafted and matrix chains. The equation of state - based model for entangled polymer dynamics is formulated in Chapter 5. Each Chapter is self-contained, incorporating its introduction (summarizing previous work and experimental findings) and the main conclusions reached. However, a separate list of the innovations at three levels (methodology, physical insight and computational tools) is provided in Chapter 6. Finally, in Chapter 7 an outlook of closely related future work is presented.

2 Theoretical Background

In this chapter we introduce definitions and background knowledge that will form the basis of the new concepts and methods to be developed in the subsequent chapters. We start our discussion by introducing the formalism of statistical mechanics and briefly describing the statistical ensembles used in computer simulations. Then, the concepts of continuum mechanics are reviewed both from the viewpoint of solid mechanics and rheology. A brief description of polymer physics follows. Analytical polymer theories usually address simplified models of polymer chains, which capture universal features such as the chain topology. Despite lacking many fine details, such models still manage to predict many physical properties of polymer solutions, melts and networks and capture the relevant physics of a phenomenon. Many polymer-specific effects and properties, such as rubber elasticity, the viscoelastic rheological response of melts in the terminal region, and overall molecular shapes in melts in the bulk and next to surfaces, are similar for polymers of different chemical structures. Finally, the simulation methods used in the thesis are briefly described and molecular simulation observables are presented from a critical point of view.

2.1 Concepts of Classical Statistical Mechanics

2.1.1 Motion in Phase Space

Statistical physics describes a system of N particles at a given state as one point in $6N$-dimensional phase space, containing the atom positions and momenta (and neglecting the internal degrees of freedom).[67] In classical mechanics, the state of the system is completely specified in terms of a set of *generalized coordinates* $\{\mathbf{q}_i\}$ and *generalized momenta* $\{\mathbf{p}_i\}$, where $i = 1, \ldots, N$.[68] We will refer to the $3N$-dimensional set from which the generalized coordinates of the system $\{\mathbf{q}\} \equiv \{\mathbf{q}_1, \mathbf{q}_2, \ldots, \mathbf{q}_N\}$ take on values as *configuration space*, while we refer to the $3N$-dimensional set from which the generalized momenta $\{\mathbf{p}\} \equiv (\mathbf{p}_1, \mathbf{p}_2, \ldots, \mathbf{p}_N)$

take on values as *momentum space*. Any instantaneous *microscopic* state of the system can be written as a point:

$$\Gamma = (\{\mathbf{q}_i\}, \{\mathbf{p}_i\}) \tag{2.1}$$

in the *phase space* of the system. The set of values of the macroscopic observables, such as temperature, pressure, etc., describes the system's *macroscopic* state. One macroscopic state combines all the microscopic states that provide the same values of the macroscopic observables, defined by the macroscopic state.

If we know the *Hamiltonian*, $\mathcal{H}(\{\mathbf{q}_i\}, \{\mathbf{p}_i\}, t)$, for the system, then the time evolution of the quantities $\mathbf{q}_i$ and $\mathbf{p}_i$ ($i = 1, \ldots, N$) is given by Hamilton's equations of motion

$$\dot{\mathbf{p}}_i \equiv \frac{\partial \mathbf{p}_i}{\partial t} = -\frac{\partial \mathcal{H}(\{\mathbf{q}_i\}, \{\mathbf{p}_i\}, t)}{\partial \mathbf{q}_i} \tag{2.2}$$

and

$$\dot{\mathbf{q}}_i \equiv \frac{\partial \mathbf{q}_i}{\partial t} = \frac{\partial \mathcal{H}(\{\mathbf{q}_i\}, \{\mathbf{p}_i\}, t)}{\partial \mathbf{p}_i} \tag{2.3}$$

where $i = 1, 2, \ldots, N$ and $\partial/\partial\mathbf{x} \equiv \nabla_{\mathbf{x}}$ symbolizes the gradient operator with respect to the vectorial quantity **x**. As the system evolves in time and its state changes, the system point traces out a trajectory in Γ-space. Since the subsequent motion of a classical system is uniquely determined from the initial conditions, it follows that no two trajectories in phase space can cross. If the Hamiltonian $\mathcal{H}$ does not depend explicitly on time, then $\mathcal{H}$ is a constant of the motion. Such is the case for *conservative* systems.

2.1.1/i Time average

Any property of the system, $\mathcal{A}$, is then a function of the points traversed by the system in phase space. The instantaneous property at a time t is $\mathcal{A}(\Gamma(t))$ and the macroscopically meaningful observable property $\mathcal{A}_{\text{obs}}$ is the time average of this,

$$\mathcal{A}_{\text{obs}} = \langle \mathcal{A}(\Gamma(t)) \rangle_t = \lim_{t_{\text{obs}} \to \infty} \frac{1}{t_{\text{obs}}} \int_0^{t_{\text{obs}}} \mathcal{A}(\Gamma(t))\, \mathrm{d}t \tag{2.4}$$

In experiments, the *time average* comes about quite naturally, since almost all experimental methods measure over much longer time scales than the longest relaxation time of the system. A straightforward approach, in order to get $\mathcal{A}$ from molecular simulations, is to determine a time average, taking a discrete sum over M time steps of length Δt:

$$\mathcal{A}_{\text{obs}} \simeq \lim_{M \to \infty} \frac{1}{M \Delta t} \sum_{i=1}^{M} \mathcal{A}(\Gamma(i\Delta t))\, \Delta t \tag{2.5}$$

This is the approach undertaken in Molecular Dynamics (MD) simulations, where the atoms trajectory is followed as a function of time, so it is straightforward to obtain the average.

2.1.1/ii Phase space probability density

When we deal with real systems, we can never specify exactly the state of the system, despite the deterministic character of its motion in phase space. There will always be some uncertainty in the initial conditions. Therefore, it is useful to consider Γ as a stochastic variable and to introduce a probability density $\rho\left(\Gamma, t\right)$ on the phase space. In doing so, we envision the phase space filled with a continuum (or fluid) of state points. If the fluid were composed of individual discrete points, then each point would be equipped with a probability in accordance with our initial knowledge of the system and would carry this probability for all time, since probability is conserved. Because state points must always lie somewhere in the phase space, we have the normalization condition

$$\int_{\Gamma} \rho\left(\Gamma, t\right) \mathrm{d}\Gamma \equiv \int_{\Gamma} \rho\left(\{\mathbf{q}_i\}, \{\mathbf{p}_i\}, t\right) \mathrm{d}^{3N}p \, \mathrm{d}^{3N}q = 1 \tag{2.6}$$

where the integration takes place over the entire phase space. Similarly, the probability of finding the system in a small finite region D of Γ-space at time t is found by integrating the probability density over that region:

$$P\left(D, t\right) = \int_{D} \rho\left(\{\mathbf{q}_i\}, \{\mathbf{p}_i\}, t\right) \mathrm{d}^{3N}p \, \mathrm{d}^{3N}q \tag{2.7}$$

The probability density for finding a system in the vicinity of Γ depends on the macroscopic state of the system, i.e. on the macroscopic constraints defining the system's size, spatial extent, and interactions with its environment. A set of microscopic states distributed in phase space according to a certain probability density is called an *ensemble*. A very important measure of the probability distribution of an equilibrium ensemble is the *partition function* Q. This appears as a normalizing factor in the probability distribution defined by the ensemble.

2.1.1/iii Ensemble average

The *ergodic hypothesis*, originally due to L. Boltzmann,[69] states that, over long periods of time, the time spent by a system in some region of the phase space of microstates with the same energy is proportional to the volume of that region, i.e., that all accessible microstates are equiprobable over a long period of time. Ergodicity is based on the assumption (provable for some Hamiltonians) that any dynamical trajectory, given sufficient time, will visit all "representative" regions in phase space, the density distribution of points in phase space traversed by the trajectory converging to a stationary distribution.

According to the ergodic hypothesis we can calculate the observables of a system in equilibrium as averages over phase space with respect to the probability density of an equilibrium ensemble, $\rho_{\text{ens}}(\Gamma)$. If $\rho_{\text{ens}}(\Gamma)$ obeys the normalization condition, eq 2.6, on the entire phase space Γ and also is zero for all points outside the hypersurface $\mathcal{H}(\Gamma) = E$, the ensemble average can be defined as:

$$\mathcal{A}_{\text{obs}} = \langle \mathcal{A} \rangle_{\text{ens}} = \int \mathcal{A}(\Gamma)\, \rho_{\text{ens}}(\Gamma)\, \mathrm{d}\Gamma \tag{2.8}$$

In MC simulations, the desired thermodynamic quantities are determined as *ensemble averages*:

$$\langle \mathcal{A} \rangle_{\text{ens}} = \frac{\sum\limits_{\Gamma} \mathcal{A}(\Gamma)}{\sum\limits_{\Gamma} \rho_{\text{ens}}(\Gamma)} \tag{2.9}$$

If we wish to obtain an average over points in phase space, there is no need to simulate any real time dependence of the system; one need only construct a sequence of states in phase space in the correct ensemble. In the context of equilibrium simulations, it is always important to make sure that the algorithm used in the simulation is ergodic. This means that no particular region in phase space should be excluded from sampling by the algorithm. Such an exclusion would render the simulation wrong, even if the simulated object itself is ergodic. From a practical point of view, the ergodicity of the system can and should be checked through reproducibility of the calculated thermodynamic properties (pressure, temperature, etc.) in runs with different initial conditions.

2.1.2 Statistical Ensembles

2.1.2/i Microcanonical (NVE) Ensemble

In the *microcanonical* (NVE) ensemble the number of particles, N, the volume of the system, V and the total energy, E, are conserved. This corresponds to a completely closed system which does not interact in any way with the environment and lies in a container of fixed volume, V. For simplicity, we neglect the internal degrees of freedom. Then, the system energy will be a sum of kinetic, $\mathcal{K}$, and potential, $\mathcal{V}$ energies. Since the total energy E must be conserved, the criterion for adding states in the ensemble would be

$$\mathcal{H}\left(\{\mathbf{q}_i\},\{\mathbf{p}_i\}\right)=\mathcal{K}\left(\{\mathbf{q}_i\},\{\mathbf{p}_i\}\right)+\mathcal{V}\left(\{\mathbf{q}_i\},\{\mathbf{p}_i\}\right)=\text{constant}=E_0 \tag{2.10}$$

which means that not all, but only those states in phase space Γ that have total energy E_0 are allowed. This can also be stated so that the probability density of the ensemble is

$$\rho_{NVE}\left(\{\mathbf{q}_i\},\{\mathbf{p}_i\}\right)=\frac{1}{Q_{NVE}}\delta\left[\mathcal{H}\left(\{\mathbf{q}_i\},\{\mathbf{p}_i\}\right)-E_0\right] \tag{2.11}$$

where δ is the Kronecker delta for a discrete system, and the Dirac delta function for a continuous one. The partition function in the microcanonical ensemble, Q_{NVE}, is:

$$Q_{NVE}=\sum_{\Gamma}\delta\left[\mathcal{H}\left(\Gamma\right)-E_0\right] \tag{2.12}$$

The summation over states, $\sum_{\Gamma}$, is used if microscopic states are discrete and $\rho\left(\Gamma\right)$ has the meaning of a probability. For one-component classical systems, the sum can be replaced by an integral, yielding

$$\begin{aligned} Q_{NVE} &= \frac{1}{N!}\frac{1}{h^{3N}}\int \mathrm{d}\Gamma\delta\left[\mathcal{H}\left(\Gamma\right)-E_0\right] \\ &= \frac{1}{N!}\frac{1}{h^{3N}}\int\prod_{i=1}^{N}\mathrm{d}^3r_i\,\mathrm{d}^3p_i\,\delta\left[\mathcal{H}\left(\{\mathbf{q}_i\},\{\mathbf{p}_i\}\right)-E_0\right] \end{aligned} \tag{2.13}$$

where $N!$ takes care of the indistinguishability of particles of the same species and h^{3N} is the ultimate resolution for counting states allowed by the uncertainty principle.

The proper thermodynamic potential for the microcanonical ensemble is the *entropy*:

$$S=k_{\mathrm{B}}\ln\left(Q_{NVE}\right) \tag{2.14}$$

where k_{B} is the Boltzmann constant. We therefore have a statistical thermodynamic definition of entropy as a quantity proportional to the logarithm of the number of microscopic states under given N, V, E. Eq 2.14 establishes a fundamental thermodynamic equation in the entropy representation.

2.1.2/ii Canonical (NVT) ensemble

In the *canonical* (NVT) ensemble the number of particles, N, the volume of the system, V, and temperature, T are conserved. This corresponds to a closed system, which, however, can exchange heat with a large surrounding bath. The energy is fluctuating, but the temperature is constant, describing the probability distribution of energy fluctuations. The total energy of the system is given by its Hamiltonian, $\mathcal{H}\left(\{\mathbf{q}_i\},\{\mathbf{p}_i\}\right)$. The probability density of the ensemble is:

$$\rho_{NVT}\left(\{\mathbf{q}_i\},\{\mathbf{p}_i\}\right) = \frac{1}{Q_{NVT}}\frac{1}{N!h^{3N}}\exp\left[-\frac{\mathcal{H}\left(\{\mathbf{q}_i\},\{\mathbf{p}_i\}\right)}{k_\mathrm{B}T}\right] \tag{2.15}$$

with k_B being the Boltzmann's constant and Q_{NVT} the partition function in the NVT ensemble:

$$Q_{NVT} = \frac{1}{N!h^{3N}}\int\prod_{i=1}^{N}\mathrm{d}^3q_i\ \mathrm{d}^3p_i\ \exp\left[-\frac{\mathcal{H}\left(\{\mathbf{q}_i\},\{\mathbf{p}_i\}\right)}{k_\mathrm{B}T}\right] \tag{2.16}$$

The thermodynamic function of the system is the *Helmholtz energy*:

$$A = -k_\mathrm{B}T\ln\left(Q_{NVT}\right) \tag{2.17}$$

Eq 2.17 defines a fundamental equation in the Helmholtz energy representation by expressing A as a function of N, V, T.

2.1.2/iii Isothermal - isobaric ensemble (NpT)

The isothermal-isobaric ensemble describes the equilibrium distribution in phase space of a system under constant number of particles, temperature, and pressure. The volume of the system is allowed to fluctuate. Thus, a point in phase space is specified by specifying V, $\{\mathbf{q}_i\}$ and $\{\mathbf{p}_i\}$, where the domain from which the $\mathbf{q}_i$s take on values depend on the value of V.

The probability density of the NpT ensemble can be derived from that of the microcanonical ensemble, by considering a bath around the system which acts as both a heat and a work reservoir for the system under study. The probability density, in a classical statistical mechanical formulation, is:

$$\rho_{NpT}\left(\{\mathbf{q}_i\},\{\mathbf{p}_i\};V\right) = \frac{1}{Q_{NpT}}\exp\left[-\frac{\mathcal{H}\left(\{\mathbf{q}_i\},\{\mathbf{p}_i\}\right)+pV}{k_\mathrm{B}T}\right] \tag{2.18}$$

where Q_{NpT} is the *isothermal-isobaric partition function*:

$$Q_{NpT} = \frac{1}{N!h^{3N}}\frac{1}{V_0}\int\mathrm{d}V\int\prod_{i=1}^{N}\mathrm{d}^3q_i\ \mathrm{d}^3p_i\exp\left[-\frac{\mathcal{H}\left(\{\mathbf{q}_i\},\{\mathbf{p}_i\}\right)+pV}{k_\mathrm{B}T}\right] \tag{2.19}$$

where V_0 denotes some basic unit of volume introduced to make the partition function dimensionless (the exact magnitude of V_0 is immaterial).

The connection between the formalism of the isothermal - isobaric ensemble and macroscopic thermodynamic properties is established via the Gibbs energy:

$$G\left(N,p,T\right) = -k_{\mathrm{B}}T\ln\left(Q_{NpT}\left(N,p,T\right)\right) \tag{2.20}$$

2.1.2/iv Configurational integral

As long as the *Born-Oppenheimer approximation*[70] is valid (as it practically always is in equilibrium thermodynamics) the potential energy of the system, $\mathcal{V}\left(\Gamma\right)$, depends only on the generalized coordinates, $\{\mathbf{q}_i\}$. Similarly, the kinetic energy, $\mathcal{K}\left(\Gamma\right)$ depends only on the momenta, i.e. momenta $\{\mathbf{p}_i\}$. Hence we can rewrite the expression for the system Hamiltonian as:

$$\mathcal{H}\left(\Gamma\right) = \mathcal{K}\left(\{\mathbf{p}_i\}\right) + \mathcal{V}\left(\{\mathbf{q}_i\}\right) \tag{2.21}$$

It can be now seen that, in a classical (as opposed to quantum mechanical) treatment, the partition function, e.g. of the NVT ensemble, factorizes into a product of kinetic (ideal gas) and potential (excess) parts:

$$Q_{NVT} = \frac{1}{N!}\frac{1}{h^{3N}}\int\prod_{i=1}^{N}\mathrm{d}^3p_i\ \exp\left[-\frac{\mathcal{K}\left(\{p_i\}\right)}{k_{\mathrm{B}}T}\right]\int\prod_{i=1}^{N}\mathrm{d}^3q_i\exp\left[-\frac{\mathcal{V}\left(\{q_i\}\right)}{k_{\mathrm{B}}T}\right] \tag{2.22}$$

This can be written as a product of the ideal gas contribution, and the excess contribution as:

$$Q_{NVT} = Q_{NVT}^{\mathrm{id}}V^{-N}\mathcal{Z}_{NVT} \tag{2.23}$$

where:

$$\mathcal{Z}_{NVT} = \int\prod_{i=1}^{N}\mathrm{d}^3q_i\ \exp\left[-\frac{\mathcal{V}\left(\{q_i\}\right)}{k_{\mathrm{B}}T}\right] \tag{2.24}$$

is the so called *configurational integral.* The partition function of the ideal gas is:

$$Q_{NVT} = \frac{V^N}{N!\Lambda^{3N}} \tag{2.25}$$

with Λ being the *de Broglie* or *thermal wavelength*:

$$\Lambda = \left(\frac{h^2}{2\pi mk_{\mathrm{B}}T}\right)^{1/2} \tag{2.26}$$

From the perspective of a particle-based model, the fundamental problem of equilibrium statistical mechanics, according to Chandler,[71] is to evaluate a configurational partition function of the form of eq 2.24.

Two important consequences arise from eq 2.23. First, all the thermodynamic properties can be expressed as a sum of an ideal gas part and an excess part. The chemical details which govern the interactions between the atoms of the system are included in the latter. In fact, in MC simulations the momentum part of the phase space is usually omitted, and all calculations are performed in configuration space. The second important consequence of eq 2.23 is that the total average kinetic energy is a universal quantity, independent of the interactions in the system. Indeed, computing the average of

$$\mathcal{K} = \sum_{i=1}^{N} \frac{\mathbf{p}_i^2}{2m} \tag{2.27}$$

with respect to the probability distribution of eq 2.15 and using the factorization of eq 2.23 we obtain that:[67]

$$\langle \mathcal{K} \rangle = \frac{3}{2} N k_{\mathrm{B}} T \tag{2.28}$$

or, more generally $\langle \mathcal{K} \rangle = 1/2 N_{\mathrm{dof}} k_{\mathrm{B}} T$ for a system of N_{dof} degrees of freedom.[a]

2.2 Elements of Continuum Mechanics

2.2.1 Deformation and its Description

The result of action of external forces can either be moving a body in space or changing its shape. Continuum mechanics is interested in changes occurring inside a body. The change of the body shape is essentially the change of distances between different sites inside material, and this phenomenon is called *deformation*. Deformation is just a geometrical concept and all interpretations of this concept have clear geometrical images.

From the continuum viewpoint, a given portion of matter is treated as a collection of elements, called *material particles*, which at any given instant can be placed in a one-to-one correspondence with the points of a closed region of three-dimensional Euclidean space.[73] The *configuration* of a solid is the region of space occupied by the solid. When we describe motion, we normally choose some convenient configuration of the solid to use as *reference*.

---

[a] If the kinetic energy can be separated into a sum of terms, each of them being quadratic in only one momentum component, the average kinetic energy per degree of freedom is $1/2 k_{\mathrm{B}} T$, which is a special case of the *equipartition theorem*.[72]

We denote the reference configuration by $\mathscr{R}$; this is often the initial, undeformed solid, but it can be any convenient region of space.[74] The material changes its shape under the action of external loads, and after some time t occupies a new region which is called the *deformed* or *current* configuration of the solid.

2.2.1/i Deformation gradient tensor

The concept of *deformation gradient* is introduced in order to quantify the change in shape of infinitesimal line elements in a solid body. Let imagine drawing a straight line, d$\mathbf{x}$ on the initial configuration of a solid, as shown in Figure 2.1. The line would be mapped to a smooth curve on the deformed configuration. However, we focus our attention on a line segment d$\mathbf{x}'$, much shorter than the radius of curvature of this curve, as shown. The segment is straight in the initial (undeformed) configuration, and would also be (almost) straight in the deformed configuration. Thus, no matter how complex the deformation we impose on a solid is, infinitesimal line segments are merely stretched and rotated by a deformation. We will use $\mathbb{F}$ to denote the deformation gradient tensor, defined through a mapping of the infinitesimal vector d$\mathbf{x}$ of the initial configuration onto the infinitesimal vector d$\mathbf{x}'$ after the deformation:

$$\mathrm{d}\mathbf{x}' = \mathbb{F}\mathrm{d}\mathbf{x} \tag{2.29}$$

A slightly altered calculation is possible by noting that the displacement $\mathbf{u}$ of any point can be defined as

$$\mathbf{u} = \mathbf{x}' - \mathbf{x} \tag{2.30}$$

and this leads to $\mathbf{x}' = \mathbf{x} + \mathbf{u}(\mathbf{x})$, and

$$\mathbb{F} = \frac{\partial}{\partial \mathbf{x}}\left(\mathbf{x} + \mathbf{u}(\mathbf{x})\right) = \frac{\partial \mathbf{x}}{\partial \mathbf{x}} + \frac{\partial \mathbf{u}(\mathbf{x})}{\partial \mathbf{x}} = \mathbb{I} + \frac{\partial \mathbf{u}}{\partial \mathbf{x}} \tag{2.31}$$

where $\mathbb{I}$ is the unit tensor. The inverse of the deformation gradient, $\mathbb{F}^{-1}$, arises also in many calculations.

2.2.1/ii Stretch ratio, λ

If we think of the vector d$\mathbf{x}$ connecting two material points in the reference (undeformed) configuration, the *stretch ratio* is the ratio of the current separation of these two particles to their separation in the reference configuration. The stretch ratio for the differential element

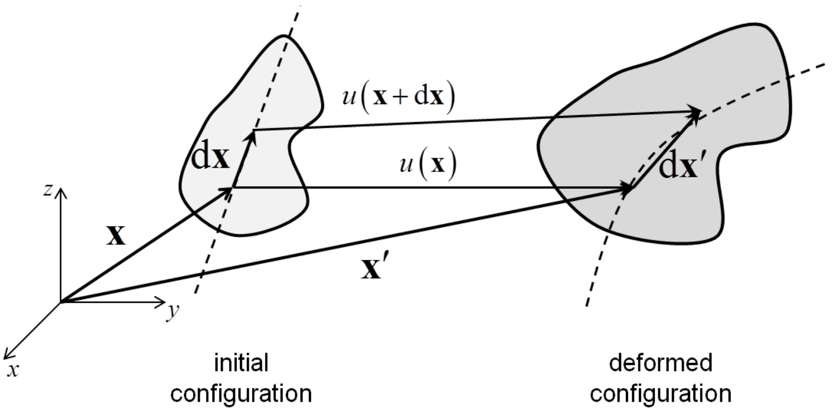

Figure 2.1: Deformation of a continuum body

$\mathrm{d}\mathbf{x} = \hat{\mathbf{n}}\mathrm{d}x$ in the direction of the unit vector $\hat{\mathbf{n}}$, in the undeformed configuration, is defined as:

$$\lambda_{(\hat{\mathbf{n}})} = \lim_{\mathrm{d}x \to 0} \frac{\mathrm{d}x'}{\mathrm{d}x} \tag{2.32}$$

where $\mathrm{d}x'$ is the magnitude of the deformed line element $\mathrm{d}\mathbf{x}'$. In the case of a material line, the stretch ratio is defined as $\lambda = L'/L$ where L is the length of the line before in the undeformed state and L' the length of the same line in the deformed state. The stretch ratio is used in the analysis of materials that exhibit large deformations, such as elastomers, which can sustain stretch ratios of 3 or 4 before failing.

In the principal axis system of the deformed body, the deformation gradient tensor becomes:

$$\mathbb{F} = \begin{bmatrix} \lambda_1 & 0 & 0 \\ 0 & \lambda_2 & 0 \\ 0 & 0 & \lambda_3 \end{bmatrix} \tag{2.33}$$

with $\lambda_i, i = 1, 2, 3$ being the *principal stretch ratios*. The volume of the deformed body is connected to λ_i by:

$$V = V_{\mathscr{R}} \det(\mathbb{F}) = V_{\mathscr{R}} \lambda_1 \lambda_2 \lambda_3 \tag{2.34}$$

where we use $\mathscr{R}$ for defining the undeformed configuration.

2.2.1/iii Engineering strain, ϵ

The *Cauchy strain* or *engineering strain* is defined as the ratio of the total deformation to the initial dimension of the material body in which the forces have been applied. The engineering normal strain, or engineering extensional strain, or nominal strain, ϵ, of a material line element or fiber axially loaded is expressed as the change in length ΔL per unit of the original length L

of the line element or fiber. The normal strain is positive if the material fiber is stretched and negative if it is compressed. Thus, we have

$$\epsilon = \frac{\Delta L}{L} = \frac{L' - L}{L} \tag{2.35}$$

where L is the original length of the fiber and L' the length of the fiber after deformation. The normal engineering strain, $\epsilon_{(\hat{\mathbf{n}})}$ in any direction $\hat{\mathbf{n}}$ can be expressed as a function of the stretch ratio (eq 2.32):

$$\epsilon_{(\hat{\mathbf{n}})} = \frac{\mathrm{d}x' - \mathrm{d}x}{\mathrm{d}x} = \lambda_{(\hat{\mathbf{n}})} - 1 \tag{2.36}$$

This equation implies that the engineering strain is zero, i.e. no deformation, when the stretch ratio is equal to unity. For infinitesimal motions the relation between strain and displacement, **u** (eq 2.30), is: [b]

$$\epsilon_{\alpha\beta} = \frac{1}{2}\left(\frac{\partial u_\alpha}{\partial x_\beta} + \frac{\partial u_\beta}{\partial x_\alpha}\right) \tag{2.37}$$

2.2.1/iv Logarithmic strain, ϵ_{L}

The *logarithmic* strain ϵ_{L}, also called *true* strain or *Hencky* strain, is defined as:[75]

$$\epsilon_{\mathrm{L}} = \ln\left(\frac{L'}{L}\right) = \ln(\lambda) = \ln(1 + \epsilon) \tag{2.38}$$

where λ and ϵ are the stretch ratio (eq 2.32) and the engineering strain (eq 2.161), respectively. The logarithmic strain is very useful because it provides the correct measure of the final strain when deformation takes place in a series of increments, taking into account the influence of the strain path.[76]

2.2.1/v Green-Lagrange strain, ϵ_{G}

The Green-Lagrange strain is defined as:

$$\epsilon_{\mathrm{G}} = \frac{1}{2}\left(\lambda^2 - 1\right) \tag{2.39}$$

---

[b] The displacement field giving rise to a particular strain field, cannot be recovered if only the strains are known. The integration of the strain field produces the displacement field to within an arbitrary rigid motion. Any rigid motion produces no strain, so the displacements can only be completely determined if there is some additional information (besides the strain) that will reveal how much the solid has rotated and translated.

2.2.2 Rheology

In this section we will describe the basic features of *rheology*, which can be defined as the science of deformation and flow of matter.[77] [c] As with most experimental techniques, rheology can be subdivided into linear and nonlinear rheology. In the following, we will limit ourselves only to the linear regime. Linear rheology considers small deformations, which do not perturb the internal structure of the system and thus probe "equilibrium dynamics". According to the fluctuation–dissipation theorem (please see discussion in Section 2.4.3 on page 52), the relaxation of the system after an infinitesimal perturbation by an external field is equivalent to the relaxation of spontaneous thermal fluctuations. This fact allows simple and effective characterization of equilibrium dynamics by calculating correlation functions at equilibrium.

2.2.2/i Shear relaxation modulus

The response to a small shear deformation γ is given by

$$\tau_{xy}\left(t\right) = \gamma G\left(t\right) \tag{2.40}$$

where $G(t)$ is the *shear relaxation modulus*, the key function of linear rheology. One can show that the relaxation after any small deformation will be proportional to $G(t)$, and thus $G(t)$ fully characterizes linear rheology of a fluid system with given external parameters. We can also consider a homogeneous shear flow with a time-dependent shear rate, $\dot{\gamma}(t)$. For a Newtonian fluid, the shear stress $\tau_{xy}(t)$ at any time would be proportional to the instantaneous shear rate $\dot{\gamma}(t)$. For a complex fluid, the measured shear stress will not jump immediately to its steady-state value at the start-up of a steady shear flow. If we assume that the shear rate is infinitely small, then a linear expression of the form:

$$\tau_{xy} = -\int_{-\infty}^{t} G\left(t - t'\right) \dot{\gamma}\left(t'\right) \mathrm{d}t' \tag{2.41}$$

is expected. Eq 2.41 is the fundamental equation of linear viscoelasticity. When, for large times, t, a steady state is reached, we can identify the steady-state *viscosity*, as:

$$\eta = \int_{0}^{\infty} G\left(t'\right) \mathrm{d}t' \tag{2.42}$$

---

[c] This definition was invented by Professor Bingham of Lafayette College of Indiana and was accepted when the American Society of Rheology was founded in 1929.

2.2.2/ii Loss and storage moduli

If we were supposed to measure the shear relaxation modulus $G(t)$ directly, we would need to perform a small instantaneous shear step of size γ. In practice, it is quite difficult to produce steps in shear strain or strain rate. It is often advantageous to perform oscillatory experiments, $\dot{\gamma}(t) = \dot{\gamma}_0 \cos(\omega t)$, where $\dot{\gamma}_0$ is a small amplitude and ω is the angular frequency. In oscillatory flow, one can measure the *storage modulus*:

$$G'(\omega) = \omega \int_0^\infty G(t) \sin(\omega t) \mathrm{d}t \tag{2.43}$$

and the *loss modulus*

$$G''(\omega) = \omega \int_0^\infty G(t) \cos(\omega t) \mathrm{d}t \tag{2.44}$$

by recording the in-phase and out-of-phase responses, respectively. A *complex modulus* can be defined as

$$G^*(\omega) = G'(\omega) + iG''(\omega) = i\omega \int_0^\infty G(t) e^{-i\omega t} \mathrm{d}t \tag{2.45}$$

2.3 Polymer Physics

2.3.1 General Remarks

2.3.1/i Fundamental definitions

A *macromolecule* (or *polymer*) is a large molecule composed of many small simple chemical units called *structural units*.[78,79] In some polymers each structural unit is connected to precisely two other structural units, and the resulting chain structure is called a *linear* macromolecule. In other polymers, most structural units are connected to two other units, although some structural units connect three or more units, and therefore we talk of *branched* molecules. Where the polymeric chains terminate, special units called *end groups* are found. A *monomer* is the substance that the polymer is made of (mostly coinciding with the structural unit). We will use the terms *segment* or *strand* in order to denote an entity consisting of several structural units. The process that converts a monomer to a polymer is called *polymerization*. We should also mention that in some macromolecular materials all structural units are interconnected, resulting in a three-dimensional *cross-linked* or *network* structure rather than in separate molecules.

The term *configuration* refers to the "permanent" stereo-structure of a polymer. The configuration is defined by the polymerization method, and a polymeric chain preserves its configuration until it reacts chemically. A change in configuration requires the rupture of chemical bonds. Different configurations exist in polymers with stereo centers (*tacticity*) and double bonds (*cis* and *trans* forms). Tacticity is the orderliness of the succession of configurational structural units in the main chain of a polymer molecule. An *isotactic* polymer is a regular polymer consisting only of one species of configurational structural units. A *syndiotactic* polymer consists of an alternating sequence of the different configurational structural units. An *atactic* polymer has equal numbers of randomly distributed configurational structural units. Adjacent configurational units that are called *dyads*, *triads*, *tetrads*, etc. A chain with 100% meso dyads is perfectly isotactic whereas a chain with 100% racemic dyads is perfectly syndiotactic.

2.3.1/ii Polymer configurations

For a general polymer model with $N+1$ particles per chain, the configurational partition function of a single chain can be expressed by a formula similar to eq 2.24:[34]

$$\mathcal{Z}_0 = \int \mathrm{d}\mathbf{r}^{N+1} \exp\left[-\frac{\mathcal{V}_0\left(\{\mathbf{r}_i\}\right)}{k_\mathrm{B}T}\right] \tag{2.46}$$

where $\{\mathbf{r}_i\} = \{\mathbf{r}_0, \ldots, \mathbf{r}_N\}$ denotes the set of $N+1$ particle positions and $\mathcal{V}_0\left(\{\mathbf{r}_i\}\right)$ is the potential energy associated with a particular configuration of the polymer. The notation $\mathrm{d}\mathbf{r}^{N+1}$ is a shorthand for the $3(N+1)$-dimensional integral over the $N+1$ particle positions within a three-dimensional domain of volume V. For an ideal chain model, $\mathcal{V}_0$ contains only interaction potential terms reflecting short-ranged interferences. Based on eq 2.46 the probability density can also been defined.

An alternative representation of the configurational degrees of freedom of the $(N+1)$-mer chain is to retain only one position vector as "external" coordinate describing the overall location of the chain and N "internal" coordinates. A particularly convenient choice is the position of a chain end, e.g. $\mathbf{r}_0$ and the set of N *bond vectors*, $\{\mathbf{b}_i\} = \{\mathbf{b}_1, \mathbf{b}_2, \ldots, \mathbf{b}_N\}$, where $\mathbf{b}_i \equiv \mathbf{r}_i - \mathbf{r}_{i-1}$, as shown in Figure 2.2. In the absence of an external potential acting on the polymer, $\mathcal{V}_0$ depends only on the internal coordinates $\mathbf{b}^N$. The Jacobian of the transformation from coordinates $\mathbf{r}^{N+1}$ to $\left(\mathbf{r}_0, \mathbf{b}^N\right)$ is unity, allowing eq 2.46 to be reexpressed as:

$$\mathcal{Z}_0 = V \int \mathrm{d}\mathbf{b}^{N} \exp\left[-\frac{\mathcal{V}_0\left(\{\mathbf{b}_i\}\right)}{k_\mathrm{B}T}\right] \tag{2.47}$$

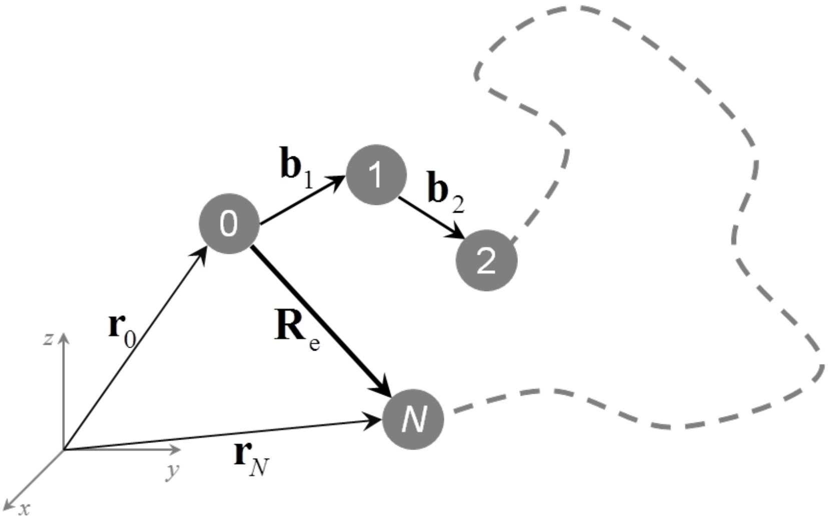

Figure 2.2: A coarse-grained chain with $N+1$ particles and N connecting springs (indicated by bold connecting arrows). The particle positions, with respect to an external coordinate system, are denoted by $\mathbf{r}_0$, $\mathbf{r}_1$, ..., $\mathbf{r}_N$, bond vectors by $\mathbf{b}_1$, $\mathbf{b}_2$, ..., $\mathbf{b}_N$ and the chain end-to-end vector by $\mathbf{R}_\mathrm{e}$.

2.3.1/iii Measures of shape

The simplest measure of the spatial extent of a chain is its end-to-end vector:

$$\mathbf{R}_\mathrm{e} = \mathbf{r}_N - \mathbf{r}_0 \tag{2.48}$$

defined as the vector connecting the first with the last structural unit of the chain. Moreover, of ultimate importance is the *mean-square end-to-end distance*, defined as either an ensemble or a time average of the squared norm of the end-to-end vector,

$$\left\langle R_\mathrm{e}^2 \right\rangle = \left\langle \|\mathbf{R}_\mathrm{e}\|^2 \right\rangle \tag{2.49}$$

The mean-square end-to-end distance of a linear polymer is not an experimentally observable quantity. Of more experimental relevance is the so-called *radius of gyration about the center of mass*. We define the center of mass by:

$$\mathbf{r}_\mathrm{cm} = \frac{\sum_{j=0}^{N} m_j \mathbf{r}_j}{\sum_{j=0}^{N} m_j} \tag{2.50}$$

where m_j is the mass of particle j. The position vector of the j-th atom in a frame of reference with origin at the center of mass of the chain is then:

$$s_j = \mathbf{r}_j - \mathbf{r}_{\text{cm}} \tag{2.51}$$

Now, we can form the *radius of gyration tensor* of the chain as:[80]

$$\mathbf{S} = \frac{1}{N+1} \sum_{j=0}^{N} \mathbf{s}_j \otimes \mathbf{s}_j^{\mathrm{T}} \tag{2.52}$$

We can diagonalize **S** by transforming to a principal axis system, where:

$$\mathbf{S} = \operatorname{diag}\left(S_x^2, S_y^2, S_3^2\right) \tag{2.53}$$

so that the eigenvalues of **S**, S_x^2, S_y^2 and S_z^2 are in descending order, i.e. $S_x^2 \geq S_y^2 \geq S_z^2$. The first invariant of **S** is the squared *radius of gyration*:

$$R_{\mathrm{g}}^2 = S_x^2 + S_y^2 + S_z^2 \tag{2.54}$$

If we assign equal masses to all particles, we can deduce the squared radius of gyration in an alternative way, as:[78]

$$R_{\mathrm{g}}^2 = \frac{1}{(N+1)^2} \sum_{i=0}^{N} \sum_{j=0}^{i-1} \left\| \mathbf{r}_i - \mathbf{r}_j \right\|^2 \tag{2.55}$$

which is a purely geometrical equation, well-known in the polymer literature.

2.3.2 Simplified Polymer Chain Models

2.3.2/i Theoretical treatment of polymer configurations

The first ingredient in a theoretical description of a polymer is a mesoscopic model describing the statistical mechanics associated with the conformational states of a single chain. The key issue is to extract the probability of finding one end of chain at a specific position, relative to the other, or estimate the average size of the chain. In the following we will deal with the so-called *ideal chain models*, which take into account only local interferences in the statistical mechanics of a polymer chain. An important observation is that, regardless of the particular form of the short-ranged interferences, all ideal chain models exhibit universal scaling properties at sufficiently large length scales. We will use the term *unperturbed* to denote polymer chain configurations which are not affected by nonlocal interactions.

In order to proceed, we assume that the structural units of the polymer, at our level of description, form a sequence of displacements, $\mathbf{b}_1$, $\mathbf{b}_2$, ..., $\mathbf{b}_N$ starting from one end of the chain and advancing towards the other. The magnitude and direction of each displacement is independent of all the preceding ones. However, the probability that the i-th displacement lies between $\mathbf{b}_i$ and $\mathbf{b}_i + \mathrm{d}\mathbf{b}_i$ is governed by a distribution function $w_i\left(\mathbf{b}_i\right)$, which has been *a priori* assigned. Under the above assumptions, the polymer chains can be described as *random flights* in space. We will follow the method developed by Markoff and elegantly described by Chandrashekar[81] in order to answer the fundamental question: *What is the probability* $W_N\left(\mathbf{R}_\mathrm{e}\right)\mathrm{d}\mathbf{R}_\mathrm{e}$ *that after* N *displacements the coordinates of the particle (or the chain segment) lie in the interval* $\mathbf{R}_\mathrm{e}$ *and* $\mathbf{R}_\mathrm{e} + \mathrm{d}\mathbf{R}_\mathrm{e}$*?*

The position $\mathbf{R}_\mathrm{e}$ of the particle (or the chain segment), after N displacements (or preceding segments) is given by:

$$\mathbf{R}_\mathrm{e} = \sum_{i=1}^{N} \mathbf{b}_i \tag{2.56}$$

where $\mathbf{b}_i$'s $(i = 1, \ldots, N)$ denote the different displacements and assuming the origin of the random flight to coincide with the origin of our coordinate system. According to our discussion above, the probability that the i-th displacement lies between $\mathbf{b}_i$ and $\mathbf{b}_i + \mathrm{d}\mathbf{b}_i$ is given by

$$w_i\left(b_{x,i}, b_{y,i}, b_{z,i}\right)\mathrm{d}b_{x,i}\mathrm{d}b_{y,i}\mathrm{d}b_{z,i} = w_i\mathrm{d}\mathbf{b}_i, \quad (i = 1, \ldots, N) \tag{2.57}$$

The probability $W_N\left(\mathbf{R}_\mathrm{e}\right)\mathrm{d}\mathbf{R}_\mathrm{e}$ that the position $\mathbf{R}_\mathrm{e}$ of the particle will be found in the interval $\left(\mathbf{R}_\mathrm{e}, \mathbf{R}_\mathrm{e} + \mathrm{d}\mathbf{R}_\mathrm{e}\right)$ is given by:[81]

$$W_N\left(\mathbf{R}_\mathrm{e}\right) = \frac{1}{8\pi^3}\int_{-\infty}^{\infty} \exp\left(-i\,\mathbf{k}\cdot\mathbf{R}_\mathrm{e}\right)\mathcal{S}_N\left(\mathbf{k}\right)\mathrm{d}\mathbf{k} \tag{2.58}$$

where

$$\mathcal{S}_N\left(\mathbf{k}\right) = \prod_{j=1}^{N}\int_{-\infty}^{+\infty} w_j\left(\mathbf{b}_j\right)\exp\left(i\,\mathbf{k}\cdot\mathbf{b}_j\right)\mathrm{d}\mathbf{b}_j \tag{2.59}$$

with $\mathbf{k}$ being a vector in the inverse space. In eq 2.59, $w_j\left(\mathbf{b}_j\right)$ governs the probability of occurrence of a displacement $\mathbf{b}_j$ on the j-th move. The explicit form which $W_N\left(\mathbf{R}_\mathrm{e}\right)$ takes will depend on the assumptions made concerning the probabilities of the individual steps, $w_j\left(\mathbf{b}_j\right)$. We shall now consider specific cases of interest.

2.3.2/ii Freely jointed chain model

The freely jointed chain model is the simplest ideal chain model in which all interactions, except the connectivity, between structural units, are neglected. The bond vectors connecting successive particles are constrained to have a fixed length, $\|b_i\| = b_{\mathrm{K}}$, but the orientations of the N bond vectors are distributed isotropically and independently. Under these circumstances, we can define the distribution functions w_j by:

$$w_j\left(\mathbf{b}_j\right) = \frac{1}{4\pi b_{\mathrm{K}}^3}\delta\left(\|\mathbf{b}_j\|^2 - b_{\mathrm{K}}^2\right), \quad (j = 1, \ldots, N) \tag{2.60}$$

with δ being the Dirac's δ function. Accordingly, our expression for $\mathcal{S}_N\left(\mathbf{k}\right)$, eq 2.59, becomes:

$$\mathcal{S}_N\left(\mathbf{k}\right) = \prod_{j=1}^{N}\frac{1}{4\pi b_{\mathrm{K}}^3}\int_{-\infty}^{\infty}\exp\left(i\,\mathbf{k}\cdot\mathbf{b}_j\right)\delta\left(b_j^2 - b_{\mathrm{K}}^2\right)\mathrm{d}\mathbf{b}_j \tag{2.61}$$

or, using polar coordinates with the z-axis in the direction of **k**:

$$\begin{aligned}\mathcal{S}_N\left(\mathbf{k}\right) =& \prod_{j=1}^{N}\frac{1}{4\pi b_{\mathrm{K}}^3}\\ &\int_0^{\infty}\int_0^{\pi}\int_0^{2\pi}\exp\left(i\,kb_j\ \cos\theta\right)\delta\left(b_j^2 - b_{\mathrm{K}}^2\right)b_j^2\sin\theta\ \mathrm{d}b_j\mathrm{d}\theta\mathrm{d}\phi\end{aligned} \tag{2.62}$$

which, after the integration over the polar and azimuthal angles, θ and ϕ, respectively, yields:

$$\mathcal{S}_N\left(\mathbf{k}\right) = \prod_{j=1}^{N}\frac{\sin\left(kb_{\mathrm{K}}\right)}{kb_{\mathrm{K}}} \tag{2.63}$$

Thus, the end-to-end distribution, according to eq 2.58 becomes:

$$W_N\left(\mathbf{R}_{\mathrm{e}}\right) = \frac{1}{8\pi^3}\int_{-\infty}^{+\infty}\exp\left(-i\,\mathbf{k}\cdot\mathbf{R}_{\mathrm{e}}\right)\prod_{j=1}^{N}\frac{\sin\left(kb_{\mathrm{K}}\right)}{kb_{\mathrm{K}}}\mathrm{d}\mathbf{k} \tag{2.64}$$

Finally, if we choose the polar coordinates, but with the z axis pointing this time in the direction of $\mathbf{R}_{\mathrm{e}}$, and after performing the integrations over the polar and azimuthal angles, we obtain:

$$\begin{aligned}W_N\left(\mathbf{R}_{\mathrm{e}}\right) =& \frac{1}{2\pi^2 R_{\mathrm{e}}}\int_0^{\infty}\sin\left(kR_{\mathrm{e}}\right)\left\{\prod_{j=1}^{N}\frac{\sin\left(kb_{\mathrm{K}}\right)}{kb_{\mathrm{K}}}\right\}k\ \mathrm{d}k\\ =& \frac{1}{2\pi^2 R_{\mathrm{e}}}\int_0^{\infty}\sin\left(kR_{\mathrm{e}}\right)\left[\frac{\sin\left(kb_{\mathrm{K}}\right)}{kb_{\mathrm{K}}}\right]^N k\ \mathrm{d}k\end{aligned} \tag{2.65}$$

which is the solution to the problem, as obtained by Rayleigh.[82,83] Rayleigh has also evaluated analytically the integral for selected cases of N, up to $N = 6$.

Treloar[84] and later authors[85] have used more powerful techniques than Rayleigh's to derive a closed-form expression for $W_N\left(\mathbf{R}_\mathrm{e}\right)$ for arbitrary N. The general solution, assuming constant step size of b_K is:

$$\begin{aligned} W_N\left(\mathbf{R}_\mathrm{e}\right) = & \frac{1}{\pi b_\mathrm{K}^2 R_\mathrm{e}} \frac{1}{2^{N+1}\left(N-2\right)!} \\ & \times \sum_{j=0}^{N} \left(-1\right)^j \binom{N}{j} \left[\frac{R_\mathrm{e}}{b_\mathrm{K}} + N - 2j\right]^{N-2} H\left(2j - N - \frac{R_\mathrm{e}}{b_\mathrm{K}}\right) \end{aligned} \tag{2.66}$$

where H denotes Heaviside's unit step function (please see page xxxvii), and $\binom{N}{j}$ is the binomial coefficient of N, j (please see page xxxvi).

By far the most interesting case is for $N >> 1$. Under these circumstances,

$$W_{(N>>1)}\left(\mathbf{R}_\mathrm{e}\right) = \frac{1}{2\pi R_\mathrm{e}} \int_0^\infty \exp\left(-\frac{N b_\mathrm{K} k^2}{6}\right) k \sin\left(R_\mathrm{e} k\right) \mathrm{d}k \tag{2.67}$$

and after evaluating the integral on the right-hand side:

$$W_{(N>>1)}\left(\mathbf{R}_\mathrm{e}\right) = \frac{1}{\left(\frac{2\pi N b_\mathrm{K}^2}{3}\right)^{3/2}} \exp\left(-\frac{3R_\mathrm{e}^2}{2N b_\mathrm{K}^2}\right) \tag{2.68}$$

By applying eq 2.68 we can examine a variety of statistical properties of the freely jointed chain. The isotropic distribution of the b_i on the surface of a sphere of radius b_K implies that $\langle \mathbf{b}_i \rangle = 0$, and, hence, a vanishing first moment for $\mathbf{R}_\mathrm{e}$:

$$\langle \mathbf{R}_\mathrm{e} \rangle = 0 \tag{2.69}$$

Moreover, we can extract, in an analytical way an expression for the average norm of $\mathbf{R}_\mathrm{e}$:

$$\langle R_\mathrm{e} \rangle = \frac{\int_0^\infty R_\mathrm{e} W_{(N>>1)}\left(R_\mathrm{e}\right) \mathrm{d}R_\mathrm{e}}{\int_0^\infty W_{(N>>1)}\left(R_\mathrm{e}\right) \mathrm{d}R_\mathrm{e}} \tag{2.70}$$

The integral in the denominator is equal to unity, since the $W_{(N>>1)}\left(R_\mathrm{e}\right)$ function is a normalized probability density for a chain that has started at the origin to find its end at distance R_e, irrespectively of orientation. In order to calculate $W_{(N>>1)}\left(R_\mathrm{e}\right) \mathrm{d}R_\mathrm{e}$ from $W_{(N>>1)}\left(\mathbf{R}_\mathrm{e}\right)$ we need to multiply by the volume of a spherical shell extending from R_e to $R_\mathrm{e} + \mathrm{d}R_\mathrm{e}$:

$$W_{(N>>1)}\left(R_\mathrm{e}\right) \mathrm{d}R_\mathrm{e} = \frac{1}{\left(\frac{2\pi N b_\mathrm{K}^2}{3}\right)^{3/2}} \exp\left(-\frac{3R_\mathrm{e}^2}{2N b_\mathrm{K}^2}\right) 4\pi R_\mathrm{e}^2 \, \mathrm{d}R_\mathrm{e} \tag{2.71}$$

Now, the integral in the nominator of eq 2.70 can be calculated as:

$$\langle R_{\mathrm{e}} \rangle = \int_0^\infty R_{\mathrm{e}} W_{(N>>1)}\left(R_{\mathrm{e}}\right) \mathrm{d}R_{\mathrm{e}} = \left(\frac{8}{3\pi}\right)^{1/2} N^{1/2} b_{\mathrm{K}} \tag{2.72}$$

and the mean-square end-to-end distance:

$$\left\langle R_{\mathrm{e}}^2 \right\rangle = \int_0^\infty R_{\mathrm{e}}^2 W_{(N>>1)}\left(R_{\mathrm{e}}\right) \mathrm{d}R_{\mathrm{e}} = N b_{\mathrm{K}}^2 \tag{2.73}$$

Finally, the mean-square radius of gyration of a freely jointed chain can be calculated by using its geometrical definition, eq 2.55, and the fact that in a random walk of step length b_{K} the following equation holds:

$$\left\langle \left\|\mathbf{r}_i - \mathbf{r}_j\right\|^2 \right\rangle = (i-j)\, b_{\mathrm{K}}^2 \tag{2.74}$$

which reduces eq 2.55 to:

$$\left\langle R_{\mathrm{g}}^2 \right\rangle = \frac{b_{\mathrm{K}}^2}{(N+1)^2} \sum_{i=0}^{N} \sum_{j=0}^{N-1} (i-j) = \frac{b_{\mathrm{K}}^2}{2\,(N+1)^2} \sum_{j=1}^{N} j\,(j-1) \tag{2.75}$$

Since $\sum_{j=1}^{N} j^2 = \frac{1}{6} N\,(N+1)\,(2N+1)$, we finally deduce that:

$$\left\langle R_{\mathrm{g}}^2 \right\rangle = \frac{1}{6} N b_{\mathrm{K}}^2 \left(1 - \frac{1}{N^2}\right) \simeq \frac{1}{6} \left\langle R_{\mathrm{e}}^2 \right\rangle \quad \text{as} \quad N \to \infty \tag{2.76}$$

Now, we have for the specific case of the random flight model, a relation between the mean-square radius of gyration $\left\langle R_{\mathrm{g}}^2 \right\rangle$ and the mean-square end-to-end distance, $\langle R_{\mathrm{e}}^2 \rangle$.

2.3.2/iii Gaussian chain (bead-spring model)

A case of special interest arises when the distribution of the individual displacements can be described by a Gaussian:

$$w_j\left(\mathbf{b}_j\right) = \frac{1}{\left(\frac{2\pi b_{\mathrm{K}}^2}{3}\right)^{3/2}} \exp\left(-\frac{3 b_j^2}{2 b_{\mathrm{K}}^2}\right) \tag{2.77}$$

where b_{K}^2 denotes the mean-square displacement to be expected on the j-th occasion. We assume that all the displacements occur in random directions. The probability of an end-to-end vector $\mathbf{R}_\mathrm{e}$ can be obtained:

$$W_N\left(R_\mathrm{e}\right)=\frac{1}{\left(\frac{2\pi N\left\langle b_\mathrm{K}^2\right\rangle}{3}\right)^{3/2}}\exp\left(-\frac{3R_\mathrm{e}^2}{2N\left\langle b_\mathrm{K}^2\right\rangle}\right) \tag{2.78}$$

which is an exact solution for any value of N. Eq 2.78 coincides with eq 2.68 obtained by treating the chain as a random walk of step b_K. The statistical properties discussed in the framework of the freely jointed chain hold for the Gaussian chain, too.

The *bead-spring model* represents a polymer chain as a collection of beads connected by elastic springs. The coarse-graining is based on the polymer chain self-similarity, with a single bead corresponding to a chain fragment containing many structural units or monomers. Springs reproduce the Gaussian distribution of separations (eq 2.77) between monomers connected through a large number of chemical bonds. The spring constant is given by $3k_\mathrm{B}T/\left\langle R_\mathrm{e}^2\right\rangle$, where $\left\langle R_\mathrm{e}^2\right\rangle$ is the mean square end-to-end distance of the actual chain strand represented by the spring. The spring reproduces the entropic free energy rise associated with the reduction of conformations of a strand as its two ends are pulled apart (please refer to Section 2.3.3 on page 35 for more details).

2.3.2/iv Freely rotating chain model

This model ignores differences between the probabilities of different torsion angles and assumes all torsion angles $-\pi\leq\phi_i\leq+\pi$ to be equally probable. Thus, the *freely rotating chain model* assumes all bond lengths and bond angles are fixed(constant) and all torsion angles equally likely and independent of each other. The mean-square end-to-end distance of the freely rotating chain can be cast in terms of the number of bonds in the chain N_b, the length of each bond, l, and the acute angle between consecutive bond vectors, θ:[86]

$$\left\langle R^2\right\rangle=N_\mathrm{b}l^2+2N_\mathrm{b}l^2\frac{\cos\theta}{1-\cos\theta}=N_\mathrm{b}l^2\,\frac{1+\cos\theta}{1-\cos\theta} \tag{2.79}$$

2.3.2/v Real polymer chain configuration

In a typical polymer chain, there are correlations between bond vectors (especially between neighboring ones). The physical origins of these local correlations between bond vectors are restricted bond angles and steric hindrance. If we assume that the length of every skeletal bond of the real chain is l we can ask this chain to follow the scaling law of a freely jointed chain, $N_\mathrm{b}l^2$, with N_b being the count of skeletal bonds along the chain. In order to achieve a quantitative agreement, we should introduce a coefficient, C_N in order to account for the stiffness of the chain:

$$\left\langle R_{\mathrm{e}}^{2}\right\rangle = N_{\mathrm{b}} C_N l^2 \tag{2.80}$$

with C_N being the Flory's *characteristic ratio*. The characteristic ratio is larger than unity ($C_N > 1$) for all polymers.[86] All models of ideal polymers ignore steric hindrance between monomers separated by many bonds and result in characteristic ratios saturating at a finite value C_∞ for large number of backbone bonds ($N_{\mathrm{b}} \rightarrow \infty$). Thus, the mean-square end-to-end distance can be approximated for long chains as:

$$\left\langle R_{\mathrm{e}}^{2}\right\rangle = N_{\mathrm{b}} C_\infty l^2 \tag{2.81}$$

The numerical value of Flory's characteristic ratio depends on the local stiffness of the polymer chain with typical values of 7 to 9 for many flexible polymers. There is a tendency of polymers with bulkier side groups to have higher C_∞, owing to the side groups sterically hindering bond rotation (as in polystyrene), but there are many exceptions to this general tendency (such as polyethylene).

Flexible polymers exhibit universal properties that are independent of the local chemical structure. A simple unified description of all ideal polymers was needed. The first attempts to use random flight concepts to describe the linear polymers in solution are usually attributed to Kuhn,[87] who argued that the Rayleigh random flight model might be used. It soon became evident that such a model was not appropriate to very short chains (less than a few hundred chemical bonds), or to relatively stiff chains which cannot adopt tortuous configurations. Moreover, it is not appropriate to use as "steps" in the random flight the individual bond lengths, or even the monomeric units the chain consists of. Thus, the length of an individual step, b_{K}, became an adjustable parameter of the model, namely the *Kuhn length*. The *equivalent freely jointed chain* should have the same mean-square end-to-end distance $\langle R_{\mathrm{e}}^2\rangle$ and the same end-to-end distance at full extension, R_{full}, as the actual polymer but have N freely-jointed effective bonds of length b_{K}. The contour length of this equivalent freely jointed chain is:

$$R_{\mathrm{full}} = N b_{\mathrm{K}} \tag{2.82}$$

and its mean-square end-to-end distance is:

$$\left\langle R^{2}\right\rangle = N b_{\mathrm{K}}^2 = C_\infty N_{\mathrm{b}} l^2 \tag{2.83}$$

where N_{b} and l are the number of backbone bonds and their length, respectively.

2.3.3 Free Energy of an Ideal Chain

The entropy, S, can be defined as the product of the Boltzmann constant k_B and the logarithm of number of states, Ω, a system can assume (eq 2.14):

$$S = k_\mathrm{B} \ln \Omega \tag{2.84}$$

Now, we can denote as $\Omega\left(N, \mathbf{R}_\mathrm{e}\right)$ the number of conformations of a freely jointed chain of N segments with end-to-end vector $\mathbf{R}_\mathrm{e}$. Thus, the entropy can be written as a function of N and $\mathbf{R}_\mathrm{e}$:

$$S\left(N, \mathbf{R}_\mathrm{e}\right) = k_\mathrm{B} \ln \Omega(N, \mathbf{R}_\mathrm{e}) \tag{2.85}$$

The probability distribution, function, $W_N\left(R_\mathrm{e}\right)$, eq 2.58, is defined such that $W_N\left(R_\mathrm{e}\right) \mathrm{d}\mathbf{R}_\mathrm{e}$ is the fraction of all conformations that have an end-to-end vector between $\mathbf{R}_\mathrm{e}$ and $\mathbf{R}_\mathrm{e} + \mathrm{d}\mathbf{R}_\mathrm{e}$:

$$W_N\left(R_\mathrm{e}\right) = \frac{\Omega\left(N, \mathbf{R}_\mathrm{e}\right)}{\int \Omega\left(N, \mathbf{R}_\mathrm{e}\right) \mathrm{d}\mathbf{R}_\mathrm{e}} \tag{2.86}$$

The entropy of an ideal chain with N segments and an end-to-end vector $\mathbf{R}_\mathrm{e}$ is thus related to the probability distribution function:

$$S\left(N, \mathbf{R}_\mathrm{e}\right) = k_\mathrm{B} \ln W_N\left(\mathbf{R}_\mathrm{e}\right) + k_\mathrm{B} \ln \left[\int \Omega\left(N, \mathbf{R}_\mathrm{e}\right) \mathrm{d}\mathbf{R}_\mathrm{e}\right] \tag{2.87}$$

If we assume that the chain can be described as either a Gaussian or a freely jointed one in the limit of inifinite N, eq 2.78 holds and its entropy can be obtained as:

$$S\left(N, \mathbf{R}_\mathrm{e}\right) = -\frac{3}{2} k_\mathrm{B} \frac{R_\mathrm{e}^2}{N b_\mathrm{K}^2} + \frac{3}{2} k_\mathrm{B} \ln \left(\frac{3}{2\pi N b_\mathrm{K}^2}\right) + k_\mathrm{B} \ln \left[\int \Omega\left(N, \mathbf{R}_\mathrm{e}\right) \mathrm{d}\mathbf{R}_\mathrm{e}\right] \tag{2.88}$$

with the last two terms depending only on the number of segments, N, but not on the end-to-end vector, and denoted by $S\left(N, 0\right)$:

$$S\left(N, \mathbf{R}_\mathrm{e}\right) = -\frac{3}{2} k_\mathrm{B} \frac{R_\mathrm{e}^2}{N b_\mathrm{K}^2} + S\left(N, 0\right) \tag{2.89}$$

Finally, we can extract the Hemlmholtz energy of the chain, $A\left(N, \mathbf{R}_{\mathrm{e}}\right)$:

$$\begin{aligned} A\left(N, \mathbf{R}_{\mathrm{e}}\right) &= U\left(N, \mathbf{R}_{\mathrm{e}}\right) - TS\left(N, \mathbf{R}_{\mathrm{e}}\right) \\ &= \frac{3}{2} k_{\mathrm{B}} T \frac{R_{\mathrm{e}}^2}{N b_{\mathrm{K}}^2} + A\left(N, 0\right) \end{aligned} \tag{2.90}$$

where $A\left(N, 0\right) = U\left(N, 0\right) - TS\left(N, 0\right)$ is the free energy of the chain with both ends at the same point. We have assumed that the potential energy of an ideal chain, $U\left(N, \mathbf{R}_{\mathrm{e}}\right)$ is independent of the end-to-end vector, $\mathbf{R}_{\mathrm{e}}$, since the structural units of an ideal chain have no interaction energy.

The free energy of an ideal chain increases quadratically with the magnitude of the end-to-end vector, implying that the entropic elasticity of an ideal chain satisfies Hooke's law. The coefficient of proportionality $3k_{\mathrm{B}}T/\left(Nb_{\mathrm{K}}^2\right)$ is the *entropic spring constant* of an ideal chain. The fact that the spring constant is proportional to the temperature is a signature of entropic elasticity. The linear entropic spring result for the stretching of an ideal chain is extremely important for our subsequent discussion of polymer dynamics. The linear dependence is due to the Gaussian approximation.

2.3.4 Simplified Polymer Dynamics Models

2.3.4/i Rouse model

As we have seen earlier, the static properties of a polymer can be represented by a set of beads connected along a chain. Even though the individual atoms move about with the same equilibrium distribution of speeds, as if they were disconnected, their motion is constrained by the chemical bonds keeping the chain together. Thus, it would be natural to model the dynamics of the polymer by the Brownian motion of such beads, connected by entropic springs. The beads move as (tethered) Brownian particles subject to random forces and to frictional forces proportional to their velocity exerted from their environment. This is the basis of the model proposed by Rouse.[88] It should be emphasized that the essence of the *Rouse model* is the universal nature of modeling the dynamics of a linearly-connected object. The central assumption in the Rouse model is that the dynamics is governed by the localized interactions along the chain.

The equation of motion of the beads in the Rouse model can be described by the Langevin equation:[89]

$$\frac{\partial}{\partial t}\mathbf{r}_i\left(t\right)=\sum_{j=0}^{N}\mathbf{H}_{ij}\cdot\left(-\frac{\partial\mathcal{V}_{\text{Rouse}}}{\partial\mathbf{r}_j}+\boldsymbol{\mathcal{F}}_j\left(t\right)\right)+\frac{1}{2}k_{\text{B}}T\sum_{j=0}^{N}\frac{\partial}{\partial\mathbf{r}_j}\mathbf{H}_{ij} \tag{2.91}$$

where $\{\mathbf{r}_i\}=(\mathbf{r}_0,\mathbf{r}_1,\ldots,\mathbf{r}_N)$ are the positions of the beads, **H** is the mobility tensor and $\boldsymbol{\mathcal{F}}_j$ the random force acting on bead j. The mobility tensor takes the form:

$$\mathbf{H}_{ij}=\frac{1}{\zeta}\delta_{ij}\mathbb{I} \tag{2.92}$$

with $\mathbb{I}$ being the unit tensor and ζ the friction coefficient of the bead. The interaction potential:

$$\mathcal{V}_{\text{Rouse}}=\frac{3k_{\text{B}}T}{2b^2}\sum_{i=1}^{N}\left(\mathbf{r}_i-\mathbf{r}_{i-1}\right)^2 \tag{2.93}$$

In the Rouse model, excluded volume and hydrodynamic interactions are disregarded (diagonality of **H**), leading to a Langevin equation linear for $\mathbf{r}_i$. This takes the forms:

$$\begin{aligned}\zeta\frac{\mathrm{d}\mathbf{r}_0}{\mathrm{d}t}&=\frac{3k_{\text{B}}T}{b^2}\left(\mathbf{r}_1-\mathbf{r}_0\right)+\boldsymbol{\mathcal{F}}_0\\ \zeta\frac{\mathrm{d}\mathbf{r}_i}{\mathrm{d}t}&=\frac{3k_{\text{B}}T}{b^2}\left(\mathbf{r}_{i+1}-2\mathbf{r}_i+\mathbf{r}_{i-1}\right)+\boldsymbol{\mathcal{F}}_i\\ \zeta\frac{\mathrm{d}\mathbf{r}_N}{\mathrm{d}t}&=-\frac{3k_{\text{B}}T}{b^2}\left(\mathbf{r}_N-\mathbf{r}_{N-1}\right)+\boldsymbol{\mathcal{F}}_N\end{aligned} \tag{2.94}$$

for internal ($i=1,2,\ldots,N-1$) and end beads ($i=0$ and $i=N$), respectively. The distributions of random forces $\boldsymbol{\mathcal{F}}_i$ is Gaussian, characterized by the moments:

$$\begin{aligned}\langle\mathcal{F}_{i\alpha}\rangle&=0\\ \langle\mathcal{F}_{i\alpha}\left(t\right)\mathcal{F}_{j\beta}\left(t'\right)\rangle&=2\zeta k_{\text{B}}T\delta_{ij}\delta_{\alpha\beta}\delta\left(t-t'\right)\end{aligned} \tag{2.95}$$

implying that there are no correlations of the random forces, neither across different beads nor across different times. Moreover, different Cartesian components (α,β) of the same random force are not correlated. As in the case of the Gaussian chain, the index i running along the beads in the Rouse model, can be regarded as a continuous variable $s\in[0,1]$, running along the contour of the chain. In the continuous limit, eq 2.94 can be written as:

$$\zeta\frac{\partial\mathbf{r}(s)}{\partial t}=\frac{3k_{\text{B}}T}{2}\frac{\partial^2\mathbf{r}(s)}{\partial s^2}+\boldsymbol{\mathcal{F}}\left(s,t\right) \tag{2.96}$$

In order to rewrite eq 2.94 in the continuous limit, we assume that the two end beads can be defined in the continuous limit,

$$\left.\frac{\mathrm{d}\mathbf{r}(s)}{\mathrm{d}s}\right|_{s=0} = 0, \quad \left.\frac{\mathrm{d}\mathbf{r}(s)}{\mathrm{d}s}\right|_{s=1} = 0 \tag{2.97}$$

Also, the moments of the random forces, $\boldsymbol{\mathcal{F}}\left(s,t\right)$ are now given as:

$$\begin{aligned} \left\langle \mathcal{F}_\alpha\left(s,t\right)\right\rangle &= 0 \\ \left\langle \mathcal{F}_\alpha\left(s,t\right)\mathcal{F}_\beta\left(s',t'\right)\right\rangle &= 2\zeta k_\mathrm{B} T\delta(s-s')\delta_{\alpha\beta}\delta(t-t') \end{aligned} \tag{2.98}$$

The continuous Rouse model is fully defined by eqs 2.96, 2.97 and 2.98.

2.3.4/ii Stress relaxation in the Rouse model

The linear viscoelastic response of polymeric liquids measures the full spectrum of relaxation times. Since polymer chains are self-similar objects, they also exhibit dynamic self-similarity. This means that smaller sections of a polymer chain, containing $N_\text{sub} < N$ segments, relax like a whole polymer chain that has N_sub segments. In all unentangled models for polymer dynamics (both Rouse and Zimm[90]) the relaxation is described by N different *relaxation modes*. The modes are numbered by mode index $\upsilon = 1, 2, \ldots, N$. These modes are analogous to the modes of a vibrating string. Mode υ involves coherent motion of sections of the whole chain with N/υ segments, and the corresponding relaxation time of this node τ_υ is similar to the longest relaxation time of a chain with N/υ segments.

The spectrum of relaxation times of the Rouse model is given as:[91]

$$\tau_\upsilon = \frac{\zeta b_\mathrm{K}^2}{12k_\mathrm{B}T}\sin^{-2}\left(\frac{\pi\upsilon}{2\left(N+1\right)}\right) \qquad \upsilon = 1, 2, \ldots N \tag{2.99}$$

The longest relaxation time, τ_1 (also called *Rouse relaxation time* $\tau_\mathrm{R} = \tau_1$), is:

$$\tau_\mathrm{R} \equiv \tau_1 = \frac{\zeta b_\mathrm{K}^2}{12k_\mathrm{B}T}\sin^{-2}\left(\frac{\pi}{2\left(N+1\right)}\right) \approx \frac{\zeta b_\mathrm{K}^2\left(N+1\right)^2}{3\pi^2 k_\mathrm{B}T} \tag{2.100}$$

For all unentangled flexible polymer dynamics, the shortest mode has mode index $\upsilon = N$, with the corresponding time being $\tau_N \approx \zeta b_\mathrm{K}^2/12k_\mathrm{B}T$ which is half the relaxation time of a single segment ($N = 1$). However, in the literature,[86] one often finds the definition of the fastest relaxation time as

$$\tau_0 = \frac{\tau_\mathrm{R}}{\left(N+1\right)^2} \approx \frac{\zeta b_\mathrm{K}^2}{3\pi^2 k_\mathrm{B}T} \tag{2.101}$$

which is called the *Kuhn segment relaxation time*, τ_0, and is 2.5 times smaller than τ_N.

Rouse also derived an exact relation for the shear relaxation modulus,

$$G\left(t\right) = \rho_{\mathrm{mol}} k_{\mathrm{B}} T \sum_{v=1}^{N} \exp\left(-\frac{2t}{\tau_v}\right) = \rho_{\mathrm{mol}} k_{\mathrm{B}} T \sum_{v=1}^{N} \exp\left(-\frac{2v^2 t}{\tau_{\mathrm{R}}}\right) \tag{2.102}$$

where ρ_{mol} is the density of polymer chains. Equation 2.102 has a simple interpretation: according to the equipartition theorem in a system of linear oscillators, each mode carries equal elastic energy, $k_{\mathrm{B}}T$. In particular, we see that the Rouse model predicts that $G\left(t\right)$ starts from a value $\rho_{\mathrm{mol}}\left(N+1\right)k_{\mathrm{B}}T$. For $t << \tau_{\mathrm{R}}$, the sum over v in eq 2.102 can be approximated by an integral over v:[92]

$$G\left(t\right) = \rho_{\mathrm{mol}} k_{\mathrm{B}} T \int_0^{\infty} \mathrm{d}v \exp\left(-\frac{2v^2 t}{\tau_{\mathrm{R}}}\right) = \frac{\sqrt{\pi}}{2\sqrt{2}} \rho_{\mathrm{mol}} k_{\mathrm{B}} T \left(\frac{\tau_{\mathrm{R}}}{t}\right)^{1/2} \tag{2.103}$$

Therefore $G\left(t\right)$ decays as a power law $t^{-1/2}$ on short time scales. This characteristic behavior is also seen in the frequency domain. If we use eq 2.102 in eqs 2.43 and 2.44, we find that $G'\left(\omega\right)$ and $G''\left(\omega\right)$ increase in proportion to $\omega^{1/2}$ in the high-frequency regime $\omega\tau_{\mathrm{R}} >> 1$. Such behavior is indeed observed in polymeric fluids at high frequency. Summarizing, the following regimes can be observed for $G\left(t\right)$:[91]

$$\frac{G\left(t\right)}{\rho_{\mathrm{mol}}\left(N+1\right)k_{\mathrm{B}}T} = \begin{cases} 1 - \frac{12 k_{\mathrm{B}} T}{\zeta b_{\mathrm{K}}^2} t, & t < \tau_N \\ \sqrt{\frac{\pi}{8(N+1)^2} \frac{\tau_{\mathrm{R}}}{t}} = \sqrt{\frac{\zeta b_{\mathrm{K}}^2}{24 \pi k_{\mathrm{B}} T}} \ t^{-1/2}, & \tau_N < t < t_{\mathrm{R}} \\ \frac{1}{N} \exp\left(-\frac{2t}{\tau_{\mathrm{R}}}\right), & t > \tau_{\mathrm{R}} \end{cases} \tag{2.104}$$

2.3.4/iii Chain diffusion in the Rouse model

Let us now study the consequences of the Rouse model concerning the motion at microscopic level. The motion of the chains can be described in terms of the mean-square displacement of their centers of mass, $g_{\mathrm{cm}}\left(t\right)$:

$$g_{\mathrm{cm}}\left(t\right) = \left\langle \left(\mathbf{r}_{\mathrm{cm}}\left(t_0 + t\right) - \mathbf{r}_{\mathrm{cm}}\left(t_0\right)\right)^2 \right\rangle \tag{2.105}$$

which can be obtained from the solution of the Rouse model, as:

$$g_{\mathrm{cm}}^{\mathrm{Rouse}}\left(t\right) = \frac{6 k_{\mathrm{B}} T}{\left(N+1\right)\zeta} \ t \tag{2.106}$$

with $N+1$ being the number of beads, ζ the friction coefficient of a bead and T the temperature. The self diffusion constant of the center of mass of the chain can be obtained as:

$$D_{\mathrm{cm}}^{\mathrm{Rouse}} = \lim_{t\to\infty} \frac{1}{6t} g_{\mathrm{cm}}^{\mathrm{Rouse}}(t) = \frac{k_{\mathrm{B}}T}{(N+1)\,\zeta} \tag{2.107}$$

Moreover, the *rotational relaxation time*, τ_{R}, of the system (which is also the longest relaxation time), given by eq 2.100, can be thought as the time needed from the chain in order to diffuse a distance equal to its size $\sqrt{\langle R_{\mathrm{e}}^2\rangle}$. The longest relaxation time is significant because the relaxation of internal stresses occurs on this time scale.

Since N is proportional to the molecular weight, M, the Rouse model predicts a scaling of the self diffusion and the longest relaxation time:

$$\begin{aligned} D_{\mathrm{cm}}^{\mathrm{Rouse}} &\propto M^{-1} \\ \tau_{\mathrm{R}} &\propto M^{2} \end{aligned} \tag{2.108}$$

which are not consistent with the experimental results from dilute solutions, which, under Θ conditions, are:[89]

$$\begin{aligned} D_{\mathrm{cm}}^{\mathrm{Rouse}} &\propto M^{-1/2} \\ \tau_{\mathrm{R}} &\propto M^{3/2} \end{aligned} \tag{2.109}$$

The deviation of Rouse model from the experimental results, comes from neglecting the hydrodynamic interactions. However, its simplicity makes it conceptually important and also it has turned out to be a useful model for the dynamics of polymers in melts.

2.3.4/iv Bead motion in the Rouse model

We can then consider the mean-square displacement (MSD) of a Rouse segment, as a function of time, $g_i\,(t)$:

$$g_i\,(t) = \left\langle \left(\mathbf{r}_i\,(t_0+t) - \mathbf{r}_i\,(t)\right)^2 \right\rangle \tag{2.110}$$

The shortest time scale in the Rouse model is set by the Kuhn segment relaxation time, τ_0, as was obtained in eq 2.101. The time scale for motion of individual segments, τ_0, is the time scale at which a segment would diffuse a distance of order of its size, b_{K}, if it were not attached to the chain. When probed on time scales smaller than τ_0, the polymer essentially does not move and exhibits elastic response. On time scales longer than τ_{R}, the polymer moves diffusively and exhibits the response of a simple liquid.

The mean-square displacement of a Rouse bead varies as $\sim t^{1/2}$ over time intervals (t) less than the maximum relaxation time of the chain (τ_{R}), and only for times greater than the maximum relaxation time ($t > \tau_{\mathrm{R}}$) does it become proportional to t as in the case of ordinary diffusion of a Brownian particle:

$$g_i^{\mathrm{Rouse}}(t) \sim t^{1/2}, \quad \tau_0 < t < \tau_{\mathrm{R}} \tag{2.111}$$

$$g_i^{\mathrm{Rouse}}(t) \sim t, \quad t > \tau_{\mathrm{R}} \tag{2.112}$$

2.3.4/v Tube model

Concentrated polymer solutions and polymer melts are extremely complex systems. For that reason, it is unquestionably important to make judicious assumptions in describing the dynamics of polymers in such systems. The concept of *reptational motion*[93] is an assumption that has led to a widely and successfully applied class of molecular models for the polymer dynamics in concentrated solutions and melts. The first detailed reptation model for the rheology of undiluted polymers was developed in a series of papers by Doi and Edwards.[94–97] The *Doi-Edwards model* is based on the assumption that each polymer chain in an entangled system moves like a snake ("reptates") in a tube formed by other chains. In other words, fluctuations of chain segments perpendicular to some tube contour will be restricted by other chains, whereas fluctuations parallel to this contour will be unaffected. It was assumed that at times longer than the equilibration time of the chain inside the tube one does not need to distinguish between the chain and the tube, and the stress relaxation and other quantities can be computed from the tube evolution equations. Several further assumptions need to be made, and several different representations of the reptating polymer are used (e.g. the "slip-link" model in addition to the "tube-model") in order to derive the final diffusion equation describing the polymeric motion. In order to derive the rheological properties of such systems, Doi and Edwards have employed a formula for the stress tensor based on rubber elasticity.

The motion of the chain along the contour of the tube (*the primitive path*) is unhindered by topological interactions. Displacement of segments in the direction perpendicular to the primitive path is restricted by surrounding chains to an average distance, a_{pp}, called the *tube diameter*. The number of Kuhn segments in a strand of size equal to the tube diameter (the amplitude of transverse fluctuations) is N_{e}, the number of structural units (or monomers) in an entanglement strand. For melts, excluded volume interactions are thought to be screened, and the tube diameter can be determined by ideal chain statistics

$$a_{\mathrm{pp}} \approx b_{\mathrm{K}} N_{\mathrm{e}}^{1/2} \tag{2.113}$$

The average contour length $\langle L\rangle$ of the primitive path (the center of the confining tube) is the product of the entanglement strand length a_{pp} and the average number of entanglement strands per chain, $(N+1)/N_{\mathrm{e}}$,

$$\langle L\rangle \approx a_{\mathrm{pp}}\frac{(N+1)}{N_{\mathrm{e}}} \approx \frac{b_{\mathrm{K}}^{2}(N+1)}{a_{\mathrm{pp}}} \approx \frac{b_{\mathrm{K}}(N+1)}{\sqrt{N_{\mathrm{e}}}} \tag{2.114}$$

$\langle L\rangle$ is shorter the the contour length of the chain $b_{\mathrm{K}}(N+1)$ by the factor $a_{\mathrm{pp}}/b_{\mathrm{K}} \sim \sqrt{N_{\mathrm{e}}}$ because each entanglement strand in a melt is a random walk of N_{e} Kuhn segments.

2.3.4/vi Bead motion in the tube model

On times shorter than the relaxation time of an entanglement strand, τ_{e}, the sections of a linear chain involved in motion are shorter than the entanglement strand and do not feel the topological constraints generated by their environment. Since hydrodynamic interactions are screened in polymer melts, the motion on very short time scales $t<\tau_{\mathrm{e}}$, is Rouse-like with mean-square monomer displacement, $g_i(t)$ given by the subdiffusive motion of the Rouse model, eq 2.111:

$$g_i^{\mathrm{tube}}(t) \approx b_{\mathrm{K}}^{2}\left(\frac{t}{\tau_0}\right)^{1/2} = \left(\frac{k_{\mathrm{B}}Tb_{\mathrm{K}}^{2}}{\zeta}\right)^{1/2} t^{1/2} \sim t^{1/2}, \quad t<\tau_{\mathrm{e}} \tag{2.115}$$

where the above formula is correct when the average displacement is much less than the tube diameter. Let τ_{e} be the time at which the segmental displacement becomes comparable to the tube diameter a_{pp}:

$$\tau_{\mathrm{e}} \simeq \frac{a_{\mathrm{pp}}^{4}\zeta}{k_{\mathrm{B}}Tb_{\mathrm{K}}^{2}} \tag{2.116}$$

On longer time scales, $t>\tau_{\mathrm{e}}$, topological constraints restrict polymer motion to the confining tube. Displacements of the monomers perpendicular to the axis of the tube (primitive path) on length scales larger than the tube diameter a_{pp} are suppressed by the surrounding chains. Monomer displacement along the contour of the tube is unconstrained and follows the Rouse subdiffusive behavior, *only along the primitive path*. Thus, the mean-square monomer displacement in space exhibits a one-fourth power law scaling when the chain feels the confinement of the tube:

$$g_i^{\mathrm{tube}}(t) \approx a_{\mathrm{pp}}^{2}\left(\frac{t}{\tau_{\mathrm{e}}}\right)^{1/4} = \left(\frac{a_{\mathrm{pp}}^{4}k_{\mathrm{B}}Tb_{\mathrm{K}}^{2}}{\zeta}\right)^{1/4} t^{1/4} \sim t^{1/4}, \quad \tau_{\mathrm{e}}<t<\tau_{\mathrm{R}} \tag{2.117}$$

The above time dependence is slower than for unrestricted Rouse motion because displacement *along the contour* of the tube leads to a smaller overall displacement *in space*.

At the Rouse time of the chain, τ_{R}, each segment participates in a coherent Rouse motion of the whole chain along the tube. The mean-square displacement of a segment along the tube at the Rouse time of the chain is of the order of magnitude of the mean-square size of the whole chain. The chain diffuses along the tube, with a curvilinear diffusion coefficient given by the Rouse model, eq 2.107. Thus, the mean-square displacement of individual segments in space is:

$$\begin{aligned} g_i^{\mathrm{tube}}(t) &\approx a_{\mathrm{pp}}^2 \left(\frac{N+1}{N_{\mathrm{e}}}\right)^{1/2} \left(\frac{t}{\tau_{\mathrm{R}}}\right)^{1/2} \\ &= \left(\frac{3\pi^2 k_{\mathrm{B}} T a_{\mathrm{pp}}^2}{\zeta (N+1)}\right)^{1/2} t^{1/2} \sim t^{1/2}, \quad \tau_{\mathrm{R}} < t < \tau_{\mathrm{d}} \end{aligned} \tag{2.118}$$

This curvilinear diffusion continues up to the *disentanglement* or *reptation* time, τ_{d}:

$$\tau_{\mathrm{d}} = \frac{(N+1)^3 \zeta b_{\mathrm{K}}^4}{\pi^2 k_{\mathrm{B}} T a_{\mathrm{pp}}^2} \tag{2.119}$$

where the chain has curvilinearly diffused the complete length of the tube, of order $a_{\mathrm{pp}}(N+1)/N_{\mathrm{e}}$.

At times longer than the disentanglement time, $t > \tau_{\mathrm{d}}$, the mean-square displacement of a segment is approximately the same as the center of mass of the chain and is simple diffusion with coefficient $D_{\mathrm{cm}}^{\mathrm{Rouse}}$, eq 2.107:

$$g_i^{\mathrm{tube}}(t) \approx \frac{k_{\mathrm{B}} T a_{\mathrm{pp}}^2}{(N+1)^2 \zeta b_{\mathrm{K}}^2} t \sim t, \quad t > \tau_{\mathrm{d}} \tag{2.120}$$

Summarizing, there are four different regimes of monomer displacement in entangled linear polymer melts, shown in Figure 2.3:

$$g_i^{\mathrm{tube}}(t) \sim t^{1/2}, \quad t < \tau_{\mathrm{e}} \tag{2.115}$$

$$g_i^{\mathrm{tube}}(t) \sim t^{1/4}, \quad \tau_{\mathrm{e}} < t < \tau_{\mathrm{R}} \tag{2.117}$$

$$g_i^{\mathrm{tube}}(t) \sim t^{1/2}, \quad \tau_{\mathrm{R}} < t < \tau_{\mathrm{d}} \tag{2.118}$$

$$g_i^{\mathrm{tube}}(t) \sim t, \quad t > \tau_{\mathrm{d}} \tag{2.120}$$

2.3.4/vii Chain diffusion in the tube model

According to Likhtman,[91] and early simulation works,[98,99] the reptation model predicts three regimes for the diffusion of the center of mass of the chains. For times smaller than the τ_{e}, the

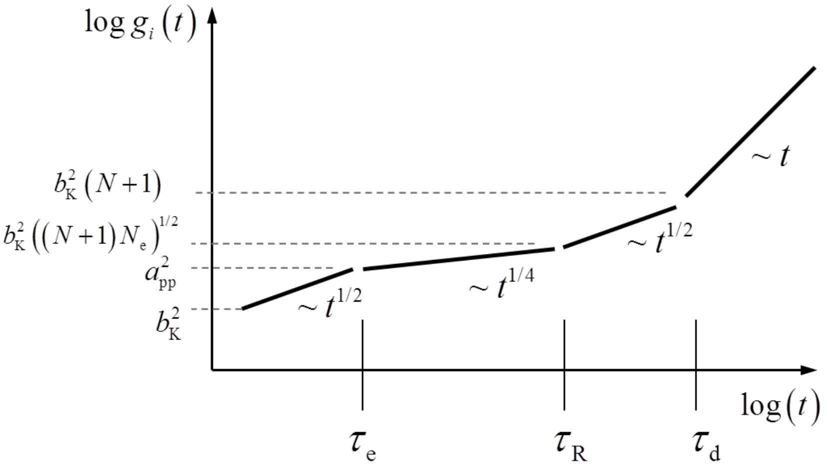

Figure 2.3: Time dependence of the mean-square segmental displacement, $g_i(t)$, predicted by the reptation model for a melt of entangled linear chains on logarithmic scales.

segments of the chain execute Brownian motion, following the subdiffusive $t^{1/2}$ scaling of the Rouse model. The center of mass of the chain follows the same Rouse behavior with:

$$g_{\mathrm{cm}}^{\mathrm{tube}}(t) \sim t, \quad t < \tau_{\mathrm{e}} \tag{2.121}$$

When the segments of the chain feel the topological constraints of the surrounding chains, $g_{\mathrm{i}}(t) \sim t^{1/4}$, the diffusion of the center of mass is significantly slowed down:

$$g_{\mathrm{cm}}^{\mathrm{tube}}(t) \sim \left(\frac{t}{(N+1)^2}\right)^{1/2}, \quad t < \tau_{\mathrm{R}} \tag{2.122}$$

till the Rouse time, τ_{R}, when the center of mass enters the diffusive regime again:

$$g_{\mathrm{cm}}^{\mathrm{tube}}(t) \sim \frac{t}{(N+1)^2}, \quad t > \tau_{\mathrm{R}} \tag{2.123}$$

2.3.4/viii Stress relaxation in the tube model

Entanglements are manifested in long chains ($N >> N_{\mathrm{e}}$) by the appearance of a wide region in time (or frequency) where the modulus is almost constant in stress relaxation (or oscillatory shearing) experiments. This region is referred as the *rubbery plateau* in analogy with crosslinked rubbers. The nearly constant value of the modulus in this regime is called the *plateau modulus*, G_{e}. In analogy with a perfect network, whose modulus is in the order of $k_{\mathrm{B}}T$ per network strand, the plateau modulus is of the order $k_{\mathrm{B}}T$ per entanglement strand. The plateau modulus of an entangled polymer melt can be calculated as:

$$G_\mathrm{e} \approx \frac{\rho \mathcal{N}_\mathrm{A} k_\mathrm{B} T}{M_\mathrm{e}} \tag{2.124}$$

with ρ being the mass density and $\mathcal{N}_\mathrm{A}$ being Avogadro's constant.

2.3.4/ix Additional mechanisms to the tube model

The tube model, as described till now, is not able to quantitatively describe the linear relaxation modulus of polymers.[91,100,101] Fluctuations of the tube along its backbone and in the lateral directions should also be considered. These additional relaxation modes are termed contour-length fluctuation (CLF)[102] and constraint release (CR); the former is the fluctuation of the curvilinear tube length, representing the spring-like fluctuation of the chain inside the tube, whereas the latter is the fluctuation of the tube in the lateral direction resulting from the disentanglement of the surrounding chains. Thus, CLF is a refinement of the single-chain dynamics in the tube, whereas CR is a reflection of the multichain dynamics. This fundamental difference between CLF and CR causes a large difference in the technical description of each mechanism. Specifically, the implementation of CLF into tube theory is almost established,[103,104] whereas the description of CR is still controversial.

There have been three major branches for theoretical expression of CR. Double reptation theory, which was developed by Tsenoglou[105] and des Cloizeaux,[106] proposes that the relaxation modulus is proportional to the squared-tube survival probability. This theory is a sort of mixing rule, based on the binary assumption of entanglement. These authors assume that one entanglement consists of two chain segments and relaxes when one of the two segments diffuses outward. Another idea is to cast the tube fluctuation owing to CR into a Rouse dynamics, where the Rouse bead friction corresponds to the disentanglement frequency.[107] Marrucci[108] proposed yet another implementation, called dynamic tube dilation, in which the primitive path (the center line of the tube) is immobile but the tube cross-section swells according to the disentanglement of surroundings.

2.3.5 Equations of State

The thermodynamics of polymeric systems play an important role in the polymer industry and are often a key factor in polymer production, processing and material development. An *equation of state* is a relation between the *state variables* of a system.[109] The most prominent use of an equation of state is to correlate densities of liquids (and gases) to temperatures and pressures ($p - V - T$ data). In statistical mechanics, the Gibbs energy, G, is related to the configurational integral, $\mathcal{Z}$ in the isothermal-isobaric ensemble by eq 2.20:

$$G = -k_{\mathrm{B}}T \ln\left[\mathcal{Z}_{NpT}\left(T, p\right)\right] \tag{2.125}$$

where the configurational integral in the NpT ensemble is:

$$\mathcal{Z}_{NpT}\left(T, p\right) = \sum_{V}\sum_{E}\Omega\left(E, V, n\right)\exp\left[-\frac{E + pV}{k_{\mathrm{B}}T}\right] \tag{2.126}$$

with $\Omega\left(E, V, n\right)$ being the number of configurations available to a system of n molecules whose potential (configurational) energy and volume are E and V, respectively. The summations extend over all feasible values of E and V. The isothermal-isobaric ensemble and the associated Gibbs potential are the most convenient of the potential ensembles to utilize in the study of fluid phase equilibria.

The fundamental problem of deriving the equation of state for a system is to determine Ω. One of the most widely-used equations of state for polymer fluids is the one derived by Sanchez and Lacombe.[110] These authors have employed a lattice formulation, wherein the polymer chains are occupying discrete lattice sites, while there also exist vacant lattice sites(holes). The Gibbs energy, based on the Sanchez-Lacombe equation of state can be expressed in dimensionless variables as:

$$\begin{aligned}\frac{G}{nr\varepsilon^{*}} &\equiv \tilde{G} \\ &= -\tilde{\rho} + \tilde{p}\tilde{v} + \tilde{T}\left[\left(\tilde{v} - 1\right)\ln\left(1 - \tilde{\rho}\right) + \frac{1}{r}\ln\left(\frac{\tilde{\rho}}{w}\right)\right]\end{aligned} \tag{2.127}$$

where $\tilde{T}$, $\tilde{p}$, $\tilde{v}$ and $\tilde{\rho}$ are the reduced temperature, pressure volume and density. The parameter w is connected to the number of different configurations available to a system of n r-mers. It will be examined in detail later. The Sanchez-Lacombe parameters are presented in Table 2.1.The corresponding equation of state can be extracted, by minimizing G:

$$\left.\frac{\partial\tilde{G}}{\partial\tilde{v}}\right)_{\tilde{T},\tilde{p}} = 0 \tag{2.128}$$

which yields the *equation of state* for the system:

$$\tilde{\rho}^{2} + \tilde{p} + \tilde{T}\left[\ln\left(1 - \tilde{\rho}\right) + \left(1 - \frac{1}{r}\right)\tilde{\rho}\right] = 0 \tag{2.129}$$

It should be noted that, in the isothermal-isobaric ensemble, $\tilde{p}$ and $\tilde{T}$ are the independent vari-

Table 2.1: Sanchez-Lacombe notation

Symbol	Explanation	Units
n	number of molecules	-
M	molecular weight	kg
r	Sanchez-Lacombe segments per molecule	-
V	volume of the system	m^3
ρ	mass density of the system	$\mathrm{kg/m}^3$
$\rho_{\mathrm{mol}} = \frac{n}{V}$	molecular density	m^{-3}
v^*	close packed volume of a mer	m^3
rv^*	close packed volume of an r-mer molecule	m^3
$V^* = n\left(rv^*\right)$	close packed volume of the n r-mers	m^3
$\rho^* = \frac{M}{rv^*}$	close packed mass density	$\mathrm{kg/m}^3$
$T^* = \varepsilon^*/k_{\mathrm{B}}$	characteristic temperature	K
$p^* = \varepsilon^*/v^*$	characteristic pressure	$\mathrm{kg/}\left(\mathrm{ms}^2\right)$
$\tilde{T} = T/T^*$	reduced temperature	-
$\tilde{p} = p/p^*$	reduced pressure	-
$\tilde{\rho} = \rho/\rho^* = \rho_{\mathrm{mol}}M/\rho^*$	reduced density	
$\tilde{v} = 1/\tilde{\rho} = V/V^*$	reduced volume	-

ables, while $\tilde{\rho}$ is the dependent one. Therefore, eq 2.129 defines the value of $\tilde{\rho}$ at given $\left(\tilde{T}, \tilde{p}\right)$ that minimizes the free energy. Equations 2.127 and 2.129 contain the complete thermodynamic description of the model fluid.

Since the Sanchez-Lacombe theory is not a corresponding states theory, the state parameters are predicted to vary with chain length. It has been shown that expansion coefficients, compressibilities and free volumes are predicted by the Sanchez-Lacombe equation of state to decrease with increasing degree of polymerization, in agreement with experiment. The decrease of the free volume with increasing molecular weight is supported by the observation that the glass temperature increases with increasing molecular weight.[111]

If we wish to obtain some physical insight into the parameter w, we can compare the Sanchez - Lacombe Equation of State (EoS) with the ideal gas EoS. The former should reduce to the latter, in the limit of zero molecular density, $\rho_{\mathrm{mol}} = n/V$:

$$\lim_{\rho_{\mathrm{mol}} \to 0^+} A^{\mathrm{SL}} = \lim_{\rho_{\mathrm{mol}} \to 0^+} A^{\mathrm{id.g.}} \tag{2.130}$$

where we have used A^{SL} and $A^{\mathrm{id.g.}}$ to denote the Helmholtz energy obtained from the Sanchez-Lacombe and the ideal gas equations of state, respectively.

The Helmholtz energy can be obtained from eq 2.127:

$$\begin{aligned} A^{\mathrm{SL}}(\rho, T) =& G - pV = G - \tilde{p}\frac{Nr\epsilon^*}{\tilde{\rho}} \\ =& -\tilde{\rho}Nrk_{\mathrm{B}}T^* + Nrk_{\mathrm{B}}T\left[(\tilde{v}-1)\ln(1-\tilde{\rho}) + \frac{1}{r}\ln\left(\frac{\tilde{\rho}}{w}\right)\right] \end{aligned} \tag{2.131}$$

Thus, the limit appearing in the left-hand side of eq 2.130 is:

$$\begin{aligned} \lim_{\rho_{\mathrm{mol}}\to 0^+} A^{\mathrm{SL}} =& \lim_{\rho_{\mathrm{mol}}\to 0^+}\left(-\frac{Nrk_{\mathrm{B}}T^*M\rho_{\mathrm{mol}}}{\rho^*}\right) + \lim_{\rho_{\mathrm{mol}}\to 0^+}\left[\frac{Nrk_{\mathrm{B}}T\rho^*}{\rho_{\mathrm{mol}}M}\ln\left(1-\frac{\rho_{\mathrm{mol}}M}{\rho^*}\right)\right] \\ &- \lim_{\rho_{\mathrm{mol}}\to 0^+}\left[Nrk_{\mathrm{B}}T\ln\left(1-\frac{\rho_{\mathrm{mol}}M}{\rho^*}\right)\right] + \lim_{\rho_{\mathrm{mol}}\to 0^+}\left[Nk_{\mathrm{B}}T\ln\left(\frac{\rho_{\mathrm{mol}}M}{\rho^* w}\right)\right] \end{aligned}$$

which reduces to:[d]

$$\lim_{\rho_{\mathrm{mol}}\to 0^+} A^{\mathrm{SL}} = Nk_{\mathrm{B}}T\left[\lim_{\rho_{\mathrm{mol}}\to 0^+}\ln\left(\frac{\rho_{\mathrm{mol}}M}{\rho^* w}\right) - r\right] \tag{2.132}$$

On the other hand, the Helmholtz energy of an ideal gas can be written as:

$$\begin{aligned} A^{\text{id.g.}}(\rho, T) &= G^{\text{id.g.}}(\rho, T) - p^{\text{id.g.}}V \\ &= N\mu^{\text{id.g.}}(\rho, T) - Nk_{\mathrm{B}}T \\ &= Nk_{\mathrm{B}}T\left[\ln\left(\frac{\rho\prod_i \Lambda_i^3}{M\mathscr{Z}_0}\right) - 1\right] \end{aligned} \tag{2.133}$$

with Λ_i being the thermal wavelength of atom i of a molecule (eq 2.26 on page 19) of the fluid and $\mathscr{Z}_0$ the configurational integral of a single molecule with respect to all but three translational degrees of freedom (please see discussion preceding eq 2.47 on page 26). The molar mass of the molecule is denoted by M. The limit of eq 2.133 for $\rho_{\mathrm{mol}} \to 0^+$ is:

$$\lim_{\rho_{\mathrm{mol}}\to 0^+} A^{\text{id.g.}} = Nk_{\mathrm{B}}T \lim_{\rho_{\mathrm{mol}}\to 0^+}\left[\ln\left(\frac{\rho_{\mathrm{mol}}\prod_i \Lambda_i^3}{\mathscr{Z}_0 e}\right)\right] \tag{2.134}$$

Finally, by setting the right-hand side term of eq 2.132 equal to the right-hand side term of eq 2.134 we obtain:

$$\lim_{\rho_{\mathrm{mol}}\to 0^+}\left[\ln\left(\frac{\rho_{\mathrm{mol}}M}{\rho^* w e^r}\right)\right] = \lim_{\rho_{\mathrm{mol}}\to 0^+}\left[\ln\left(\frac{\rho_{\mathrm{mol}}\prod_i \Lambda_i^3}{\mathscr{Z}_0 e}\right)\right] \tag{2.135}$$

---

[d] It holds that:

$$\lim_{x\to 0^+}\left[\frac{a}{x}\ln(1-bx)\right] = -ab$$

which results in:

$$\frac{1}{w} = \frac{\rho^* \prod_i \Lambda_i^3}{M\mathcal{Z}_0} e^{(r-1)} \tag{2.136}$$

that connects the parameter w with the thermal wavelengths of the molecules and their intramolecular configurational integral, $\mathcal{Z}_0$. The molecular weight, M, enters eq 2.136 because ρ^* refers to the critical mass density of the equation of state.

2.4 Simulation Methods

2.4.1 Molecular Dynamics

In Cartesian coordinates, and under the assumption that the potential energy $\mathcal{V}$ is independent of velocities and time, Hamilton's equations of motion read:

$$\dot{\mathbf{r}}_i \equiv \mathbf{v}_i = \frac{\mathbf{p_i}}{m_i} \tag{2.137}$$

$$\dot{\mathbf{p}}_i \equiv -\frac{\partial \mathcal{V}}{\partial \mathbf{r}_i} = \mathbf{F}_i \tag{2.138}$$

hence

$$m_i \ddot{\mathbf{r}}_i = \mathbf{F}_i \tag{2.139}$$

where $\mathbf{F}_i$ is the force acting on atom i:

$$\mathbf{F}_i = -\nabla_{\mathbf{r}_i} \mathcal{V} \tag{2.140}$$

with the gradient being taken keeping all positions other than $\mathbf{r}_i$ constant. Solving the equations of motion then involves the integration of $3N$ second-order differential equations (eq 2.139) which are Newton's equations of motion.

The classical equations of motion possess some interesting properties, the most important one being the conservation law. If we assume that $\mathcal{K}$ and $\mathcal{V}$ do not depend explicitly on time, then it is straightforward to verify that $\dot{\mathcal{H}} = \mathrm{d}\mathcal{H}/\mathrm{d}t$ is zero, i.e., the Hamiltonian is a constant of the motion. In actual calculations this conservation law is satisfied if there exist no explicitly time- or velocity-dependent forces acting on the system. A second important property is that Hamilton's equations of motion are reversible in time. This means that, if we change the signs of all velocities, we will cause the molecules to retrace their trajectories backwards. The computer-generated trajectories should also possess this property.

Concerning the solution of equations of motion, in the limit of very long times, it is clear that no algorithm provides an essentially exact solution. However, this turns out to be not a serious problem, because the main objective of an MD simulation is not to trace the exact configuration of a system after a long time, but rather to predict thermodynamic properties as time averages and calculate time correlation functions representative of the dynamics.

In the following we briefly describe the most popular family of algorithms used in MD simulations for the solution of classical equations of motion: the *Verlet algorithms*. Another family of algorithms comprises higher-order methods, whose basic idea is to use information about positions and their first, second, and higher order time derivatives at time t in order to estimate the positions and their derivatives at time $t + \Delta t$.[112] In general, higher-order methods are characterized by a much better accuracy than the Verlet algorithms, particularly at small times. However, their main drawback is that they are not reversible in time, which results in insufficient energy conservation, especially in very long-time MD simulations. On the contrary, the Verlet methods are not essentially exact for small times but their inherent time reversibility guarantees that the energy conservation law is satisfied even for very long times. This feature renders the Verlet methods, and particularly the velocity-Verlet algorithm, the most appropriate ones to use in long atomistic MD simulations.

2.4.1/i Verlet algorithm

The initial Verlet algorithm[113] ends up calculating the positions at time $t + \Delta t$ by using two Taylor expansions around times $t - \Delta t$ and $t + \Delta t$, respectively:

$$\mathbf{r}_i\left(t-\Delta t\right)=\mathbf{r}_i\left(t\right)-\mathbf{v}_i\left(t\right)\Delta t+\frac{\mathbf{F}_i\left(t\right)}{2m_i}\Delta t^2-\dddot{\mathbf{r}}_i\left(t\right)\frac{\Delta t^3}{3!}+\mathcal{O}\left(\Delta t^4\right) \tag{2.141}$$

$$\mathbf{r}_i\left(t+\Delta t\right)=\mathbf{r}_i\left(t\right)+\mathbf{v}_i\left(t\right)\Delta t+\frac{\mathbf{F}_i\left(t\right)}{2m_i}\Delta t^2+\dddot{\mathbf{r}}_i\left(t\right)\frac{\Delta t^3}{3!}+\mathcal{O}\left(\Delta t^4\right) \tag{2.142}$$

Summing these two equations we obtain:

$$\mathbf{r}_i\left(t+\Delta t\right)\approx 2\mathbf{r}_i\left(t\right)-\mathbf{r}_i\left(t-\Delta t\right)+\frac{\mathbf{F}_i\left(t\right)}{m_i}\Delta t^2 \tag{2.143}$$

The estimate of the new positions contains an error that is in the order of Δt^4, where Δt is the time step employed in our MD scheme. It should be noted that the Verlet algorithm does not use the velocities to compute the new positions. One can, however, derive the velocities from knowledge of the trajectory, using

$$\mathbf{v}_i\left(t\right)=\frac{\mathbf{r}_i\left(t+\Delta t\right)-\mathbf{r}_i\left(t-\Delta t\right)}{2\Delta t}+\mathcal{O}\left(\Delta t^2\right) \tag{2.144}$$

which is only accurate to order Δt^2.

2.4.1/ii Velocity-Verlet algorithm

The problem of defining the positions and velocities at the same time can be overcome by casting the Verlet algorithm in a different way. This is the velocity-Verlet algorithm,[114] according to which positions are obtained through the usual Taylor expansion

$$\mathbf{r}_i\left(t+\Delta t\right)=\mathbf{r}_i\left(t\right)+\mathbf{v}_i\left(t\right)\Delta t+\ddot{\mathbf{r}}_i\left(t\right)\frac{\Delta t^2}{2} \tag{2.145}$$

whereas velocities are calculated through

$$\mathbf{v}_i\left(t+\Delta t\right)=\mathbf{v}_i\left(t\right)+\frac{\Delta t}{2}\left[\ddot{\mathbf{r}}_i\left(t\right)+\ddot{\mathbf{r}}_i\left(t+\Delta t\right)\right] \tag{2.146}$$

with all accelerations computed from the forces at the configuration corresponding to the considered time.

2.4.2 Monte Carlo

In their simplest version, MC simulations of simple fluids are carried out by sampling trial moves for the molecules from a uniform distribution. For example, in a canonical (NVT) ensemble simulation, a molecule is chosen at random, and then displaced, also randomly to a new position. The trial move is accepted or rejected according to an importance sampling scheme.[112,115,116] MC algorithms can also involve sampling from other distributions, which need not to be analytical (e.g. the force-bias method of Pangali et al.[116] provides a classical example of such algorithms).

The probability of accepting a move, P_{accept}, of the form:

$$P_{\text{accept}}=\min\left[1,\frac{P\left(\mathscr{O}|\mathscr{N}\right)P\left(\mathscr{N}\right)}{P\left(\mathscr{N}|\mathscr{O}\right)P\left(\mathscr{O}\right)}\right] \tag{2.147}$$

will asymptotically sample the configuration space according to a probability P. In eq 2.147, P_{accept} is the probability with which trial moves are accepted or rejected, $P\left(\mathscr{N}|\mathscr{O}\right)$ is the transition probability of making a trial move from state $\mathscr{O}$ to state $\mathscr{N}$, and $P\left(\mathscr{O}\right)$ is the probability of being at state $\mathscr{O}$. This means that, at equilibrium, the average number of accepted trial moves that result in the system leaving state $\mathscr{O}$ must be exactly equal to the number of accepted trial moves from all other states $\mathscr{N}$ to the state $\mathscr{O}$. This is a looser statement of the *detailed balance condition*, reflected in eq 2.147, that at equilibrium the average number of accepted moves from $\mathscr{O}$ to any other state $\mathscr{N}$ should be exactly canceled by the number of reverse moves.

In the original Metropolis scheme,[115] the probabilities $P\left(\mathscr{N}|\mathscr{O}\right)$ form a symmetric matrix.

In this case, there is no bias involved in making the move and eq 2.147 reduces to the standard Metropolis acceptance criterion:

$$P_{\text{accept}} = \min\left\{1, \exp\left[-\frac{\mathcal{V}(\mathscr{N}) - \mathcal{V}(\mathscr{O})}{k_{\mathrm{B}}T}\right]\right\} \tag{2.148}$$

The advanced MC methods are based on judicious choices of $P(\mathscr{N}|\mathscr{O})$.[112] Moreover, a computational advantage of MC over MD is that only the energy needs to be calculated, not the forces, rendering the central processing unit (CPU) time needed per step smaller than that of an MD simulation.

2.4.3 Langevin Dynamics

When a large system is simulated, it is generally desired to keep the number of degrees of freedom as low as possible. If a certain subset of particles can be distinguished, of which details of the motion are not relevant, these particles can be omitted from a detailed MD simulation. However, the forces they exert on the remaining particles must be represented as faithfully as possible. This means that correlations of such forces with positions and velocities of particle i must be incorporated in the equations of motion of particle i, while uncorrelated contributions can be represented by random forces. This brings us to the field of Langevin Dynamics (LD).[117,118] In LD a frictional force, proportional to the velocity, is added to the conservative force, in order to mimic an implicitly treated background (e.g. solvent). The friction removes kinetic energy from the system. In order to compensate for the friction, a random force adds kinetic energy to the system.

In the simplest case of LD, the random force is taken to have white-noise character, and no correlations between the various degrees of freedom are assumed to exist. Under these conditions, the velocity dependent frictional forces become proportional to the instantaneous velocity of the particle considered. Thus, the equation of motion of a particle i is transformed into the stochastic equation:

$$m_i\dot{\mathbf{v}}_i(t) = \mathbf{F}_i(\{\mathbf{r}_i(t)\}) - \zeta_i\mathbf{v}_i(t) + \boldsymbol{\mathcal{F}}_i(t) \tag{2.149}$$

where the friction coefficient of a particle is denoted by ζ_i and the random force by $\boldsymbol{\mathcal{F}}_i$. The systematic force $\mathbf{F}_i$ is the explicit mutual force between the N particles of the system, which is to be derived from the potential (or free) energy of the system, which depends on the positions of all particles, denoted by $\{\mathbf{r}_i\}$.

The stochastic force, $\boldsymbol{\mathcal{F}}_i(t)$, is assumed to be a stationary Gaussian random variable with zero mean and to have no correlations with prior velocities or with the systematic force:

$$\langle \boldsymbol{\mathcal{F}}_i(0)\,\boldsymbol{\mathcal{F}}_j(t)\rangle_{\text{ens}} = 2\zeta_i k_{\text{B}} T_{\text{ref}} \delta_{ij} \delta(t) \tag{2.150}$$

$$W(\boldsymbol{\mathcal{F}}_i) = \left(2\pi \left\langle \boldsymbol{\mathcal{F}}_i^2 \right\rangle_{\text{ens}}\right)^{-1/2} \exp\left(-\frac{\boldsymbol{\mathcal{F}}_i^2}{2\left\langle \boldsymbol{\mathcal{F}}_i^2 \right\rangle_{\text{ens}}}\right) \tag{2.151}$$

$$\langle \boldsymbol{\mathcal{F}}_i \rangle_{\text{ens}} = 0 \tag{2.152}$$

$$\langle \mathbf{v}_i(0)\,\boldsymbol{\mathcal{F}}_j(t)\rangle_{\text{ens}} = 0, \quad t \geq 0 \tag{2.153}$$

$$\langle \mathbf{F}_i(0)\,\boldsymbol{\mathcal{F}}_j(t)\rangle_{\text{ens}} = 0, \quad t \geq 0 \tag{2.154}$$

where $\langle \ldots \rangle_{\text{ens}}$ denotes averaging over an equilibrium ensemble, k_{B} is Boltzmann's constant, T_{ref} is the reference temperature of the LD simulation and $W(\boldsymbol{\mathcal{F}})$ is the (Gaussian) probability distribution of the stochastic force. According to van Gunsteren et al.,[119] the solution of the linear, inhomogeneous, first order differential equation, eq 2.149, is:

$$\begin{aligned}\mathbf{v}(t) = &\mathbf{v}_i(0)\exp\left(-\frac{\zeta_i}{m_i}t\right)\\ &+\frac{1}{m_i}\int_0^t \exp\left[-\frac{\zeta_i}{m_i}(t-t')\right]\left[\mathbf{F}_i(t') + \boldsymbol{\mathcal{F}}_i(t')\right]\mathrm{d}t'\end{aligned} \tag{2.155}$$

2.4.3/i Fluctuation-dissipation theorem

To generate a canonical ensemble, the friction and random force have to obey the *fluctuation - dissipation theorem*.[120] Einstein was the first to extract the diffusion coefficient and mobility in a special case of Brownian motion,[121] and made allusions to the existence of a balance between random forces and friction. Then, Nyquist[122] formulated a limited version of the theorem, in his study of noise in resistors. Later, Callen and Welton[123] proved the theorem in a generalized form.

According to Kubo[124] two different kinds of the fluctuation-dissipation theorem can be distinguished. The fluctuation-dissipation theorem of the first kind relates the linear response of a system to an externally applied perturbation and a two-time correlation function of the system in the absence of external forces. The latter form is closely related to the famous Green-Kubo expressions for transport coefficients. The fluctuation-dissipation theorem of the second kind constitutes a relationship between the frictional and random forces in the system, relying on the assumption that the response of a system in thermodynamic equilibrium to a small applied perturbation is the same as its response to a spontaneous fluctuation.[39]

2.4.3/ii Mori-Zwanzig projection operator formalism

A formal way of deriving LD is the *projection operator formalism* of Zwanzig[125,126] and Mori.[127,128] The basis of the formulation is the assumption that we have partial knowledge of the evolving system, for example we can only track certain variables, while the effect of the other variables is modeled or approximated in a rigorous way. In this approach the phase space is divided into two parts, which we are called *interesting* and *uninteresting* degrees of freedom. For the approach to be useful, the uninteresting degrees of freedom should be rapidly varying with respect to the interesting ones. Mori introduced two projection operators, which project the whole phase space onto the sets of interesting and uninteresting degrees of freedom. The full equations of motion are projected only onto the set of interesting degrees of freedom. The result is a differential equation with three force terms: a mean force between the interesting degrees of freedom, a dissipative or frictional force exerted by the uninteresting degrees of freedom onto the interesting ones and a third term containing forces not correlated with the interesting degrees. When the uncorrelated force is approximated by a random force the interesting degrees of freedom are considered independent of the uninteresting degrees of freedom.

2.4.4 Brownian Dynamics

If the friction exerted by the background to the particles under consideration is high, correlations in the velocity will decay in a period over which changes in the systematic force are negligible. Such a system can be called *overdamped*. In this case, the left-hand side of eq 2.149 can be neglected, after averaging over short times. The result is BD, which is described by the position Langevin equation:

$$\mathbf{v}_i\left(t\right) = \frac{1}{\zeta_i}\mathbf{F}_i\left(\{\mathbf{r}_i\left(t\right)\}\right) + \frac{1}{\zeta_i}\boldsymbol{\mathcal{F}}_i\left(t\right) \tag{2.156}$$

The time scale separation makes possible the exchange of the second order stochastic differential equation (eq 2.149) for a first order stochastic differential equation, eq 2.156, without affecting the dynamics on time scales longer than $1/\left(m_i\zeta_i\right)$.

Van Gunsteren and Berendsen[129,130] have proposed several algorithms for integrating eq 2.156. In this work we choose the one which reduces to the Verlet algorithm for zero friction. If we assume a timestep of Δt, for large values of $m_i\zeta\Delta t$ in the diffusive regime, when the friction is so strong that the velocities relax within Δt, the BD algorithm reduces to:

$$r_{i,\alpha}\left(t_n + \Delta t\right) = r_{i,\alpha}\left(t_n\right) + \frac{1}{\zeta_i}\left[F_{i,\alpha}\left(t_n\right)\Delta t + \frac{1}{2}\dot{F}_{i,\alpha}\left(t_n\right)\left(\left(\Delta t\right)^2\right)\right] + \mathcal{R}_{i,\alpha}\left(\Delta t\right) \tag{2.157}$$

with i enumerating the particles, $1 \leq i \leq N$, and α marking a Cartesian component of the vectors. The random displacement $\mathcal{R}\left(\Delta t\right)$ is sampled from a Gaussian distribution with zero mean and width:

$$\left\langle \mathcal{R}_{i,\alpha}^{2}\left(\Delta t\right)\right\rangle = \frac{2k_{\mathrm{B}}T_{\mathrm{ref}}}{\zeta_i}\Delta t \tag{2.158}$$

The integration scheme for BD (eq 2.157) resembles a MC algorithm, except that there is no acceptance criterion. Rossy et al.[131] have derived the correct acceptance probability and introduced their method under the name “Smart Monte Carlo”.

2.5 Stress Tensor in Model Systems

The calculation of the stress tensor from molecular simulations is of paramount importance and is connected with many applications. We present three derivations of the stress tensor from simulations of macromolecular systems in thermodynamic equilibrium. The stress is considered an ensemble average of a mechanical quantity depending on atomic positions and momenta. Such expressions constitute important links between molecular constitution and the macroscopic thermodynamic and mechanical behavior of liquid, solid or rubbery polymers. The *virial theorem* of Clausius[132,133] for a bounded atomic or molecular system, is inapplicable to a periodic model system where there are no wall forces.[134] This constitutes an important difference between the model systems used in simulations and macroscopic bounded systems. We start from the correct expression for the atomic virial[134] and we gradually generalize it to its continuum definition. The intermediate step in this route is to express stress as the derivative of the free energy with respect to strain (infinitely small deformations). Finally, we express it as the derivative with respect to the deformation gradient tensor (arbitrary deformations). Our main concern is to provide a rigorous general framework for calculating the stress tensor in systems whose atoms interact through arbitrary two-, three- and four-body potentials and conservative fields (like walls or long-range interactions). In Appendix A the relevant expressions for all necessary derivatives are provided.

2.5.1 Definitions

The most fundamental and commonly used stress quantity is the *Cauchy stress*, also known as the *true stress*. It is defined by studying the forces acting on an infinitesimal area element in the deformed body. Both the force components and the normal to the area vector have fixed directions in space. This means that if a stressed body can be subjected to a pure rotation, the actual values of the stress components will change. What might be originally a uniaxial stress state can be transformed into a full tensor with both normal and shear stress components.

Table 2.2: Strain and stress conjugate pairs

Strain	Stress	Volume	Symmetry	Orientation
Engineering, ϵ (eq 2.35)	Cauchy (true stress)	Deformed	Yes	Spatial
	Kirchhoff	Original	Yes	Spatial
Logarithmic, ϵ_{L} (eq 2.38)	Cauchy (true stress)	Deformed	Yes	Spatial
	Kirchhoff	Original	Yes	Spatial
Deformation gradient (eq 2.29)	First Piola-Kirchhoff	Original	No	Mixed
Green-Lagrange, ϵ_{G} (eq 2.39)	Second	Original	Yes	Material

The Cauchy stress tensor is in general (in absence of body couples) a symmetric tensor. Another stress measure is the *First Piola-Kirchhoff* or *Piola-Langrange* stress. It is a multiaxial generalization of the nominal (or engineering) stress. The stress is defined as the force in the current configuration acting on the original area. The First Piola-Kirchhoff is an unsymmetric tensor, and is for that reason less attractive to work with. The *Second Piola-Kirchhoff* stress is a modified version of the first Piola-Kirchhoff stress, where the resulting tensor is generally symmetric by proper translation of the force vectors generating the relevant stresses. Sometimes the *Kirchhoff* stress may also be encountered. The Kirchhoff stress is just the Cauchy stress scaled by the volume change.

In continuum mechanics the *principle of virtual work* is very important. It states that the internal work done by an infinitesimal strain variation operating on the current stresses is equal to the external work done by a corresponding virtual displacement operating on the loads. The stress and strain measures must then be selected so that their product gives an accurate energy density. This energy density may be related either to the undeformed or deformed volume, depending on whether the internal virtual work is integrated over the geometry of the original or the deformed state.[73] The various pairs of strain and stress measures are summarized in Table 2.2. In the following, no distinction between material and spatial stress is made.

2.5.2 Atomic Virial Approach

Theodorou et al.[134] have discussed extensively the calculation of the stress tensor from molecular simulations of atomistic model polymer systems employing periodic boundary conditions. Starting from the dynamical equations governing the motion of the sites in a classical (as opposed to quantum mechanical) formulation, these authors have derived correct double summation formulas of the atomic and molecular virial equations, for flexible, infinitely stiff and rigid chain models. For such systems, the *equilibrium stress* tensor $\tau_{\alpha\beta}$ is:

$$\begin{aligned}\tau_{\alpha\beta} &= \langle \sigma_{\alpha\beta} \rangle_{\text{ens}} \\ &= \left\langle -\frac{1}{V}\sum_{i=1}^{N}\frac{p_{i,\alpha}\cdot p_{i,\beta}}{m_i} - \frac{1}{2V}\sum_{i=1}^{N}\sum_{j=1}^{N}\left(r_{i,\alpha}-r_{j,\alpha}\right)^{\text{min.im.}} F_{ij,\beta}^{\text{min.im.}} \right\rangle_{\text{ens}} + \tau_{\alpha\beta}^{\text{tail}}\end{aligned} \tag{2.159}$$

Eq 2.159 is an expression of the $\alpha\beta$-component (Greek indices denote the Cartesian components) of the instantaneous stress tensor $\boldsymbol{\sigma}$ in a system with periodic boundary conditions containing a fixed number, N, of interaction sites and occupying total volume V, where $p_{i,\alpha}$ is the α-component of the momentum of site i with mass m_i. $\mathbf{r}_i$ and $\mathbf{r}_j$ are the position vectors of atoms i and j, respectively. The superscript "min.im." indicates interatomic distances and forces calculated according to the "minimum image convention". $\mathbf{F}_{ij}$ is the force exerted on atom i by the image of atom j located at the closest distance from atom i. In general, the force $\mathbf{F}_{ij}$ between two sites i and j in the infinite periodic model system is defined as $\mathbf{F}_{ij} = -\nabla_{\mathbf{r}_i-\mathbf{r}_j}\mathcal{V}$, where the gradient of the total potential energy function, $\mathcal{V}$, is taken keeping all intersite separation vectors other than $\mathbf{r}_i - \mathbf{r}_j$ constant.

2.5.3 Strain Derivative Approach

In the case of an elastic solid, we can use as *state variables*[109] the temperature, T, and the components $\epsilon_{\alpha\beta}$ of the material strain tensor, describing the homogeneous deformation from a specified reference configuration, $\mathscr{R}$. The conjugate mechanical variables are $V_{\mathscr{R}}\tau_{\alpha\beta}$ where $V_{\mathscr{R}}$ is the volume of the system in the reference configuration $\mathscr{R}$ and $\tau_{\alpha\beta}$ is the material (or second Piola-Kirchhoff [e]) stress tensor.[74] We then assume that the nine variables $\epsilon_{\alpha\beta}$ and the entropy S constitute a complete set of independent variables and that the internal energy U of the solid may be given as a function of these variables, $U = U\left(\epsilon_{\alpha\beta}, S; \mathscr{R}\right)$. The designation of the reference configuration, $\mathscr{R}$, has been included in order to emphasize that the variables $\epsilon_{\alpha\beta}$ are meaningful only when $\mathscr{R}$ is specified (please see discussion in Section 2.2.1 on page 20). The stress tensor of the solid is:

$$\tau_{\alpha\beta} = \frac{1}{V_{\mathscr{R}}}\left.\frac{\partial U}{\partial \epsilon_{\alpha\beta}}\right)_{S,\epsilon_{[\alpha\beta]}} \tag{2.160}$$

where we have introduced the notation $[\alpha\beta]$ to indicate that all Cartesian components of the tensor, other than the $\alpha\beta$ component, are kept constant during differentiation.

---

[e] While the Cauchy stress is a measure of force per unit area in the deformed state, the second Piola-Kirchhoff stress is a measure of force in the deformed body per unit undeformed area.

Given the function $U\left(\epsilon_{\alpha\beta}, S; \mathscr{R}\right)$, the Helmholtz energy of the solid may be defined as $A = U - TS$. Then, the stress tensor, $\tau_{\alpha\beta}$, is the derivative of the Helmholtz energy with respect to strain, $\epsilon_{\alpha\beta}$, under constant temperature and all other components of the strain matrix:

$$\tau_{\alpha\beta} = \frac{1}{V_{\mathscr{R}}} \left.\frac{\partial A}{\partial \epsilon_{\alpha\beta}}\right)_{T,\epsilon_{[\alpha\beta]}} \tag{2.161}$$

and the differential of the Helmholtz energy becomes:[135]

$$\mathrm{d}A = V_{\mathscr{R}} \sum_{\alpha\beta} \tau_{\alpha\beta} \mathrm{d}\epsilon_{\alpha\beta} - S\mathrm{d}T \tag{2.162}$$

The condition for $\mathrm{d}A$ to be a perfect differential is: [f]

$$\left.\frac{\partial S}{\partial \epsilon_{\alpha\beta}}\right)_{T,\epsilon_{[\alpha\beta]}} = -V_{\mathscr{R}} \left.\frac{\partial \tau_{\alpha\beta}}{\partial T}\right)_{\boldsymbol{\epsilon}} \tag{2.165}$$

where we have introduced $V_{\mathscr{R}}$ as the volume in the underformed (reference) state and the derivative in the right-hand side is taken while keeping the whole strain tensor, $\boldsymbol{\epsilon}$, constant. The left-hand side of eq 2.165 can be identified as the Grüneisen coefficient:[74]

$$\gamma_{\alpha\beta} = \frac{1}{C_{\mathrm{V}}} \left.\frac{\partial S}{\partial \epsilon_{\alpha\beta}}\right)_{T,\epsilon_{[\alpha\beta]}} = -\frac{V_{\mathscr{R}}}{C_{\mathrm{V}}} \left.\frac{\partial \tau_{\alpha\beta}}{\partial T}\right)_{\boldsymbol{\epsilon}} \tag{2.166}$$

The Grüneisen coefficients (elements of the Grüneisen tensor) provide a measure of entropic contributions to the elastic moduli.

Now, we can expand eq 2.161:

$$\tau_{\alpha\beta} = \frac{1}{V_{\mathscr{R}}} \left.\frac{\partial U}{\partial \epsilon_{\alpha\beta}}\right)_{T,\epsilon_{[\alpha\beta]}} - \frac{1}{V_{\mathscr{R}}} T \left.\frac{\partial S}{\partial \epsilon_{\alpha\beta}}\right)_{T,\epsilon_{[\alpha\beta]}} \tag{2.167}$$

Using eq 2.165:

$$\tau_{\alpha\beta} = \frac{1}{V_{\mathscr{R}}} \left.\frac{\partial U}{\partial \epsilon_{\alpha\beta}}\right)_{T,\epsilon_{[\alpha\beta]}} + T \left.\frac{\partial \tau_{\alpha\beta}}{\partial T}\right)_{\boldsymbol{\epsilon}} \tag{2.168}$$

---

[f] It can also be proved that:

$$\left.\frac{\partial T}{\partial \epsilon_{\alpha\beta}}\right)_{S,\epsilon_{[\alpha\beta]}} = V_{\mathscr{R}} \left.\frac{\partial \tau_{\alpha\beta}}{\partial S}\right)_{\boldsymbol{\epsilon}} \tag{2.163}$$

and:

$$\left.\frac{\partial \epsilon_{\alpha\beta}}{\partial S}\right)_{T,\epsilon_{[\alpha\beta]}} = -\frac{1}{V_{\mathscr{R}}} \left.\frac{\partial T}{\partial \sigma_{\alpha\beta}}\right)_{\boldsymbol{\epsilon}} \tag{2.164}$$

where we have extracted the stress tensor, $\tau_{\alpha\beta}$ for infinitesimal deformations of the reference state, $\mathscr{R}$.

In order to get some insight into the terms of eq 2.168, we study the case of an ideal gas. For an ideal gas, $\partial U/\partial \epsilon_{\alpha\beta} = 0$, since the internal energy of an ideal gas is of purely kinetic contribution and does not depend on the volume of the system. Thus, the stress tensor of an ideal gas takes the form:

$$\tau_{\alpha\beta}^{\text{id.g.}} = T \left.\frac{\partial \tau_{\alpha\beta}}{\partial T}\right)_{\boldsymbol{\epsilon}} = -\rho_0 k_{\mathrm{B}} T \delta_{\alpha\beta} = -p^{\text{id.g.}} \delta_{\alpha\beta} \tag{2.169}$$

resulting in a diagonal tensor with $-p^{\text{id.g.}}$ components along its diagonal, corresponding to an ideal gas of number density $\rho = n/V$, with n being the number of molecules.

Finally, by applying eq 2.168, in the NVT ensemble of a classical system characterized by potential energy $\mathcal{V}$, the stress tensor can be cast as:

$$\tau_{\alpha\beta} = \left\langle \sigma_{\alpha\beta}^{\mathcal{V}} \right\rangle_{NVT} - \rho k_{\mathrm{B}} T \delta_{\alpha\beta} \tag{2.170}$$

with

$$\sigma_{\alpha\beta}^{\mathcal{V}} = \frac{1}{V_{\mathscr{R}}} \left.\frac{\partial \mathcal{V}}{\partial \epsilon_{\alpha\beta}}\right)_{T,\epsilon_{[\alpha\beta]}} \tag{2.171}$$

We will refer to $\sigma_{\alpha\beta}^{\mathcal{V}}$ as the potential energy contribution to the stress tensor (Born term[136]), and to the term $\rho k_{\mathrm{B}} T$ as the kinetic (or ideal gas contribution). The former is the zero-temperature limit of the thermodynamic stress. The brackets for $\sigma_{\alpha\beta}^{\mathcal{V}}$ denote the appropriate NVT ensemble average. Eq 2.170 can be connected to eq 2.159 where, for a classical system, the momentum term is replaced by the ideal gas term thanks to the equipartition theorem.

Lutsko[137,138] has provided a proof of eq 2.170 by transforming the coordinates as proposed by Ray and Rahman[139] and calculating the derivatives of the configurational integral with respect to strain, in the NVT ensemble. Later, van Workum et al.[140] have derived the same expression by following a procedure similar to that of Lutsko. Despite the fact that our line of thought sketched above may be less rigorous, it is based on simple thermodynamic arguments which provide critical insight into the derivation of eq 2.170.

2.5.4 Deformation Gradient Tensor Derivative Approach

We consider the free energy per unit mass, $A\left(T,V\right)/m$ of the system. The thermodynamic stress tensor, $\boldsymbol{\tau}$ is:[141,142]

$$\boldsymbol{\tau} = \rho \mathbb{F} \cdot \left(\frac{\partial \left(A/m \right)}{\partial \mathbb{F}} \right)^{\mathrm{T}} \tag{2.172}$$

where A is the Helmholtz energy, m is the total mass in the system and $\mathbb{F}$ denotes the deformation gradient tensor defined by eq 2.29. The same equation can be written in component form as:

$$\tau_{\alpha\beta} = \rho \sum_{\gamma=1}^{3} \mathbb{F}_{\alpha\gamma} \frac{\partial \left(A/m \right)}{\partial \mathbb{F}_{\beta\gamma}} \tag{2.173}$$

If we assume that our simulation box does not exchange mass with its environment, the stress tensor can further be simplified:

$$\tau_{\alpha\beta} = \frac{1}{V_{\mathscr{R}}} \sum_{\gamma=1}^{3} \mathbb{F}_{\alpha\gamma} \frac{\partial A}{\partial \mathbb{F}_{\beta\gamma}} \tag{2.174}$$

where $V_{\mathscr{R}}$ is the volume of the simulation box in the reference state $\mathscr{R}$ (see Table 2.2). In general the prefactor should be $1/V$ with V being the current volume of the system. The density, ρ, generally changes with $\mathbb{F}$ and $V = V_{\mathscr{R}} \left(1 + \det\left(\mathbb{F}\right)\right)$.

3 Segmental Dynamics and Stresses in PS - Fullerene Mixtures

The polymer dynamics of homogeneous C_{60}-polystyrene (PS) mixtures in the molten state are studied via molecular simulations using two interconnected levels of representation for polystyrene nanocomposites: (a) A coarse-grained representation, in which each polystyrene repeat unit is mapped into a single "superatom" and each fullerene is viewed as a spherical shell. Equilibration of coarse-grained polymer-nanoparticle systems at all length scales is achieved via connectivity-altering Monte Carlo (MC) simulations. (b) An atomistic representation, where both nanoparticles and polymer chains are represented in terms of united-atom forcefields. Initial configurations for atomistic Molecular Dynamics (MD) simulations are obtained by reverse mapping well-equilibrated coarse-grained configurations. By analyzing MD trajectories under constant energy, the segmental dynamics of polystyrene (for neat and filled systems) is characterized in terms of bond orientation time autocorrelation functions. Nanocomposite systems are found to exhibit slightly slower segmental dynamics than the unfilled ones, in good agreement with available experimental data. Moreover, by employing a Voronoi tessellation of the simulation box, the mean-square displacement of backbone carbon atoms is quantified in the vicinity of each fullerene molecule. Fullerenes are found to suppress the average motion of polymeric chains, in agreement with neutron scattering data, while slightly increasing the dynamic and stress heterogeneity of the melt. Atomic-level and local (per Voronoi cell) stress distributions are reported for the pure and the filled systems.

3.1 Introduction

3.1.1 Experimental Findings

Nanomaterials fabricated by dispersing nanoparticles in polymer melts have the potential for performance that far exceeds that of traditional composites. Nanoparticles have been shown to influence mechanical properties, as well as transport properties, such as viscosity. Until recently, the commonly held opinion was that particle addition to liquids, including polymeric liquids, produces an increase in viscosity, as predicted by Einstein a century ago.[143,144] However, it was recently found by Mackay and coworkers[145–147] that the viscosity of polystyrene melts blended with crosslinked polystyrene particles (and later also with fullerenes and other particles) decreases and scales with the change in free volume (due to introduction of athermal excluded volume regions in the melt) and not with the decrease in entanglement. Later,[147] fullerenes and magnetite particles were found to produce the same non-Einstein viscosity decrease effect.

Despite the macroscopic viscosity reduction, fullerene-polystyrene nanocomposites exhibit slower segmental dynamics, as Kropka et al.[148] have reported. The fully miscible C_{60} - polymer nanocomposites were made via a solution-dissolution / solvent-evaporation method. The molecular weight of the polystyrene chains was $M_{\mathrm{w}} = 156$ kg/mol with a narrow molecular weight distribution, $M_{\mathrm{w}}/M_{\mathrm{n}} = 1.06$. The focus of their study was on nanocomposites containing a weight fraction $\varphi^{\mathrm{wt}}_{\mathrm{C}_{60}} = 0.01$ because the most significant changes in T_{g} occur at this concentration. These materials exhibited an increase in their “bulk” T_{g} of about 1 K, as measured by differential scanning calorimetry and dynamic mechanical analysis. The mechanical measurements performed on these nanocomposites showed no evidence of excess structural or dynamic heterogeneity relative to the neat polymer and suggested that the effect of the particles may be described in terms of an increased segmental friction coefficient for the polymer. Quasi-elastic neutron scattering (QENS) measurements revealed that the influence of C_{60} on polymer melt dynamics is limited to the vicinity of the particle surfaces at the nanosecond time scale. The addition of C_{60}s was found to supress the polymer segmental dynamics of two more polymer hosts (PMMA and TMPC). These authors suggested that the suppression of the local relaxation dynamics of the composite is consistent with an enhancement of cohesive interactions in the system, which may be the root of the increase in T_{g} for the nanocomposites. The system must acquire more thermal energy before polymer segments can overcome local energy barriers and thereby enable polymer center-of-mass motions. Specifically, local polymer chain backbone motions in the nanocomposites are suppressed relative to those in the neat polymer, an effect which likely plays a role in the observed increases in T_{g} of the materials. In the melt, the dynamics of the polymer segments in the vicinity of the particle surfaces is suppressed relative to the neat polymer, and this effect results in an excess elastic fraction of polymer segments at the nanosecond time scale.

On the contrary, Sanz et al.[149] reported increased segmental motion in polystyrene-fullerene nanocomposites. These authors prepared bulk nanocomposites of (hydrogenous and ring-deuterated) polystyrene and poly(4-methyl styrene) using a rapid precipitation method where the C_{60} relative mass fraction ranged from 0% to 4%. Elastic window scan measurements, using a high resolution (0.9 μeV) neutron backscattering spectrometer, were reported over a wide temperature range ($2 - 450$ K). Based on the measured intensity, apparent Debye-Waller factors $\langle u^2 \rangle$, characterizing the mean-square amplitude of proton displacements, were determined as a function of temperature. Sanz et al. found that the addition of C_{60} to these polymers leads to a progressive increase in $\langle u^2 \rangle$ relative to the pure polymer value over the entire temperature range investigated, where the effect is larger for larger nanoparticle concentration. This general trend seems to indicate that the C_{60} nanoparticles plasticize the fast dynamics of these polymer glasses.

Later, Wong et al.,[150] investigated the same system (as Sanz et al.[149]) by inelastic incoherent neutron scattering, small angle neutron scattering, calorimetric and dielectric spectroscopy methods. They found that the dispersion of fullerenes increased the glass transition temperature, slowing down the alpha relaxation dynamics associated with glass formation, while at the same time causing a softening of the material at high frequencies (as determined by the Debye-Waller factor). These effects are interpreted in terms of the particle modifying the polymer packing, causing an increase of the fragility of glass formation. The observed increase in T_g lies in apparent contradiction with the same group's previous inelastic neutron scattering findings.[149] From the point of view of these authors, this may indicate that the low-temperature slope of $\langle u^2 \rangle$ increases with the addition of fullerene nanoparticles. The comparatively larger amplitude of proton delocalization in nanocomposites at the same temperatures is interpreted as a softening of the local potential of proton motion. In summary, inelastic neutron scattering indicates a simultaneous increase in amplitude of fast proton motion (increased mobility at fast time scales $\sim 10^{-15}$ s and Å-lengthscales), while restricted segmental motion associated with the glass transition is manifested by a T_g increase.

3.1.2 Previous Work

From the standpoint of molecular simulations, Vacatello[151] performed MC simulations of particles dispersed in a polymer matrix; he found that polymer segments adhere to the particles and some chains are connected to different particles, thereby forming “bridges”. Each chain visits the interface layer of several particles and each particle can be in contact with multiple chains. Even in the absence of strong interactions between particles and polymeric chains, Vacatello observed that the particles behave as multifunctional physical crosslinks. These crosslinks do not immobilize the polymer chains, but can reduce their diffusion rates considerably.

That view was complemented by MD simulations by Desai et al.,[152] who found that chain diffusivity is enhanced (relative to that in the pure polymer) when polymer - particle interactions are repulsive, and is reduced when polymer - particle interactions are strongly attractive. These authors were the first to report that chain diffusivity is spatially inhomogeneous, adopting its pure-polymer value when the chain center of mass is about one radius of gyration away from a particle's surface. Smith et al.[153] reported increase of the viscosity of a coarse-grained bead-necklace model polymer upon the addition of attractive and neutral nanoparticles, while viscosity reduction was observed upon the addition of repulsive particles. Further MD simulations of polymer melts by Smith et al.[154] have suggested that both increased polymer segment packing densities and the energy topography of a surface can lead to stronger caging of polymer segments near an attractive surface. They suggested that the dramatic increase in structural relaxation time for polymer melts at the attractive structured surface is largely a result of dynamic heterogeneity induced by the surface and does not resemble dynamics of a bulk melt approaching T_g. The results of Kropka et al.[148] may indicate that C_{60}s induce similar effects in the glassy state of the polymers investigated.

More recently, Ndoro et al.[155] employed atomistic MD simulations in order to study the interfacial dynamics of 20-monomer atactic polystyrene chains surrounding a silica nanoparticle. The effect of the nanoparticle curvature and grafting density on the mean-square displacement of free polystyrene chains and on the mean relaxation time of various intramolecular vectors was investigated as a function of separation from the surface. Confinement, reduced surface curvature, and densification resulted in a reduction of the mean-square displacement and an increase in the mean relaxation time of the C-H bond vector and chain end-to-end vector in the vicinity of the surface.

Toepperwein et al.[156] have addressed the influence of nanorods on the entanglement network of composites through MC and MD simulations. The presence of particles enriched the nanocomposite systems by nucleating additional topological constraints of polymer-particle origin. Later, Li et al.[157] observed that highly entangled polymer chains were disentangled upon increasing the volume fraction of spherical non-attractive nanoparticles. These authors report a critical volume fraction controlling the crossover from polymer chain entanglements to nanoparticle-induced entanglements. While below this critical volume fraction, the polymer chain relaxation accelerates upon filling, above this volume fraction, the situation reverses. The same authors[158] have also studied the structural, dynamical and viscous behaviors of polyethylene matrices under the influence of differently shaped nanoparticles, including C_{60} buckyballs, at fixed volume fraction (4 vol %). The nanoparticles were found to be able to nucleate polymer entanglements around their surfaces and to increase the underlying entanglement density of the matrix in the proximity of the particles. However, the overall primitive path networks of PE matrices were found very similar to those of pure polyethylene, since polymer entanglements still dominated the rheological behavior.

3.1.3 Proposed Approach

In this work we are trying to understand the microscopic mechanisms involved in the peculiar behavior of PS-C_{60} nanocomposites, through a hierarchical simulation approach. To this end, we focus our study on polystyrene melts having specifications identical to those studied by Kropka et al.[148] The computational prediction of physical properties is particularly challenging for polymeric materials, because of the extremely broad spectra of length and time scales governing structure and molecular motion in these materials. This challenge can only be met through the development of hierarchical analysis and simulation strategies encompassing many interconnected levels, each level addressing phenomena over a specific window of time and length scales.[17] In order to shed some light into the segmental dynamics of PS-C_{60} systems, molecular simulations have been conducted using two interconnected levels of representation for polystyrene nanocomposites: (a) A coarse-grained representation,[159] in which each polystyrene repeat unit is mapped into a single “superatom” and each fullerene is viewed as a spherical shell. Equilibration of coarse-grained polymer-nanoparticle systems at all length scales is achieved via connectivity-altering Monte Carlo (MC) simulations.[32] (b) An atomistic representation, where both nanoparticles and polymer chains are represented in terms of united-atom forcefields. Initial configurations for atomistic Molecular Dynamics (MD) simulations are obtained by reverse mapping well-equilibrated coarse-grained configurations. The reverse mapping procedure retains the tacticity which is implicit in the coarse-grained representation, while regrowing atomistic sites by a quasi-Metropolis procedure that avoids unphysical conformations. By analyzing MD trajectories under constant energy, the segmental dynamics of polystyrene (for neat and filled systems) can then be characterized in terms of bond orientation time autocorrelation functions and local atomic mean-square displacement.

3.2 Coarse Grained Monte Carlo (CG-MC)

3.2.1 Systems Studied

In this work, monodisperse melts of atactic PS chains with 50 % meso diads obeying Bernoullian statistics and with chain lengths of 80 (8.3 kg/mol), 185 (19.3 kg/mol), 323 (34 kg/mol), 922 (96 kg/mol), 1460 (152 kg/mol) and 4032 (420 kg/mol) coarse grained (CG) sites (diads) were generated and simulated. Initial configurations were generated and equilibrated at the temperature of 500 K, at which the CG forcefield has been developed. Then the reverse-mapped well-equilibrated configurations were subjected to MD runs which cooled them down to the glass transition temperature. Bearing in mind the limitations of the atomistic MD simulations, the main part of this work is based on systems composed of $n = 10$ chains of molecular weight 152 kg/mol with 20 fullerenes randomly dispersed, leading to a weight fraction $\varphi^{\mathrm{wt}}_{\mathrm{C}_{60}} = 1\%$. System specifications are close to experimentally studied systems by quasi-elastic neutron scattering[148] and adequate for avoiding finite-size effects.[160] For comparison, neat polymeric systems of the same characteristics have also been simulated along with the composite ones. In order to improve statistics, three independent configurations of both the neat and the filled systems were generated, equilibrated and reverse-mapped. Moreover, a single 80-mer chain system was atomistically built and simulated with MD, without involving MC equilibration.

The major contribution to the computational cost of our study stems from the MD simulations. Despite the fact that our MC and reverse mapping codes are running serially, the time needed to fully equilibrate our systems and generate the corresponding atomistic configurations is reasonable (10-15 days of wall-clock time on a single 2.8 GHz central processing unit (CPU) core). On the contrary, the MD simulations of the systems described above required 40 days of real wall-clock time for 170 ns integration time, when run on a hybrid machine consisting of eight 2.8 GHz CPU cores and one programmable graphics processing unit (GPU). Since the polymer relaxation times (e.g., the disentanglement or reptation time, τ_{d}) far exceed our current computational resources, the use of MC to equilibrate our samples is of vital importance.

3.2.2 Coarse Grained Model

The coarse graining scheme adopted in this work is very efficient for the representation of vinyl polymers, since one is able to keep information on stereochemical sequences along the polymer chain. Given a direction along the main chain, it is possible to assign an absolute configuration to each asymmetric carbon. The chain can be represented as a sequence of diads, each diad containing two asymmetric carbons. Depending on the absolute configuration of the asymmetric carbons, i.e., *RR* (or *SS*) and *RS* (or *SR*), the diads can be of type *m* (*meso*) or *r* (*racemo*), respectively (Figures 1 and 2 of ref 159). The chain ends can be either *em* (*end-meso*) or *er* (*end-racemo*) as far as the bonded potentials are concerned, but their nonbonded interaction is common and slightly different from *m* and *r* nonbonded interactions. A detailed description of the model can be found in ref 159 and the parameter values used are taken from the Supporting Information of ref 32. They were derived from a detailed atomistic potential using the Iterative Boltzmann Inversion (IBI) method. The coarse-grained effective potential was refined in order to better reproduce the target distributions, extracted from all-atom simulations of a 9mer fluid at 500 K and 1 bar. All MC simulations of the present work have been conducted at the same temperature.

At the coarse grained level of description, fullerenes are considered as spherical shells of infinitesimal thickness. It is assumed that carbon atoms are uniformly smeared over the surface of the shell. The potential between a spherical shell of interaction sites and a single coarse grained PS site (treated as a point), on the grounds of Hamaker theory,[161] is:

$$\begin{aligned}\mathcal{V}^{\mathrm{CG}}_{\mathrm{C}_{60}}(r) = 8\pi\varepsilon_{\mathrm{m}}\rho_{\mathrm{C}_{60}}\delta r_{\mathrm{C}_{60}} \Bigg[& \frac{\sigma_{\mathrm{m}}^{12}}{10r}\left(\frac{R_{\mathrm{C}_{60}}}{\left(r-R_{\mathrm{C}_{60}}\right)^{10}} - \frac{R_{\mathrm{C}_{60}}}{\left(r+R_{\mathrm{C}_{60}}\right)^{10}}\right) \\ & - \frac{\sigma_{\mathrm{m}}^{6}}{4r}\left(\frac{R_{\mathrm{C}_{60}}}{\left(r-R_{\mathrm{C}_{60}}\right)^{4}} - \frac{R_{\mathrm{C}_{60}}}{\left(r+R_{\mathrm{C}_{60}}\right)^{4}}\right)\Bigg] \end{aligned} \tag{3.1}$$

where r is the center-to-center separation distance. The external radius of the shell representing the fullerene, $R_{\mathrm{C}_{60}}$, is set to $0.35\,\mathrm{nm}$. The density of interaction sites of fullerene is $\rho_{\mathrm{C}_{60}}$, the thickness of the shell $\delta r_{\mathrm{C}_{60}}$, and the product $\rho_{\mathrm{C}_{60}}\delta r_{\mathrm{C}_{60}}$ represents the surface density of interaction sites of the fullerene. The mean Lennard-Jones interaction parameters, ε_{m} and σ_{m}, take into account the interaction of fullerene carbons with all kinds of interaction sites a coarse-grained bead consists of. In the case of PS, for every bead we sum up five different kinds of interactions, namely the interaction of CH_3, aliphatic CH_2, aromatic CH and C groups with the fullerene. Each interaction is weighted with the number of interaction sites of each kind present in the CG bead. The detailed united-atom forcefield, which is essential for the calculation of ε_{m} and σ_{m}, is described in the “Target atomistic representation” section, which follows (Section 3.3.1 on page 71). In Table 3.1 are listed the nonbonded interaction parameter values of the united-atom forcefield, as well as coarse-grained model parameters derived from them and used in this work.

Following the work of Girifalco,[162] the interaction between fullerenes at the coarse-grained level is modeled as an integrated Lennard-Jones potential over two spherical shells:

$$\begin{aligned}\mathcal{V}_{\mathrm{C}_{60}\text{-}\mathrm{C}_{60}}(r) = & -\mathcal{A}\left(\frac{1}{r_{\mathrm{s}}(r_{\mathrm{s}}-1)^3} + \frac{1}{r_{\mathrm{s}}(r_{\mathrm{s}}+1)^3} - \frac{2}{r_{\mathrm{s}}^4}\right) \\ & + \mathcal{B}\left(\frac{1}{r_{\mathrm{s}}(r_{\mathrm{s}}-1)^9} + \frac{1}{r_{\mathrm{s}}(r_{\mathrm{s}}+1)^9} - \frac{2}{r_{\mathrm{s}}^{10}}\right) \end{aligned} \tag{3.2}$$

where $r_{\mathrm{s}} = r/\left(2R_{\mathrm{C}_{60}}\right)$ and the values of the remaining parameters are presented in Table 3.1. This potential has been used throughout the literature to study the molecular properties of C_{60}, which were found to be consistent with available experimental data, making it a reasonable choice. A priori, there should be an entropic contribution included in the coarse-grained polymer-particle potentials,[163] which is not taken into account by using Hamaker-type poten-

Table 3.1: PS united-atom potential interaction parameters and CG model parameters derived from them.

Parameter	Value	Reference
Polystyrene		
$\varepsilon_{\mathrm{CH_3}}, \varepsilon_{\mathrm{alCH_2}}, \varepsilon_{\mathrm{arCH}}, \varepsilon_{\mathrm{arC}}$	0.12 kcal/mol	Mondello et al.[164]
$\varepsilon_{\mathrm{alCH}}$	0.09 kcal/mol	
$\sigma_{\mathrm{alCH}}, \sigma_{\mathrm{arC}}, \sigma_{\mathrm{arCH}}$	3.69 Å	
$\sigma_{\mathrm{CH_3}}, \sigma_{\mathrm{alCH_2}}$	3.85 Å	
Fullerene		
$\varepsilon_{\mathrm{C_{60}}}$	0.066 kcal/mol	Girifalco[162]
$\sigma_{\mathrm{C_{60}}}$	3.47Å	
$\mathcal{A}$	1.079 kcal/mol	
$\mathcal{B}$	1.957×10^{-3} kcal/mol	
Mixed		
ε_{m}	$\sqrt{\varepsilon_{\mathrm{PS}}\varepsilon_{\mathrm{C_{60}}}}$	where "PS" subscript represents all united-atom species
σ_{m}	$1/2\left(\sigma_{\mathrm{PS}} + \sigma_{\mathrm{C_{60}}}\right)$	

tials. However, our coarse-graining is relatively modest, so we believe that this contribution is small. As our PS coarse-graining serves mainly for creating initial configurations, any fault in the local structure caused by the coarse-grained potential will be fixed by the subsequent atomistic MD simulation.

3.2.3 Initial CG Structure Generation

To start the CG MC simulation, an initial configuration is generated by placing the fullerenes at randomly selected positions, so that they do not overlap, and then building stepwise the polymeric chains around them, following the work of Theodorou and Suter.[165] At each step a site type is chosen according to the overall probability of *meso* and *racemo* diads. In our work the tacticity of atactic PS is represented by a Bernoullian diad distribution with a probability of *meso* diads of $(m) = 0.5$ (in equilibrium atactic polystyrene the configuration statistics is almost Bernoullian with the fraction of *meso* dyads around 0.46[166–168]). The "Euler angles" defining the direction of the first and the second coarse-grained bonds, are arbitrarily set at the beginning. Since torsion angle potentials are not used in the CG representation, for each subsequent superatom a bond angle is chosen according to a probability resulting from the effective bending potential for the specific angle type and the segment is placed, accordingly, on a circle forming the base of a cone with apex at the previously placed superatom and side length equal to the average CG bond length of $l_{\mathrm{CG}} = 2.46$ Å. In every step, nonbonded interactions with already created superatoms are taken into account, refining the probabilities of accepting a trial position for the bead to be grown. If, after a certain number of iterations, all attempts to grow the superatom fail, a local derivative-free minimization of the potential energy is undertaken in order to ensure that the bead is placed at the most energetically favorable position. Since the degrees of freedom of the optimization are only three, i.e. the cartesian coordinates of the new superatom to be built, a numerically stable Nelder-Mead algorithm is a reasonable choice.[169]

Each initial guess structure is then "relaxed" to a state of minimal potential energy. The total potential energy is the sum of all bonded potentials of the polymeric matrix, nonbonded interactions between polymer superatoms, between polymer superatoms and fullerenes, and between fullerenes and fullerenes. Minimization is carried out using the Large-scale Atomic/-Molecular Massively Parallel Simulator (LAMMPS)[170] with the CG potentials incorporated in its source code. Since IBI PS coarse-grained nonbonded potentials are tabulated, a Polak-Ribière[171,172] (PR) variant of the conjugate gradient method is used. At each iteration the force gradient is combined with the previous iteration information to compute a new search direction perpendicular (conjugate) to the previous search direction. The PR variant affects how the direction is chosen and how the conjugate gradient method is restarted when it ceases to make progress. The PR variant is thought to be the most efficient conjugate gradient choice for most problems.

3.2.4 Monte Carlo Equilibration

Enabling the equilibration of high molar mass polymer nanocomposites at the coarse-grained level was one of the main objectives of this work. For this purpose, connectivity altering moves,[28] such as double bridging (DB)[29] were employed in MC simulations of linear chains of four types of sites, *m*, *r*, *em* and *er*. In the DB move two trimers are excised from two chains of equal length and two new trimer bridges are constructed, leading to two new chains of the same length but of drastically different conformations. The internal shape of the chains was rearranged by using the symmetric variant of the concerted rotation move,[22,26] which modifies the local conformation of an internal chain section (of five superatoms) while leaving the preceding and following parts of the chain unaffected. In addition, the internal conformations of chains are sampled using flips of internal beads, end segment rotations and reptations. The mixture of MC moves included a newly developed and specially adapted configurational bias move,[24] capable of regrowing an arbitrary number of coarse-grained beads, starting from a chain end, in the confined environment formed by the nanoparticles. For every kind of move undertaken, special care was taken to discard moves leading to overlaps of coarse-grained beads and dispersed nanoparticles.

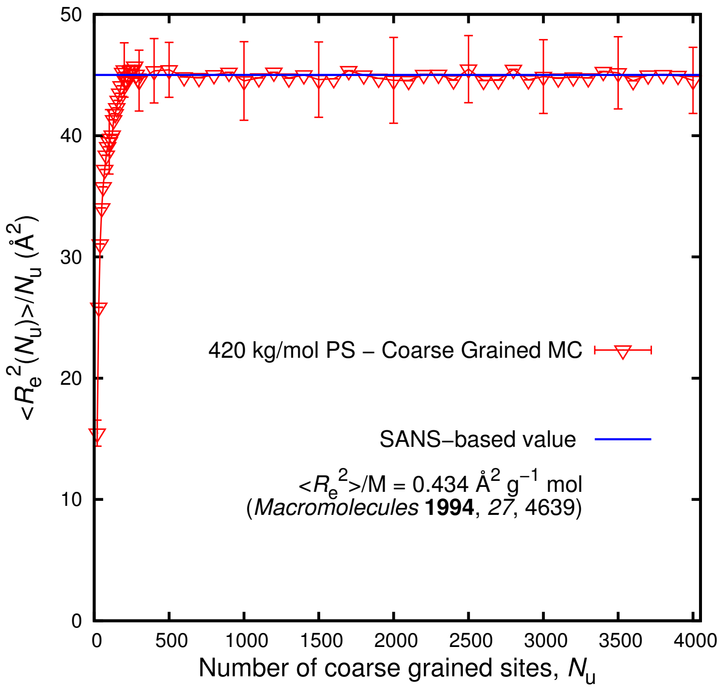

Figure 3.1: Average squared end-to-end distance, $\langle R_{\mathrm{e}}^2(N_{\mathrm{u}})\rangle$, of subchains of length N_{u} diads divided by N_{u} versus N_{u} for coarse-grained 4000-mer chains at 500 K. Some indicative error bars are shown. The dotted line is the SANS-based value for PS at 413 K.[174]

3.2.5 Conformational Properties of CG Configurations

As a measure of the obtained chain conformations one may use the quantity $\langle R_{\mathrm{e}}^2(N_{\mathrm{u}})\rangle/N_{\mathrm{u}}$, where N_{u} is the number of diads (repeat units) in a subchain and $R_{\mathrm{e}}^2(N_{\mathrm{u}})$ is the squared end-to-end distance of the subchain. It has been shown that,[173] for well equilibrated chains, $\langle R_{\mathrm{e}}^2(N_{\mathrm{u}})\rangle\,/N_{\mathrm{u}}$ increases monotonically with N_{u} until it reaches a plateau. In Figure 3.1, $\langle R_{\mathrm{e}}^2(N_{\mathrm{u}})\rangle\,/N_{\mathrm{u}}$ is depicted as a function of N_{u} for a system containing 8 chains of 4000 diads each, at $T = 500\,$K. For $N_{\mathrm{u}} > 200$ an asymptotic value is reached of approximately 45 Å which corresponds to $\langle R_{\mathrm{e}}^2\rangle\,/M$ equal to 0.43 Å^{2}g^{-1}mol, with M being the chain molar mass. This is in excellent agreement with the Small Angle Neutron Scattering (SANS)-based value (shown with the dotted line) of $\langle R_{\mathrm{e}}^2\rangle = 0.434$ Å^{2}g^{-1}mol given for PS at $T = 413$ K.[174]

The calculated root mean-square radius of gyration $\left\langle R_{\mathrm{g}}^2\right\rangle^{1/2}$ as a function of the molecular weight M_{w} is shown in Figure 3.2. Neutron scattering results[175] for monodisperse PS of M_{w} ranging from 21 kg/mol to 1100 kg/mol in the bulk at 393 K have also been drawn (continuous thin line) for comparison over the M_{w} scale of interest. Very good agreement is observed for all the molar masses examined. This confirms that chains in our CG melts are well equilibrated and adopt close to unperturbed configurations. At the CG level of representation, nanoparticles do not seem to affect the dimensions of the chains, yielding identical results with the neat

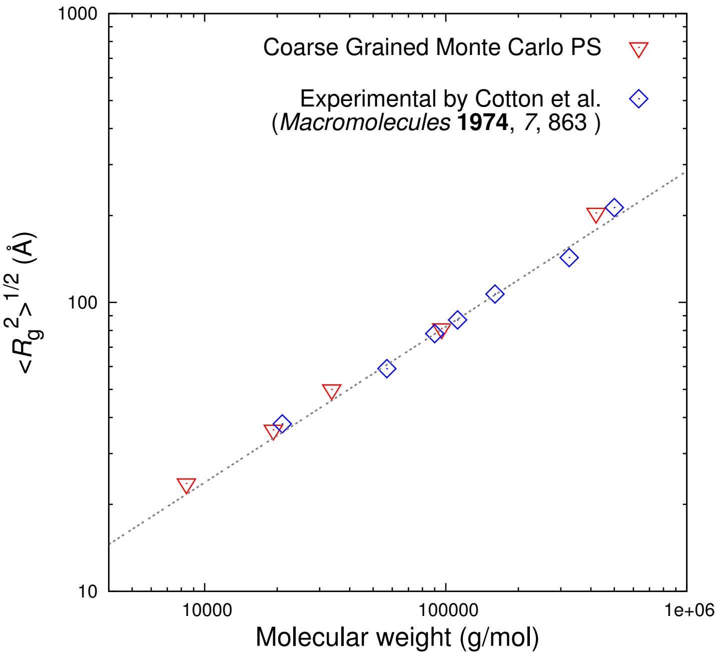

Figure 3.2: Root mean-square radius of gyration of the coarse grained chains as a function of molecular weight, M_w, in the melt at 500 K (triangular symbols). Neutron scattering measurements for high molar mass PS are also included (rhomboid symbols).[175] Grey dotted line is linear least-squares fit.

polystyrene systems. However, this cannot be considered as a generally valid statement for polystyrene nanocomposite melts (e.g. polystyrene chains have been found to swell upon the addition of crosslinked polystyrene nanoparticles[176]).

3.3 Reverse Mapping

3.3.1 Target Atomistic Representation

The equilibrated coarse-grained configurations are reverse mapped to detailed configurations which can be described by a united-atom model without partial charges, based on the works of Mondello et al.[164] and Lyulin and Michels.[177] This united-atom model will be referred to as “atomistic” in the following. It takes into account the following contributions to the system potential energy: (i) Lennard-Jones nonbonded interaction potential between all united atoms that are three or more bonds apart or belong to different images of the same parent chain; (ii) bond stretching potential for every covalent bond; (iii) bending potential for all bond angles, including those in the phenyl rings; (iv) torsional potential for all rotatable backbone bonds; (v) torsional potential for the torsions of phenyl rings around their stems; (vi) out-of-plane bending potential to preserve the coplanarity of the phenyl and the phenyl stem; (vii) torsional potential about all bonds connecting aromatic carbons in the phenyl ring to preserve the planarity of the ring and (viii) improper torsional potential to preserve the chirality of all carbons bearing a phenyl substituent.[178] Lennard-Jones parameters employed by the model are listed in Table 3.1. All Lennard-Jones potentials are cut at an inner cutoff distance of 2.35σ, beyond which force smoothing to zero using a cubic spline is applied up to a distance of 2.5σ. No tail corrections are used for the nonbonded interaction potential. Our experience has been that this united-atom model does a reasonable job predicting structure, volumetric properties, elastic constants and stress-strain behavior in the melt and glassy state. In particular, the system adopts density values close to those measured experimentally upon quenching into the glassy state.[179]

Fullerenes are described as fully flexible carbon cages. As far as intramolecular (bond stretching, bending and torsional) contributions are concerned, the DREIDING forcefield has been used.[180] Intramolecular nonbonded interactions are not taken into account, while the intermolecular nonbonded interactions are described by a Lennard-Jones potential using the values of $\varepsilon_{C_{60}}$ and $\sigma_{C_{60}}$ reported in Table 3.1, following the early but well validated work of Girifalco.[162] A comprehensive review of C_{60} forcefields can be found in the work of Monticelli.[181] In order to ensure the reliability of our atomistic MD simulations, all sets of parameters reported by Monticelli have been tested, rendering indistinguishable results, as far as the trajectories and the thermodynamic properties of the systems were concerned.

3.3.2 Procedure

The reconstruction of the atomistic detail, given a well-equilibrated coarse-grained configuration, is accomplished in four stages. During the first stage, atomistic fullerenes are placed at the positions of the coarse-grained beads used during the CG-MC equilibration, while paying attention to select the orientation that minimizes the interaction energy with their environment. The second stage consists of an iterative quasi-Metropolis introduction of the atomistic sites of the polymer, obeying the atomistic potential described above. During the third stage, local MC moves try to optimize the generated configuration. At the final stage, energy minimization is undertaken before initiating the MD integration. Throughout the atomistic reconstruction procedure, CH_2 united atoms containing the achiral carbons of the chains are kept fixed at the positions of the superatoms of the coarse-grained configuration.

In order to restore the atomistic detail of the coarse-grained PS, a quasi-Metropolis procedure is followed.[165] During the reconstruction of the atomistic sites, the positions of the united atoms added (aliphatic CH groups containing the chiral carbons of the chains, aromatic C and CH groups constituting the phenyl substituents) are selected from a set of properly created candidates, using as a criterion the increase in the total energy of the system. The first chiral

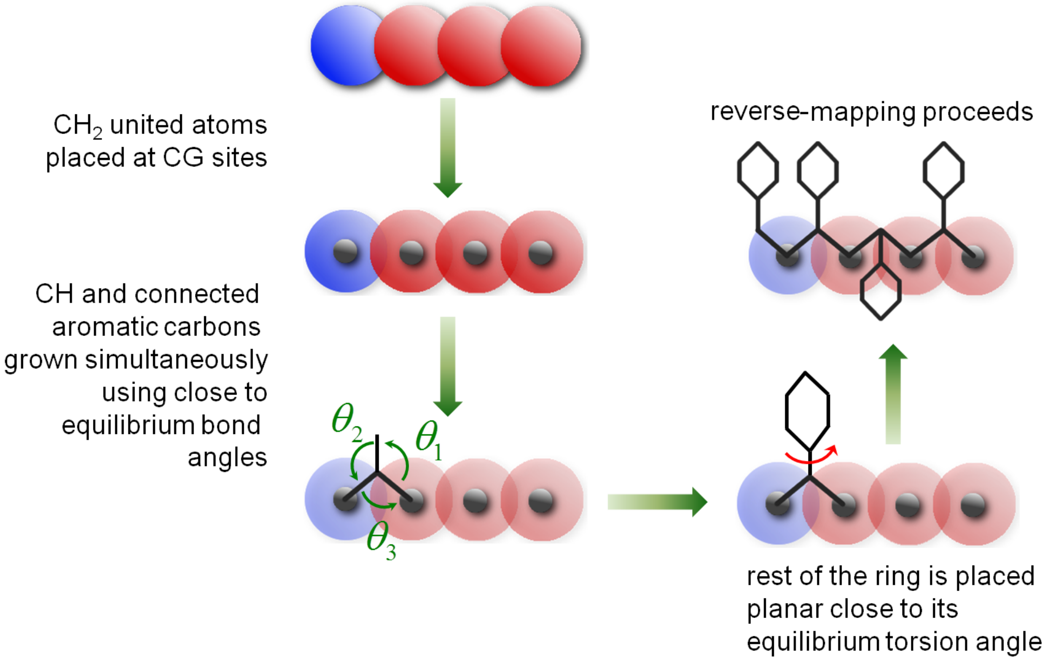

Figure 3.3: Schematic of the initial reconstruction of the atomistic detail.

carbon of each chain is assigned randomly an absolute configuration, since this is not determined by the coarse-grained model, and the rest of the chiral carbons are placed according to the chirality of the dyads. Starting from the CH$_2$ sites, whose position vectors are the degrees of freedom of the coarse-grained representation, backbone CH united atoms are selected from a set of candidate positions lying in the circle formed by the intersection of two spheres, one centered at the previous CH$_2$ atom and the other centered at the next one. The radii of the spheres correspond to the equilibrium length of the backbone C-C bond. Based on the positions of the aliphatic CH$_2$ and CH united atoms, the carbon defining the stem of the phenyl ring is placed so that the aliphatic CH - aromatic C bond generates close to equilibrium bending angles. Finally, the rings are introduced as planar objects, the plane of each ring containing the axis of its stem, using as the only degree of freedom of the candidate positions the torsion angle of the ring around its stem. During the whole regrowth, insertions of carbon atoms leading to a $\bar{g}$ (*gauche-bar*)[182] conformation are strictly prohibited by assigning to them zero probability.

Following Spyriouni et al.,[32] the configuration is optimized via local MC moves. These moves include flip of a segment, rotation of the phenyl ring around its stem and configurationally biased regrowth of a whole monomer, preserving the chirality of the CG site. A flip move displaces an inner skeletal segment of the chain along the locus (circle) defined by the lengths of the two bonds adjacent to the segment. The moves employed flipped a chiral carbon (one carrying a phenyl) to a new position on the circumference of a circle drawn perpendicular to the line connecting the carbons flanking it on either side. In addition, moves which regrow

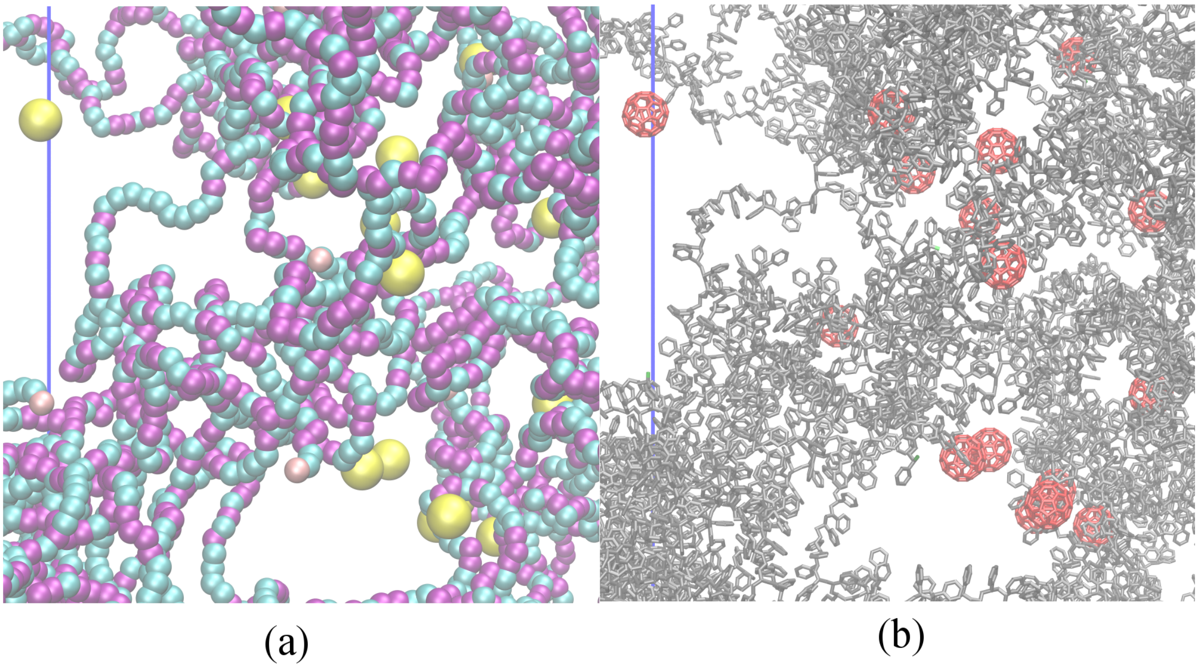

Figure 3.4: Illustration of the reverse mapping scheme. On the left hand side is shown a part of the simulation box with fullerenes depicted as yellow spheres and PS chains as sequences of *m* (cyan), *r* (purple), and *em*/*er* (brown) segments. On the right is the reverse-mapped atomistic system. PS chains are unfolded and neighboring chains have been omitted for clarity. Visualization made by using the VMD software.[183]

a whole segment in a configurationally biased way have been used.

The potential energy of the atomistic system is minimized with respect to the Cartesian coordinates of all atoms, excluding the CH_2 united atoms which coincide with the positions of the coarse-grained sites. In this way, the equilibrated MC configuration is not distorted during the reconstruction of carbon atoms through reverse mapping (Figure 3.4). For the minimization, LAMMPS is used with a Hessian-free truncated Newton minimization method.[184] Minimization is performed in turns, by gradually blowing up the atomic radii.[165] One starts with atoms of reduced size (sigma equal to half its actual value), adjusting that size in stages so that the atoms reach their full size at the end. As in earlier works, a modified potential energy function was used to describe nonbonded interactions in early stages of the minimization, the so-called soft sphere potential. After the introduction of the Lennard-Jones interactions, the collision diameter, σ, is gradually increased from half to its final value. The reverse mapping scheme just described was designed in order to prevent locking of the local configuration in torsional states which are inconsistent with the unperturbed conformational statistics adopted by PS in the melt, without departing at all from the well-equilibrated configurations provided by the coarse-grained simulations. Validation of the reverse-mapped configuration against experimentally available information from pure polystyrene melts is necessary before proceeding to examine the properties of nanocomposites. It is discussed in the following section.

3.3.3 Thermodynamic Properties and Structure of the Reverse-mapped Configurations

The cohesive energy, U_{coh}, is the energy associated with the intermolecular interactions only and can be estimated by taking the difference between the total energy of the simulation box, U_{tot}, and that of the isolated polymeric chains, U_{intra}. In order to determine the intramolecular energy, chains are considered not to interact with their periodic images. Hildebrand's solubility parameter, δ, is the square root of the cohesive energy density:

$$\delta = \sqrt{\frac{U_{\text{intra}} - U_{\text{tot}}}{V}} \tag{3.3}$$

with V being the volume of the simulation box. The solubility parameter, δ, was calculated for the bulk reverse mapped structures of 1460 diads per chain. For this calculation the intermolecular interactions for each system were summed, averaged and divided by the simulation box volume to obtain an estimate of the cohesive energy density. The square root of the cohesive energy density, averaged over all structures, was found to be equal to 7 $\text{cal}^{1/2}\text{cm}^{-3/2}$ at $T = 500$ K. Experimental values for PS from viscosity measurements in different solvents, range from 8.5 to 9.3 $\text{cal}^{1/2}\text{cm}^{-3/2}$ at 298 K.[185] The discrepancy of about 18% is rather large and can be partly attributed to the temperature difference (the cohesion of the polymer drops as the temperature rises and so δ should decrease as well). The short-chain structure (made from the single 80-mer parent chain) equilibrated with MD at 500 K gave an even lower solubility parameter.

Nuclear Magnetic Resonance (NMR) measurements on atactic PS have helped gain insight into the conformations adopted by its chains. Suter and collaborators[186–189] have shown that considerable deviations may occur between experimental findings and predictions obtained from bulk atomistic model structures of PS; furthermore, they have proposed several algorithms for the generation of atomistic structures by an appropriate choice of the target conformational probabilities in the spirit of the Rotational Isomeric State (RIS) model. Having this in mind, the ability of the proposed reverse mapping scheme to generate atomistic configurations with correct conformational statistics is examined. The resulting torsional distributions are shown in Figures 3.5 and 3.6 for meso and racemo diads, respectively.

The fusion of *trans* and *gauche* states is apparently produced by the atomistic potential at

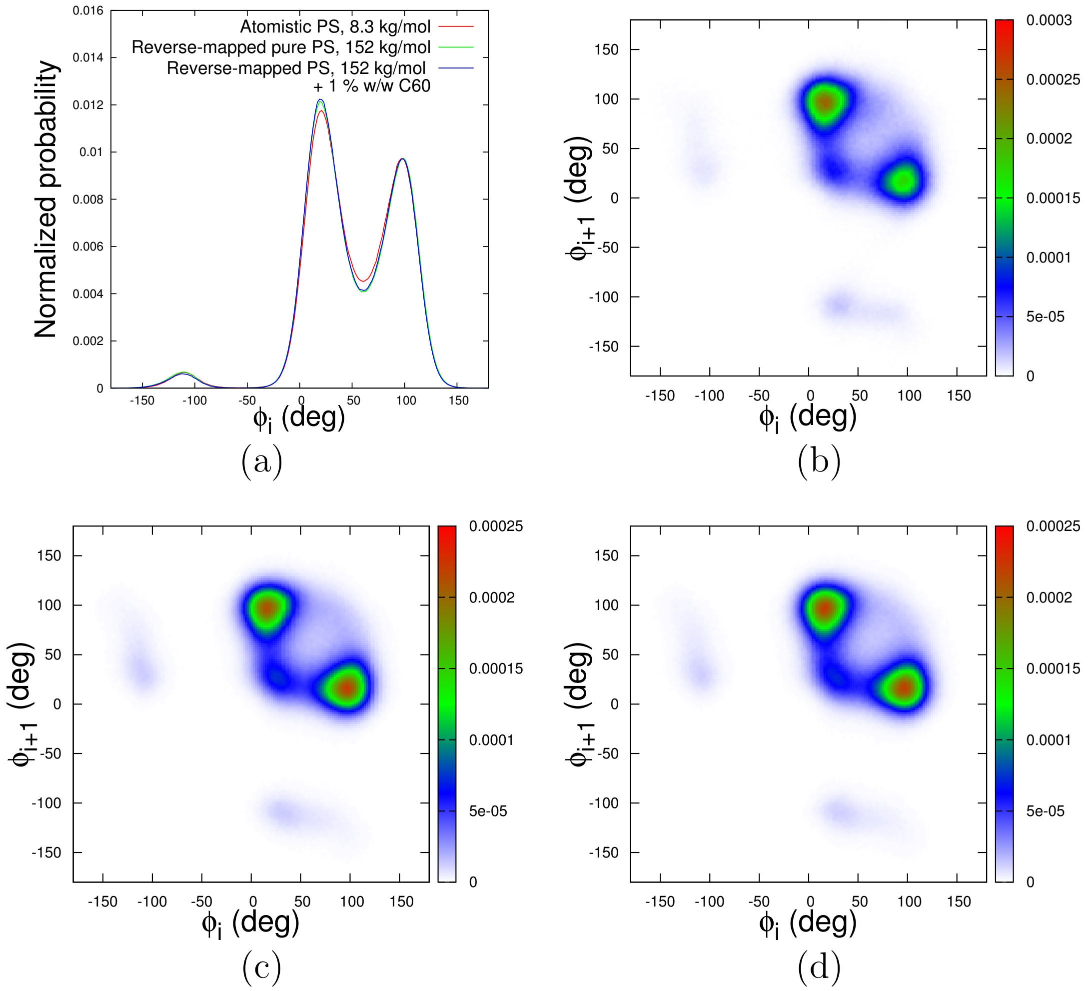

(a)

(b)

(c)

(d)

Figure 3.5: (a) Distribution of torsion angles for the *meso* diads of 1460-mer chains in the bulk systems obtained via reverse mapping (green line pure PS, blue line composite) and in an atomistic 80-mer system directly equilibrated by MD (red line). (b,c,d) Ramachandran plots for pairs of successive torsion angles belonging to meso diads from the 80-mer atomistic system (b), bulk 1460-mer system (c) and the composite 1460-mer (d).

this high temperature, since it is also present in the single-chain system which has been equilibrated by MD. Comparing the curves in Figures 3.5 and 3.6 we observe that torsion angle distributions in the reverse-mapped structures are extremely close to those obtained from the 80mer structure that was directly equilibrated by MD at the atomistic level, without intervention of any coarse-graining and reverse mapping. This observation is extremely promising for our reverse mapping scheme, implying that we can achieve well-equilibrated structures down to the atomistic scale. The percentage of *trans* states is slightly increased in the presence of fullerenes, both for *meso* and *racemo* diads. In the case of *racemo* diads, the effect is accompanied by an equal reduction of the *gauche* percentage, which may be attributed to a mild extension of the chains trying to engulf the fullerenes. The overall content of trans confor-

Table 3.2: Torsion angle distribution, averaged over all neat 1460mer reverse mapped structures

	State frequency in %		
	t: $-60° \leq \phi \leq 60°$	g: $60° < \phi \leq 180°$	$\bar{g}$: $-180° \leq \phi < -60°$
meso diads	54.2	43.4	2.4
racemo diads	66.7	31.7	1.6
overall	60.4	37.6	2.0
State a-priori RIS probability (300 K)[190]	71	29	-
Double-quantum solid-state NMR[191]	68	32	-

mations, as presented in Table 3.2 for the bulk systems, in the reverse-mapped structures is around 60%, which is in reasonable agreement with the experimental 68 ± 10 % measured by NMR.[191] The total percentage of ḡ conformations in the reverse-mapped structures was 1.8%, while, according to RIS models, it should be less than 2%.[190,192,193] Clearly, capturing the correct torsion angle distribution is a stringent test for reverse mapping from the coarse-grained representation adopted in this work. Previous efforts by Spyriouni et al.,[32] and Ghanbari et al.[194] could not capture the correct local structure of polystyrene, leading to a high percentage of unrealistic ḡ conformations.

Along with the torsion angle distributions in Figures 3.5 and 3.6, Ramachandran plots of the two-dimensional distributions characterizing two successive torsion angles are also shown. Following Flory et al.,[182] in the case of a *meso* diad, ϕ_i is measured in the right-handed sense and ϕ_{i+1} in the left-handed sense. In the *racemo* diad obtained by inverting the chirality of the second methine carbon of the diad, both torsion angles are measured in the right-handed sense (the mirror image diad would require two left-handed frames of reference). Overall, the convention used to define the sense of rotation of the torsional angles is such that the same angles lead to the same molecular environments around the considered bond.[195] In Figure 3.5(b) the plot concerns the single-chain 80-mer system. It can be seen that for this system, *tg* and *gt* conformation probabilities are not equal, since the two regions are not evenly populated; this reflects incomplete equilibration by MD, even in this short-chain melt. On the other hand, systems produced by the proposed reverse mapping methodology, result in fully symmetric *tg* and *gt* conformations. The presence of fullerenes does not seem to affect the probabilities of successive torsion angles. In all cases, conformations involving ḡ torsion angles are extremely rare.

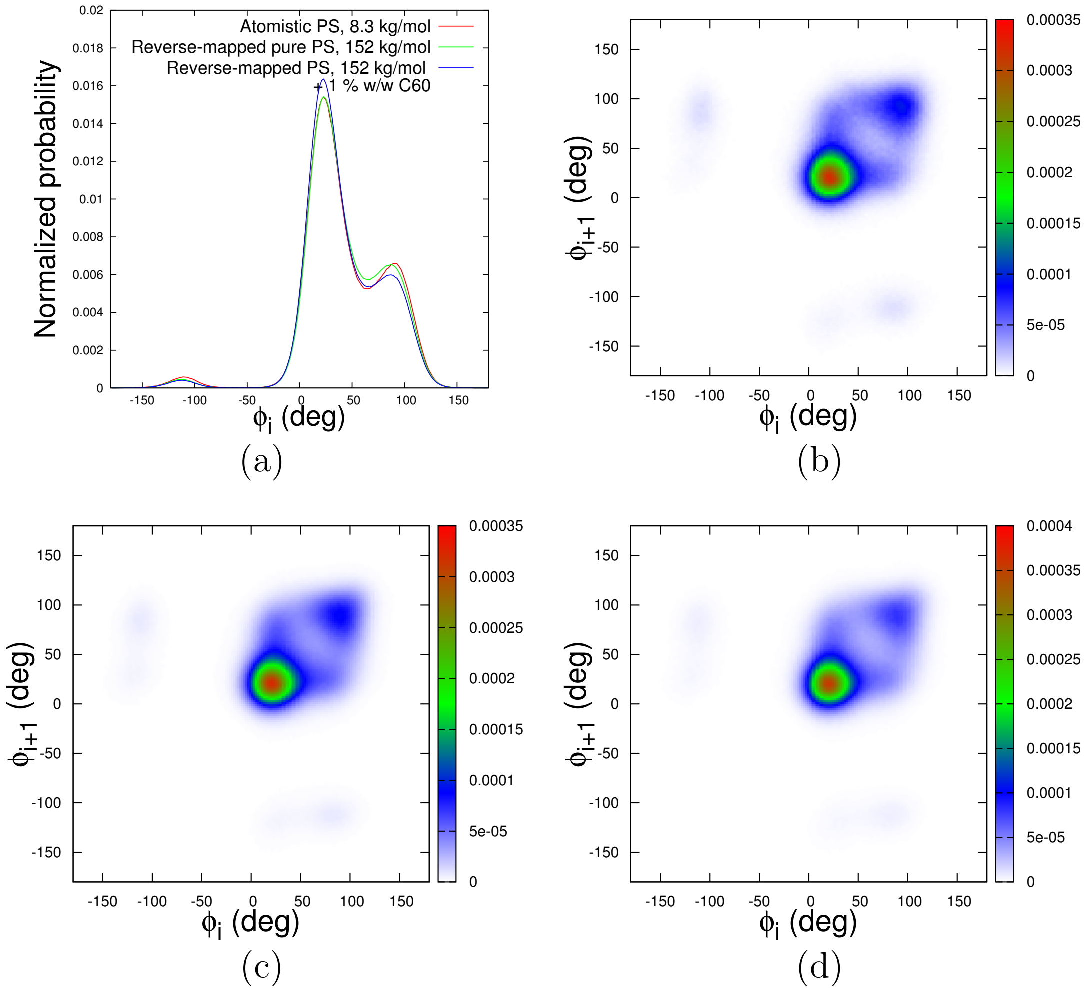

Figure 3.6: (a) Distribution of torsion angles for the *racemo* diads of 1460-mer chains in the bulk systems obtained via reverse mapping (green line pure PS, blue line composite) and in an atomistic 80-mer system equilibrated directly by MD (red line). (b,c,d) Ramachandran plots for pairs of successive torsion angles belonging to meso diads from the 80-mer atomistic system (b), bulk 1460-mer system (c) and the composite 1460-mer (d).

3.4 Atomistic Molecular Dynamics

All MD simulations have been conducted using LAMMPS,[170] extended with the united-atom force field of Lyulin and Michels,[177] which we have incorporated into the LAMMPS source code. The equations of motion are those of Shinoda et al.,[196] integrated by the time-reversible measure-preserving Verlet integrator derived by Tuckerman et al.[197] In all cases, a timestep of 1 fs was used.

Initially, the reverse-mapped configurations were subjected to 50 ns of isothermal-isobaric (NpT) MD under $T = 500$ K and $p = 101.325$ kPa, using the barostat of LAMMPS. Keeping the temperature fixed, 20 ns of isothermal (NVT) integration followed, leading to the final 100 ns time integration under constant energy (NVE), where the coordinates of the atoms were tracked in order to extract the dynamical properties. The final configuration from the melt at 500 K was subjected to further NpT simulation with the set temperature T lowered by 20 K every 40 ns (effective cooling rate 0.5 K/ns) down to a final temperature of 200 K. At every cooling step (20 K), a configuration of the system was recorded and used for 50 ns of NpT equilibration, followed by 20 ns NVT and 100 ns NVE MD run in order to extract the dynamics at this temperature. All (three neat and three composite) independent reverse-mapped configurations were subjected to the same procedure. During the NVE run, the system's pressure and temperature were monitored in order to ensure that they correspond to the desired values.

We believe that NVE simulations, where no barostatting or thermostatting take place, are the best means of studying dynamics under no external influence.[198] The thermostatting and barostatting is achieved by adding some dynamical variables which are coupled to the particle velocities (thermostatting) and simulation domain dimensions (barostatting), in order to mimic a reservoir coupled to the system. If the coupling is loose, the energy flow from the system to the reservoir is slow. On the other hand, if the coupling is strong, long-lived weakly damped oscillations in the energy occur, resulting in poor equilibration. It is necessary to choose the strength of the coupling wisely, so as to achieve satisfactory damping of these correlations.[199]

3.4.1 Hydrogen Reconstruction

Hydrogen reconstruction aims at re-introducing hydrogens of CH_3, CH_2 groups and phenyl rings. The procedure we followed is inspired by the work of Ahumada et al.[200] Methyl hydrogens are reconstructed at a staggered conformation, i.e. a methyl C-H bond being coplanar with the methyl stem and with the C-H bond of the methine group to which the methyl is connected and pointing in an opposite direction to the latter bond. For all methyls, C-H bonds are assumed to be $b_{\mathrm{C-H}} = 1.10$ Å long and to form an angle of $\theta_{\mathrm{C-C-H}} = 110°$ with the methyl stem. As far as the CH_2 united atoms are concerned, two hydrogen atoms are placed symmetrically on both sides of the plane where the C-C bond lies, obeying the equilibrium bond length $b_{\mathrm{C-H}}$ and equilibrium bond angle $\theta_{\mathrm{C-C-H}}$. In the case of the CH united atom of the backbone, the single hydrogen atom is placed entirely symmetrically to the phenyl ring, using as a plane of symmetry the backbone of the chain. Finally, one hydrogen atom is attached to every aromatic atom in the direction defined by the center of mass of the ring and the carbon atom, at a distance $b_{\mathrm{C-H}}$ from it. The addition of hydrogens to an end of a polystyrene chain is depicted in Figure 3.7.

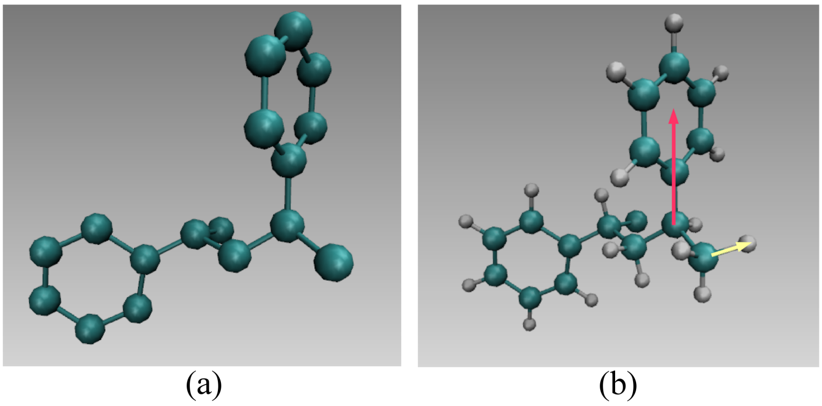
(a) (b)

Figure 3.7: Schematic of the hydrogen reconstruction of the united atom model employed in the present work. In the right-hand side figure (b) two vectors used for the study of dynamics are marked. The vector connecting the chiral carbon to the center-of-mass of the phenyl ring is marked in red, while an aliphatic C-H bond is marked in yellow.

3.4.2 Temperature Dependence of Segmental Dynamics

We examine the segmental dynamics of the atactic PS melt, as predicted by the united-atom MD simulations, by analyzing time autocorrelation functions of various vectors. In the case of polystyrene, the vectors characterizing the orientation of the phenyl ring and the orientation of the C-H bonds are of special interest (Figure 3.7). The orientational decorrelation with time for each one of these vectors can be studied by considering ensemble-averaged Legendre polynomials of order k, $P_k(t)$, of the inner product $\langle \mathbf{u}(t_0) \cdot \mathbf{u}(t_0 + \Delta t) \rangle$ of the unit vector $\mathbf{u}$ along the vector, at times t_0 and $t_0 + t$. It is quite common to fit the long-time behavior of orientational autocorrelation functions of this kind by a modified Kohlrausch - Williams - Watts (mKWW) function:[201–203]

$$P_k(t) = \alpha_{\text{lib}} \exp\left[-\frac{t}{\tau_{\text{lib}}}\right] + (1 - \alpha_{\text{lib}}) \exp\left[-\left(\frac{t}{\tau_{\text{seg}}}\right)^{\beta_{\text{KWW}}}\right] \tag{3.4}$$

The mKWW function of eq 3.4 consists of two parts. The first term describes a fast exponential decay with amplitude α_{lib}, which is associated with the fast librations of torsion angles around skeletal bonds and with the bond stretching and bond angle bending vibrations of skeletal and pendant bonds near their equilibrium values, with characteristic time τ_{lib}. The second term is a stretched exponential decay associated with cooperative conformational transitions in the polymer, with τ_{seg} being the characteristic correlation time and β_{KWW} the stretching exponent. The correlation time for segmental motion, τ_c, also referred to as “segmental relaxation time”

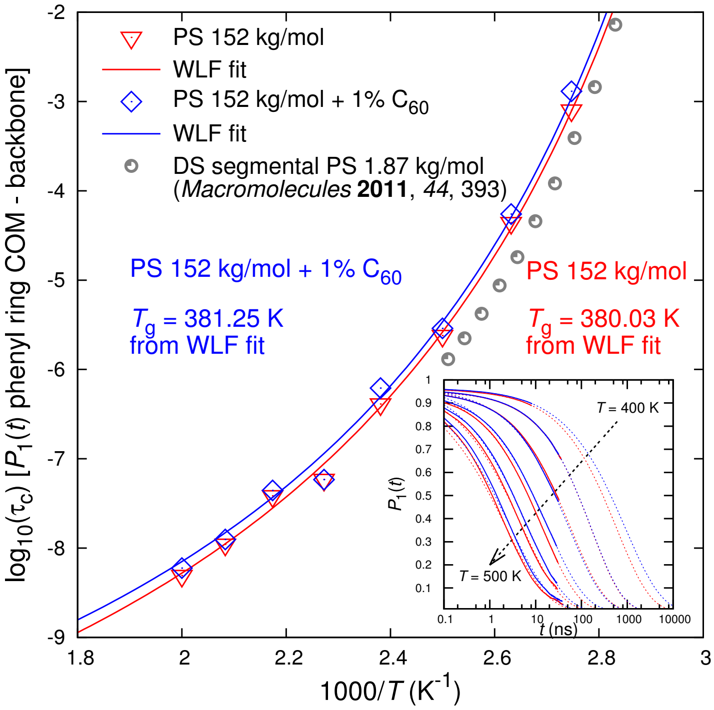

Figure 3.8: Temperature dependence of the relaxation times obtained from MD simulations corresponding to the $P_1(t)$ autocorrelation function of the vector connecting the backbone CH group with the center of mass of the phenyl ring. Experimental points come from DS measurements on neat low-molar mass PS.[204] Fits to the WLF[205] equation are also presented. In the inset to the figure, $P_1(t)$ time autocorrelation functions from MD simulations (solid lines) are depicted, along with their fits to eq 3.4 (dashed lines).

in the following, can be calculated as the integral:

$$\tau_c = \int_0^\infty P_k(t)\mathrm{d}t = \alpha_{\mathrm{lib}}\tau_{\mathrm{lib}} + (1-\alpha_{\mathrm{lib}})\tau_{\mathrm{seg}}\frac{1}{\beta_{\mathrm{KWW}}}\Gamma\left(\frac{1}{\beta_{\mathrm{KWW}}}\right) \tag{3.5}$$

with Γ being the gamma function (please see page xxxvii).

If a comparison with DS is sought, the relevant vector to study is the vector starting from the backbone CH united atom and ending at the center of mass of the phenyl ring, $\mathbf{u}_{\mathrm{CH-CM}}$. To a good approximation, monomer dipole moments are directed along this vector. DS measurements cannot discern between self and cross correlations of the dipole vectors. However, the contribution of the correlations of neighboring dipole moments to the segmental relaxation is minimal.[206,207] In this case, the quantity of interest is the Legendre polynomial of the first kind:

$$P_1(t) = \langle \hat{\mathbf{u}}_{\mathrm{CH-CM}}(t_0+t)\cdot\hat{\mathbf{u}}_{\mathrm{CH-CM}}(t_0)\rangle \quad . \tag{3.6}$$

In the inset to the Figure 3.8 the calculated $P_1(t)$ functions are presented with solid lines for

Table 3.3: Best fit parameters (mKWW equation) for the $P_1(t)$ autocorrelation functions of the vector connecting the backbone CH group with the center of mass of the phenyl ring (Figure 3.8). All parameters are characterized by an uncertainty of 7 %.

		parameters		
Temperature (K)	System	β_{KWW}	τ_{seg} (ns)	α_{lib}
500	PS	0.47	2.32	0.05
	PS + 1% C_{60}	0.48	2.91	0.05
480	PS	0.52	6.17	0.041
	PS + 1% C_{60}	0.52	7.05	0.043
460	PS	0.58	25.47	0.04
	PS + 1% C_{60}	0.55	27.21	0.04
440	PS	0.59	39.97	0.04
	PS + 1% C_{60}	0.59	39.87	0.04
420	PS	0.61	293.37	0.04
	PS + 1% C_{60}	0.61	440.26	0.04
400	PS	0.53	1480.6	0.04
	PS + 1% C_{60}	0.61	2036.3	0.04

both the bulk and the composite systems. Along with the simulation results, fits to the mKWW function (eq 3.4) are also presented. It can be seen that the mKWW expression describes well the simulation results for both cases and the whole temperature range. Each simulation curve represents the average of the three independent MD trajectories produced by the different reverse-mapped structures. The fitting to the mKWW equation allows us to analytically estimate the segmental relaxation time, τ_{c}, based on eq 3.5, using the fit parameters of Table 3.3.

The temperature dependence of the segmental relaxation times is presented in the main part of Figure 3.8. Segmental relaxation times calculated by our united-atom MD simulations are in favorable agreement with experimental DS measurements found in the work of Harmandaris et al.[204] Experimental points from ref 204 are shifted to smaller timescales, due to the smaller molecular weight of the samples used in the DS measurements. This is expected, since PS dynamics exhibits molecular weight dependence which can shift the glass transition temperature from 314 K for 1.35 kg/mol PS to 373.3 K for 243 kg/mol PS.[208] An estimate of the glass transition temperature, $T_{\mathrm{g,sim}}$, can be obtained by fitting the temperature dependence of segmental relaxation times to an equation such as Williams - Landel - Ferry.[205] Fitted values of T_{g} are given in Figure 3.8, with the coefficients of the WLF equation:

$$\log\left(\frac{\tau_{\mathrm{c}}}{\tau_{\mathrm{c,g}}}\right) = -\frac{c_1\left(T - T_{\mathrm{g}}\right)}{T - T_{\mathrm{g}} + c_2} \tag{3.7}$$

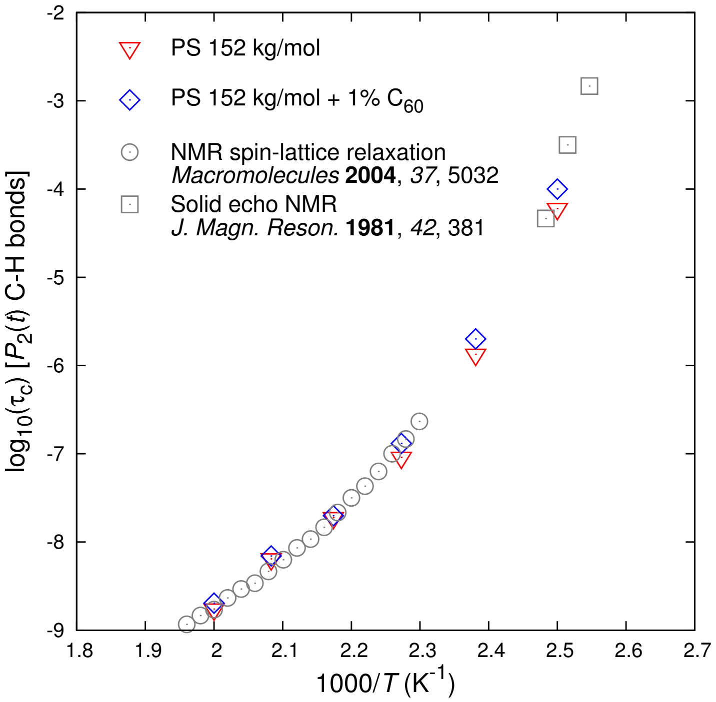

Figure 3.9: Temperature dependence of the segmental relaxation times obtained through analysis of the $P_2(t)$ curve of the C-H bond vectors. Experimental points correspond to spin-lattice relaxation[210] and solid echo[211] NMR measurements.

being $c_1 = 13.6$ and $c_2 = 56$ K, close to the universal values and the experimental ones of Kumar et al.[209] As can be seen in Figure 3.8, nanocomposite systems exhibit slightly longer segmental relaxation times, compared to their neat counterparts, for the majority of temperatures studied. This leads to an estimated glass transition shift of around 1 K upon the addition of fullerenes. The T_g-shift predicted by the MD simulations is in excellent agreement to the shift found by Differential Scanning Calorimetry (DSC) measurements of Kropka et al.[148] However, for some temperatures, the dynamical behavior of unfilled and filled systems yields completely indistinguishable results.

If one is interested in comparing with NMR data, an appropriate autocorrelation function to look at is the orientational autocorrelation function of C-H bonds. The reason is that, for ^{2}H nuclei, spin-lattice relaxation is dominated by electric quadrupole coupling and the spin relaxation time can be directly related to the reorientation of the C-^{2}H bond. In this case, the second Legendre polynomial of the unit vector $\hat{\mathbf{u}}_\mathrm{b}$ directed parallel to a C-H bond:

$$P_2(t) = \frac{3}{2}\left\langle (\cos\theta_\mathrm{b}(t_0,t))^2 \right\rangle - \frac{1}{2} = \frac{3}{2}\left\langle (\hat{\mathbf{u}}_\mathrm{b}(t_0+t)\cdot\hat{\mathbf{u}}_\mathrm{b}(t_0))^2 \right\rangle - \frac{1}{2} \tag{3.8}$$

is employed as a measure of the polymer segmental dynamics. $\theta_\mathrm{b}(t_0,t)$ is the angle of the bond vector $\mathbf{u}_\mathrm{b}$ at time t relative to its original position at the time origin t_0 and the brackets

Table 3.4: Best fit parameters (mKWW equation) for the $P_2(t)$ autocorrelation functions of the C-H bond vectors (Figure 3.9). All parameters are characterized by an uncertainty of 6 %.

		parameters		
Temperature (K)	System	β_{KWW}	τ_{seg} (ns)	α_{lib}
500	PS	0.38	0.48	0.08
	PS + 1% C_{60}	0.39	0.63	0.09
480	PS	0.40	2.10	0.09
	PS + 1% C_{60}	0.41	2.45	0.10
460	PS	0.41	9.78	0.11
	PS + 1% C_{60}	0.48	10.07	0.10
440	PS	0.53	57.57	0.14
	PS + 1% C_{60}	0.55	46.01	0.13
420	PS	0.58	907.31	0.06
	PS + 1% C_{60}	0.53	1258.52	0.13
400	PS	0.48	30898	0.12
	PS + 1% C_{60}	0.53	63912	0.12

$\langle ... \rangle$ denote an ensemble average over all C-H bonds in the system and across different time origins. Since our MD simulations were conducted using a united-atom model, hydrogens were reconstructed upon post-processing the trajectories, following the procedure described above.

Figure 3.9 presents the segmental correlation times, as extracted from the C-H vector $P_2(t)$ autocorrelation functions from the simulation trajectories. The best fit parameters for the mKWW equation used are reported in Table 3.4. To be consistent with the NMR measurements, the weighted average autocorrelation function over the eight C-H vectors of each monomer was taken into account for the estimation of relaxation times. Again, $P_2(t)$ functions were fitted with a mKWW equation (eq 3.4) in order to predict the relaxation time. C-H bond reorientation relaxation times are found to be in good agreement with the experimental data of He et al.[210] obtained by NMR spin-lattice relaxation experiments and with the solid echo NMR measurements of Spiess and Sillescu.[211] Despite the fact that our united-atom model with reconstruction of hydrogens exhibits faster dynamics at short time scales, it can capture reasonably well the evolution of autocorrelation functions at long timescales. Throughout the temperature range studied in our MD simulations, the segmental relaxation times are found to be in excellent agreement with the experimental measurements. Moreover, the nanocomposite system under study exhibits slower segmental dynamics than the bulk. However, as in the case of $P_1(t)$ analysis, the overall dynamics of the systems are really close to each other, prompting the need for a local analysis of the segmental dynamics.

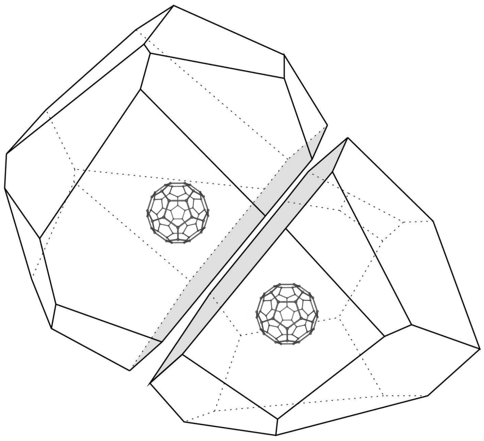

Figure 3.10: Voronoi tessellation of the space with C_{60}s acting as the centers of the tessellation.

3.4.3 Many-nanoparticle Influence on Dynamics

The study of local dynamics, when many nanoparticles are present, requires a tessellation of space, so as to quantify possible many-body effects. Two possible tessellation schemes are the partitioning of the space taken up by the material into Voronoi polyhedra, or their duals, Delaunay tetrahedra. Inspired by the work of Starr et al.[212] on glass-forming liquids, we choose to carry out an analysis based on the Voronoi tessellation of the simulation box with fullerenes acting as the centers of the Voronoi cells (Figure 3.10).

Voronoi polyhedra provide a direct way of quantifying the confinement imposed by a fullerene on its neighborhood. Smaller distances between neighboring fullerenes yield Voronoi cells of smaller volume. Thus, from now on, we will employ the volume of a Voronoi cell as a measure of the confinement experienced by the polymer lying in it (the smaller the cell the more confined the polymeric matrix around the specific fullerene). Some convenient features of the Voronoi tessellation, over its dual, are the constant number of cells (which is equal to the number of dispersed nanoparticles) and the significantly larger volume of the cells (since the Voronoi cells are always by one order of magnitude fewer than the Delaunay tetrahedra). The partitioning of the simulation box is carried out by using the well-established Voro++ software library of Rycroft et al.[213,214]

3.4.4 Local Mean-square Displacement of Backbone Carbon Atoms

A rigorous way of studying the mobility of a polymeric melt is to calculate the mean-square displacement (MSD) of backbone carbon atoms (eq 2.110). In order to avoid chain end ef-

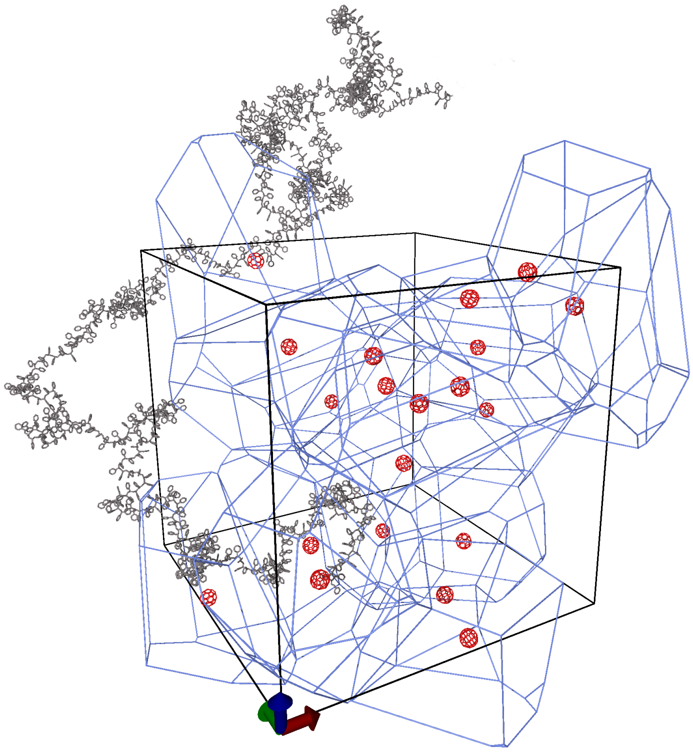

Figure 3.11: Schematic of the Voronoi tessellation of the simulation box. One unfolded atomistic 1460mer chain is also shown. Dispersed fullerenes serve as the centers of the Voronoi cells.

fects,[215,216] only the innermost backbone carbons along the chain contribute to the calculations:

$$g_i(t) = \frac{1}{2n_{\text{inner}}+1} \sum_{i=N/2-N_{\text{inner}}}^{N/2+N_{\text{inner}}} \left\langle (\mathbf{r}_i(t_0+t) - \mathbf{r}_i(t_0))^2 \right\rangle \tag{3.9}$$

with the value of the parameter N_{inner} quantifying the number of innermost atoms, on each side of the middle segment of each chain, that are monitored. In our case, N_{inner} is set in such a way that we track half of the chain, excluding one fourth of the chain close to one end and one fourth close to the other end.

Figure 3.12 presents the MSD of backbone carbon atoms as a function of time at a temperature of 480 K for both the filled and unfilled systems. As can be seen, nanocomposite systems exhibit lower mobility when compared to their neat counterparts. The MSD of backbone carbons is depressed upon the addition of fullerenes, in good agreement with the neutron scattering observations of Kropka et al.[148] In the inset to Figure 3.12, a logarithmic plot of the functions $g_i(t)$ is presented. The scaling of $g_i(t) \sim t^{1/2}$ is expected for the very short time behavior studied.[89] As the tube model predicts (eq 2.111), the segments do not feel the constraints of the entanglement network around them, following a Brownian motion in the free space available.

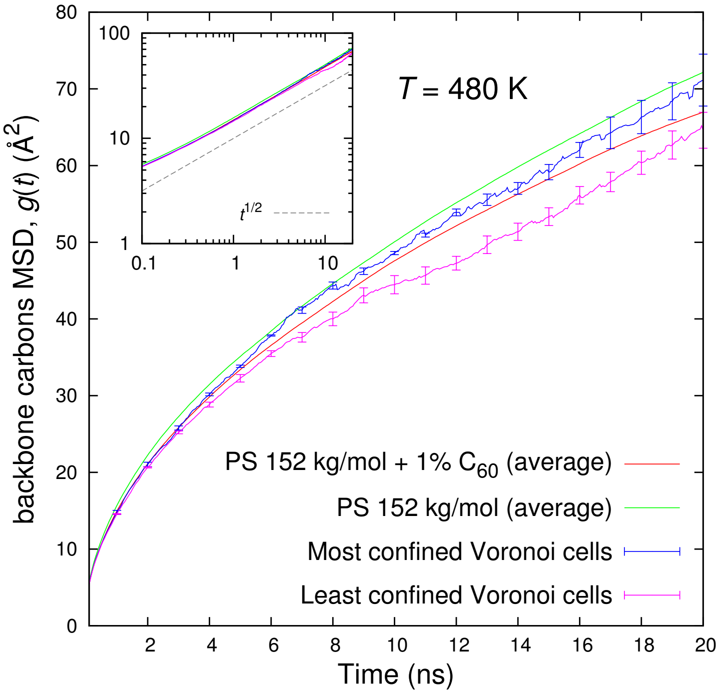

Figure 3.12: Mean-square atomic displacements of backbone carbon atoms as a function of time for filled and unfilled polystyrene systems at $T = 480$ K. In the case of fullerene nanocomposites, an analysis of the dependence of backbone MSD on confinement is also presented for most and least confined Voronoi cells (indicative error bars also included). In the inset to the figure, the same data are presented in logarithmic axes.

This behavior is expected for times t shorter than the characteristic time τ_e ($t \leq \tau_e$) when the segmental displacement becomes comparable to the tube diameter. Likhtman and McLeish[104] estimated that the time marking the onset of the effect of topological constraints on segmental motion, τ_e, is $3.36 \cdot 10^{-4}$ s for polystyrene. Since the results presented in Figure 3.12 go up to 20 ns, the scaling of $t^{1/2}$ is fully justifiable.

We now move to the estimation of the local MSD, for the timespan an atom spends inside a particular cell of the Voronoi tessellation. In our analysis we use the average MSD from the three most confined and three least confined cells, averaged over the three independent configurations created. We have observed that the volume of the Voronoi cells does not change significantly as a function of time. Based on this analysis for the nanocomposite system, the degree of depression is found to be a function of the confinement induced by the fullerenes. The diffusion of chains is spatially inhomogeneous, as observed by Desai et al.[152] Small Voronoi cells tend to lead to higher mobility of the segments. This suggests an image of fullerenes as small grinders dispersed in the polystyrene matrix. Despite the fact that the addition of fullerenes limits the diffusion of polymeric chains, there exist regions in space, where the polymer can recover part of its dynamics due to the high level of confinement.

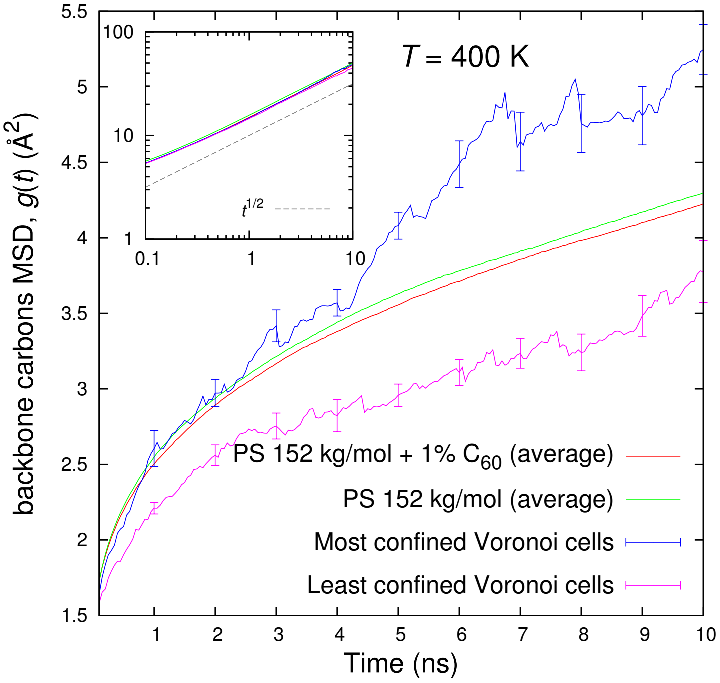

Figure 3.13: Mean-square atomic displacements of backbone carbon atoms as a function of time for filled and unfilled polystyrene systems at $T = 400$ K. In the case of fullerene nanocomposites, an analysis of the dependence of backbone MSD on confinement is also presented for the most and least confined Voronoi cells (indicative error bars also included). In the inset to the figure, the same data are presented in logarithmic axes.

The dynamic heterogeneity of the nanocomposite systems grows as the temperature is lowered. The local mean-square displacement of the backbone atoms, as a function of time, at a temperature of 400 K is presented in Figure 3.13. As happens at higher temperature, the average MSD of the nanocomposite system is smaller compared to the average MSD of the bulk one. However, carbon atoms lying in the most confined Voronoi cells present larger displacements than the ones lying in the least confined. It can be observed that, despite the fact that MSD absolute values are getting smaller as expected, their variance when one studies local dynamics is larger. This observation strengthens our hypothesis that fullerenes act as nanoscopic grinders dispersed in the polymeric matrix, yielding strong deviation of polymer local dynamics from the bulk in their close neighborhood.

3.4.5 Fullerene Rotational Diffusivity

The fact that the fullerenes are geometrically rigid on the atomistic scale (although clearly vibrating) and essentially spherical enables their rotational motion to be readily characterized using a single rotational diffusion measure. If **e** is any arbitrary unit vector embedded in the cluster and passing through its center, then the orientational correlation function:

$$\mathcal{C}_{\mathbf{e}}(t) = \langle \mathbf{e}_i(t)\mathbf{e}_i(0) \rangle \tag{3.10}$$

can be computed. The simplest approach to define **e** is to use the separation vector between each fullerene's center of mass and a specific predefined atom.

The results for two temperatures (which were considered for the local MSD calculation), are presented in Figure 3.14. The main plot contains the results for the temperature of 400 K, while in the inset the rotational decorrelation function at 480 K is plotted. Despite the noise in the measurements (since only the three most confined and three least confined fullerenes contribute), it is clear that fullerenes which lie in the most confined cells rotate faster. There are many signs of anomalous rotational diffusion of fullerenes, which imply a strongly heterogeneous environment. An in-depth study of the fullerenes' rotational diffusion is outside the scope of the present work. However, this surprising observation coheres to the image of the nanoparticles acting as nanoscopic grinders which force the polymeric chains to translate in their immediate neighborhood.

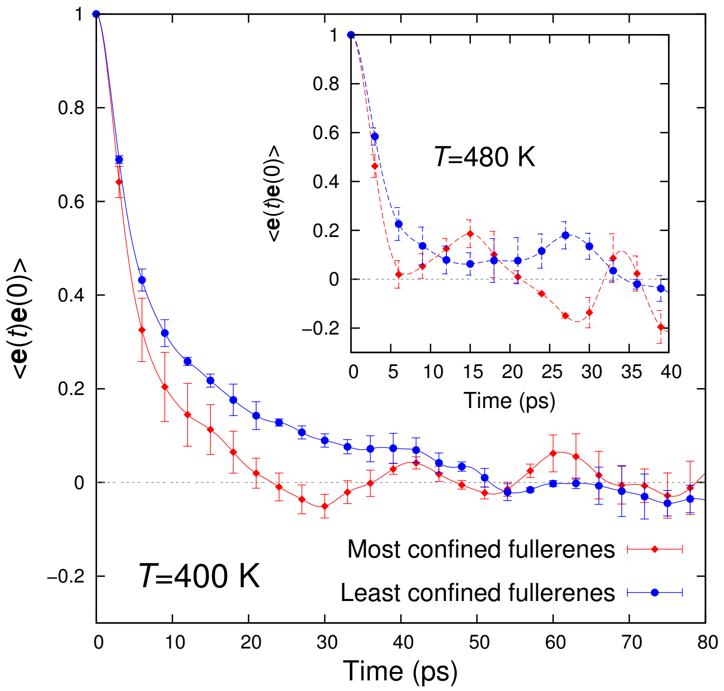

Figure 3.14: Fullerenes' rotational autocorrelation function. We consider a vector connecting a fullerene's center of mass with a predefined atom. The main figure refers to 400 K, while the inset to the figure refers to 480 K.

3.5 Local Stresses

3.5.1 Atomic-level Stresses

Atomic-level stresses can serve as a basis for characterizing local structure. Egami et al.[217] first applied atomic-level stresses to glasses in an atomistic computer model of amorphous iron. Theodorou and Suter[218] were the first to apply the idea of atomic level stresses to polymeric glasses, where both bonded and nonbonded interactions contribute to the stress. Following ref 218, we define the atomic stress tensor for atom i, in a system with central forces by

$$\sigma_{i,\alpha\beta} = -\frac{1}{V_i} m_i v_{i,\alpha} v_{i,\beta} - \frac{1}{2V_i} \sum_{j \neq i} (r_{i,L} - r_{j,\alpha})^{\text{min.im.}} F_{ij,\beta}^{\text{min.im.}} \tag{3.11}$$

where $\mathbf{r}_i$ and $\mathbf{r}_j$ are the position vectors of atoms i and j, $\mathbf{v}_i$ the velocity of atom i and $\mathbf{F}_{ij}$ is the force exerted on atom i by atom j. The indices α and β, indicating the three coordinate directions in a Cartesian system, assume the values x, y and z. The superscript "min.im." indicates interatomic distances and forces calculated according to the "minimum image convention". Thompson et al.[219] have described different ways of formulating per-atom and global virial and stress calculations, including how it is done in LAMMPS.[170] According to their formulation, a virial contribution produced by a small set of atoms (e.g. 4 atoms in a dihedral angle) is assigned in equal portions to each one of these atoms.

In order to convert the virial into a stress, a local volume V_i has to be associated with each atom. Here, we shall use a Voronoi tessellation to define atomic volumes,[213,214] such that summing over all atoms gives the total volume of the system, $V = \sum_i V_i$. Note that this atom-level Voronoi tessellation is much finer than the Voronoi tessellation with respect to fullerene centers used to partition the sample volume among different fullerenes. Summation of all atomic-level stresses $\boldsymbol{\sigma}_i$, multiplied by the appropriate volumes V_i, yields the macroscopic stress; for a system in detailed mechanical equilibrium the "internal" stress tensor $\boldsymbol{\sigma}$ is recovered (this is a restatement of the virial theorem):[134]

$$\sigma_{\alpha\beta} = \frac{1}{\sum_i V_i} \sum_i V_i \sigma_{i,\alpha\beta} \tag{3.12}$$

Note that, as defined in eq 3.11, per-atom stress is the negative of the per-atom pressure tensor divided by an appropriate atomic volume. Thus, if the diagonal components of the per-atom stress tensor are summed for all atoms in the system and the sum is divided by $3V$ where V is the volume of the system, the ensemble average of the result should be $-p$, with p being the total pressure of the system.

3.5.1/i Atomic volumes obtained from a Voronoi tessellation of the space

Based on the Voronoi tessellation of the simulation box, the *atomic volume* of the atoms can be extracted, being an alternative description of the empty space. A commonly mentioned parameter is the so-called *free volume*, which can be defined as the unoccupied volume in a configuration, in excess of that in the densest possible packing.[220] In realistic descriptions of polymeric atoms involving soft sphere potentials, the free volume cannot be unambiguously defined. However, one may still ascribe a volume to each atom to represent the space it effectively occupies, and a consistent way to do this is by employing a Voronoi tessellation of the space. For a particular atom, a larger (relative to other atoms of the same species) Voronoi volume indicates lower local packing efficiency, and thus the presence of more free volume. Figure 3.15 presents the distributions of atomic volumes accumulated for every type of interaction site separately. Aliphatic CH and aromatic C are characterized by low atomic volumes, e.g. in the case of aliphatic CH the average atomic radius is 0.23 nm. Moving to atoms with larger atomic volumes, like the aromatic CH, the effective radius becomes 0.29 nm. These values are in excellent agreement with the first peak of the pair distribution function calculated by Mondello et al.[164] using the same united-atom forcefield. Topologically, atoms lying in smaller volumes tend to be associated with higher energy cost, because a missing or ex-

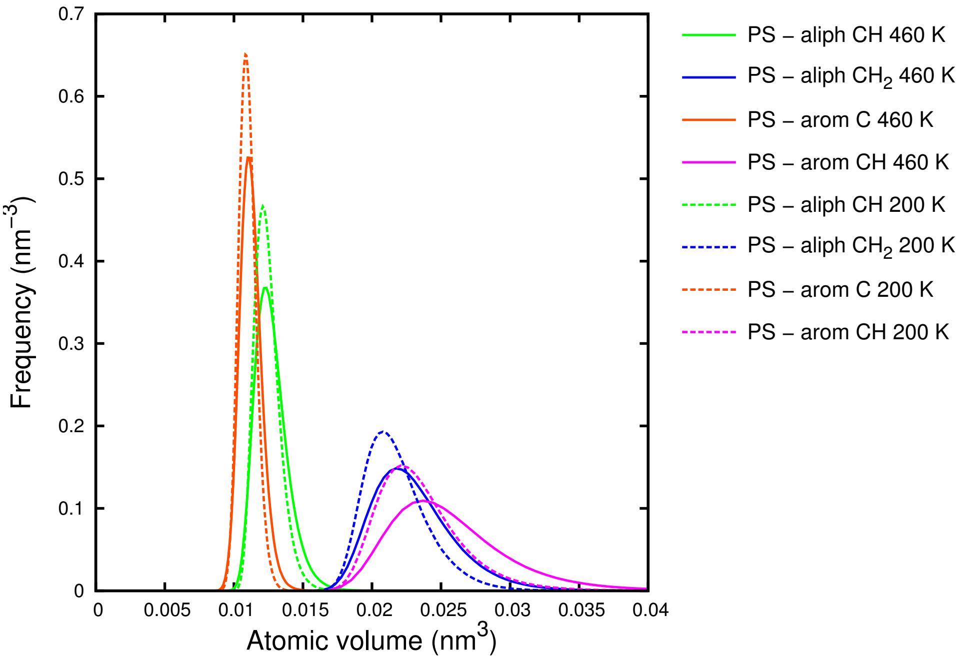

Figure 3.15: Distribution of the volume of the Voronoi cells occupied by united atoms, for the four types of centers present int the PS model (aliphatic CH, aliphatic CH$_2$, aromatic C and aromatic CH groups).

tra neighbor corresponds to a larger distortion with respect to the efficient packing scenario. Thus, it is expected that i.e. aromatic C will be associated with higher atomic level stresses. Our findings are in favorable agreement with the histograms of atomic volumes in PS presented by Dammert et al.[221] Upon cooling PS to the glassy state, we observe that the average atomic volumes become smaller, as expected. However, aromatic CH and aliphatic CH$_2$ united atom are more affected by the temperature drop, than the aliphatic CH and aromatic C.

Moreover, the tessellation of the simulation box allows the *coordination number* of the atoms to be extracted, which is a representative parameter that can describe local structure. In crystals, the coordination number for every atom is fixed and deviations are found only at or near defects. In disordered materials, like polymer melts and glasses, in contrast, each atom is characterized by its own coordination number. The distribution of coordination numbers in our model PS is presented in Figure 3.16. By employing a Voronoi tessellation of the simulation box with the polymeric atoms acting as the centers of the Voronoi cells, we obtain the coordination number of every atom from the number of faces of the Voronoi polyhedra formed around the atoms. Aliphatic CH and aromatic C are characterized by low coordination numbers, on average 12 and 13 respectively, implying an environment of high local density. On the contrary, aliphatic CH$_2$ and aromatic CH lie in lower local density neighborhoods, characterized by higher coordination numbers (17 and 18 on the average, respectively). Based on Figure

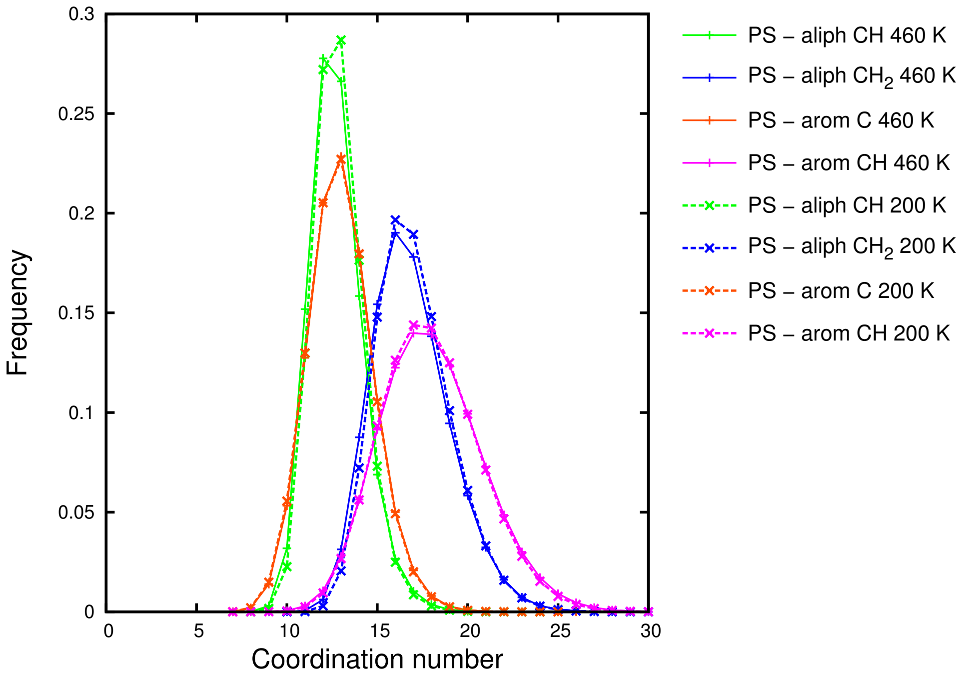

Figure 3.16: Distribution of the number of nearest neighbors per atom (coordination number), for the four types of centers present in the PS model (aliphatic CH, aliphatic CH_2, aromatic C and aromatic CH groups).

3.16, we can argue that the topology of the PS configurations is preserved during quenching into the glassy state, since the distributions of coordination numbers are not affected by the glass transition.

3.5.1/ii Atomic-level stress distributions

In polymer melts and glasses atoms are often in distorted environment, and this gives rise to atomic level stresses. The average of the atomic level stress is equal to the external stress, which is usually close to zero. We introduce two invariants of the atomic-level stress tensor[217,218] for characterizing local structure. The first is the "atomic-level hydrostatic pressure" p_i, defined by:

$$p_i = \frac{1}{3}\mathrm{Tr}(\boldsymbol{\sigma}_i) \tag{3.13}$$

Although p_i is termed a "pressure", it is really a tension or negative pressure. It can serve as a measure of local density fluctuations in the material. A high, positive value of p_i is associated with a low coordination number around atom i and with a higher than average atomic density. A low, negative value of p_i is associated with a high coordination number and with lower than average local atomic density. The second invariant is the "atomic-level von Mises shear

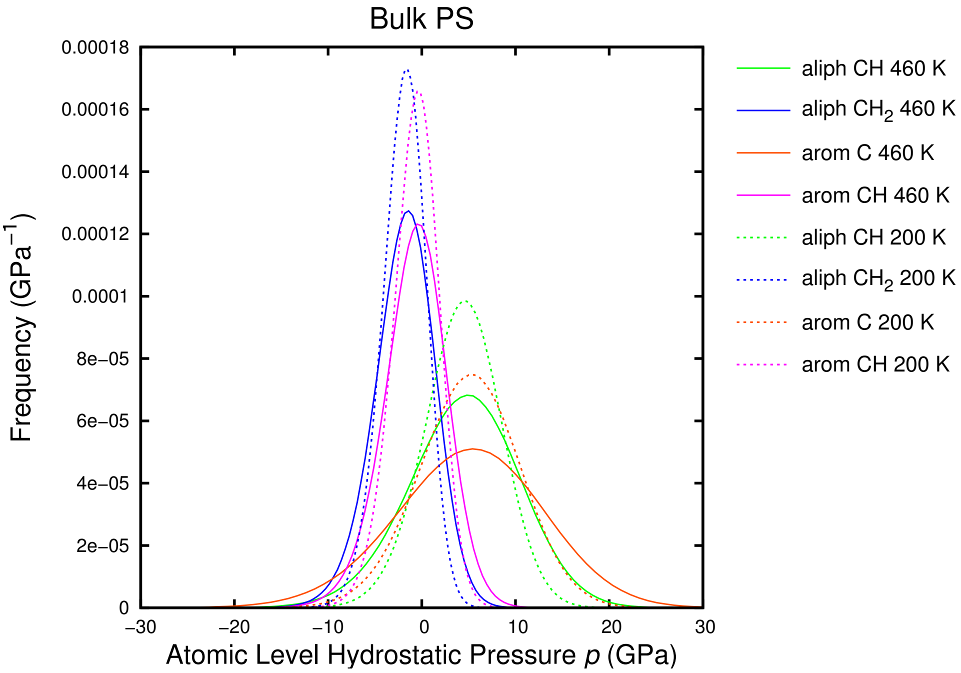

Figure 3.17: Distribution of the atomic-level hydrostatic pressure (p_i) for the four types of centers present in the model PS melt (aliphatic CH, aliphatic CH$_2$, aromatic C and aromatic CH groups). The histogram is based on 2000 configurations obtained every 20 ps of MD simulation at two temperatures, $T = 460$ K and $T = 200$ K.

stress”, $\tau_{\mathrm{vM},i}$, defined by

$$\tau^2_{\mathrm{vM},i} = \frac{1}{2}\mathrm{Tr}\left[(\boldsymbol{\sigma}_i - p_i\mathbb{I})^2\right] \tag{3.14}$$

where $\mathbb{I}$ is the matrix representation of the unit tensor. The quantity $\tau_{\mathrm{vM},i}$ reflects the degree of asymmetry of the local environment around atom i.

Atomic-level stresses were calculated for an ensemble of 2000 configurations obtained during NVE MD simulations at several temperatures. The characteristic quantities p_i and $\tau_{\mathrm{vM},i}$ were calculated according to eqs 3.13 and 3.14, respectively. The distributions of p_i and $\tau_{\mathrm{vM},i}$ were accumulated seperately for each type of united atom interaction site (aliphatic CH and CH$_2$, aromatic C and CH, fullerene C) present in our system. These distributions are plotted in Figures 3.17 and 3.19 for the bulk PS system and in Figures 3.18 and 3.20 for the composite (PS + 1% C$_{60}$) system. The results reported have been obtained for a melt temperature (460 K) and a temperature deep into the glassy state (200 K). The moments of the distributions are reported in Tables 3.5 and 3.6. A striking feature, evident from all distributions, is the expected disparity in magnitude between the atomic-level stresses $\boldsymbol{\sigma}_i$ and the box (macroscopic) internal stress $\boldsymbol{\sigma}$.[218] There is a strong compensation effect in the summation of atomic-level stresses to the overall stress (eq 3.12). Theodorou and Suter[218] have observed atomic-level stresses of the same order of magnitude as those reported here, in the case of well-relaxed configurations of

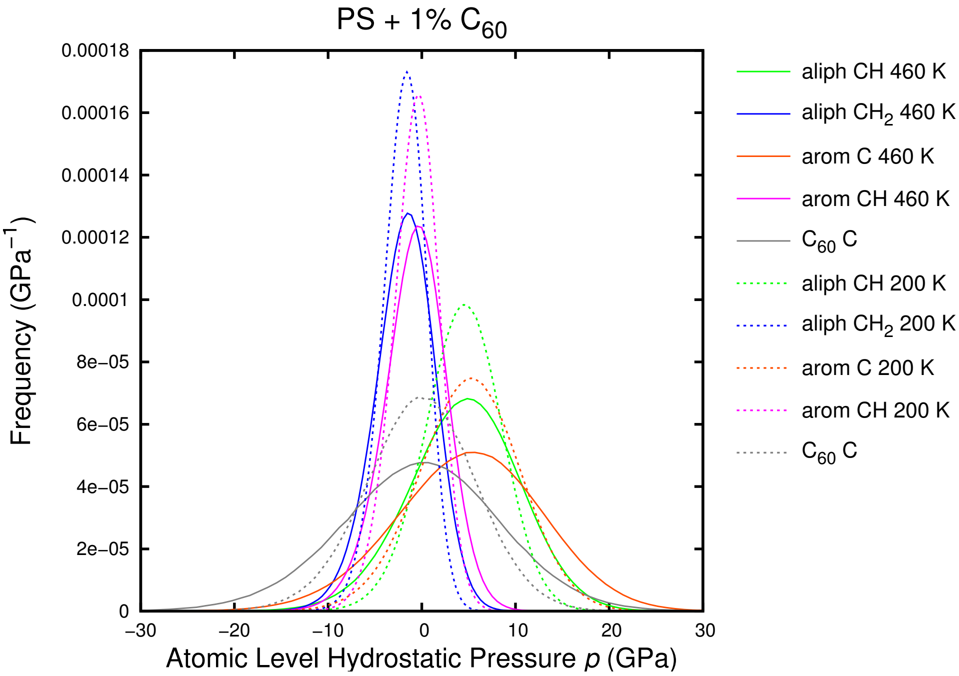

Figure 3.18: Distribution of the atomic-level hydrostatic pressure (p_i) for the five types of centers present in the model PS-C_{60} melt (aliphatic CH, aliphatic CH_2, aromatic C, aromatic CH groups and fullerene C). The histogram is based on 2000 configurations obtained every 20 ps of MD simulation at two temperatures, $T = 460$ K and $T = 200$ K.

glassy atactic polypropylene.

Figures 3.17 and 3.18 reveal a distinct difference in the shape and position of the p distribution between different interaction sites. Atomic-level stresses are sensitive to the topology of bonded systems.[218] Aliphatic CH_2 and aromatic CH united atoms are under compression ($p < 0$: low local density and high coordination number), while aliphatic CH and aromatic C united atoms are under tension ($p > 0$: high local density and low coordination number). The same observations can be made for the nanocomposite systems. Fullerene carbon atoms, in the case of nanocomposite systems, are characterized by a broad p distribution centered around zero. The second moment, which describes the width of the distribution, is the most significant parameter, and in some cases acts as an order parameter. The spread of the p distribution reflects variations in density of the local environments. The p distributions for aliphatic CH groups and aromatic carbons are considerably broader than those of aliphatic CH_2 and aromatic CH groups, implying a variety of environments experienced by the atoms belonging to the former groups. The third moment of the distribution, skewness, is close to zero implying nearly Gaussian distributions of atomic level hydrostatic pressures at both temperatures. Srolovitz et al.[222] made the same observation for the stress distributions of metallic glasses.

Upon cooling the system from the melt to the glassy state, all p distributions become nar-

Table 3.5: Characteristic quantities (mean, standard deviation and skewness) of the p distributions as depicted in Figures 3.17 and 3.18.

species	$\langle p \rangle$	$\left(\langle p^2 \rangle - \langle p \rangle^2\right)^{1/2}$	$\frac{\langle p^3\rangle - 3\langle p\rangle\left(\langle p^2\rangle - \langle p\rangle^2\right) - \langle p\rangle^3}{\left(\langle p^2\rangle - \langle p\rangle^2\right)^{3/2}}$
	GPa	GPa	
PS Melt, $T = 460$ K			
aliphatic CH	4.484	5.710	-0.151
aliphatic CH_2	-1.876	3.137	-0.281
aromatic C	5.026	7.567	-0.129
aromatic CH	-0.735	3.317	-0.257
PS Glass, $T = 200$ K			
aliphatic CH	4.328	4.102	-0.131
aliphatic CH_2	-1.939	2.370	-0.285
aromatic C	5.033	5.378	-0.107
aromatic CH	-0.689	2.505	-0.279
Composite Melt, $T = 460$ K			
aliphatic CH	4.475	5.717	-0.152
aliphatic CH_2	-1.876	3.144	-0.279
aromatic C	5.007	7.579	-0.130
aromatic CH	-0.738	3.321	-0.260
fullerene C	-0.173	8.257	-0.103
Composite Glass, $T = 200$ K			
aliphatic CH	4.338	4.113	-0.133
aliphatic CH_2	-1.916	2.376	-0.290
aromatic C	5.012	5.393	-0.109
aromatic CH	-0.696	2.507	-0.283
fullerene C	-0.145	5.920	-0.087

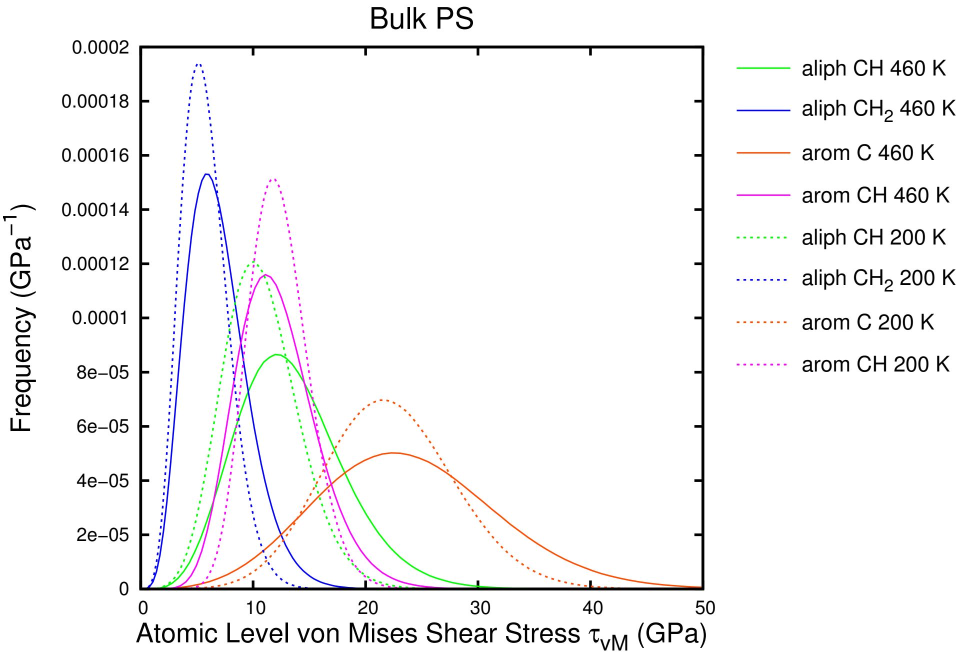

Figure 3.19: Distribution of the atomic von Mises shear stress $\tau_{\mathrm{vM},i}$ for the four united atom species present in our model PS (see legend to Figure 3.17). The histogram is based on 2000 configurations obtained every 20 ps of MD simulations at two temperatures, $T = 460$ K and $T = 200$ K.

rower, as evident from their standard deviations reported in Table 3.5. This can be partly attributed to the kinetic term which depends on the temperature. A closer look on Figures 3.17 and 3.18 reveals that the mean values of the distributions also change. As the temperature drops, aliphatic CH experience lower positive p, which means that the local density of their environment increases. The same observation can be also made for the aliphatic CH$_2$s which experience lower (negative) p. On the contrary, aromatic CH groups experience higher negative p, implying a lower coordination number in the glassy state. The average hydrostatic pressure experienced by aromatic C is a weak function of the temperature, since their position in between the chain's backbone and the phenyl ring is stable and protected from their environment. The addition of fullerenes to PS does not seem to affect the atomic-level hydrostatic pressure distributions, neither in the melt nor in the glassy state.

Different species experience different shear stresses, as evidenced from Figures 3.19 and 3.20. The means and the standard deviations listed in Table 3.6 indicate that aromatic carbons are characterized by the broadest distribution of atomic-level von Mises shear stresses. This can be attributed to the exposure of the protruding phenyls to the surroundings of a chain, which creates a highly asymmetric local environment. On the contrary, aliphatic CH$_2$ interaction sites experience a considerably lower average shear stress, due to their shielded position in the backbone of the chain. The atomic shear-stress distributions (Figures 3.19 and 3.20) are

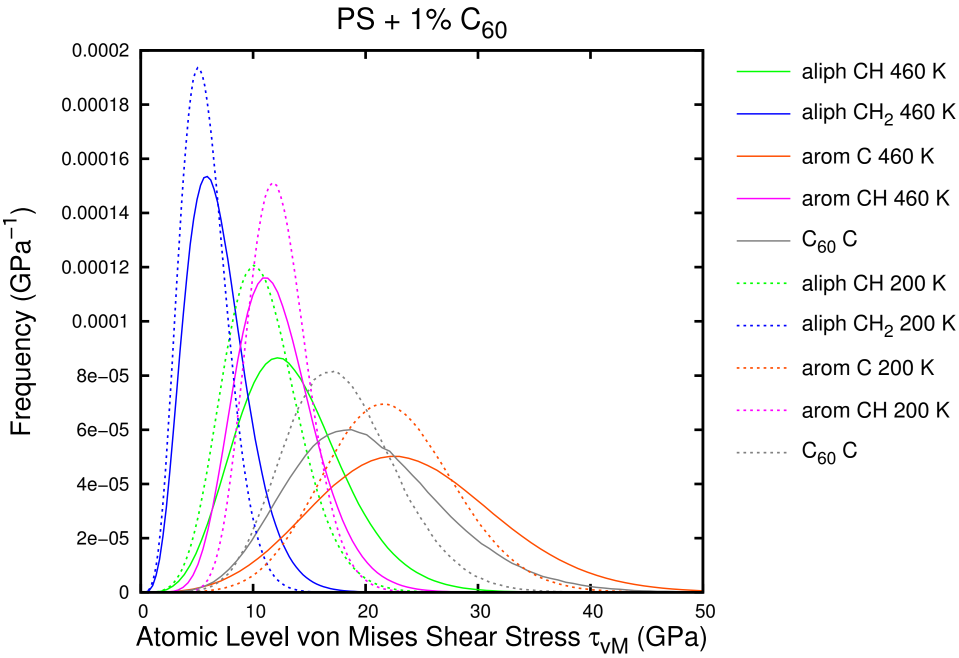

Figure 3.20: Distribution of the atomic von Mises shear stress $\tau_{\mathrm{vM},i}$ for the five united atom species present in our model PS-C_{60} (see legend to Figure 3.18). The histogram is based on 2000 configurations obtained every 20 ps of MD simulations at two temperatures, $T = 460$ K and $T = 200$ K.

all skewed to the right (this is also the shape observed by Theodorou and Suter[218]) displaying extended tails to the right. Fullerene carbon atoms exhibit high atomic von-Mises shear stress, as expected, due to the stiff intramolecular potential which keeps them rigid.

The effect of temperature on the atomic von Mises stress distributions is the same as on the hydrostatic pressure distributions. The spread of the $\tau_{\mathrm{vM},i}$ distributions in the glassy state is limited compared to their spread in the melt state. Moreover, the average von Mises shear stress experienced by all united atom species is lower upon quenching the PS into the glassy state.

3.5.2 Local Stress Definition

In addition to the atomic-level stresses, we wish to obtain coarse-grained local stresses in a control volume V_{ctrl} to examine the influence of the observation length-scale on the estimated stresses. There are several possibilities for computing the stress tensor in amorphous materials on intermediate scales. A widely accepted approach has been to partition the simulation cell into subvolumes, with only those atoms residing in each subvolume contributing to the local stress tensor of the region.[223] The stress tensor within a region can be computed by summing atomic-level contributions (eq 3.11), where the sum runs only over those atoms that are in the

Table 3.6: Characteristic quantities (mean, standard deviation and skewness) of the τ_{vM} distributions as depicted in Figures 3.19 and 3.20

species	$\langle \tau_{\mathrm{vM}} \rangle$ GPa	$\left(\langle \tau_{\mathrm{vM}}^2 \rangle - \langle \tau_{\mathrm{vM}} \rangle^2 \right)^{1/2}$ GPa	$\frac{\langle \tau_{\mathrm{vM}}^3 \rangle - 3\langle \tau_{\mathrm{vM}} \rangle \left(\langle \tau_{\mathrm{vM}}^2 \rangle - \langle \tau_{\mathrm{vM}} \rangle^2 \right) - \langle \tau_{\mathrm{vM}} \rangle^3}{\left(\langle \tau_{\mathrm{vM}}^2 \rangle - \langle \tau_{\mathrm{vM}} \rangle^2 \right)^{3/2}}$
PS Melt, $T = 460$ K			
aliphatic CH	13.039	4.556	0.543
aliphatic CH_2	6.728	2.624	0.667
aromatic C	23.596	7.660	0.320
aromatic CH	12.225	3.430	0.528
PS Glass, $T = 200$ K			
aliphatic CH	10.749	3.383	0.445
aliphatic CH_2	5.750	2.097	0.557
aromatic C	22.183	5.728	0.214
aromatic CH	12.285	2.670	0.382
Composite Melt, $T = 460$ K			
aliphatic CH	13.086	4.562	0.539
aliphatic CH_2	6.714	2.630	0.673
aromatic C	23.635	7.680	0.326
aromatic CH	12.227	3.435	0.527
fullerene C	20.033	6.608	0.548
Composite Glass, $T = 200$ K			
aliphatic CH	10.811	3.388	0.441
aliphatic CH_2	5.730	2.094	0.543
aromatic C	22.203	5.753	0.222
aromatic CH	12.282	2.679	0.384
fullerene C	17.926	4.942	0.399

given region at a particular time:[224]

$$\boldsymbol{\sigma}_{\mathrm{local}}\left(V_{\mathrm{ctrl}}\right) = \frac{1}{V_{\mathrm{ctrl}}} \sum_{i \in V_{\mathrm{ctrl}}} V_i \boldsymbol{\sigma}_i \tag{3.15}$$

This scheme converges to the stress of the simulation box, $\boldsymbol{\sigma}_{\mathrm{b}}$, eq 3.12, when the simulation box is taken as a single domain. Similarly to the atomic-level stress tensor invariants, we can define the "local hydrostatic pressure", $p_{\mathrm{local}}\left(V_{\mathrm{ctrl}}\right)$:

$$p_{\mathrm{local}}\left(V_{\mathrm{ctrl}}\right) = \frac{1}{3}\mathrm{Tr}(\boldsymbol{\sigma}_{\mathrm{local}}\left(V_{\mathrm{ctrl}}\right)) \tag{3.16}$$

and the "local von Mises shear stress":

$$\tau_{\mathrm{vM,local}}^2\left(V_{\mathrm{ctrl}}\right) = \frac{1}{2}\mathrm{Tr}\left[\left(\boldsymbol{\sigma}_{\mathrm{local}}\left(V_{\mathrm{ctrl}}\right) - p_{\mathrm{local}}\left(V_{\mathrm{ctrl}}\right)\mathbb{I}\right)^2\right] \quad . \tag{3.17}$$

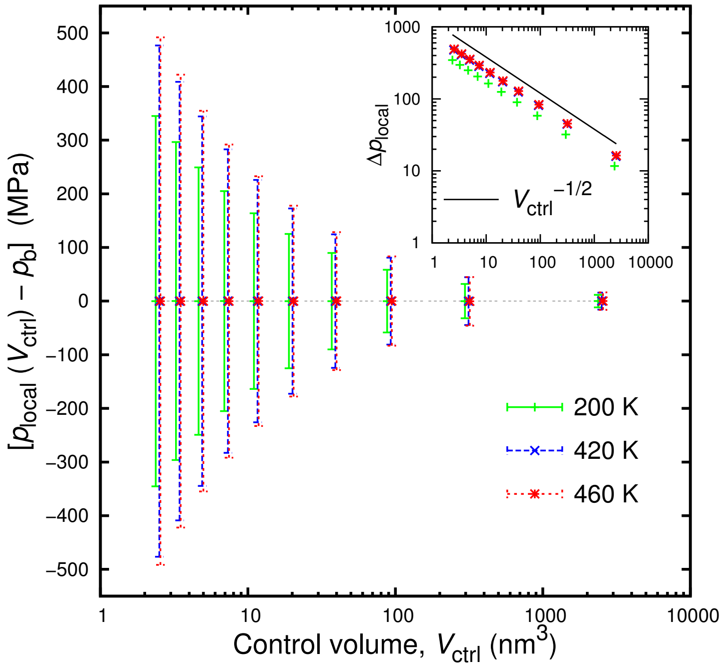

Figure 3.21: Difference of the local hydrostatic pressure from the hydrostatic pressure of the box (bulk), $p_{\text{local}} - p_{\text{b}}$, versus the size of the control volume used for summing the atomic-level contributions. In the inset to the figure the dependence of the standard deviation (errorbars of the main figure), Δp_{local}, on the size of the domain is depicted. The pressure of the box was tuned to 101.325 kPa.

3.5.3 Dependence of the Local Stress on the Observation Length-scale

The influence of the observation length-scale on local stress estimation is examined in Figures 3.21 and 3.22. As already pointed out, there is a strong compensation effect when summing atomic-level stresses. Based on our simulation protocol, we check the stress tensor of the whole simulation box in order to be on the average close to atmospheric pressure. During the runs under constant energy, the hydrostatic pressure of the system, p_{b}, as defined in Eq. 3.13, is of the order of -0.1 MPa (please note the minus sign implying the positive macroscopic pressure) without any drift. We then partition the simulation box into smaller cubic cells in order to calculate the local stresses.

It is evident from Figure 3.21 that the hydrostatic pressure can be reliably estimated, irrespectively of the observation length scale. However, the standard deviation of the obtained measurements scales as the inverse square root of the volume (inset to the Figure 3.21). The same trend is observed for both melt and glassy configurations. In the glassy state, the standard deviation is smaller, as the spread of atomic-level stress distributions is smaller (please see Table 3.5). When moving to smaller length-scales, regions of positive and negative hydrostatic pressure coexist. Regions of low density (negative pressure) resemble the distributed free-

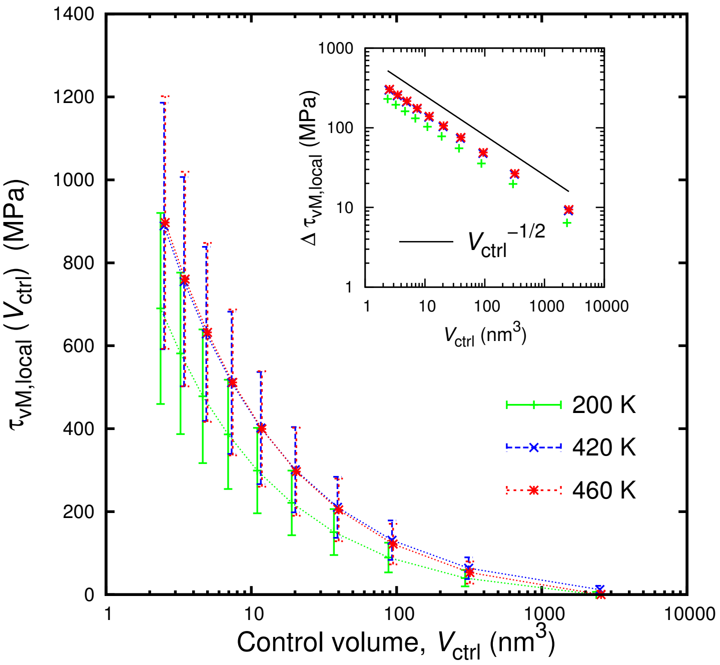

Figure 3.22: Local von Mises shear stress versus the size of the control volume used for summing the atomic-level contributions. In the inset to the figure the dependence of the standard deviation (errorbars of the main figure) of the local von Mises stress, $\Delta\tau_{\mathrm{vM,local}}$ on the size of the domain is depicted.

volume,[225] but there are also regions of high density which could be called anti-free-volume.[226] In metallic glasses, Egami et al.[226] call the free-volume-like defects as n-type defects (negative density fluctuation) and the anti-free-volume p-type defects. Unrelaxed structures have high density of n- and p-type defects. Structural relaxation is thought to occur through the recombination of n-type and p-type defects.[227] However, free-volume theory[220] was originally conceived for hard-sphere systems, such as molecular liquids and rare gas liquids, which are far from our polymer melts and glasses.

On the contrary, the local von Mises shear stress is a function of the observation length-scale, as presented in Figure 3.22. Deviations of the shear stresses from the normal ones become more pronounced, as the volume of the reference domain becomes smaller. As the length-scale of observation increases, fluctuations cancel each other, yielding lower shear stress. At the length scale of the simulation box, shear stresses vanish. The length-scale dependence of von Mises shear stress follows the inverse square root of the volume. This scaling can be envisioned as the dependence of an equilibrium fluctuation quantity on the observation length-scale. Moreover, the same dependence holds both for the melt and the glassy state.

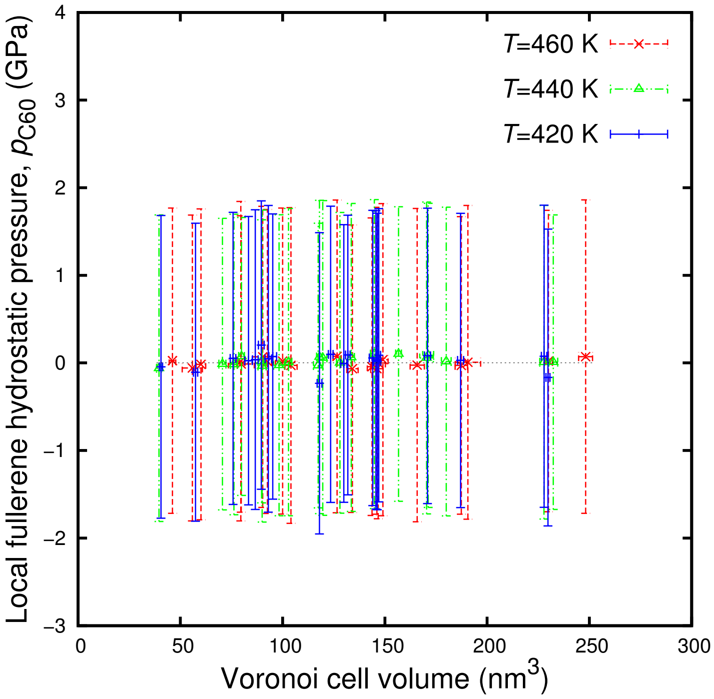

Figure 3.23: Local hydrostatic pressure of fullerenes, p_{C60}, as a function of the volume of the Voronoi cell they belong to. Error bars represent the standard deviation of the distribution obtained by analyzing 2000 configurations at each temperature, obtained every 20 ps of MD simulation.

3.5.4 Local Stresses in PS - Fullerene Mixtures

The influence of confinement on the local hydrostatic pressure, p_{local}, as defined in eq 3.16, is examined in Figures 3.23 and 3.24. We first analyze the local pressure experienced by the fullerene atoms, p_{C60}, summing the stresses only for the 60 atoms constituting each fullerene (Figure 3.23). Then we study the local hydrostatic pressure experienced by the surrounding polymer atoms, p_{polym}. These quantities, when added, yield the negative of the box pressure,

$$\frac{\sum_{i\in cells}\left(p_{\mathrm{C60},i}V_{\mathrm{C60},i}+p_{\mathrm{polym},i}V_{\mathrm{polym},i}\right)}{3V}=-p_{\mathrm{b}} \tag{3.18}$$

where $V_{\mathrm{C60},i}$ is the sum of the volumes of the small (atomic) Voronoi polyhedra around the carbon atoms constituting a fullerene. By construction, this contains the hollow space in the fullerene, i.e. $V_{\mathrm{C60},i}$ is approximately equal to the volume of the fullerene sphere. On the other hand, $V_{\mathrm{polym},i}$ is the sum of the small atomic Voronoi volumes of polymer atoms contained in a larger Voronoi polyhedron around a fullerene obtained from the tessellation of the simulation box based on C_{60} centers. The volume of the large Voronoi cell, i.e. the one used for quantifying confinement, serves as the abscissa of both Figures 3.23 and 3.24. The number of atoms per cell does not remain constant throughout the simulation but fluctuates slightly depending

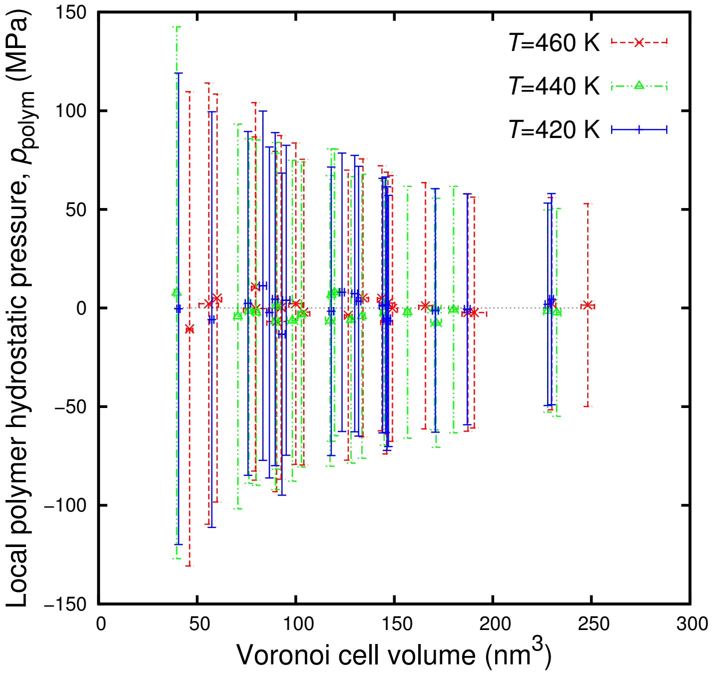

Figure 3.24: Local hydrostatic pressure of the polymeric atoms, p_{polym}, as a function of the volume of the Voronoi cell they belong to. Error bars represent the standard deviation of the distribution obtained by analyzing 2000 configurations at each temperature, obtained every 20 ps of MD simulation.

on the local particle density and the shape (number of faces) of the Voronoi cell. Inspecting the local hydrostatic pressures, we see in Figures 3.23 and 3.24 that the pressure distributions are almost symmetrically centered around the macroscopic set point pressure. The standard deviation of the distribution of local pressures becomes larger, as the volume of the Voronoi cell decreases. This fact is expected in the case of p_{polym} (Figure 3.24), where, as the length scale of the observation becomes smaller, increasing fluctuations are observed.[224] On the contrary, in the case of p_{C60} (Figure 3.23), the dispersion of local pressures is not affected by the size of the Voronoi cell the fullerenes occupy, since a constant number of atoms (60) contribute to the local hydrostatic pressure. Fullerenes experience nearly zero hydrostatic pressure with a rather narrow distribution around its mean value. Figures 3.23 and 3.24 indicate that the local hydrostatic pressures are not sensitive to the temperature, in the melt state.

Figures 3.25 and 3.26 present the local von Mises stresses of fullerenes and surrounding polymeric atoms, respectively. As evident from Figure 3.25, fullerenes experience strong shear stresses, which seem to be independent of the volume of the Voronoi cell which they occupy. The average fullerene von Mises shear stress is approximately 3 GPa, irrespectively of the simulation temperature. This high value may be attributed to the stiff intramolecular potential which makes fullerenes behave as rigid bodies. On the contrary, the local von Mises shear

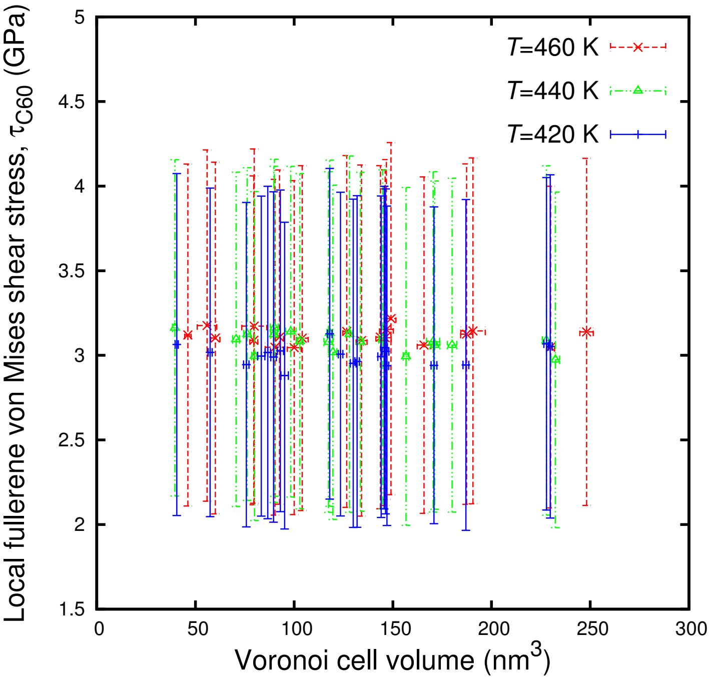

Figure 3.25: Local von Mises shear stress of the fullerenes, τ_{C60}, as a function of the volume of the Voronoi cell they belong to. Error bars represent the standard deviation of the distribution obtained by analyzing 2000 configurations at each temperature, obtained every 20 ps of MD simulation.

stress of the polymer occupying a Voronoi cell is not fixed. It is a function of the volume of the cell, as presented in Figure 3.26. Shear stresses become more pronounced, as the volume of the reference domain becomes smaller. As the length-scale of observation increases, fluctuations cancel each other, yielding lower shear stress. At the length scale of the simulation box, shear stresses almost vanish. This length-scale dependence of von Mises shear stress has been also found for pure PS. In both cases (pure and composite), the von Mises shear stress scales as the inverse square root of the volume. By a careful look at Figure 3.26, it can be observed that the addition of fullerenes shifts the von Mises shear stresses of polymeric atoms to slightly higher values, retaining the same length-scale dependence.

3.6 Summary and Conclusions

In this chapter, we have outlined a strategy for simulating monodisperse long-chain atactic polystyrene nanocomposite melts at two interconnected levels of description: a coarse-grained one, wherein each diad along the chains is represented as a single interaction site, or "super-atom", and a detailed one, employing a united-atom model representation for the polymer. Results from both levels, applied to a nanocomposite of high importance, have been presented. We focus on high molecular weight PS melts with fullerene (C_{60}) molecules dispersed at a

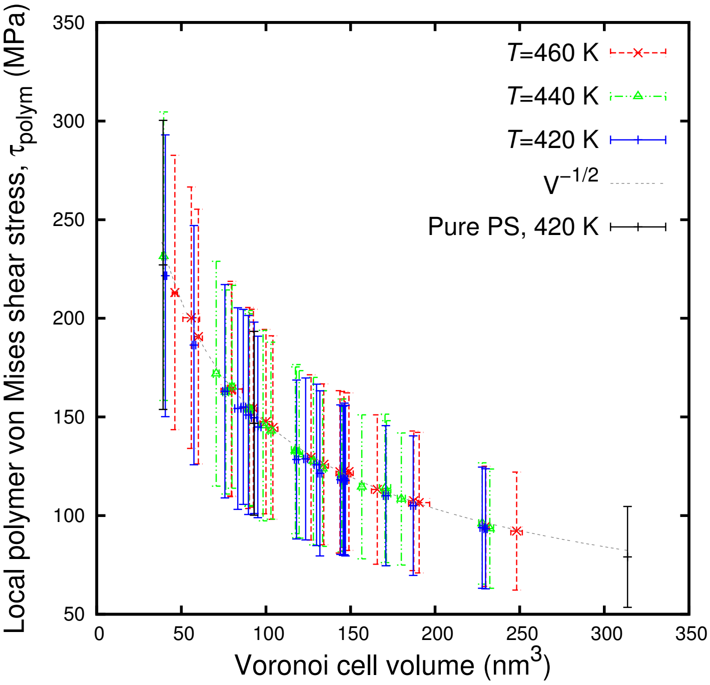

Figure 3.26: Local von Mises shear stress of the polymeric atoms, τ_{polym}, as a function of the volume of the Voronoi cell they belong to. Error bars represent the standard deviation of the distribution obtained by analyzing 2000 configurations at each temperature, obtained every 20 ps of MD simulation. The dotted line shows the $V^{-1/2}$ dependence.

mass fraction of 1% , specifications identical to systems already studied experimentally.[148]

A state-of-the-art Monte Carlo builder has been developed which can build polymeric chains of arbitrary geometry in heavily constrained environments. It is based on the well-known quasi-Metropolis scheme of Theodorou and Suter[165] for generating amorphous configurations in a bond-by-bond fashion. The original source code has been extended by an on-the-fly minimization strategy for driving the insertion of monomers in constrained environments. The minimizer generates a set of minima, from which one is selected following a quasi-Metropolis procedure.

The coarse-grained simulations of the PS-C_{60} composite were based on the PS model of Milano and Müller-Plathe.[159] The coarse-grained model was equilibrated at 500 K using connectivity-altering Monte Carlo moves along with flips, rotations, reptations and concerted rotations.[32] Chain conformations obtained through these coarse-grained simulations were found to be equilibrated at all length scales. Chain dimensions, as predicted from the mean square end-to-end distance (Figure 3.1) and from the mean square radius of gyrations (Figure 3.2) were found to be in excellent agreement with available experimental evidence. Chain conformations of the nanocomposite systems were found to be similar to the ones of the neat polymeric systems. No effect of the dispersion of C_{60}s on chain conformations has been observed at the coarse-grained level.

Well-equilibrated melt configurations sampled by coarse-grained MC were reverse-mapped to the atomistic level. In continuation to the previous efforts on reverse mapping of coarse-grained polystyrene, for the first time a rigorous and systematic approach is presented, which yields atomistic configurations exhibiting characteristics in excellent agreement with experimental measurements. Our approach encompasses three stages: (a) a quasi-Metropolis procedure for the re-introduction of the atomistic sites by selecting their locations from a set of candidate ones. (b) A local Metropolis Monte Carlo simulation where flips, ring rotations and configurationally biased regrowths of atomistic sites are used.[32] This is the key step in order to guide the reverse-mapping process into a conformationally reasonable subspace of the configuration space of the detailed model. (c) an energy minimization step using the full atomistic forcefield with gradual introduction of nonbonded interactions. During the whole reverse-mapping procedure, CH_2 sites (centers of CG sites) are kept fixed, preserving the well-equilibrated coarse-grained configurations. The distributions of torsion angles in the reverse-mapped configurations (Figures 3.5(a) and 3.6(a)) are indistinguishable from those of 80-mer configurations equilibrated directly via MD using the same united-atom model. Moreover, configurations obtained from reverse mapping exhibit populations of *trans*, *gauche* and *gauche-bar* conformations in favorable agreement with NMR data and RIS calculations. Also, Ramachandran plots for successive torsion angles along the chain backbone (Figures 3.5(b,c,d) and 3.6(b,c,d)) exhibit symmetric *tg* and *gt* peaks and extremely low percentages of $t\bar{g}$ and $\bar{g}t$ sequences. Torsion angle distributions constitute a stringent test for reverse-mapped structures, in which our reverse-mapping scheme fully succeeds.

The ultimate goal of our work, i.e. the study of PS-C_{60} dynamics at the segmental and local levels, is accomplished via analyzing long MD trajectories of our well-equilibrated reverse-mapped structures. Our simulation results generally indicate that the addition of C_{60} to PS leads to slower segmental dynamics (as estimated by characteristic times extracted from the decay of orientational time-autocorrelation functions of suitably chosen vectors). The characteristic times found by fitting the $P_1(t)$ function of the orientation of the center of mass of the phenyl rings with respect to the chain backbone suggest an increase of the bulk T_{g} of around 1 K, upon the addition of C_{60}s at a concentration of 1% by weight (Figure 3.8). This observation is in favorable agreement with DS measurements of Kropka et al.[148] who reported a T_{g} shift of 1 K. The same conclusion can be reached by studying the $P_2(t)$ function of the orientation of C-H bonds. Despite the fact that we employ a united-atom model for our MD simulations, the introduction of hydrogen atoms at a post-processing step yields reasonable dynamics for C-H bonds in good agreement with spin-lattice relaxation and solid echo NMR measurements on molten polystyrene (Figure 3.9). Again, nanocomposite systems are found to exhibit slightly slower dynamics compared to their neat polymer counterparts.

We then employ a space discretization in order to study the effect of C_{60}s on segmental dynamics at a local level. Each fullerene serves as the center of a Voronoi cell, whose volume is determined by the neighboring fullerenes. Backbone carbons lying in every cell are tracked throughout the MD trajectory and their mean-square displacement is measured for the time they reside in the same cell. Overall mean-square displacement of backbone atoms is found to be smaller in the presence of fullerenes, than in bulk PS (Figure 3.12). However, atoms moving in smaller (more confined) Voronoi cells exhibit faster motion than the atoms moving inside larger Voronoi cells. This can be correlated with the increased rotational diffusion of fullerenes, as the volume of the Voronoi cell becomes smaller. These observations drive us to envision fullerenes as nanoscopic millstones, inducing shearing stresses on their environment and thus forcing the polymeric chains to move. The dynamic heterogeneity caused by the addition of fullerenes exhibits strong temperature dependence, getting larger as the temperature is lowered.

Finally, we study the atomic-level and local stresses which are present in our systems. Each united atom is characterized by a distribution of atomic stresses whose shape and position reflect its chemical nature, connectivity, and geometric disposition within the system. The addition of fullerenes causes an imperceptible broadening of the atomic-level stress distributions, implying a slightly higher stress heterogeneity for the composite material. This observation is further elaborated by the estimation of local stresses, at the level of Voronoi cells around individual fullerenes, into which the system has been partitioned. Dispersed fullerenes are characterized by large shear stresses, probably due to their intramolecular forcefield which reflects their rigidity. The local von Mises shear stress of the polymer has been found to scale as the inverse square root of the volume of the material used for the calculation, as expected from fluctuation theory. Local von Mises stresses are very similar between the neat polymer and the nanocomposite, being slightly higher in the latter. They are also rather insensitive to temperature.

Our analysis of polymer atom mean square displacement and fullerene rotational motion implies that fullerenes greatly amplify the dynamic heterogeneity of the molten atactic PS, at the same time slowing down its overall dynamics slightly. Further work is required to establish the effect of the addition of nanoparticles on terminal relaxation and viscosity.

4 Structure of Polymer Layers Grafted to Spherical Nanoparticles

The structural features of polystyrene brushes grafted on spherical silica nanoparticles immersed in polystyrene are investigated by means of a Monte Carlo (MC) methodology based on polymer mean field theory. The nanoparticle radii (either 8 nm or 13 nm) are held constant, while the grafting density and the lengths of grafted and matrix chains are varied systematically in a series of simulations. The primary objective of this work is to simulate realistic nanocomposite systems of specific chemistry at experimentally accessible length scales and study the structure and scaling of the grafted brush. The profiles of polymer density around the particles are examined; based on them, the brush thickness of grafted chains is estimated and its scaling behavior is compared against theoretical models and experimental findings. Then, neutron scattering spectra are predicted both from single grafted chains and from the entire grafted corona. It is found that increasing both the grafting density and the grafted chain molar mass drastically alters the brush dimensions, affecting the wetting behavior of the polymeric brush. On the contrary, especially for particles dispersed in high molecular weight matrix, variation of the matrix chain length causes an almost imperceptible change of the density around the particle surface.

4.1 Introduction

Considerable research effort has been devoted recently to studying the structure of systems of polymers end-grafted onto spherical nanoparticles. The properties of end - constrained chains strongly differ, at high grafting densities, from those of free chains. Tethering forces chains to depart from their free-chain, random-walk isotropic configuration, causing them to stretch in the direction perpendicular to the interface and to form a brushlike structure. Polymer brushes find widespread industrial application as nanoparticle stabilizers. Recent experimental studies have shown that,[53,228] most often, nanoparticles tend to aggregate into clusters or to form phase separated domains; consequently the property improvements which might arise due to their nanoscale dimensions vanish. The ability to disperse nanoparticles grafted with polymer brushes in a polymer matrix is of tremendous importance for producing polymer nanocomposites with desired mechanical and rheological properties. When the coverage is high enough, the nanoparticles are sterically stabilized, which results in good spatial dispersion.[228,229] Moreover, spherical nanoparticles uniformly grafted with macromolecules robustly self-assemble into a variety of anisotropic superstructures when they are dispersed in the corresponding homopolymer matrix.[230]

4.1.1 Scaling of Planar Polymer Brushes

A simpler system that is useful for understanding polymer brushes grafted on spherical nanoparticles immersed in melts is that of a brush grafted to a planar surface in contact with a melt of chemically identical chains. Important molecular parameters for this system are the Kuhn segment length of the chains, b_{K}, the lengths (in Kuhn segments) of the grafted, N_{g}, and free, N_{f}, chains, and the surface grafting density (chains per unit area), σ_{g}. The case of planar polymer brushes exposed to low molecular weight solvent was studied theoretically by de Gennes[231] and Alexander.[232] These authors used a scaling approach in which a constant density was assumed throughout the brush: all the brush chains were assumed to be equally stretched to a distance from the substrate equal to the thickness of the brush. Aubouy et al.[233] extracted the phase diagram of a planar brush exposed to a high molecular weight chemically identical matrix. Their scaling analysis is based on the assumption of a steplike concentration profile and on imposing the condition that all chain ends lie at the same distance from the planar surface. Five regions with different scaling laws for the height, h, of the brush were identified. For low enough grafting densities, $\sigma_{\mathrm{g}} < N_{\mathrm{g}}^{-1} b_{\mathrm{K}}^{-2}$ and short free chains, $N_{\mathrm{f}} < N_{\mathrm{g}}^{1/2}$, the brush behaves as a swollen mushroom, with $h \sim N_{\mathrm{g}}^{3/5}$. By keeping the grafting density below $N_{\mathrm{g}}^{-1} b_{\mathrm{K}}^{-2}$ and increasing N_{f}, so that $N_{\mathrm{f}} > N_{\mathrm{g}}^{1/2}$, the brush becomes ideal with $h \sim N_{\mathrm{g}}^{1/2}$. For intermediate grafting densities, $N_{\mathrm{g}}^{-1} < \sigma_{\mathrm{g}} b_{\mathrm{K}}^{2} < N_{\mathrm{g}}^{-1/2}$, high molecular weight free chains, $N_{\mathrm{f}} > N_{\mathrm{g}}^{1/2}$, can penetrate the brush, thus ideally wetting it and leading to $h \sim N_{\mathrm{g}}^{1/2}$. Increasing the grafting density while keeping $N_{\mathrm{f}} < N_{\mathrm{g}}^{1/2}$ forces the chains to stretch, thus leading to a brush height scaling as $h \sim N_{\mathrm{g}}$.

A numerical Self Consistent Field (SCF) calculation has been reported by Cosgrove et al.,[234] in which the density profile is no longer assumed to be a step profile and where the end points of the chains are distributed throughout the brush. Analytical equations based on a similar model were developed by Milner et al.[235] and by Zhulina et al.[236] In the wetting state, the grafted and free chains are intermixed, along the full extent of the brush. If the matrix and the grafted chains demix, then the corona collapses and the brush is dewetted. A detailed study of moderately stretched planar brushes exposed to moderately long melt chains by Ferreira et al.[237] found that the domain where attraction exists between two grafted layers in a melt, and where partial wetting is thus expected, scales as $\sigma_{\mathrm{g}}\sqrt{N_{\mathrm{g}}} > (N_{\mathrm{g}}/N_{\mathrm{f}})^2$. This scaling law indicates that flat surfaces grafted with sparse polymer brushes in a long chain polymer melt could exhibit entropic attraction, provided that the molecular weight of the matrix is large enough. Experimental,[238] SCF[237] and Molecular Dynamics (MD)[239] works on planar polymer brushes, in a chemically identical matrix, have shown that the matrix wets the polymer brush only when the melt chains are shorter than the chains of the brush. It is experimentally observed[240] that "autophobic dewetting"[241] occurs when the brush and the matrix share the same length. Longer melt chains spontaneously dewet the brush, because the gain in mixing entropy cannot overcome the conformational entropy loss associated with the matrix chains penetrating the brush.[229]

4.1.2 Scaling of Polymer Brushes in Convex Geometries

Similar ideas[242] can be used to understand the configurations of polymer brushes grafted to spherical nanoparticles dispersed in a polymer melt. Here the radius of the nanoparticle, a_{p}, enters as an additional parameter. Long polymers grafted to a surface at fixed grafting density, σ, are strongly perturbed from their ideal random-walk conformation.[243] Planar geometry scaling (infinite radius of curvature) is inadequate to explain the case when the particle size is reduced to a level comparable with the size of the brushes. The SCF theory has been applied to convex (cylindrical and spherical) surfaces by Ball et al.[243] For the cylindrical case, under melt conditions, it was found that the free ends of grafted chains are excluded from a zone near the grafting surface. The thickness of this dead zone varies between zero for a flat surface to a finite fraction of the brush height, h, in the limit of strong curvature, when α_{p}/h is of order unity, with α_{p} being the radius of curvature of the surface. Borukhov and Leibler[244] presented a phase diagram for brushes grafted to spherical particles, in which the five regions of the work of Aubouy et al.[233] can still be located, but they also provide the scaling of the exclusion zone, where matrix chains are not present. Such exclusion zones have been observed in a special limiting case of grafted polymers, namely, star shaped polymers. Daoud and Cotton[245] showed that, in the poor-solvent limit, the free ends of the chains are pushed outward, because of high densities near the center of the star. The Daoud-Cotton model assumes that all chain ends are a uniform distance away, while the Wijmans-Zhulina model[242] has a well-defined exclusion zone. For Θ solvents, in the limit of large curvature (small particle radius, α_{p}), the segment density profile, $\phi(r)$, decreases with the radius as[242] $\phi(r) \propto \sigma_{\mathrm{g}}^{1/2}\,(\alpha_{\mathrm{p}}/r)$. It must be noted that

ϕ is not linear in σ_g because the brush height depends on σ_g. In the limit of small curvature (large R_n), a distribution of chain ends must be accounted for,[235] leading the segment density profile to a parabolic form:[242] $\phi(r') = (3\sigma_\mathrm{g} N_\mathrm{g} b_\mathrm{K}^3/h_0)\,(h/h_0)^2\,(1-(r'/h))^2$ where b_K is the statistical segment length, $r' = r - R_n$ is the radial distance from the particle surface, h_0 is the effective brush height for a flat surface and h is the brush thickness. For large nanoparticles, the above form asymptotically recovers the planar result ($h \to h_0$). In the case of intermediate particle radii, a combination of large and small curvature behaviors is anticipated:[242] the segment density profile exhibits large curvature behavior near the surface of the particle, followed by a small curvature behavior away from it. Finally, following Daoud and Cotton, the brush height is expected to scale as $h \propto \sigma_\mathrm{g}^{1/4} N_\mathrm{g}^{1/2}$.

4.1.3 Previous Work

Hasegawa et al.[229] used rheological measurements and SCF calculations to show that particles are dispersed optimally when chains from the melt interpenetrate, or wet, a grafted polymer brush (“complete wetting”). This occurs at a critical grafting density, which coincides with the formation of a stretched polymer brush on the particle surface.[231,232] Grafting just below this critical density produces aggregates of particles due to attractive van der Waals forces between them. The results of these authors suggest that mushrooms of nonoverlapping grafted polymer chains have no ability to stabilize the particles against aggregation (“allophobic dewetting”). Grafting just above this critical density also results in suboptimal dispersions, the aggregation of the particles now being induced by an attraction between the grafted brushes. For high curvature (small radius) nanoparticles, the polymer brush chains can explore more space, resulting in less entropic loss to penetrate the brush, reducing the tendency for autophobic dewetting.

Detailed MD simulations by Peters et al.[246] have been used to study the effect of passivating ligands of varying molar mass grafted to a 5-nm-diameter amorphous silica nanoparticle and placed in various alkane solvents. Their study focused on the average height and density profiles for methyl-terminated alkoxysilane ligands exposed to either explicitly modeled, short-chain hydrocarbon solvents or implicit good and poor solvents. Coating brushes equilibrated in explicit solvents were more compact in longer-chain solvents because of autophobic dewetting. The response of coatings in branched solvent was not significantly different from that in the linear solvent of equal mass. Significant interpenetration of the solvent chains with the brush coating was observed only for the shortest grafted chains. An implicit poor solvent captured the effect of the longest chain length solvent at lower temperatures, while an implicit good solvent produced coating structures that were far more extended than those found in any of the explicit solvents tested and showed little dependence on temperature.

A major challenge in simulating nanocomposite materials with chemically realistic models is that both the length and the time scales cannot be adequately treated by means of atomistic simulations because of their extensive computational requirements. This is why a variety of mesoscopic techniques have been developed for these particular systems. Kalb et al.[247] and later Meng et al.[248] have performed MD simulations where both brush and melt chains were represented using the coarse-grained bead-spring model of Kremer and Grest.[249] One of their conclusions was that the conformational transition between a stretched "wet" brush and a collapsed "dry" brush, which has been attributed to the autophobic dewetting of the brush by the melt, was not readily apparent in their brush density profiles. The calculated Potential of Mean Force (PMF) was found to go from purely repulsive to attractive by increasing the molar mass of the matrix with a well depth on the order of $k_\mathrm{B}T$. These results were purely entropic in origin and arose from the competition between brush-brush repulsion and an attractive inter-nanoparticle interaction caused by matrix depletion from the inter-nanoparticle zone. Integral equation approaches, such as the Polymer Reference Interaction Site Model (PRISM), have provided important insight and detailed information about inter-particle potentials and spatial correlations between the locations of the particles. As Schweizer and co-workers have shown,[15,250] there is a competition between tether-mediated microphase separation and matrix-induced macrophase separation for nanoparticles dispersed in a polymeric matrix.

Significant progress has been made in applying the SCF theory to nanoparticle-filled polymer matrices in the dilute and semi-dilute region.[251–254] An attempt to overcome the restrictions posed by the saddle-point approximation was made by Sides et al.[255] The coordinates of all particles in the system were explicitly retained as degrees of freedom. It was crucial to update simultaneously the coordinates and the chemical potential field variables. Laradji et al.[35] introduced the idea of evolving the explicit conformations of the molecules by standard Metropolis MC, while obeying an Edwards mean-field Hamiltonian. The paper of Laradji et al. was pioneering in introducing the concept of conducting particle-based simulations with interactions described via collective variables and also two ways of calculating these collective variables: grid-based and continuum weighting-function-based. A clearer discussion of this point is found in studies of brushes in poor solvent by Soga et al.[256] Later, Daoulas and Müller[36] and Detcheverry et al.[37] have extensively used this methodology to study a wide range of polymeric systems. This technique has been very successful in describing the self-assembly and the ordering of block copolymers on patterned substrates encountered in processes such as nanolithography.[257] Harton and Kumar[52] have developed a Flory theory, coupled with the SCF model of Scheutjens and Fleer, to probe the miscibility of homopolymer-grafted nanoparticles with homopolymer matrices. Their main conclusions were that miscibility is improved with decreasing particle radius and increasing brush chain length. They have also found that greater swelling of the brush by matrix chains is required for dispersion of larger brush-coated nanoparticles.

Striolo and Egorov[258] have employed both MC simulations and Density Functional Theory (DFT) calculations to investigate the interactions between spherical colloidal brushes both in vacuum (implicit solvent) and in explicit solutions of nonadsorbing polymers. These authors found that interactions between hard sphere particles grafted with hard-sphere chains are always repulsive in implicit solvent. The range and steepness of the repulsive interaction is sensitive to the grafting density and length of the grafted chains. When the brushes are immersed in an explicit solvent of hard-sphere chains, a weak mid-range attraction arises, provided the length of the free chains exceeds that of the grafted chains. This attraction may be due the depletion of free chains from the region between the brushes. A comparison between the two methods indicated that DFT is in semiquantitative agreement with MC results, but required a small fraction of the computer time needed by MC.

4.1.4 Experimental Findings

Until recently, the experimental verification of theoretical and simulation predictions was mostly limited to global information concerning the brush, such as its average height, but not its profile.[259] Recently Chevigny et al.[260] used a combination of X-ray and Small Angle Neutron Scattering (SANS) techniques to measure the conformation of chains in polystyrene polymer brushes grafted to silica nanoparticles with an average radius of $13\,\mathrm{nm}$ dispersed in polystyrene matrix. They found that, if the molecular weight of the melt chains becomes large enough, the polymer brushes are compressed by a factor of two in thickness compared to their stretched conformation in solution. Also, polymer brushes exposed to a high molecular weight matrix are slightly compressed in comparison to brushes exposed to a low molecular weight matrix environment. This observation implies a wet to dry conformational transition. The low molar mass free chains can penetrate into the grafted brush and swell it ("wet" brush). Conversely, when grafted and free chain molar masses are comparable, free entities are expelled from the corona ("dry" brush). Later, they examined the dispersion of these grafted particles in melts of different molar masses, M_f.[261] They showed that for $M_\mathrm{g}/M_\mathrm{f} < 0.24$, the nanoparticles formed a series of compact aggregates, whereas for $M_\mathrm{g}/M_\mathrm{f} > 0.24$, the nanoparticles were dispersed within the polymer host.

4.1.5 Proposed Approach

The present work examines the structure of atactic polystyrene brushes grafted on silica nanoparticles, dispersed at the limit of infinite dilution,in polymer matrices of the same chemical constitution (atactic polystyrene). Particular attention is given to capturing the chain conformation of both matrix and grafted chains. The analysis is based on a coarse-grained MC simulation method which has already been applied to a complex three-dimensional polymer-polymer nanocomposite system.[176] Although the level of description is coarse-grained (e.g., employing freely-jointed chains to represent the matrix), the approach developed aims at predicting the behavior of a nanocomposite with specific chemistry quantitatively, in contrast to previous coarse-grained simulations. A main characteristic of the method is that it treats polymer-polymer and polymer-particle interactions in a different manner: the former are accounted for through a suitable functional of the local polymer density, while the latter are described directly by an explicit interaction potential. The term “Field Theory-inspired Monte Carlo simulations” accounts for this fact.[262] The basic idea of FTiMC simulations is to use “soft” potentials based on mean-field considerations that allow particle overlapping in continuum MC simulations. For multichain systems, this gives much faster chain relaxation and better sampling of the configurational space than conventional molecular simulations using “hard” excluded-volume interactions that prevent particle overlapping. The main advantage of this approach over SCF is that can directly sample polymer chain conformations, which is a formidable task for pure SCF calculations. Our efforts will focus on the wetting/dewetting transition of the grafted polymer brush, which is of great importance, since it is directly related to the phase separation/miscibility of the nanocomposite systems. Moreover, neutron scattering from these systems will be predicted from a discrete Fourier transform of the real space coordinates of the whole system. To the best of our knowledge, this is the first time an analysis of this kind is undertaken for realistic nanocomposite systems matching experimentally studied ones.

4.2 Model and Simulation Methodology

4.2.1 Model

We provide here some details on the FTiMC model, which was introduced in ref 176. The configurational partition function on which the MC sampling is based, $\mathcal{Z}_{\mathrm{FTiMC}}$, is expressed as a functional integral over the paths of all chains and as an integral over all nanoparticle positions and orientations:

$$
\begin{aligned}
\mathcal{Z}_{\mathrm{FTiMC}} = \frac{1}{n_{\mathrm{f}}!} \int & \prod_{i=1}^{n_{\mathrm{f}}} \mathcal{D}\mathbf{r}_i(\bullet)\mathcal{P}_0\left[\mathbf{r}_i(s)\right] \prod_{k=1}^{n_{\mathrm{p}}} \mathrm{d}^3\mathbf{r}_{\mathrm{cm},k}\mathrm{d}^2\boldsymbol{\Omega}_k \\
& \prod_{j_k=1}^{n_{g_k}} \mathcal{D}\mathbf{r}_{j_k}(\bullet)\mathcal{P}_0\left[\mathbf{r}_{j_k}(\bullet);\mathbf{r}_{\mathrm{cm},k},\boldsymbol{\Omega}_k\right] \\
& \times \exp\left(-\frac{\mathcal{H}_{\mathrm{p}}\left[\left\{\mathbf{r}_{\mathrm{cm},k}\right\},\left\{\mathbf{r}_i(\bullet)\right\},\left\{\mathbf{r}_{j_k}(\bullet)\right\}\right] + \mathcal{H}_{\mathrm{nb}}\left[\rho\left(\mathbf{r}\right)\right]}{k_{\mathrm{B}}T}\right)
\end{aligned}
\tag{4.1}
$$

For spherical nanoparticles, orientations play a role only when grafted chains are present. Here n_{p} is the total number of nanoparticles, n_{f} is the total number of free chains and $n_{\mathrm{g},k}$ is the number of chains grafted to nanoparticle k. $\mathbf{r}_{\mathrm{cm},k}$ and $\boldsymbol{\Omega}_k$ stand for the center of mass position and orientation (Euler angles) of nanoparticle k, respectively. Each one of the $n_{\mathrm{g},k}$ chains that are grafted to nanoparticle k is rigidly affixed to its surface by one of its ends. $\mathcal{D}\mathbf{r}_i\left(\bullet\right)$ denotes functional integration over all possible conformations ("paths") of chain i. The statistical weights $\mathcal{P}_0\left[\mathbf{r}_i(\bullet)\right]$ and $\mathcal{P}_0\left[\mathbf{r}_{j_k}(\bullet);{}_{\mathrm{cm},k},\boldsymbol{\Omega}_k\right]$ incorporate bonded interactions along each one of the chains; in the implementation employed here, they correspond to freely jointed chains.

4.2.1/i Polymer non bonded interactions

The effective Hamiltonian $\mathcal{H}_{\mathrm{nb}}\left[\rho\left(\mathbf{r}\right)\right]$ represents nonbonded interactions among chains, either free or grafted. An approximation based on the mean-field averaging out of small scale fluctuations is applied to this latter contribution. Instead of expressing the nonbonded interaction energy as a sum of pairwise interactions between segments, as is done in atomistic and coarse-grained simulations, we assume that it is as a functional of the three-dimensional density distribution of polymer segments, $\rho\left(\mathbf{r}\right)$. The density distribution is calculated by partitioning the system into cells using a cubic grid of spacing ΔL. We then assign each polymer segment to the center of the cell to which it belongs. The contribution from terminal segments is assumed to be half that of the interior segments in this assignment. The volume of each cell is taken as $\left(\Delta L\right)^3$ minus the volume of any sections of nanoparticles that find themselves in the cell; it is computed via a fast analytic algorithm.[263] Following early work by Helfand and Tagami,[264] a functional of local density is derived heuristically, guided by the macroscopic thermodynamic behavior of the system. The nonbonded effective Hamiltonian, punishes departures of the local density in each cell from the mean segment density ρ_0 in the melt under the temperature and pressure conditions of interest:

$$\mathcal{H}_{\text{nb}}\left[\widehat{\rho}\left(\mathbf{r}\right)\right] = \frac{\kappa_0\left(\Delta L\right)^3}{2\rho_0}\sum_{m=1}^{N_{\text{cells}}}\left(\widehat{\rho}_m - \rho_0\right)^2 \tag{4.2}$$

The prefactor κ_0 is related to the isothermal compressibility κ_{T} of the melt via

$$\kappa_0 = \frac{1}{k_{\text{B}}T\kappa_{\text{T}}\rho_0} \quad . \tag{4.3}$$

4.2.1/ii Nanoparticle - polymer and nanoparticle-nanoparticle interactions

The effective Hamiltonian $\mathcal{H}_{\text{p}}\left[\left\{\mathbf{r}_{\text{cm},k}\right\},\left\{\mathbf{r}_i(s)\right\},\left\{\mathbf{r}_{j_k}(s)\right\}\right]$ encompasses, in general, nanoparticle - nanoparticle and polymer - nanoparticle interactions:

$$\begin{aligned}\mathcal{H}_{\text{p}}\left[\left\{\mathbf{r}_{\text{cm},k}\right\},\left\{\mathbf{r}_i(s)\right\},\left\{\mathbf{r}_{j_k}(s)\right\}\right] = \sum_{k=1}^{n_{\text{p}}}&\left\{\sum_{i=1}^{n_{\text{f}}}\sum_{s=0}^{N_{\text{f}}}\mathcal{V}_{\text{ps}}\left(\mathbf{r}_i(s) - \mathbf{r}_{\text{cm},k}\right)\right.\\ &\left.+\sum_{l=1}^{n_{\text{p}}}\sum_{j_l=1}^{n_{\text{g}_l}}\sum_{s=0}^{N_{\text{g}}}\mathcal{V}_{\text{ps}}\left(\mathbf{r}_{j_l}(s) - \mathbf{r}_{\text{cm},k}\right)\right\}\\ &+\sum_{k=1}^{n_{\text{p}}-1}\sum_{l=k}^{n_{\text{p}}}\mathcal{V}_{\text{pp}}\left(\mathbf{r}_{\text{cm},l} - \mathbf{r}_{\text{cm},k}\right)\end{aligned} \tag{4.4}$$

where $\mathcal{V}_{\text{ps}}$ stands for the nanoparticle - polymer and $\mathcal{V}_{\text{pp}}$ for the nanoparticle - nanoparticle interaction potentials. The summation of the former, $\mathcal{V}_{\text{ps}}$, extends over all free and grafted segments of the system, excluding only the interaction between the segments which are directly connected to a particle and the particle itself. The latter one is summed over all pairs of nanoparticles. They are calculated from the center of mass positions and radii of the nanoparticles and polymer segments and from the densities of the atoms constituting each nanoparticle and each polymer segment, as a sum of Hamaker integrated potentials.

The interaction of a polymeric segment and a nanoparticle can be calculated using eqs 11-13 of ref 176, with suitable Hamaker constants for the polymer and the particle. The polymer - nanoparticle interaction term, $\mathcal{V}_{\text{ps}}\left(\mathbf{r}_i\left(s\right) - \mathbf{r}_{\text{cm},k}\right)$, can be split into an attractive and repulsive term as:

$$\mathcal{V}_{\text{ps}}\left(\mathbf{r}_i\left(s\right) - \mathbf{r}_{\text{cm},k}\right) = \mathcal{V}_{\text{rep}}\left(r_{\text{ps}}\right) - \mathcal{V}_{\text{att}}\left(r_{\text{ps}}\right) \tag{4.5}$$

where we introduce $r_{\text{ps}} = \left\|\mathbf{r}_i\left(s\right) - \mathbf{r}_{\text{cm},k}\right\|$ as the distance between the center of mass of the k-th nanoparticle, $\mathbf{r}_{\text{cm},k}$, and the s-th segment of the i-th chain, $\mathbf{r}_i\left(s\right)$. The attractive term, following a Hamaker type integration (e.g. assuming uniform density of interaction sites), is given as:[265]

$$\mathcal{V}_{\text{ps,att}}\left(r_{\text{ps}}\right) = \frac{\mathscr{A}^{\text{eff}}_{\text{PS-SiO}_2}}{6}\left[\frac{2\alpha_{\text{p}}\alpha_{\text{s}}}{r_{\text{ps}}^2 - \left(\alpha_{\text{p}} + \alpha_{\text{s}}\right)^2} + \frac{2\alpha_{\text{p}}\alpha_{\text{s}}}{r_{\text{ps}}^2 - \left(\alpha_{\text{p}} - \alpha_{\text{s}}\right)^2} \right.$$
$$\left. + \ln\left(\frac{r_{\text{ps}}^2 - \left(\alpha_{\text{p}} + \alpha_{\text{s}}\right)^2}{r_{\text{ps}}^2 - \left(\alpha_{\text{p}} - \alpha_{\text{s}}\right)^2}\right)\right] \tag{4.6}$$

The repulsive term is given as:[265]

$$\mathcal{V}_{\text{ps,rep}}(r_{\text{ps}}) = \frac{\mathscr{A}^{\text{eff}}_{\text{PS-SiO}_2}\sigma^6_{\text{eff}}}{37800 r_{\text{ps}}}\left[\frac{r_{\text{ps}}^2 - 7r_{\text{ps}}\left(\alpha_{\text{p}} + \alpha_{\text{s}}\right) + 6\left(\alpha_{\text{p}}^2 + 7\alpha_{\text{p}}\alpha_{\text{s}} + \alpha_{\text{s}}^2\right)}{\left(r_{\text{ps}} - \alpha_{\text{p}} - \alpha_{\text{s}}\right)^7}\right.$$
$$+ \frac{r_{\text{ps}}^2 + 7r_{\text{ps}}\left(\alpha_{\text{p}} + \alpha_{\text{s}}\right) + 6\left(\alpha_{\text{p}}^2 + 7\alpha_{\text{p}}\alpha_{\text{s}} + \alpha_{\text{s}}^2\right)}{\left(r_{\text{ps}} + \alpha_{\text{p}} + \alpha_{\text{s}}\right)^7}$$
$$- \frac{r_{\text{ps}}^2 + 7r_{\text{ps}}\left(\alpha_{\text{p}} - \alpha_{\text{s}}\right) + 6\left(\alpha_{\text{p}}^2 - 7\alpha_{\text{p}}\alpha_{\text{s}} + \alpha_{\text{s}}^2\right)}{\left(r_{\text{ps}} + \alpha_{\text{p}} - \alpha_{\text{s}}\right)^7}$$
$$\left. - \frac{r_{\text{ps}}^2 - 7r_{\text{ps}}\left(\alpha_{\text{p}} + \alpha_{\text{s}}\right) + 6\left(\alpha_{\text{p}}^2 - 7\alpha_{\text{p}}\alpha_{\text{s}} + \alpha_{\text{s}}^2\right)}{\left(r_{\text{ps}} - \alpha_{\text{p}} + \alpha_{\text{s}}\right)^7}\right] \tag{4.7}$$

where α_{p} corresponds to the radius of the particle and α_{s} corresponds to an effective radius of the polymeric segment.[176] The effective radius of the sphere representing a polymeric segment, α_{s}, is chosen such that $(4/3)\pi\alpha_{\text{s}}^3$ equals the volume per Kuhn segment in the bulk polymer, as calculated from the mass corresponding to a Kuhn segment and the experimental mass density ($\alpha_{\text{s}} \simeq 0.67$ nm for polystyrene (PS)). The closest distance of approach is equal or greater than the radius that is used for the estimation of the Hamaker interaction between the nanoparticle and the Kuhn segment. The magnitude of the interactions is determined by the Hamaker constant $\mathscr{A}^{\text{eff}}_{\text{PS-SiO}_2}$, which governs the effective interaction between a polymeric segment and a nanoparticle. We describe below how this parameter can be evaluated. The same expressions can be used for the interaction between two nanoparticles. In this case, the Hamaker constant to be used is $A^{\text{eff}}_{\text{SiO}_2}$.

4.2.1/iii Hamaker constants estimation

The Hamaker constant governing the interaction between two spherical bodies can be calculated as:[265]

$$\mathscr{A} = 4\pi^2\epsilon_{\text{LJ}}\left(\rho_{\text{LJ}}\sigma_{\text{LJ}}^3\right)^2 \tag{4.8}$$

where ϵ_{LJ}, σ_{LJ} are the atomistic Lennard-Jones interaction parameters, and ρ_{LJ} the density of atomistic interaction sites in the macroscopic body. The silica particle contributes only the interaction of its oxygens with the polymeric matrix (ϵ_{O},σ_{O} for silica[266]), while atomistic Lennard-Jones parameters for CH(aromatic), $\mathrm{CH_2}$(aliphatic) and $\mathrm{CH_3}$(aliphatic) sites of PS are used.[32] For every kind of interaction site of PS, the corresponding Hamaker constant is calculated by assuming ρ_{LJ} to be the density of the corresponding kind of sites in the bulk polymer. Electrostatic interactions are not taken into account either for silica or for polystyrene. Hamaker constants, obtained here by integration of the Lennard-Jones potentials used in atomistic simulations of the system, are within experimental range for polystyrene[267,268] and silica.[269] The corresponding values are provided in the "Simulation Details" subsection.

The repulsive term includes an effective collision diameter, σ_{eff}, which can be calculated as $\sigma_{\mathrm{eff}} = \left(\bar{\sigma_{\mathrm{p}}} + \bar{\sigma_{\mathrm{s}}}\right)/2$ with $\bar{\sigma_{\mathrm{p}}}$ and $\bar{\sigma_{\mathrm{s}}}$ being the weighted arithmetic mean of σ parameters of nanoparticle and polymeric segment interaction sites, respectively. The weights correspond to the number of sites of each kind contributing to the coarse-grained site. For the silica particle $\sigma_{\mathrm{p}} = 0.3$ nm and for polystyrene $\bar{\sigma_{\mathrm{s}}} = 0.371$ nm.

The reference level of the employed Hamiltonian (eq 4.2) for the homopolymer melt is that of a melt with uniform density profile. In this case, the effective interaction energy between two polymeric beads is taken as zero. The effective Hamaker constant of polymer-nanoparticle interaction should be such that, if the volume of the nanoparticle were occupied by bulk homopolymer, then the energy of the system would be zero. The insertion of a nanoparticle in a uniformly-distributed melt can be thermodynamically accomplished in two steps: a spherical volume of polymer, whose net interaction with the rest of the polymer matrix depends on $\mathscr{A}_{\mathrm{PS}}$, is removed from the melt and a nanoparticle with equal volume is placed in its position, introducing a new net interaction depending on $\sqrt{\mathscr{A}_{\mathrm{PS}}\,\mathscr{A}_{\mathrm{SiO_2}}}$ with the remaining bulk polymer.[270] Thus, the Hamaker constant of the effective interaction can be calculated as:

$$\mathscr{A}^{\mathrm{eff}}_{\mathrm{PS\text{-}SiO_2}} = \sqrt{\mathscr{A}_{\mathrm{PS}}\,\mathscr{A}_{\mathrm{SiO_2}}} - \mathscr{A}_{\mathrm{PS}}\ , \tag{4.9}$$

and used for the nanoparticle - polymeric segment interaction, $\mathcal{V}_{\mathrm{ps}}$, following the expressions presented above. The corresponding Hamaker constant of the effective interaction between two nanoparticles can be obtained as:

$$\mathscr{A}^{\mathrm{eff}}_{\mathrm{SiO_2\text{-}SiO_2}} = \mathscr{A}_{\mathrm{SiO_2}} + \mathscr{A}_{\mathrm{PS}} - 2\sqrt{\mathscr{A}_{\mathrm{SiO_2}}\,\mathscr{A}_{\mathrm{PS}}} \tag{4.10}$$

4.2.2 Initial Configuration

To start the FTiMC simulation, an initial configuration is generated by placing the nanoparticles at randomly selected positions, so that they do not overlap, and then building the polymeric chains around them. The first chains to be built are the grafted ones. Initially, the grafting points are randomly selected on the surface of the particle. Then, these points are allowed to move freely on the surface of the particle (via a MD-like procedure), under the influence of a repulsive pseudo-potential between them. This step is undertaken in order to mimic the more or less uniform distribution of initiators and linkers connecting grafted chains to the nanoparticle surface, observed experimentally. Both grafted and free chains are grown as random walks in a segment-by-segment fashion. When the addition of a segment fails (due to the constrained environment imposed by the particle), a geometric algorithm is used in order to drive the insertion of the segment towards higher free-volume regions. The initial configurations created by this method exhibit large local density fluctuations. These fluctuations increase with increasing chain length. A zero temperature MC optimization procedure takes place in order to reduce the density fluctuations. During this stage, all moves leading to a more uniform density profile, thus decreasing the density fluctuations, are accepted. In the opposite case, they are rejected.[173]

4.2.3 Equilibration

Equilibration during a FTiMC run is achieved through MC based on the probability density associated with the partition function $\mathcal{Z}_{\text{FTiMC}}$. The fact that chain-chain interactions are accounted for only approximately through $\mathcal{H}_{\text{nb}}$, allows bold rearrangements of the chain conformations to be attempted with significant probability of success. Rigid displacements and rotations of the chains, mirroring transformations through planes passing through the chain centers of mass, and exchanges of entire chains keeping their center of mass positions fixed, are used.[173] In addition, the internal conformations of chains are sampled using flips of internal segments,[176] end segment rotations,[176] reptation[271] and pivot[272] moves. Grafted chains equilibrate only through flip, end rotation and pivot moves, which keep their grafted end constrained. An additional MC move entails attempting random translations of the origin of the grid used for the estimation of local densities, within a cube of edge length ΔL. Following each such translation the energy of the system is recalculated and the move is accepted or rejected according to the standard Metropolis selection criterion. This grid translation move has been included in order to avoid artifacts due to spatial discretization.

In order to equilibrate the structure of the polymeric matrix, a mixture of MC moves is

Table 4.1: Mixture of moves and their acceptance rates for a system consisting of an 8-nm-radius SiO_2 particle grafted with 20 kg/mol grafted PS chains ($\sigma_g = 0.7$ nm^{-2}) dispersed in 100kg/mol PS matrix.

Moves	Mix of moves (%)	Acceptance rate (%)
Free chains		
Translation	8.9	0.048
Rotation	4.4	$\sim 10^{-3}$
Reflection	4.4	$\sim 10^{-3}$
Inversion	4.4	$\sim 10^{-3}$
Exchange	4.4	$\sim 10^{-3}$
Flip	9.0	38.72
End rotation	4.4	30.09
Reptation	13.3	19.52
Pivot	35.6	1.083
Grafted chains		
Flip	2.2	31.26
End rotation	1.0	27.14
Pivot	8.0	4.929
Grid		
Translation	10^{-4}	$\sim 10^{-2}$

utilized. Five moves are employed which treat the entire chains as rigid bodies: translation of individual chains in random direction, rotation of individual chains by random angles around random axes through their centers of mass, reflection of individual chains at random mirror planes going through the center of mass, inversion of individual chains at their centers of mass and exchange of two chains preserving the center of mass positions. Furthermore, the internal shape of the chains is restructured by four intramolecular moves: the flip, the end rotation, the reptation and the pivot move.[176] The exact mixture of moves used for the equilibration of a system consisting of a densely grafted particle is presented in Table 4.1. Moreover, the equilibrium acceptance rate of each move is included in the table.

4.2.4 Simulation Details

The systems considered were dilute dispersions of silica nanoparticles with atactic PS chains grafted on their surface, in atactic polystyrene melts. Molecular parameters needed for the FTiMC simulations, as explained above, are summarized in Table 4.2. The radius of the nanoparticles, α_p, was either 8 nm or 13 nm. Both grafted and free chains of polystyrene were strictly monodisperse. The molecular weight of the free chains, M_f, and of the grafted chains, M_g, was varied, and the corresponding numbers of Kuhn segments, N_f and N_g, were

Table 4.2: FTiMC simulation parameters

Parameter	Value
Temperature, T	500 K
Mean polymer density, ρ_0	0.953 g/cm^3
Amorphous silica density, ρ_{SiO_2}	2.19 g/cm^3
Compressibility, κ_T	1.07×10^{-9} Pa^{-1}
Kuhn segment length, b_K	1.83 nm
Kuhn segment molar mass	729.05 g/mol
Estimated $\mathscr{A}_\mathrm{PS}$	5.84×10^{-20} J
Estimated $\mathscr{A}_{\mathrm{SiO}_2}$	6.43×10^{-20} J
Grid edge length, ΔL	2.5 nm

calculated based on the molar mass of a Kuhn segment, listed in 4.2. The molecular characteristics of the systems studied, i.e., the degree of polymerization of the chains, the radius and grafting density of the silica nanoparticles, have been selected *in such a way as to match systems which have been or can be studied experimentally.*[260,273,274] All simulations were carried out in the canonical statistical ensemble. The temperature of the system was $T = 500\mathrm{K}$. The simulation box was cubic with varying edge length from 80 nm to 200 nm. Within such a box a single nanoparticle was placed, thus leading to a volume fraction of nanoparticles, φ, less than 1%. It should be noted that, for all chain lengths, the edge length is at least an order of magnitude larger than $R_{\mathrm{g},0}$, with $R_{\mathrm{g},0}$ being the unperturbed radius of gyration of a chain, so as to avoid finite size effects ($R_{\mathrm{g},0} \simeq 8.7$ nm for 100 kg/mol PS). The grafting density, σ_g, varied from 0.2 nm^{-2} to 1.1 nm^{-2}. It was manipulated by defining the number of grafted chains, n_g, on the nanoparticle surface. Most experimental work up to now has been concentrated on low grafting densities (around 0.2 nm^{-2}).[230,273] However, silica particles with higher grafting densities (around 1.0 nm^{-2}) coated with asymmetric block copolymers have also been synthesized.[275] The number of free polymer chains in the system, n_f, was varied according to the chain length so that the mean density of polymer in the accessible volume of the model system was 0.953 g/cm^3, matching the experimentally measured value.[276] The Kuhn segment length, b_K, is 1.83 nm, which corresponds to seven styrene monomers.

4.3 Results and Discussion

4.3.1 Equilibration Efficiency

The ability of the simulation scheme to equilibrate the systems under study, is first demonstrated in Figure 4.1, which displays the orientational autocorrelation function $\mathcal{A}_\mathbf{u}(t) = \langle \mathbf{u}(t) \cdot$

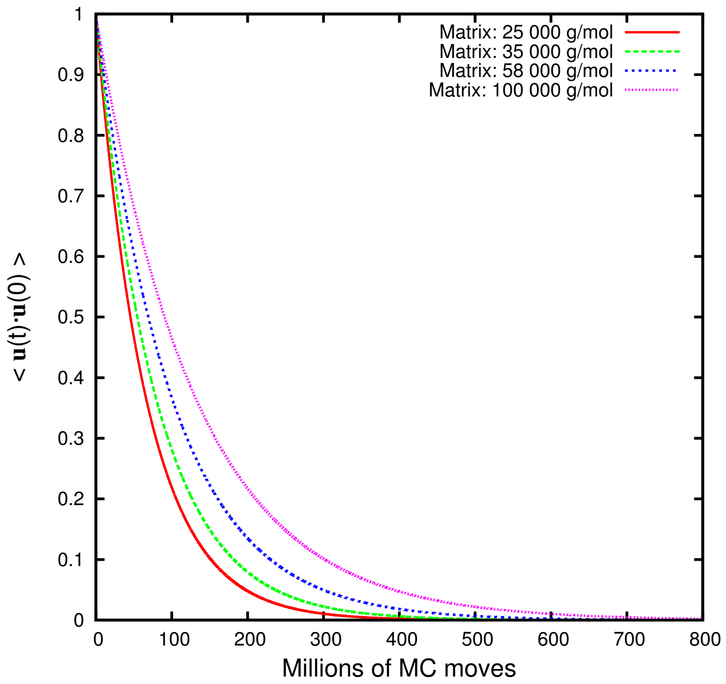

Figure 4.1: Decay of the chain end-to-end vector orientational autocorrelation function $\mathcal{A}_{\mathbf{u}}(t) = \langle \mathbf{u}(t) \cdot \mathbf{u}(0) \rangle$ for four systems consisting of a 8-nm-radius nanoparticle grafted with 25 kg/mol grafted chains at $\sigma_{\mathrm{g}} = 0.2\,\mathrm{nm}^{-2}$ grafting density.

$\mathbf{u}(0)\rangle$ of a unit vector $\mathbf{u}$ directed along the chain end-to-end vector, which was evaluated as a function of the number of MC moves tried. The autocorrelation functions in Figure 4.1 are studied for four different molecular weights of free chains. All different molecular weights are studied in the highly constrained systems consisting of a 13-nm-radius nanoparticle with $M_{\mathrm{g}} = 25$ kg/mol grafted chains. The shortest chain systems exhibit the fastest equilibration rate due to the intramolecular moves, especially pivot, which alters a significant part of the chain in a step. As we switch to longer molecules, intramolecular moves become less efficient, rendering the relaxation of these systems slower. We note that the equilibration length of our simulations varied between 60 and 80 billions of MC moves, more than two times the time needed for the slowest end-to-end vector orientational autocorrelation function to drop to zero.

In order to assess the equilibration of grafted chains, we select the decay of the orientational autocorrelation of the projection of their end-to-end vector on a plane tangent to the surface of the particle at the grafting point. The vector $\mathbf{u}_p$ is shown in Figure 4.2 for a simple chain consisting of five Kuhn segments. The autocorrelation function can then be defined as $\mathcal{A}_{u_p}(t) = \langle \mathbf{u}_p(t) \cdot \mathbf{u}_p(0) \rangle$. The behavior of this function is presented in Figure 4.3 for increasing grafting density. For all grafting densities, the autocorrelation function exhibits an oscillation, implying that chains can change efficiently their orientation relative to the surface

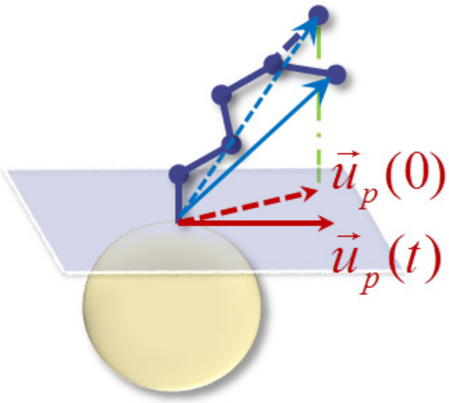

Figure 4.2: The projection of the end-to-end vector of the grafted chains, $\mathbf{u}_p$ at two different configurations, separated by t MC moves, during the course of the simulation.

of the particle, exploring a variety of configurations during the simulation.

4.3.2 Discretization Effects

4.3.2/i Long-ranged correlations

In a dense polymer melt, density fluctuations are strongly supressed on large length scales, resulting in the screening of excluded volume interactions among the segments. The correlations of local segment density in homopolymer melts are characterized by the structure factor $S_{\text{tot}}(\mathbf{k})$, i.e. the Fourier transform with respect to distance $\mathbf{r}-\mathbf{r}'$ of the density correlation function $\langle \rho(\mathbf{r})\,\rho(\mathbf{r}')\rangle$, where brackets denote the average in the canonical ensemble. Since our simulations deal with explicit particle coordinates, $S_{\text{tot}}(\mathbf{k})$ can be calculated according to:

$$S_{\text{tot}}(\mathbf{k}) = \frac{1}{n_{\text{f}}\,(N_{\text{f}}+1)} \left\langle \left| \sum_{j=1}^{n_{\text{f}}} \sum_{s=0}^{N_{\text{f}}} e^{-i\mathbf{k}\cdot\mathbf{r}_j(s)} \right|^2 \right\rangle \tag{4.11}$$

where $\mathbf{r}_j(s)$ stands for the position vector of the s-th segment of the j-th chain. The limiting value of the total structure factor at large length scales, $\mathbf{k} \rightarrow 0$, is directly connected to the compressibility of the system:

$$\lim_{|\mathbf{k}|\rightarrow 0} S_{\text{tot}}(\mathbf{k}) = \frac{1}{k_{\text{B}}T\rho_0\kappa_{\text{T}}} \tag{4.12}$$

where ρ_0 is the mean segment density and κ_T the isothermal compressibility. By calculating $S_{\text{tot}}(\mathbf{k})$ for a range of k-vectors, the compressibility of the system can be estimated as a function of the observation length scale.

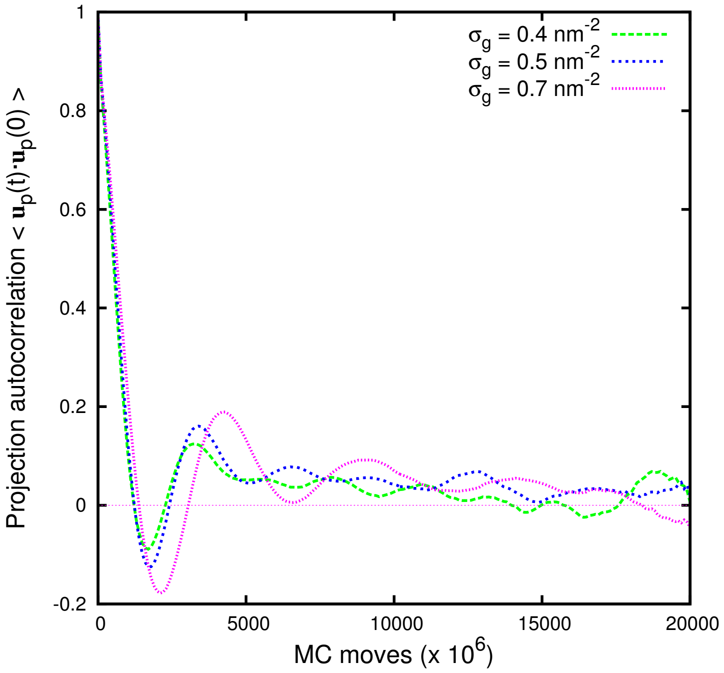

Figure 4.3: Decay of the autocorrelation function of the projection of the end-to-end vector of grafted chains on a plane tangent to the surface of the particle. All systems consist of an 8-nm-radius particle grafted with 20 kg/mol immersed in 100 kg/mol matrix.

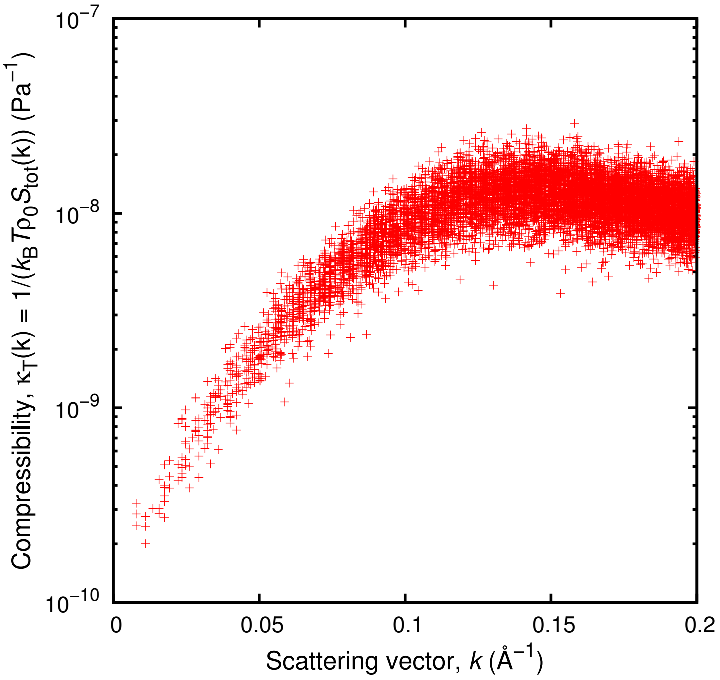

Figure 4.4: Compressibility as a function of the observation length scale. Compressibility is estimated from the static structure factor, $S_{\text{tot}}(\mathbf{k})$ of a 100 kg/mol homopolymer melt simulated at $T = 500$ K. The edge length of the simulation box is 80 nm. The spacing of the discretization grid is $\Delta L = 2.5$ nm.

Figure 4.4 presents the compressibility of a bulk PS homopolymer system as a function of the scattering vector **k** used for the calculation of the total structure factor. Coarse-grained simulations with soft interactions are performed with potential expressions and parameters which yield more compressible systems than their atomistically simulated counterparts. This applies to our simulations, if compressibility is estimated at small lenght scales. However, at large length scales compressibility values lie in the range expected for experimental systems.

4.3.2/ii Absence of preferred packing relative to the grid

Throughout the course of the simulation, random translations of the grid are employed (subjected to a Metropolis acceptance criterion) in order to avoid possible grid induced artifacts. Grid-based interactions might induce a preferential location of Kuhn segments within a grid cell. In order to elucidate whether such an artifactual local packing effect exists, Figure 4.5 presents a two-dimensional contour plot of the density distribution of segments belonging to both free and grafted chains in a plane cutting through the center of the particle. In order to calculate the contour of density, a 4-nm-thick slab is defined along the z-axis. All free and grafted segments lying inside it are counted and the resulting density is averaged across a MC simulation of 20 billion moves. The $xy-$plane is discretized in such a way that the projection of a grid cell is split into 25 equally-sized squares. The estimated density is then normalized. If any square of the slab resolution lattice contained exactly the same number of Kuhn segments, the contour plot would have a uniform color. However, deviations from mean density exist, but the distribution of local densities is random. Based on the contour plot of Figure 4.5 no preferential positioning of Kuhn segments with respect to the density discretization grid can be observed.

4.3.3 Local Structure

The local density of the polymer in proximity of the surface is often employed as a measure of the strength of polymer-surface interactions. Radial mass density profiles and cumulative mass distributions are studied here for various combinations of particle radii, grafting densities, and embedding matrices in order to quantify how these factors affect the size and form of the corona of grafted chains, as well as the distribution of free chains around a nanoparticle.

4.3.3/i Influence of grafting density

Figure 4.6 depicts the effect of grafting density on the packing of free and grafted chains near the surface of the particle. Grafted chains dominate the interfacial region, thus contributing more than free chains to the total density calculated near the nanoparticle surface. The ten-

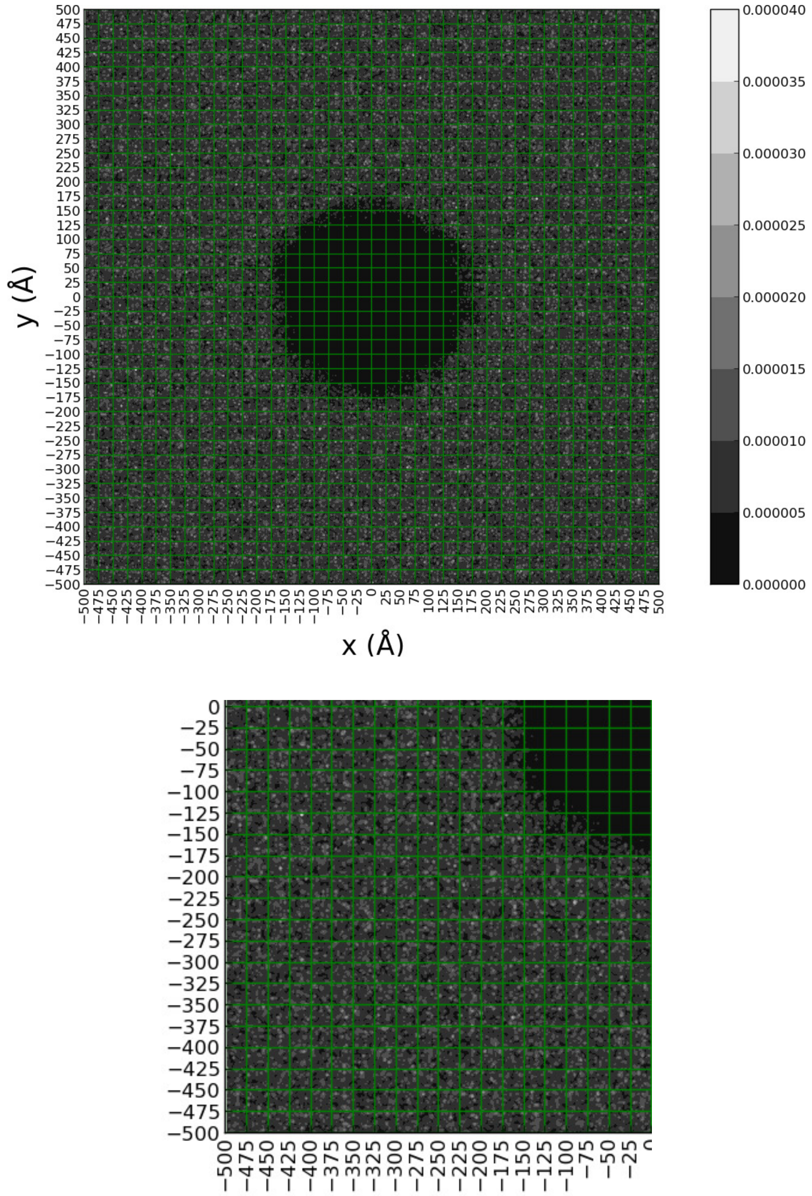

Figure 4.5: Contour plot of the normalized local density of free and grafted segments lying in a slab passing through the center of an 8-nm-radius particle. The grafting density is $0.7\,\mathrm{nm}^{-2}$, the molar masses of grafted and free chains are 20 kg/mol and 100 kg/mol, respectively. Green lines represent the density discretization, whose spacing is $\Delta L = 2.5$ nm.

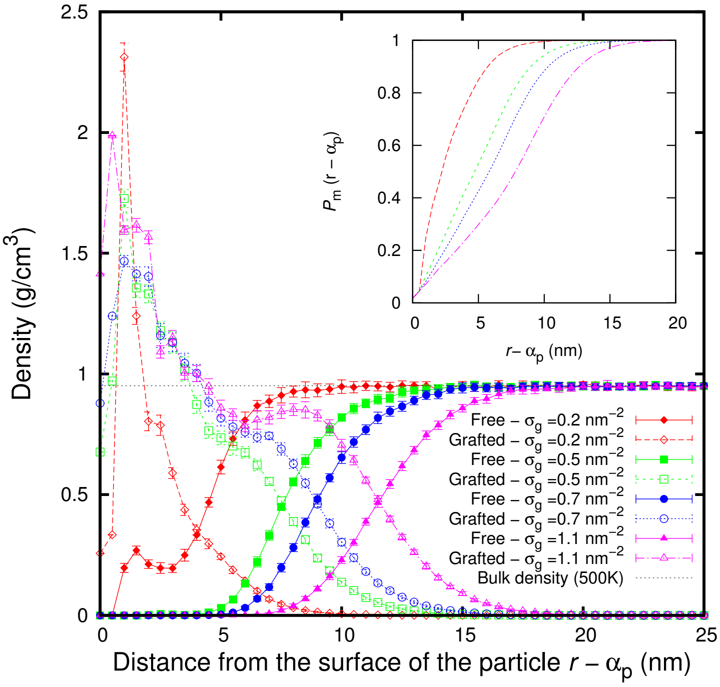

Figure 4.6: Radial density profiles for free and grafted segments as a function of distance from the surface of the particle. The grafting density, σ_g, varies from $0.2\,\mathrm{nm}^{-2}$ to $1.1\,\mathrm{nm}^{-2}$, while the radius of the nanoparticle is $a_p = 8$ nm and the molar mass of the matrix is $M_f = 100$ kg/mol. The molar mass of grafted chains is 20 kg/mol. In the inset to the figure, the normalized cumulative mass distribution for the grafted chains is depicted as a function of distance from the surface of the particle. (Density profiles are accumulated in 0.5-nm-thick bins.)

dency of grafted chains to stretch away from the surface increases with increasing grafting density; congestion with neighboring grafted chains forces them to extend more. The density profile of the grafted segments exhibits two regimes: a parabolic decay near the surface of the particle, and an exponential tail which extends far into the matrix. This form is in agreement with predictions from theoretical,[277] SCF,[242] MD[247,278] and off-lattice MC[35] simulations of grafted chains in melt and solvent environments. The presence of chemically grafted chains on the surface inhibits the approach of free chains to the nanoparticle, with the strength of the exclusion of free chains increasing with increasing grafting density. Far from the nanoparticle surface we observe a smooth decay of the density profile. The parabolic decay is continuous for $\sigma_g = 0.2\,\mathrm{nm}^{-2}$, while for higher grafting densities the decay is manifested by two parabolic branches, which can be attributed to the concentrated polymer brush regime (CPB) close to the surface and the semi-dilute polymer brush regime (SDPB) away from it.[279] The sum of the grafted and free chain density profiles suggests that the system is essentially incompressible, except in the immediate vicinity of the grafting surface. Accumulated mass distributions in the inset of Figure 4.6 show the relation between grafting density and brush (grafted layer) propagation.

It can been seen that higher grafting density leads to a more extended grafted layer, thus increasing the thickness of the polymeric brush around the nanoparticle. For the highest grafting density examined, $\sigma_{\mathrm{g}} = 1.1$ nm^{-2}, the interfacial region has a thickness of at least 20 nm, as evidenced from the cumulative mass distribution. Moreover, the density profile of grafted chains density profile exhibits a second smooth maximum before its parabolic decay. This feature is also present in previous simulation studies. Atomistic simulations of 20-mer grafted chains on a 2-nm-radius particle by Ghanbari et al.[280] exhibit this extra hump for a grafting density of 1.0 nm^{-2}. The length scale at which this feature appears depends on the segment size, but it seems to be rather a real effect than an artifact of the model employed in this work. The first parabolic profile (CPB regime) is separated from the second one (SPDB regime) by a region of thickness equal to one Kuhn length, at the end of which this extremely shallow and smooth local maximum appears.

Borukhov and Leibler[244] have predicted the phase diagram for grafted polymer (index of polymerization N_{g}) in contact with a chemically identical polymer melt (index of polymerization N_{f}), by using a scaling model along with SCF calculations. For long enough matrix chains, $N_{\mathrm{f}} > N_{\mathrm{g}}$, three regions exist as a function of the reduced grafting density $\widehat{\sigma}_{\mathrm{g}} = \sigma_{\mathrm{g}}/\alpha_{\mathrm{s}}^2$ with α_{s} being the size of the monomer in their description (in our case, $\alpha_{\mathrm{s}} \to b_{\mathrm{K}}/2$). For $\widehat{\sigma}_{\mathrm{g}} < N_{\mathrm{g}}^{-1}$ the brush is in the ideal mushroom regime, for $N_{\mathrm{g}}^{-1} < \widehat{\sigma}_{\mathrm{g}} < N_{\mathrm{g}}^{-1/2}$ the brush is ideally wet, while for $\widehat{\sigma}_{\mathrm{g}} > N_{\mathrm{g}}^{-1/2}$ the brush is dry. Following the reasoning of Borukhov and Leibler, the lowest grafting density of $\sigma_{\mathrm{g}} = 0.2$ nm^{-2} (4.6) lies in the proximity of the ideal wet brush regime of the phase diagram. This is evident from the fact that some free segments have penetrated the corona and lie close to the surface of the particle, thus leading to a local maximum in the radial density distribution of free chains, in this case located around a Kuhn length ($b_{\mathrm{K}} = 1.83$ nm) away from the surface of the particle. For higher grafting densities, our brushes fall in the dry brush regime, where free chains are completely expelled from the surface of the particle over a distance which scales as $N_{\mathrm{g}}^{1/3}\sigma_{\mathrm{g}}^{1/3}$. High grafting densities of end-adsorbed polymers in the presence of chemically identical matrix polymers have been shown previously to promote autophobicity (i.e., incompatibility between the grafted chains and the matrix).[238,241,281] It is found here that increasing σ_{g} promotes greater matrix/brush incompatibility by drying the polymer brush; however, the effects are much less prominent for curved surfaces than for planar ones,[237] since polymers end-grafted to small spherical surfaces face less chain crowding moving away from the surface.

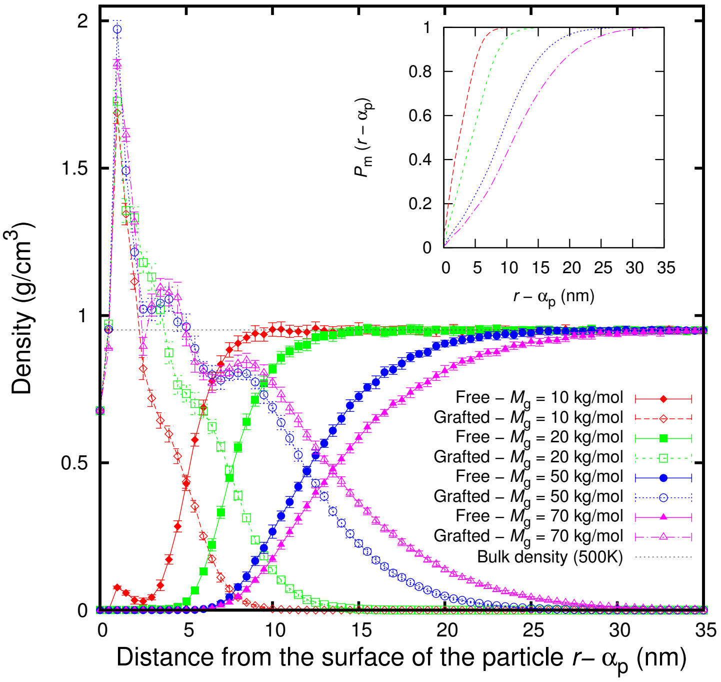

Figure 4.7: Radial density profiles for grafted and free segments as a function of the grafted chain molar mass. The radius of the nanoparticle is $\alpha_p = 8$ nm, while the molar mass of the matrix is $M_f = 100$ kg/mol. The grafting density is $\sigma_g = 0.5\text{nm}^{-2}$. In the inset to the figure, the normalized cumulative mass distribution for the grafted chains is depicted as a function of distance from the surface of the particle. (Density profiles are accumulated in 0.5-nm-thick bins.)

4.3.3/ii Influence of grafted chain molar mass

The influence of grafted chain molar mass on the distribution of grafted and free chains around the surface of the particle is examined in Figure 4.7. The grafting density is kept fixed at $\sigma_g = 0.5\text{nm}^{-2}$, while the molar mass of the grafted chains varies from 10 kg/mol to 70 kg/mol. The profiles of the grafted chains start at the same point for $r-\alpha_p = 0$, since there their volume density is dictated by the surface grafting density. The grafted chain profiles exhibit almost identical density peaks, located around one Kuhn length away from the particle surface, since the grafting density is kept constant. The higher the molar mass of the grafted chains, the more the brush extends into the matrix. For high molar mass chains ($M_g = 50$ and 70 kg/mol) grafted density profiles exhibit a second peak, attributed to the second neighbors of the segments which are permanently attached to the surface of the nanoparticle. Long grafted chains lead to the formation of a dry brush around the particle and only for $M_g = 10$ kg/mol do some free segments lie inside the grafted corona, wetting the corona. The phase behavior of the grafted corona is in accordance with the already mentioned scaling theory of Borukhov and Leibler.[244] Nanoparticle/polymer miscibility should be generally high when the wet brush conditions are

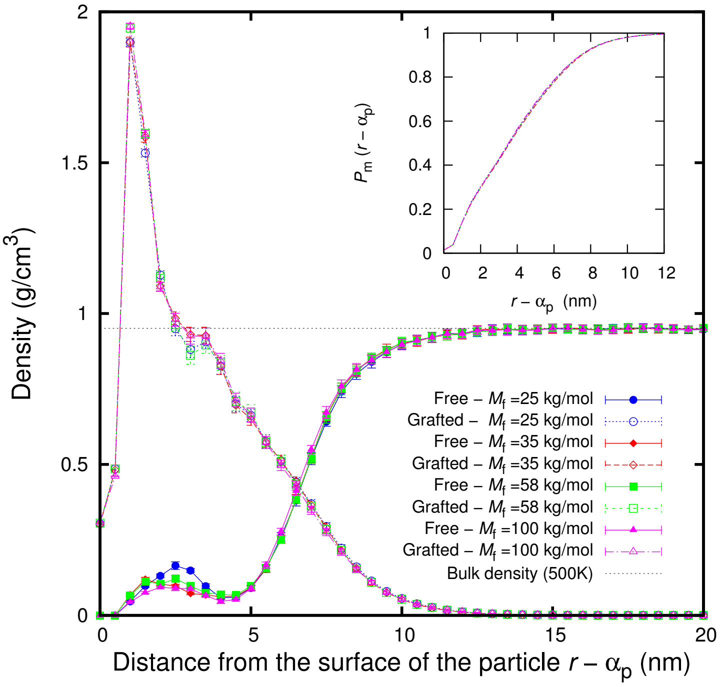

Figure 4.8: Radial mass density distribution of free and grafted segments from the surface of the nanoparticle, as a function of the matrix molar mass. The radius of the particle is 13nm, the molar mass of the grafted chains $M_g = 25\,$kg/mol and the grafting density is $\sigma_g = 0.2$chains/nm^2. Matrix molar mass varies from $M_f = 25\,$kg/mol to $M_f = 100\,$kg/mol. In the inset to the figure, the normalized cumulative mass distribution for the grafted chains is depicted as a function of the distance from the surface of the particle. (Density profiles are accumulated in 0.5-nm-thick bins.)

met and decrease under dry brush conditions. The degree of overlap between grafted and free segments can be quantified by calculating an interpenetration parameter, δ_{in}, as this was defined by Egorov and Binder.[282] From our simulations, the interpenetration width extends from 7.2 nm for 10 kg/mol grafted chains, up to 23.5 nm for 70 kg/mol grafted chains.

4.3.3/iii Influence of matrix molar mass

Figure 4.8 depicts the effect of matrix material on the spatial extent of grafted chains for identical particle radii and grafting densities. Since the molar mass of the grafted chains and the grafting density are low enough, free chains can slightly wet the grafted corona. The effect is stronger for the shortest matrix chains, as expected, but remains present for all matrix molar masses examined. The specifications of the systems studied are chosen as close as possible to the experiments of Chevigny et al.,[260] in which it is stated that a “wet to dry” conformational transition occurs. However, based on Figure 4.8, a conformational transition of the grafted chains can not be observed. The cumulative mass distributions, shown in the inset to Figure 4.8, are almost identical for all matrix molar masses. Since $\alpha_p/R_g > 1$, the theory of Trombly and Ganesan[283] predicts that the "wet to dry" transition should occur for $N_\mathrm{f}/N_\mathrm{g} < 1$. This requirement would be fullfilled by studying even shorter matrix chains. Unfortunately, the coarse character of our methodology cannot allow us to study shorter polymeric chains. In this regard, the trend predicted by the theory seems to be in accordance with our simulation and qualitatively consistent with the experimental data. According to our single particle simulations, the brush profiles are almost insensitive to changes in $N_\mathrm{f}/N_\mathrm{g}$ when $N_\mathrm{f} > N_\mathrm{g}$. This suggests that the experimentally observed phase behavior of these systems may be sensitive to subtle changes in the distribution of brush and matrix segments when two or more particles come together. Also, from the experimental point of view, a more exact comparison with theoretical predictions and simulations would require monodisperse nanoparticles and highly monodisperse polymers.

4.3.4 Height of the Grafted Polymer Brush

Spatial integration of the radial mass density profiles allows for estimating the height of the grafted polymer brush, which is usually defined as the second moment of the segment density distribution, $\rho(r)$, as:[242,284]

$$\left\langle h^2 \right\rangle^{\frac{1}{2}} = \left[\frac{\int_{\alpha_\mathrm{p}}^{\infty} 4\pi r^2 \mathrm{d}r (r-\alpha_\mathrm{p})^2 \rho(r)}{\int_{\alpha_\mathrm{p}}^{\infty} 4\pi r^2 \mathrm{d}r \rho(r)} \right]^{\frac{1}{2}} \tag{4.13}$$

with respect to the height $h \equiv r - \alpha_\mathrm{p}$. We therefore use this root mean-square (rms) height to define the brush thickness. However, comparison with experimental brush heights requires a measurement of where the major part of the grafted material is found. To this effect, the brush height can also be arbitrarily defined as the radius marking the location of a spherical Gibbs dividing surface, in which 99% of the grafted material is included. Table 4.3 reports the two estimates of the brush height for all systems considered in this study, for different grafting densities and molar masses of the free and grafted chains.

The theory of spherical polymer brushes was pioneered by Daoud and Cotton.[245] In analogy to the scaling model developed by Alexander and de Gennes for planar interfaces, Daoud and Cotton developed a model for spherical surfaces through geometric considerations based on starlike polymers. The spherical brush is divided into three regions, an inner meltlike core region, an intermediate concentrated region (dense brush), and an outer semidilute region (swollen brush). Daoud and Cotton predicted for star shaped polymers in the matrix a change in the scaling behavior as the blobs of the chains become non-ideal. The density profile is directly related to the average brush height, h, or the extension of the corona chains.

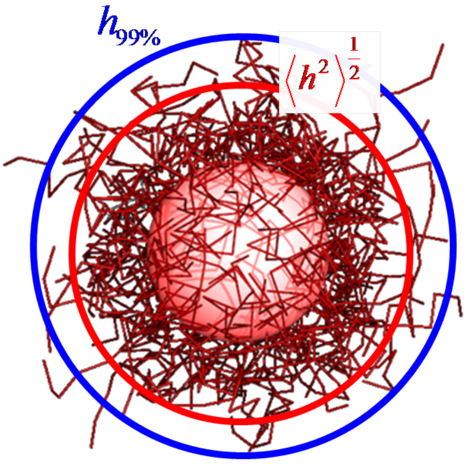

Figure 4.9: Definitions of the brush thickness measure employed in this work. The red circle around the nanoparticle corresponds to $\langle h^2 \rangle^{1/2}$, as that was defined by the eq 4.13. The blue circle corresponds to the radius of the shell in which the 99% of the brush material can be found, $h_{99\%}$.

Table 4.3: Brush heights for different silica nanoparticles, free chains molar mass, grafted chains molar mass and grafting densities. Also, brush thickness estimations based on fitting SANS spectra by Meyer[274] have been included.

M_f (kg/mol)	M_g (kg/mol)	α_p (nm)	σ_g (nm^{-2})	$\langle h^2 \rangle^{\frac{1}{2}}$ (nm) FTiMC	$\langle h^2 \rangle^{\frac{1}{2}}$ (nm) SANS[274]	$h_{99\%}$(nm) FTiMC	$h_{99\%}$(nm) SANS[274]
100	20	8	0.2	2.98	3.3-3.3	16.49	16.3-17.2
			0.4	4.49	4.1-5.0	18.99	19.2-19.6
			0.5	5.18	4.4-5.7	20.33	19.9-20.9
			0.7	6.25	4.9-6.8	21.76	21.2-23.1
			1.1	8.02		24.13	
100	10	8	0.5	3.05	2.8-3.8	16.22	16.0-17.3
	20			5.26	4.4-5.7	20.19	19.9-20.9
	50			10.30	7.8-9.1	30.87	27.5-28.4
	70			13.08		36.85	
25	25	13	0.24	4.80		27.22	
35				4.74		27.21	
58				4.74		27.22	
100				4.73		27.22	

Neglecting the contribution of the core to the radius of the star, they found that:

$$h \sim N_{\mathrm{g}}^{1/2} \widehat{\sigma}_{\mathrm{g}}^{1/4} b_{\mathrm{K}} \tag{4.14}$$

Although the former relation exhibits "ideal" scaling with respect to the chain length dependence, the presence of the factor $\widehat{\sigma}_{\mathrm{g}}^{1/4}$ shows that the radius is in fact larger than it would be for a single linear chain. Thus, although we are in a regime where the chain seems to be ideal, the structure is actually stretched.

In Figure 4.10 the average thickness of all analyzed systems is plotted versus $N_{\mathrm{g}}^{1/2}\sigma_{\mathrm{g}}^{1/4}$. N_{g} is measured in Kuhn segments per chain and σ_{g} in nm^{-2}. The scaling prediction of Daoud and Cotton seems to be fullfilled for both the rms height $\langle h^2 \rangle^{\frac{1}{2}}$ and the height containing 99% of the brush material, $h_{99\%}$. The dashed lines are linear fits, confirming the good agreement of the simulation data with the theoretical scaling behavior. The agreement seems to be better for the $h_{99\%}$ data points. This was expected, since the average brush thickness, as defined in eq 4.13, is more sensitive to the discretization of the model and to the post processing of the data, than the straightforward definition of the shell in which the 99% of the brush material can be found. The least squares linear regression analysis of $h_{99\%}$ data is more successful, yielding a coefficient of determination,[285] R^2_{LR}, higher than the corresponding for $\langle h^2 \rangle^{\frac{1}{2}}$ data points.

4.3.5 Scattering Predictions

While previous works have focused on a single measure of the spatial distribution of polymeric chains, the mean brush height, examining the full distribution of polymeric segments is a more sensitive and critical test of the theories and simulations. This type of comparison is best performed against scattering patterns from SANS. SANS has been shown to be the most suitable technique to reveal the microstructure of polymers in confined environments, thanks to the specific contrast variation method which allowed the measurement of the form factor of a single chain through the use of index-matched fillers.[273,286] Neutron wavelengths are commensurate with interatomic separations, while neutron energies are of the same order as molecular vibrational energies. When used with partially deuterated polymers, SANS permits a close monitoring of macromolecular conformations in polymer solutions, melts, and blends. This advantage has made it a unique tool for the understanding of the morphology of polymer materials and of the relation between their structures and physical properties. Elastic scattering of neutrons measures spatial correlations between scattering centers; for polymers this enables the conformation to be determined. The incoherent cross-section is isotropic and does not depend on a phase term; therefore no information can be obtained from it about the relative positions

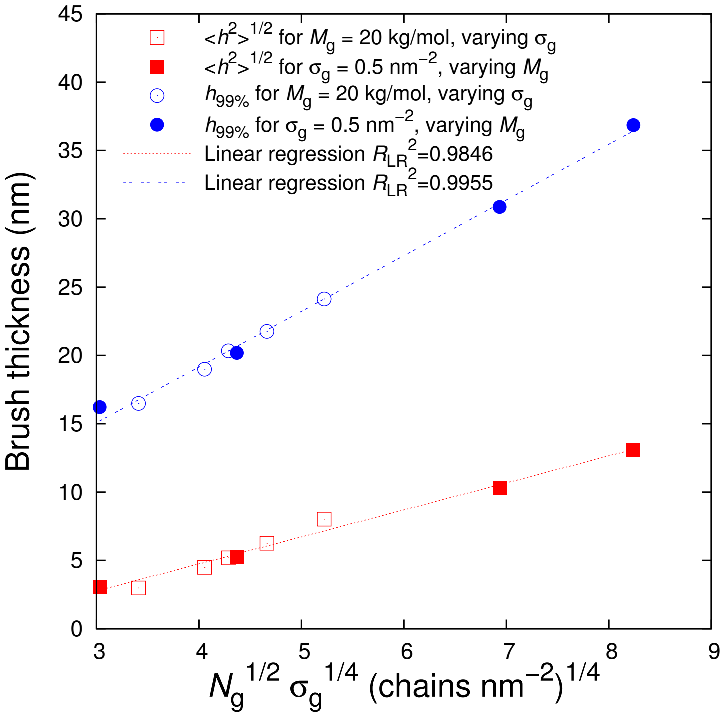

Figure 4.10: The calculated brush thickness (either $\langle h^2 \rangle^{\frac{1}{2}}$ or $h_{99\%}$) is plotted versus the degree of polymerization of grafted chains, N_g, times the grafting density, $\sigma_\mathrm{g}^{1/4}$. Points correspond to all systems containing an 8-nm-radius particle of 4.3. Linear behavior is predicted by the model proposed by Daoud and Cotton (eq 4.14) for star shaped polymers.[245]

of the nuclei in an array. Information about the relative positions of the nuclei can be obtained if coherent scattering is measured. The total amplitude from the sample in the detector can be written as:

$$A\left(\mathbf{k}\right) = b_{\mathrm{c}} \sum_{k=1}^{\mathcal{N}} e^{-i\mathbf{k}\cdot\mathbf{r}_k} \quad . \tag{4.15}$$

with b_{c} being the mean coherent scattering length, k running over all $\mathcal{N}$ nuclei of the sample and the vector **k** which completely characterizes the scattering geometry: the incident and scattered beam directions and the wavelength. The normalized amplitude defined here is related to the intensity by:

$$I\left(\mathbf{k}\right) = \left\langle \left|A\left(\mathbf{k}\right)\right|^2 \right\rangle = \left\langle \left|A(\mathbf{k})A^*(\mathbf{k})\right| \right\rangle \tag{4.16}$$

where the angle brackets $\langle \cdots \rangle$ indicate that the intensity observed is a time average.

4.3.5/i Single chain scattering

To connect FTiMC simulations with experimentally measured coherent scattering intensity, the single chain form factor can be calculated from the real space positions of polymeric segments as:

$$\mathcal{P}\left(\mathbf{k}\right) = \frac{1}{(N+1)^2} \left\langle \left| \sum_{s=0}^{N} e^{-i\mathbf{k}\cdot\mathbf{r}_j(s)} \right|^2 \right\rangle_n \tag{4.17}$$

where $N = N_{\mathrm{f}}, n = n_{\mathrm{f}}$ for the free and $N = N_{\mathrm{g}}, n = n_{\mathrm{g}}$ for the grafted chains, respectively. With $\mathbf{r}_j(s)$ we dente the s-th segment of the j-th chain. The average is taken over all the free or grafted chains, across different configurations of the system. At equilibrium, the ensemble average equals the time average which is measured experimentally.

The form factor of a freely jointed chain, which follows Rayleigh random walk statistics, can be analytically calculated by combining and extending the work of Chandrasekhar,[81] Daniels[287] and Burchard and Kajiwara:[288]

$$\mathcal{P}_{\text{Rayleigh}}\left(k\right) = \frac{2}{\left(N+1\right)^2} \left[\frac{N+1}{1-\frac{\sin(kb_{\mathrm{K}})}{kb_{\mathrm{K}}}} - \frac{N+1}{2} - \frac{1-\left(\frac{\sin(kb_{\mathrm{K}})}{kb_{\mathrm{K}}}\right)^{N+1}}{\left(\frac{\sin(kb_{\mathrm{K}})}{kb_{\mathrm{K}}}\right)^2} \cdot \frac{\sin(kb_{\mathrm{K}})}{kb_{\mathrm{K}}} \right] \tag{4.18}$$

where N again refers either to free or grafted chains and b_{K} being the Kuhn length. For $N >> 1$, chains follow Gaussian statistics with their form factor given by the well known Debye expression:

$$\mathcal{P}_{\text{Debye}}\left(k\right) = \frac{2\left(e^{-R_{\mathrm{g},0}^2 k^2} - 1 + R_{\mathrm{g},0}^2 k^2\right)}{\left(R_{\mathrm{g},0}^2 k^2\right)^2} \tag{4.19}$$

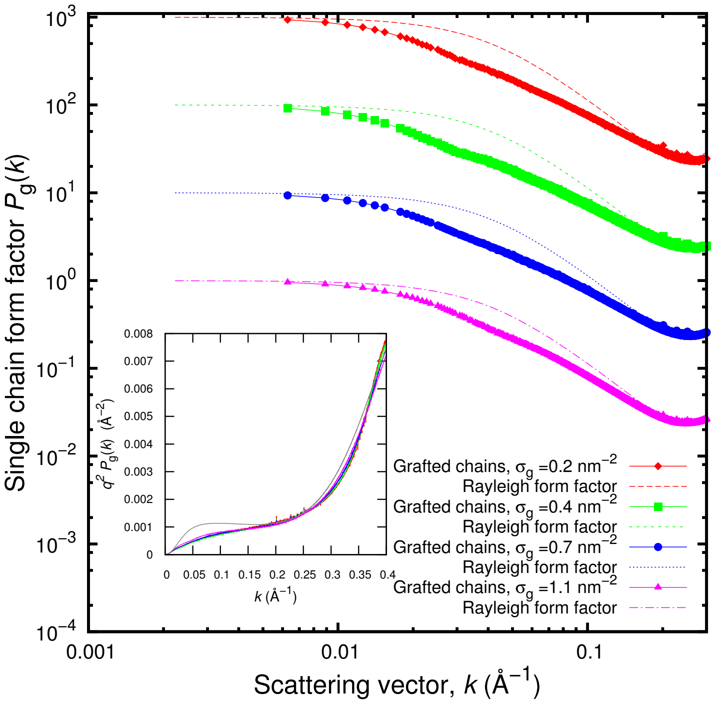

Figure 4.11: Form factor, $\mathcal{P}_{\rm g}(k)$, of 20 kg/mol grafted chains as a function of grafting density. Systems consist of an 8 nm-radius grafted particle immersed in 100 kg/mol matrix. The Kuhn length $b_{\rm K}$ is 1.83 nm and the unperturbed radius of gyration of grafted chains $R_{\rm g,0}$ is 3.91 nm. The curves for $\sigma_{\rm g} = 0.4,\ 0.7,\ 1.1$ nm^{-2} have been vertically displaced by one, two and three decades respectively, for clarity. In the inset to the figure, the corresponding Kratky plot is presented. Dashed lines display the analytically calculated Rayleigh form factor from eq 4.18.

where $R^2_{\rm g,0}$ is the unperturbed mean squared radius of gyration given by $R^2_{\rm g,0} = Nb^2_{\rm K}/6$, where N is the number of statistical (Kuhn) segments along the contour and $b_{\rm K}$ is the Kuhn length of the polymer. The Debye form factor is valid under the additional condition of $kb_{\rm K} << 1$. Since it exhibits a plateau at high k, it cannot capture the rise of the form factor of real polymers due to their stiffness. The advantage of the former equation (eq 4.18) over the well-known Debye form factor (eq 4.19) stems from the incorporation of the finite extensibility of freely jointed chains, which represent real chains better than the Gaussian model at large extensions. However, $\mathcal{P}_{\rm Rayleigh}(k)$ is not a well-behaved function at large N, rendering its algebraic manipulation difficult.

In Figure 4.11, the effect of grafting density form factor of grafted chains is depicted. The form factor of grafted chains, calculated by eq 4.17 during the course of the FTiMC simulation, is compared to the theoretically predicted form factor from eq 4.18. It is evident that grafted chains deviate from their unperturbed melt configuration. The attachment of their one end to the surface of an excluded volume sphere strongly affects their scaling behavior at low k-values. While at small length scales (large k, see Kratky plot in the inset to the figure)

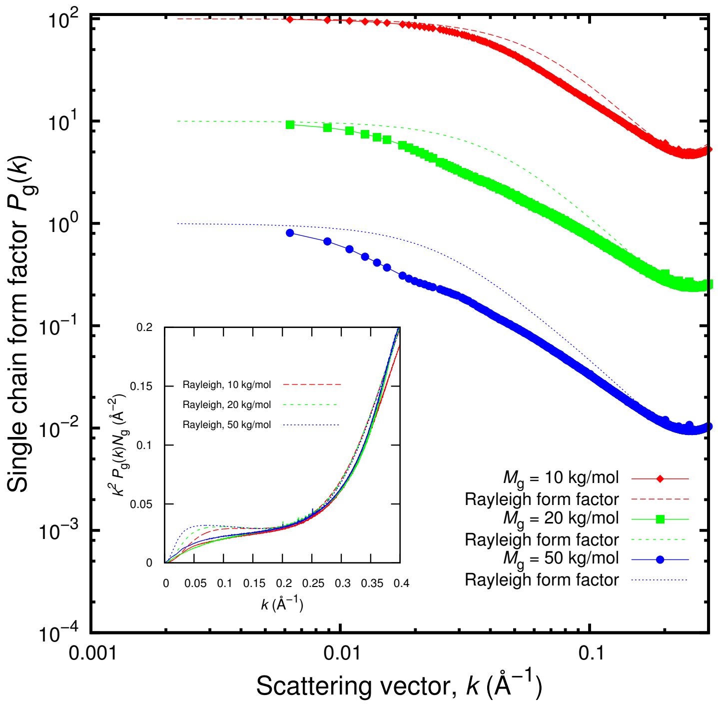

Figure 4.12: Form factor, $P_{\mathrm{g}}(k)$, of grafted chains as a function of their molar mass. Systems consist of an 8 nm-radius particle at $\sigma_{\mathrm{g}} = 0.5$ nm^{-2} surface coverage immersed in 100 kg/mol matrix. The curves for $M_{\mathrm{g}} = 20$ and 50 kg/mol have been vertically displaced by one and two decades, respectively, for clarity. The unperturbed radii of gyration, $R_{\mathrm{g},0}$, are 2.77 nm (10 kg/mol), 3.91 nm (20 kg/mol) and 6.19 nm (50 kg/mol). In the inset to the figure, the Kratky plot is presented, where form factors have been scaled with chain length in order the plateaus to coincide for all systems. Dashed lines correspond to analytically calculated Rayleigh form factors from eq 4.18.

their conformations are close to unperturbed, at large length scales, their confinement dictates their behavior. The deviation of the form factor of grafted chains from that of unperturbed freely jointed chains does not depend monotonically on surface grafting density. The radius of the particle sets the length scale ($k \sim (2\pi)/\alpha_{\mathrm{p}}$) where the deviation is manifested, which is common across the different systems depicted in Figure 4.11.

The effect of increasing the grafted chain molar mass on the calculated scattering from single grafted chains is examined in Figure 4.12. For all molar masses examined, chains deviate strongly from their unperturbed configurations. The confinement affects their behavior at low and intermediate k-values, while leaving large k-values (small length scales) unaffected. The permanent link between one of their ends and the particle surface and the excluded volume of the particle forces the grafted chains to extend more into the bulk. This tendency increases with increasing grafted chain molar mass; there, the deviation of grafted single chain scattering from the theoretical Rayleigh prediction becomes more pronounced. Moreover, this deviation moves systematically to smaller k-values as M_{g} increases. By careful examination one de-

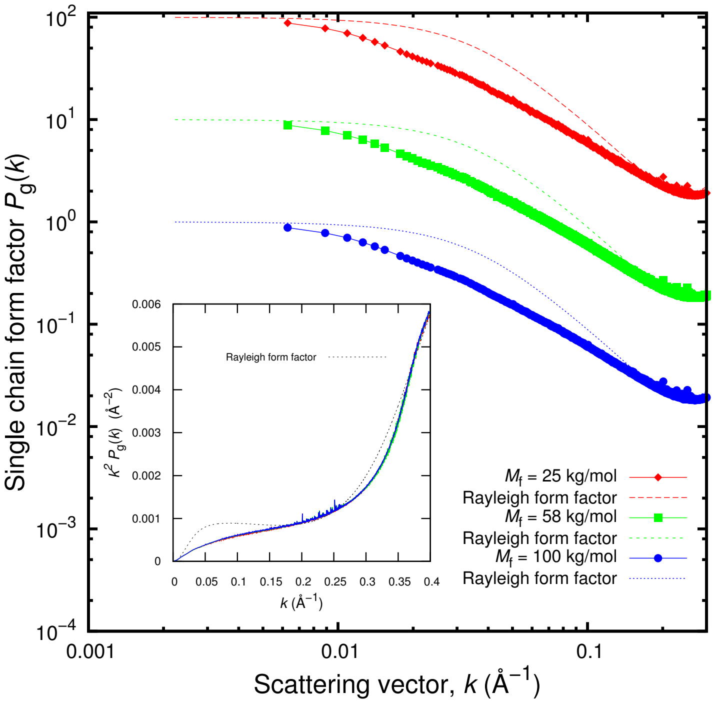

Figure 4.13: Form factor, $P_{\mathrm{g}}\left(k\right)$, of grafted chains as a function of the surrounding matrix molar mass. Systems consist of an 8 nm-radius particle with grafted chains of M_{g} = 20 kg/mol at $\sigma_{\mathrm{g}} = 0.5 \mathrm{nm}^{-2}$ surface coverage immersed in matrices of $M_{\mathrm{f}} = 25, 58$ and $100 \mathrm{kg/mol}$. In the inset to the figure, the Kratky plot is presented. The dotted line corresponds to the analytically calculated Rayleigh form factor from eq 4.18.

ternines that the lowest k-value at which this deviation is manifested is around $k\alpha_{\mathrm{p}} \sim 2$, with R_{g} being the root mean squared unperturbed radius of gyration, $R_{\mathrm{g}} = \sqrt{R^2_{\mathrm{g},0}}$. This implies that all chains deform due to their confinement in the same way, with the actual length scale of the deformation following their unperturbed dimensions. A similar observation was made by Grest et al.[289] who calculated from MD simulations the scattering from single chains within a star polymer. At higher k values, the radius of the particle sets the length scale of the scattering in this region, causing grafted chains to deviate from their unperturbed configurations and pushing them to acquire conformations which are closer to a shell-like structure than to an uncostrained random walk.

In Figure 4.13 the grafted chain form factor is shown as a function of the molar mass of the surrounding matrix. The scattering of grafted chains depends weakly on the molar mass of the matrix in which the nanoparticles are immersed. However, it seems that the grafted chains immersed in the matrix of molar mass 25 kg/mol deviate more at low k-values than in the matrices of higher molar mass. This implies that low molecular weight grafted chains are further extended in the presence of low molar mass free chains, due to their interpenetration with the grafted corona, as was seen by radial density distribution also.

4.3.5/ii Corona scattering

In FTiMC simulations, the grafted corona structure factor can be calculated by summing the contributions of all grafted segments and then analyzed by comparison to theoretical models and experimental results, obtained through matching the silica core, in order to see only the grafted corona. The corona structure factor, $S_{\text{g}}(\mathbf{k})$, is evaluated as:

$$S_{\text{g}}(\mathbf{k}) = \frac{1}{n_{\text{g}}(N_{\text{g}}+1)} \left\langle \left| \sum_{j=1}^{n_{\text{g}}} \sum_{s=0}^{N_g} e^{-i\mathbf{k}\cdot\mathbf{r}_j(s)} \right|^2 \right\rangle \tag{4.20}$$

where the double sum goes over all segments belonging to grafted chains. In Figure 4.14 the resulting curve for a grafted corona is shown. The points represent the average over all **k**-vectors sharing the same norm. In order to get an impression of the scattering curve, a Piecewise cubic Hermite (PcH) spline interpolation scheme is used.[290] Along with the simulation results, the behavior of two theoretical models is also illustrated in Figure 4.14. The first one is the form factor of a spherical shell of uniform density and thickness equal to the estimated brush thickness, $\langle h^2 \rangle^{1/2}$.[291] The other one is a model initially developed by Pedersen and Gestenberg[292,293] for block copolymer micelles. On the average, the constant density shell form factor exhibits the well-known dominant k^{-4} behavior. The periodic steps suggest a rather sharp cutoff in the segment density at radius equal to $\alpha_{\text{p}} + \langle h^2 \rangle^{1/2}$, which is a crude approximation to the real brush, since the brush density distribution actually exhibits a smooth and continuous variation as a function of distance from the surface of the particle. The assumption that the brush is a homogeneous spherical shell of thickness $\langle h^2 \rangle^{1/2}$ shifts the position of the structure factor minimum to larger k-values (smaller length scales), compared to its actual position.

A better approximation to the corona structure factor is the model introduced by Pedersen. This model is based on several different terms which have to be determined: the self correlation of the spherical core, the self correlation of the chains, the cross term between spheres and chains, and the cross term between different chains. In contrast-matching conditions for which the silica core is matched to see only the polymer corona, the Pedersen model is reduced to a weighted sum of the single chain form factor and the intra-chain cross correlation form factor:

$$S_{\text{Pedersen}}(\mathbf{k}) = n_{\text{g}} \cdot (P_{\text{g}}(\mathbf{k}) + (n_{\text{g}}-1) S_{\text{chain-chain}}(\mathbf{k})) \tag{4.21}$$

where $P_{\text{g}}(\mathbf{k})$ is the single chain form factor of the grafted chains and $S_{\text{chain-chain}}(\mathbf{k})$ is the cross term between different chains. In our approach, the single chain form factor can be directly calculated from the segmental positions (eq 4.17) and therefore can be used for the evaluation of Pedersen structure factor, thus taking into account the stretching of the chains due to the

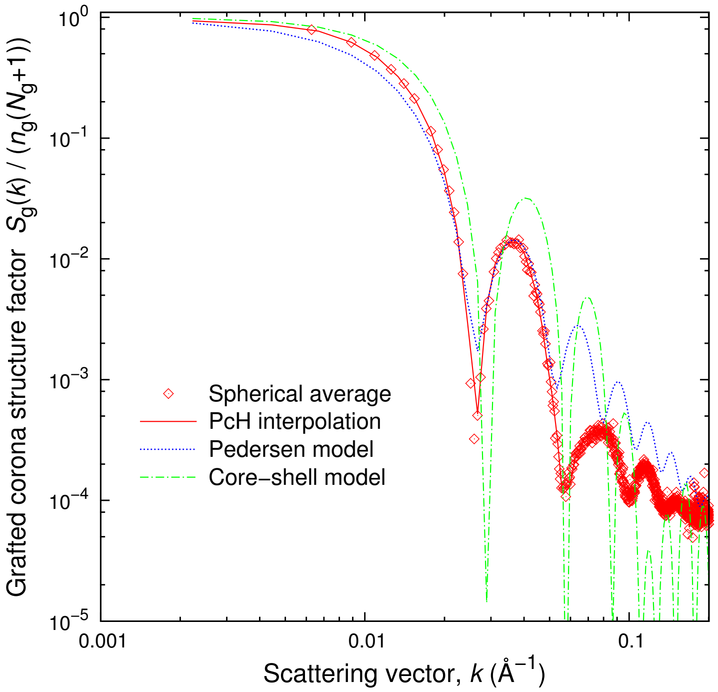

Figure 4.14: Scattering curve, $S_g(k)$, of a grafted corona consisting of 20kg/mol chains, grafted onto a 8nm-radius particle, at 0.5 nm^{-2} surface density, immersed in a 100 kg/mol matrix. Simulation results are presented along with several theoretical models.

particle. The cross term related to the interaction between chains which are assumed to be evenly distributed on the surface of the sphere and follow Gaussian statistics can be analytically expressed as:[292]

$$S_{\text{chain-chain}}(\mathbf{k}) = \left[\frac{1-e^{-kR_g}}{kR_g}\right]^2 \left[\frac{\sin k\alpha_\text{p}}{k\alpha_\text{p}}\right]^2 \quad . \tag{4.22}$$

Alternatively, for freely jointed chains following the Rayleigh distribution, a numerical integration of the cross-term between two chains obeying eq 4.18 should be carried out. In the derivation of the Pedersen structure factor, the chains are free to penetrate into the core. In order to mimic the presence of the excluded volume of the nanoparticle, the starting points of the chains are shifted from the distance α_p to $\alpha_\text{p} + \delta\alpha \cdot R_\text{g}$, with $\delta\alpha$ close to unity.[293]

The corona scattering curves are shown in Figure 4.15 as a function of the grafting density. All curves are normalized so as to approach unity for $k \to 0$. At the lowest k-values, the intensity reaches a plateau, indicating finite-size objects, which confirms that there is no interference between the periodic images of the particles. At intermediate k-values, an oscillation is present with its position being characteristic of the corona size:[294] the thicker the corona, the smaller the value of k at which the sharp oscillation appears. Here again, our results support the fact that increasing σ_g leads to more extended grafted brushes. In the inset of Figure 4.15 is shown the behavior of the Pedersen model with non-interacting chains obeying Rayleigh statistics.

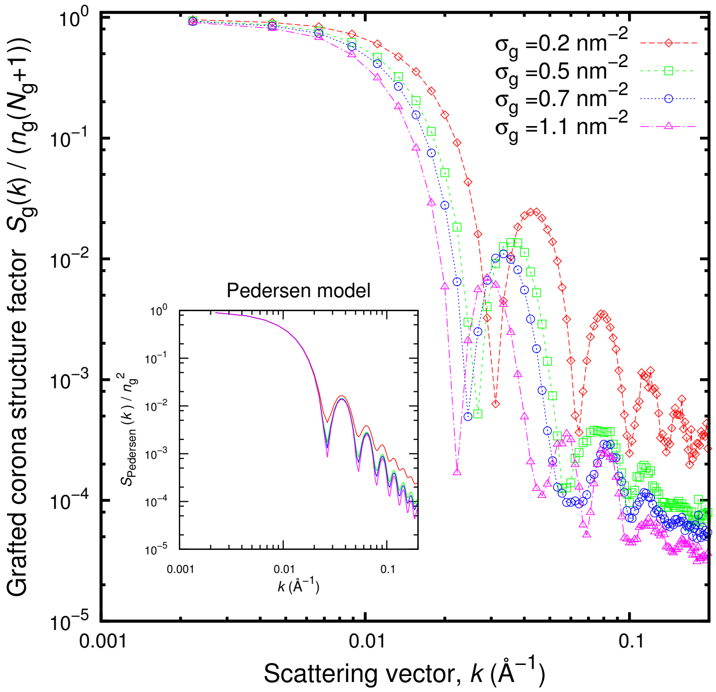

Figure 4.15: Scattering curves of the deuterated grafted corona ($M_\mathrm{g} = 20$ kg/mol) inside the silica matched matrix ($M_\mathrm{f} = 100$ kg/mol). The radius of the particle is $\alpha_\mathrm{p} = 8$ nm, while the grafting density varies from 0.2 nm to 1.1 nm.

At low grafting densities, the simulated scattering curves are close to the ones predicted by the Pedersen model. At higher grafting densities the simulation results deviate from the model. The Pedersen model considers chains which are stretched due to the excluded volume of the particle, but are not stretched due to crowding with their end-grafted partners. This assumption is valid for low enough grafting densities, where the dominant non-ideal contribution comes from the particle's excluded volume. As the neighborhood becomes more crowded, however, the Pedersen model becomes incapable of capturing the behavior of the grafted chains, since it does not consider chain-chain interactions. The brush thickness of the model does not depend on the grafting density, as can be seen from the inset to Figure 4.15, where the position of the oscillation is roughly the same for all systems.

The effect of grafted molar mass on the scattering of the corona is illustrated in Figure 4.16. In analogy to the figure before, the structure factor of the grafted corona is presented under silica-matched conditions. It is evident that increasing the molar mass of the grafted chains increases the height of the polymeric brush. This is clearly manifested by the shifting of the structure factor oscillation to smaller k-values. The molar mass dependence of the corona scattering is also predicted by the Pedersen model, as can be seen in the inset of Figure 4.16, where both the position and the shape of the oscillation changes as a function of the chains molar mass. As the molar mass of the grafted chains increases, the "terraced" profile of $S_\mathrm{g}(k)$

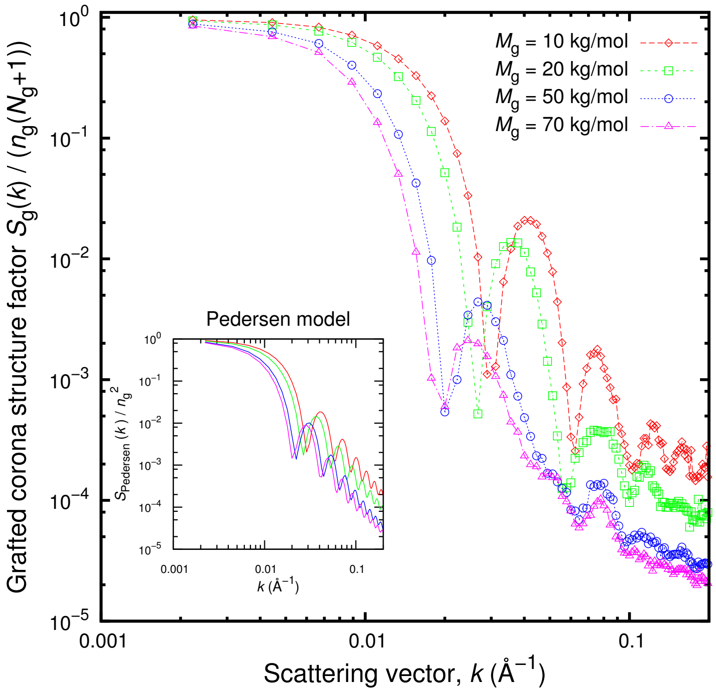

Figure 4.16: Scattering curves of the deuterated grafted corona inside the silica matched matrix ($M_\mathrm{f} = 100$ kg/mol). The molar mass of the grafted chains varies from 10 to 70 kg/mol. The radius of the particle is $\alpha_\mathrm{p} = 8$ nm with grafting density of 0.5 nm^{-2}.

becomes less structured and falls off very rapidly. This is due to the high interpenetration of the chains as the brush becomes denser.

Finally, the influence of the matrix molar mass on the scattering of grafted chains is examined in Figure 4.17. Along with the simulation results and the theoretical modeling, experimental results from Chevigny et al.[260] are also presented. The variation of the matrix seems not to affect strongly the form of the grafted corona. The proposed FTiMC methodology seems to capture rather well the profile of $S_\mathrm{g}(q)$. The position of the oscillations is the same between experimental and simulation results. However, simulation results are more structured, with strong peak maxima and minima, which are most likely due to the inherently discrete nature of the FTiMC model (chain mass localized in discrete Kuhn segments, rather than distributed along chain backbone). Moreover, the simulations consider only monodisperse grafted and free chains, which is not the case for the experimental studies. The incorporation of polydispersity in the FTiMC simulations would yield smoother scattering curves.

4.4 Summary and Conclusions

Soft polymer properties are improved by inclusion of small hard inorganic particles inside the melt matrix. The strategy of tethering polymer chain ends onto the surface of the filler parti-

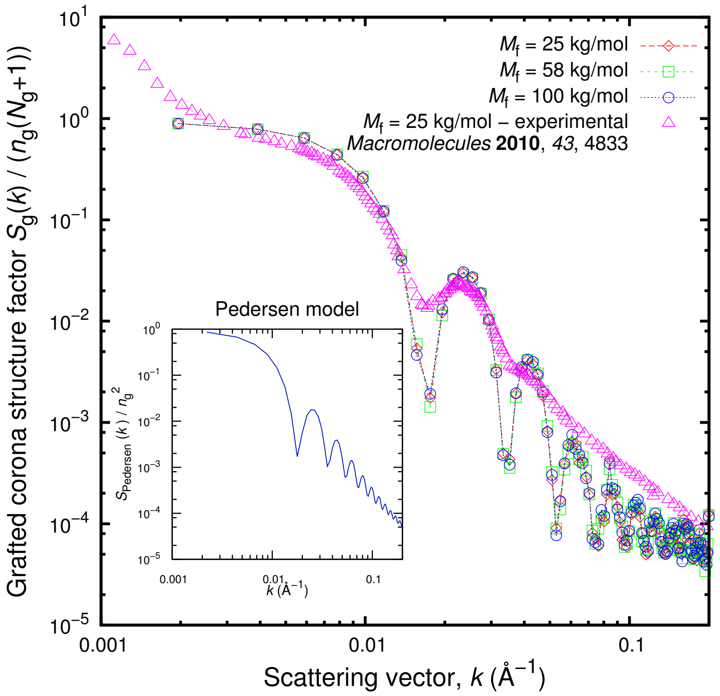

Figure 4.17: Scattering curves of the grafted corona ($M_g = 25$kg/mol) inside the silica matched matrix. The radius of the particle is 13 nm while the molar mass of the matrix varies from 25 to 100 kg/mol. Experimental results by Chevigny et al.[260] for the same system are also presented.

cles, in order to render the nanoparticles miscible with their homopolymer hosts, is promising. The structural features of such mixtures are surprisingly rich, since competing interactions between the nanoparticles, grafted and matrix chains engender the formation of different phases. Overall, the phase behavior of these polymer nanocomposites may be tailored through control of the following parameters: grafting chain length, host chain length and grafting density, for a given filler. In this work we have presented a methodology that is capable of treating realistic polymer nanocomposites at experimentally relevant length scales. The sampling, through a MC procedure, of a composite system obeying a simplified Hamiltonian based on polymer mean field theory, can give us insights into structure at length scales on the order of hundreds of nanometers.

Our results include a number of salient points: (i) We show that by increasing the particle grafting density the brush of grafted chains undergoes a phase transition from its stretched to its collapsed form, in agreement to scaling theories[244] and MD simulations.[247] The phase transition has been attributed to the autophobic dewetting of the brush by the melt. (ii) Increasing the brush chain length leads to thicker grafted brushes, which improve the miscibility of nanoparticles with the homopolymer matrix, in agreement with SCF studies.[242] (iii) The density distributions around a nanoparticle seem to depend only on grafting density and grafted chain length, especially when the matrix chain length is equal to or longer than the grafted chain length. "Wet-to-dry" conformational transition[260] has not been observed. (iv) The scaling of polymeric layers grafted to nanoparticles can be well described by the model proposed by Daoud and Cotton[232] for star-shaped polymers. The brush thickness scales with the inverse second power of the grafted chain length and the inverse fourth power of the grafted density.

For the first time, a real experimental system is mapped onto a simulation framework and results which can be directly compared with experimental findings are provided. The coarse-grained model employed in the present work can treat length scales accessible by SANS experiments. Single chain and corona scattering spectra have been estimated from simulations in order to investigate the influence of grafted chain specifications on their conformations and overall brush thickness. At the single chain level, grafted chains deviate strongly from their random walk statistics, especially for high surface coverage and molar mass. Moreover, the scattering of the whole corona has been analyzed. The brush thickness increases with increasing molar mass of the grafted chains, shifting the scattering peaks to lower k-values, in agreement with the model proposed by Pedersen[293] for the scattering of block copolymer micelles. The corona structure factors for 13-nm-radius grafted particles dispersed in different molar mass matrices have been validated against experimental findings of Chevigny et al.[260]

The present study is limited to the case of a single nanoparticle immersed in a homogeneous polymer matrix. As Kalb et al.[247] stated, simulations of a single particle at infinite dilution cannot reveal the critical conditions that distinguish aggregation from dispersion. It is highly interesting to analyze the collective effects on the structure of the brush and the melt when two or more nanoparticles are present at experimental volume fractions. Also, the interaction and the equilibrium conformation of these systems would be of ultimate importance.

5 Equation of State Based Slip Spring Model for Polymer Dynamics

A particle based, Brownian Dynamics (BD) methodology for the simulation of entangled polymer melts and rubbers has been developed in order to access the ms-timescale of these systems. The polymeric beads consist of several Kuhn segments. Their motion is dictated by the Helmholtz energy of the sample which is initially written as a sum of three contributions: entropy springs, representing the entropic elasticity of chain strands between beads; slip-springs; and non-bonded interactions. The entanglement effect is introduced by the slip-springs, which are springs connecting nodes on two different polymer chains. The terminal positions of slip-springs are altered during the simulation through a hopping kinetic Monte Carlo (kMC) scheme. In addition, there are construction/destruction processes for the slip-springs. The free energy of nonbonded interactions is derived from an appropriate equation of state and it is computed as a functional of the local density by passing an orthogonal grid through the simulation box; accounting for it is necessary for reproducing the correct compressibility of the polymeric material. Parameters needed in the model can be derived from experimental volumetric and viscosity data or from atomistic Molecular Dynamics (MD) simulations (Chapter 3). Initial configurations of the network are obtained from further coarse-graining Field Theory-inspired Monte Carlo (FTiMC) structures (Chapter 4). Natural rubber is the material of choice, since the ultimate goal of this effort is to address the mechanical reinforcement of nanoparticle-filled elastomers.

5.1 Introduction

5.1.1 Previous Work

One of the fundamental concepts in the molecular description of structure - property relations of polymer melts is chain *entanglement*. When macromolecules interpentrate, the term entanglements intends to describe the topological interactions resulting from the *uncrossability* of chains. The fact that two polymer chains cannot cross though each other in the course of their motion changes dramatically their dynamical behavior, without altering their equilibrium properties. Anogiannakis et al.[19] have examined microscopically at what level topological constraints can be described as a collective entanglement effect, as in tube model theories, or as certain pairwise uncrossability interactions, as in slip-link models. They employed a novel methodology, which analyzes entanglement constraints into a complete set of pairwise interactions, characterized by a spectrum of confinement strengths. As a measure of the entanglement strength, these authors used the fraction of time for which the links are active. The confinement was found to be mainly imposed by the strongest links. The weak, trapped, uncrossability interactions cannot contribute to the low frequency modulus of an elastomer, or the plateau modulus of a melt.

In tube model theories,[21,89,295,296] (Section 2.3.4/v on page 41) it is postulated that the entanglements generate a confining mean field potential, which restricts the lateral monomer motion to a tube-like region surrounding each chain. In polymer melts the confinement is not permanent, but leads to the one- dimensional diffusion of the chain along its tube, called *reptation*.[93] An alternative, discrete, localized version of the tube constraint is utilized in models employing *slip-links*.[95,297–302] The tube is replaced by a set of slip-links along the chain, which restrict lateral motion but permit chain sliding through them. The real chain is represented by its primitive path (PP), which is a series of strands of average molar mass M_e connecting the links.

Following Hua and Schieber,[300,301] the molecular details on the monomer or Kuhn-length level are smeared out in the slip-link model, while the segmental network of generic polymers is directly modeled, by introducing links between chains, which constrain the motion of segments of each chain into a tubular region. The motion of segments is updated stochastically, and the positions of slip-links can either be fixed in space, or mobile. When either of the constrained segments slithers out of a slip-link constraint, they are considered to be disentangled, and the slip-link is destroyed. Conversely, the end of one segment can hop towards another segment and create another new entanglement or slip-link. The governing equations in the slip-link model can be split into two parts: the chain motion inside its tube is governed by Langevin equations and the tube motion is governed by deterministic convection and stochastic constraint release processes. Based on the tube model,[89] it is assumed that the motion of the primitive path makes the primary contribution to the rheological properties of entangled polymer melts. Therefore, from the microscopic information given by the slip-link model, these authors could precisely access the longest polymer chain relaxation time. Moreover, by employing an elegant formulation, the macroscopic properties of polymer melts, i.e., stress and dielectric relaxation can be extracted from the ordering, spatial location and aging of the entanglements or slip-links in the simulations.

Later, Schieber and co-workers studied the fluctuation effect on the chain's entanglement and viscosity using a mean-field model.[303] Shanbhag et al.[304] developed a dual slip-link model with chain-end fluctuations for entangled star polymers, which explained the observed deviations from the "dynamic dilution" equation in the dielectric and stress relaxation data. Doi and Takimoto[305] adopted the dual slip-link model to study the nonlinear rheology of linear and star polymers with arbitrary molecular weight distribution.

Likhtman[306] has shown that the standard tube model cannot be applied to neutron spin-echo measurements because the statistics of a one-dimensional chain in a three-dimensional random-walk tube become wrong on the length scale of the tube diameter. He then introduced a new single-chain dynamic slip-link model to describe the experimental results for neutron spin echo, linear rheology and diffusion of monodisperse polymer melts. All the parameters in this model were obtained from one experiment and were applied to predict other experimental results. The model was formulated in terms of stochastic differential equations, suitable for BD simulations. The results were characterized by some systematic discrepancies, suggesting possible inadequacy of the Gaussian chain model for some of the polymers considered, and possible inadequacy of the time - temperature superposition principle.

Masubuchi et al.[307] performed several multichain simulations for entangled polymer melts by utilizing slip links to model the entanglements. These authors proposed a primitive chain network model, in which the polymer chain is coarse-grained into segments connected by entanglements. Different segments are coupled together through the force balance at the entanglement node. The Langevin equation is applied to update the positions of these entanglement nodes, by incorporating the tension force from chain segments and an osmotic force caused by density fluctuations. The entanglement points, modeled as slip-links, can also fluctuate spatially (or three dimensionally). The creation and annihilation of entanglements are controlled by the number of monomers at chain ends. The longest relaxation time and the self-diffusion coefficient scaling, as predicted from the model, were found in good agreement with experimental results. Later on, the primitive chain network model was extended to study the relationship between entanglement length and plateau modulus.[308–311] It was also extended to study star and branched polymers,[312] nonlinear rheology,[313–315] phase separation in polymer blends,[316] block copolymers[317] and the dynamics of confined polymers.[318]

Chappa et al.[319] proposed a slip-link model, in which the topological effect of noncrossability of long flexible macromolecules is effectively taken into account by *slip-springs*. Entanglements in this model are represented by local, pairwise, translationally and rotatationally invariant interactions between polymer beads that do not affect the equilibrium properties of the melt. The conformations of polymers and slip springs are updated by a hybrid Monte Carlo (MC) scheme. At every step, either the positions of the beads are evolved via a short Dissipative Particle Dynamics (DPD) run or the configuration of the slip-springs is modified by MC moves, involving discrete jumps of the slip-springs along the chain contour and creation or deletion at the chain ends. The number of slip-springs can vary during the simulation, obeying a prescribed chemical potential. That model can correctly describe many aspects of the dynamical and rheological behavior of entangled polymer liquids in a computationally efficient manner, since everything is cast into only pairwise-additive interactions between beads. The mean-square displacement of the beads evolving according to this model was found to be in favorable agreement with the tube model predictions (Section 2.3.4/v on page 41). Moreover, the model exhibited realistic shear thinning, deformation of conformations, and a decrease of the number of entanglements at high shear rates.

Closely related to the work of Chappa et al.[319] is the slip-spring model introduced by Ramírez-Hernández et al.[320] In that model, the discrete hopping of a slip-spring along the chain contour is replaced by a one-dimensional continuous Langevin equation. Slip-springs consist of two rings that slip along different chain contours, and are connected by a harmonic spring. The rings move in straight lines between beads belonging to different chains, scanning the whole contour of the chains in a continuous way. More recently, Ramírez-Hernández et al.[321] presented a more general formalism in order to qualitatively capture the linear rheology of pure homopolymers and their blends, as well as the nonlinear rheology of highly entangled polymers and the dynamics of diblock copolymers. The number of slip-springs in their approach remains constant throughout the simulation, albeit their connectivity changes.

The idea of slip-springs was in parallel used by Uneyama and Masubuchi,[322] who proposed a multi-chain slip-spring model inspired by the single chain slip-spring model of Likhtman.[306] Differently from the primitive chain network model of the same authors, they defined the total free energy for the new model, and employed a time evolution equation and stochastic processes for describing its dynamical evolution. All dynamic ingredients satisfy the detailed balance condition, thus capable of reproducing the thermal equilibrium which is characterized by the free energy. The number of slip-springs varies. Later, Langeloth et al.[323] presented a simplified version of the slip-spring model of Uneyama and Masubuchi,[322] where the number of slip-springs remains constant throughout the simulation.

Working on a different problem than melt rheology, Terzis et al.[324–326] have invoked the microscopic description of entanglements and the associated processes envisioned in the slip-link models, in order to generate entanglement network specimens of interfacial polymeric systems and study their deformation to fracture. The specimens were created by sampling the configurational distribution functions derived from a Self Consistent Field (SCF) lattice model. Despite the fact that overstretched strands were allowed to relax by a MC method, the specimens generated were not in *detailed mechanical equilibrium*. To this end, these authors developed a method for relaxing the network with respect to its density distribution, and thereby imposing the condition of mechanical equilibrium, without changing the network topology.[326] The free energy function of the network was minimized with respect to the coordinates of all entanglement points and chain ends. Contributions to the free energy included (a) the elastic energy due to stretching of the chain strands and (b) the free energy due to the repulsive and attractive (cohesive) interactions between segments. The latter was calculated by superimposing a simple cubic grid on the network and taking into account contributions between cells and within each cell. The free energy minimization procedure was first applied to a bulk polypropylene system, serving as a basis for parametrizing the model and validating the method against experimental data. The free energy minimization was then applied to mechanically relax computer specimens of a polypropylene/polyamide6 (PP/PA6) interfacial system, strengthened by PP chains grafted onto the PA6 surface. The fully relaxed networks served as a starting point for the mesoscopic simulation of fracture phenomena, caused by the application of tensile stress perpendicular to the interface. The network was deformed at a constant strain rate and the network topology evolved according to elementary mechanical processes of chain scission, chain slippage, disentanglement, and reentanglement, in analogy to processes envisioned in slip-link models. Chain slippage across an entanglement point occurs according to a Zhurkov activated rate equation with parameters derived from viscosity data. Each cycle of the kMC algorithm used to track the deformation process, consisted of the imposition of a small incremental strain on the network, relaxation to mechanical equilibrium, introduction of the micromechanical processes mentioned above, and again relaxation to mechanical equilibrium. The MC cycles were repeated until fracture occured.

5.1.2 Proposed Approach

In Chapter 4,[176,327] we have developed a methodology in order to generate and equilibrate (nanocomposite) polymer melts at large length scales (in the order of 100 nm). This coarse-grained representation is based on the idea that the polymer chains can be described as random walks at length scales larger than that defined by the Kuhn length of the polymer. Now, we develop a methodology to track the dynamics of the system at this coarse-grained level, by

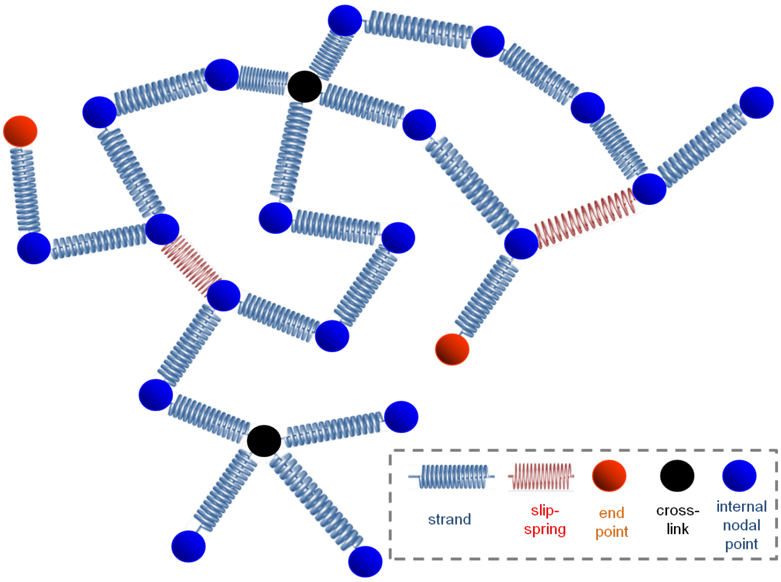

Figure 5.1: Network representation of a polymer melt or rubber. End beads, internal beads, crosslink beads (if present) are shown as red, blue and black spheres, respectively. Entropic springs along the chain contour are shown in blue, while slip-springs are shown in red.

invoking a well defined free energy functional for the model, where both conformational and nonbonded interactions are taken into account. Once the free energy is known, BD simulations driven by the free energy functional can be used in order to obtain thermodynamic averages and correlation functions. When macromolecules interpenetrate, the term *entanglement* intends to describe the interactions resulting from the uncrossability of chains. At this level of description, we introduce the entanglements as slip-springs connecting beads belonging to different chains. In the course of a simulation, the topology of the entanglement network changes through the introduction of elementary kMC events governed by rate expressions which are based on the reptation picture of polymer dynamics and the free energy defined.

5.2 Model and Simulation Methodology

5.2.1 Polymer Description

Our melt consists of chains, represented by specific points (i.e. internal beads or ends) along their contour, connected by entropy springs. Each coarse-grained bead represents several Kuhn segments of the polymer under consideration. Our construction results in a set of nodes for each chain, where each node i has a specific contour position along the chain, positional vector in three-dimensional space, $\mathbf{r}_i$, and pairing with other nodes, as shown in Figure 5.1. The piece of chain between two nodes (blue spring in Figure 5.1) is referred to as a *strand*.

We introduce the effect of entanglement by dispersing slip-springs,[319] which are designed to bring about reptational motion of chains along their contours, as envisioned in theories and simulations of dynamics in entangled polymer melts and as observed by topological analysis of molecular configurations evolving in the course of MD simulations.[19] In more detail, a slip-spring connects two internal nodal points of two different polymer chains and is stochastically destroyed when one of the nodes it connects is a chain- end. To compensate for slip-spring destruction, new slip springs are created stochastically by free chain ends in the polymer network. Along with the BD simulation of the beads' motion in the periodic simulation box, a parallel kMC evolution of the slip-springs present is undertaken. The rates used for the kMC procedure are described in detail in the following paragraphs. The initial contour length between consecutive entanglement points (slip-spring anchoring beads) on the same chain is commensurate with the entanglement molecular weight, M_{e}, of the simulated polymer.

The relative importance of reptation, constraint release and contour-length fluctuation mechanisms depends on the specific melt of interest. As expected, in a monodisperse sample of long molecules, reptation plays a dominant role. In contrast, in a bidisperse sample composed of short and long macromolecules, constraint release and contour length fluctuations may dominate the relaxation process.[328–331]

5.2.2 Model Free Energy

We postulate that the entangled melt specimen of given spatial extent, defined by the edge vectors of our periodic simulation box (L_x, L_y, L_z), under temperature T, is governed by a Helmholtz energy function, which has a direct dependence on the set of local densities $\{\rho(\mathbf{r})\}$, the temperature, T, and the separation vectors between pairs of connected polymer beads, $\{\mathbf{r}_{ij}\}$:

$$A\big(\{\mathbf{r}_{ij}\},\{\rho(\mathbf{r})\},T\big) = A_{\text{b}}\big(\{\mathbf{r}_{ij}\},T\big) + A_{\text{nb}}\big(\{\rho(\mathbf{r})\},T\big) \tag{5.1}$$

The first term on the right-hand side of eq 5.1, A_{b}, is the contribution of bonded interactions, whereas the second one, A_{nb} is the contribution of the nonbonded interactions to the Helmholtz energy.

We start by considering the bonded contribution to the Helmholtz energy, which can be written as a sum over all bonded pairs, (i,j), where i is connected to j with either intramolecular springs or slip-springs:

$$A_{\text{b}}\big(\{\mathbf{r}_{ij}\},T\big) = A_{\text{b}}\big(\{r_{ij}\},T\big) = \sum_{(i,j)} A_{\text{pair}}(r_{ij},T) \tag{5.2}$$

The sum runs over all pairs, where each pair is thought to interact via a distance-dependent Helmholtz energy, $A_{\text{pair}}\left(r_{ij},T\right)$. The elastic force depends on the coordinates of the nodes, but it does not depend on the local network density. The elastic force between connected beads arises due to the retractive force acting to resist the stretching of a strand. This force originates in the decrease in entropy of a stretched polymer strand. For a detailed discussion, please consult section 2.3.3 on page 35. In this approximation, the force on bead i, due to its connection to bead j is:

$$\mathbf{F}_{ij}^{\text{b}} = -\nabla_{\mathbf{r}_{ij}} A_{\text{pair}}\left(r_{ij},T\right) \tag{5.3}$$

The Gaussian approximation can be used for most extensions.[332] The conformational entropy of strands is taken into account via a simple harmonic expression (eq 2.90, page 36):

$$A_{\text{pair}}^{\text{intra}}\left(r_{ij},T\right) = \frac{3}{2} k_{\text{B}} T \frac{r_{ij}^2}{N_{ij} b_{\text{K}}^2} \tag{5.4}$$

where N_{ij} is the number of Kuhn segments assigned to the strand, b_{K} the Kuhn length of the polymer and k_{B} the Boltzmann constant. The summation is carried over all pairs (i,j) which lie along the contour of the chains. The Helmholtz energy of slip-springs, which are included to account for the entanglement effect, is described by the following equation:

$$A_{\text{pair}}^{\text{sl}}\big(r_{ij},T\big) = \frac{3}{2} k_{\text{B}} T \frac{r_{ij}^2}{l_{\text{sl}}^2} \tag{5.5}$$

where l_{sl} is an adjustable parameter which should be larger than the Kuhn length, b_{K}, and smaller than or equal to the tube diameter of the polymer, a_{pp}.

In order to account for nonbonded (excluded volume and van der Waals attractive) interactions in the network representation, we introduce a free energy:

$$A_{\text{nb}}\left(\rho,T\right) = \int_{\text{box}} \text{d}^3 r \; a_{\text{vol}}\left[\rho\left(\mathbf{r}\right),T\right] \tag{5.6}$$

where a_{vol} is a free energy density (free energy per unit volume) and $\rho\left(\mathbf{r}\right)$ is the local mass density at position $\mathbf{r}$. Expressions for $a_{\text{vol}}\left(\rho,T\right)$ may be extracted from equations of state (please see Section 2.3.5 on page 45). Local density, $\rho\left(\mathbf{r}\right)$, will be resolved only at the level of entire cells, defined by passing an orthogonal grid through the entire simulation domain. Thus, eq 5.6 will be approximated by a discrete sum over all cells of the orthogonal grid:

$$A_{\text{nb}}\left(\rho,T\right) = \sum_{k\in\text{cells}} V_{\text{cell},k}^{\text{acc}} \, a_{\text{vol}}\left(\rho_{\text{cell},k},T\right) \tag{5.7}$$

where $V_{\text{cell},k}^{\text{acc}}$ is the accessible volume of the cell k. The cell density, $\rho_{\text{cell},k}$, must be defined based on the beads in and around the cell k.

In this work we invoke the Sanchez-Lacombe equation of state,[110] which gives for the Helmholtz energy (eq 2.131 page 48):

$$\begin{aligned} A^{\text{SL}}(\rho, T) = & -\tilde{\rho} N r k_{\text{B}} T^{*} + N r k_{\text{B}} T \left[(\tilde{v} - 1) \ln (1 - \tilde{\rho}) + \frac{1}{r} \ln (\tilde{\rho}) \right] \\ & - N k_{\text{B}} T \ln (w) \end{aligned} \tag{5.8}$$

where k_{B} is the Boltzmann's constant and the Sanchez-Lacombe parameters are presented in Table 2.1, page 47. The last term in eq 5.8 does not depend on the density of the system, being an ideal gas contribution (please see discussion before eq 2.136 on page 49).

The Helmholtz energy density, $a_{\text{vol}}(\rho, T)$, can be calculated as:

$$a_{\text{vol}}(\rho, T) = \frac{A(\rho, T)}{V} = \frac{A(\rho, T)}{NM/\rho} = \rho \frac{A(\rho, T)}{NM} = \rho\, a_{\text{mass}}(\rho, T) \tag{5.9}$$

where the $a_{\text{mass}}(\rho, T)$ denotes the Helmholtz energy per unit mass of the system. Based on eq 5.8, we can calculate the above:

$$a_{\text{mass}}(\rho, T) = -\frac{r k_{\text{B}} T^{*} \tilde{\rho}}{M} + \frac{r k_{\text{B}} T}{M} \left[(\tilde{v} - 1) \ln (1 - \tilde{\rho}) + \frac{1}{r} \ln (\tilde{\rho}) \right] - \frac{k_{\text{B}} T}{M} \ln (w) \tag{5.10}$$

and by using $M = r \rho^{*} v^{*}$ and $r = (M p^{*}) / (\rho^{*} k_{\text{B}} T^{*})$ the above expression becomes:

$$a_{\text{mass}}(\rho, T) = -\frac{p^{*}}{\rho^{*2}} \rho + \frac{p^{*} \tilde{T}}{\rho^{*}} \left[\left(\frac{\rho^{*}}{\rho} - 1 \right) \ln \left(1 - \frac{\rho}{\rho^{*}} \right) + \frac{\rho^{*} k_{\text{B}} T^{*}}{M p^{*}} \ln \left(\frac{\rho}{\rho^{*} w} \right) \right] \tag{5.11}$$

The Helmholtz energy density (free energy per unit volume), $a_{\text{vol}}(\rho, T)$ is:

$$\begin{aligned} a_{\text{vol}}(\rho, T) = & \rho\, a_{\text{mass}}(\rho, T) \\ = & -p^{*} \tilde{\rho}^{2} + p^{*} \tilde{T} \tilde{\rho} \left[\left(\frac{1}{\tilde{\rho}} - 1 \right) \ln (1 - \tilde{\rho}) + \frac{\rho^{*} k_{\text{B}} T^{*}}{M p^{*}} \ln \left(\frac{\tilde{\rho}}{w} \right) \right] \end{aligned} \tag{5.12}$$

where everything is cast in terms of the reduced variables T^{*}, p^{*}, ρ^{*} and the molecular weight of a chain, M. All these parameters can be obtained from experimental studies.[333]

The force due to non-bonded interactions on a bead i is given by:

$$\begin{aligned}\mathbf{F}_i^{\mathrm{nb}} &= -\nabla_{\mathbf{r}_i} A_{\mathrm{nb}}\left(\{\rho_{\mathrm{cell}}\}, T\right) = -\frac{\partial}{\partial \mathbf{r}_i}\left[\sum_{k \in \mathrm{cells}} V_{\mathrm{cell},k}^{\mathrm{acc}} a_{\mathrm{vol}}\left(\rho_{\mathrm{cell},k}, T\right)\right] \\ &= -\sum_{k\,\in\,\mathrm{cells}} V_{\mathrm{cell},k}^{\mathrm{acc}} \left.\frac{\partial a_{\mathrm{vol}}(\rho, T)}{\partial \rho}\right|_{\rho=\rho_{\mathrm{cell},k}} \frac{\partial \rho_{\mathrm{cell},k}}{\partial \mathbf{r}_i} \end{aligned} \tag{5.13}$$

with the derivative of $a_{\mathrm{vol}}(\rho, T)$ with respect to density being:

$$\frac{\partial a_{\mathrm{vol}}(\rho, T)}{\partial \rho} = -\frac{2p^*}{\rho^{*2}}\rho - \frac{p^* T}{\rho^* T^*}\left[1 + \ln\left(1 - \frac{\rho}{\rho^*}\right)\right] + \frac{k_{\mathrm{B}} T}{M}\left[1 + \ln\left(\frac{\rho}{\rho^* w}\right)\right] \tag{5.14}$$

and the derivative $\partial \rho_{\mathrm{cell},k} / \partial \mathbf{r}_i$ given by eq C.5 in Appendix C on page 207.

5.2.3 Model Stress Tensor

We consider the free energy per unit mass, $A\big(\{\mathbf{r}_{ij}\}, \{\rho(\mathbf{r})\}, T\big)/m$ as a function of the separation vectors between all connected beads, $\{\mathbf{r}_{ij}\}$, local densities, $\{\rho(\mathbf{r})\} \equiv \{\rho_{\mathrm{cell}}\}$ and temperature, T. The thermodynamic stress tensor, $\boldsymbol{\tau}$ is given by eq 2.172:

$$\boldsymbol{\tau} = \rho_{\mathscr{R}}\, \mathbb{F} \cdot \left(\frac{\partial\left(A\big(\{\mathbf{r}_{ij}\}, \{\rho_{\mathrm{cell}}\}, T\big)/m\right)}{\partial \mathbb{F}}\right)^{\mathrm{T}} \tag{5.15}$$

where A is the total Helmholtz energy (eq 5.1) and m is the total mass in the system. It should be noted that density, $\rho_{\mathscr{R}}$, refers to the reference, $\mathscr{R}$, configuration of the system. $\mathbb{F}$ denotes the deformation gradient tensor defined through a mapping of a infinitesimal vector d$\mathbf{x}$ of the initial configuration onto the infinitesimal vector d$\mathbf{x}'$ after the deformation, through eq 2.29. Eq 5.15 can be written in component form as:

$$\tau_{\alpha\beta} = \rho_{\mathscr{R}} \sum_{\gamma=1}^{3} \mathbb{F}_{\alpha\gamma} \frac{\partial\left(A\big(\{\mathbf{r}_{ij}\}, \{\rho_{\mathrm{cell}}\}, T\big)/m\right)}{\partial \mathbb{F}_{\beta\gamma}} \tag{5.16}$$

Invoking the functional dependence of our Helmholtz energy:

$$\begin{aligned}\tau_{\alpha\beta} &= \frac{\rho_{\mathscr{R}}}{m} \sum_{\gamma=1}^{3} \mathbb{F}_{\alpha\gamma}\left[\frac{\partial A_{\mathrm{b}}\left(\{r_{ij}\}, T\right)}{\partial \mathbb{F}_{\beta,\gamma}} + \frac{\partial A_{\mathrm{nb}}\left(\{\rho_{\mathrm{cell}}\}, T\right)}{\partial \mathbb{F}_{\beta\gamma}}\right] \\ &= \tau_{\alpha\beta}^{\mathrm{b}}\big(\{r_{ij}\}, T\big) + \tau_{\alpha\beta}^{\mathrm{nb}}\big(\{\rho_{\mathrm{cell}}\}, T\big)\end{aligned} \tag{5.17}$$

where

$$\tau^{\mathrm{b}}_{\alpha\beta}\big(\{r_{ij}\},T\big) = \frac{1}{V_{\mathscr{R}}}\sum_{\gamma=1}^{3}\mathbb{F}_{\alpha\gamma}\left\{\frac{\partial}{\partial \mathbb{F}_{\beta\gamma}}\left[\sum_{(i,j)} A_{\text{pair}}\left(r_{ij},T\right)\right]\right\} \tag{5.18}$$

is the bonded contribution to the stress tensor, and

$$\tau^{\mathrm{nb}}_{\alpha\beta}\left(\{\rho_{\text{cell}}\},T\right) = \frac{1}{V_{\mathscr{R}}}\sum_{\gamma=1}^{3}\mathbb{F}_{\alpha\gamma}\left\{\frac{\partial}{\partial \mathbb{F}_{\beta\gamma}}\left[\sum_{k\,\in\,\text{cells}} V^{\text{acc}}_{\text{cell},k} a_{\text{vol}}\left(\rho_{\text{cell},k},T\right)\right]\right\} \tag{5.19}$$

is the nonbonded contribution to the stress tensor.

We start by calculating the bonded contribution to the stress tensor, which depends only on the distances between connected pair of atoms, r_{ij}, and temperature, T:

$$\begin{aligned}
\tau^{\mathrm{b}}_{\alpha\beta}\left(\{r_{ij}\},T\right) &= \frac{1}{V_{\mathscr{R}}}\sum_{\gamma=1}^{3}\mathbb{F}_{\alpha\gamma}\left\{\sum_{(i,j)}\left[\frac{\partial A_{\text{pair}}\left(r_{ij},T\right)}{\partial \mathbb{F}_{\beta\gamma}}\right]\right\} \\
&= \frac{1}{V_{\mathscr{R}}}\sum_{\gamma=1}^{3}\mathbb{F}_{\alpha\gamma}\left\{\sum_{(i,j)}\left[\frac{\partial A_{\text{pair}}\left(r_{ij},T\right)}{\partial r_{ij}}\frac{\partial r_{ij}}{\partial \mathbb{F}_{\beta\gamma}}\right]\right\} \\
&= \frac{1}{V_{\mathscr{R}}}\sum_{(i,j)}\frac{\partial A_{\text{pair}}\left(r_{ij},T\right)}{\partial r_{ij}}\sum_{\gamma=1}^{3}\frac{\partial r_{ij}}{\partial \mathbb{F}_{\beta\gamma}}\mathbb{F}_{\alpha\gamma} \\
&= \frac{1}{V_{\mathscr{R}}}\sum_{(i,j)}\frac{\partial A_{\text{pair}}\left(r_{ij},T\right)}{\partial r_{ij}}\sum_{\gamma=1}^{3}\frac{\partial r_{ij}}{\partial r_{ij,\beta}}\frac{\partial r_{ij,\beta}}{\partial \mathbb{F}_{\beta\gamma}}\mathbb{F}_{\alpha\gamma} \\
&= \frac{1}{V_{\mathscr{R}}}\sum_{(i,j)}\frac{\partial A_{\text{pair}}\left(r_{ij},T\right)}{\partial r_{ij}}\frac{r_{ij,\beta}}{r_{ij}}\sum_{\gamma=1}^{3}\frac{\partial r_{ij,\beta}}{\partial \mathbb{F}_{\beta\gamma}}\mathbb{F}_{\alpha\gamma}
\end{aligned} \tag{5.20}$$

where we have made use of the fact that the partial derivative of the Euclidean norm of a vector $\mathbf{a} = (a_1, a_2, ..., a_n)$ with respect to one of its components, a_j, is:

$$\frac{\partial \left\|\mathbf{a}\right\|}{\partial a_j} = \frac{\partial}{\partial a_j}\left(\sqrt{\sum_{i=1}^{n} a_i^2}\right) = \frac{1}{2\left\|\mathbf{a}\right\|}\sum_{i=1}^{n}\left[\frac{\partial}{\partial a_j}\left(a_i^2\right)\right] = \frac{a_j}{\left\|\mathbf{a}\right\|} \tag{5.21}$$

It should be noted that eq 5.20 is valid for any kind of deformation (both affine and nonaffine).

We envision, that at a certain time, a homogeneous deformation is applied on the polymer that displaces bond ends affinely, in the sense that their positions are changed in the same way as material points in a macroscopic continuum description. Straight parallel lines in the reference configuration map to straight parallel lines in the deformed configuration Let $\mathbf{r}_i$ and $\mathbf{r}_j$ be the positions of the start and the end of the bonded beads before the deformation and $\mathbf{r}'_i$

and $\mathbf{r}'_j$ the positions of the same beads after the deformation, then:

$$\mathbf{r}'_i = \mathbb{F}\mathbf{r}_i \tag{5.22}$$

$$\mathbf{r}'_j = \mathbb{F}\mathbf{r}_j \tag{5.23}$$

By subtracting eq 5.23 from eq 5.22, we get:

$$\mathbf{r}'_{ij} = \mathbb{F}\mathbf{r}_{ij} \tag{5.24}$$

Thus, one component of the deformed vector is connected to the components of the undeformed through the relation:

$$r'_{ij,\beta} = \sum_{\gamma=1}^{3} \mathbb{F}_{\beta\gamma} r_{ij,\gamma} \tag{5.25}$$

and the derivative appearing in eq 5.20 can now be calculated:

$$\frac{\partial r_{ij,\beta}}{\partial \mathbb{F}_{\beta\gamma}} = r_{ij,\gamma} \tag{5.26}$$

Eq 5.20 takes the form:

$$\begin{aligned} \tau^{\text{b}}_{\alpha\beta}\left(\{r_{ij}\},T\right) &= \frac{1}{V_{\mathscr{R}}} \sum_{(i,j)} \frac{\partial A_{\text{pair}}\left(r_{ij},T\right)}{\partial r_{ij}} \frac{r_{ij,\beta}}{r_{ij}} \sum_{\gamma=1}^{3} r_{ij,\gamma}\mathbb{F}_{\alpha\gamma} \\ &= \frac{1}{V_{\mathscr{R}}} \sum_{(i,j)} \frac{\partial A_{\text{pair}}\left(r_{ij},T\right)}{\partial r_{ij}} \frac{r_{ij,\beta} r_{ij,\alpha}}{r_{ij}} \end{aligned} \tag{5.27}$$

where the virial theorem (eq 2.159) is recovered.[134]

We now move to the estimation of the nonbonded contribution to the stress tensor, $\tau^{\text{nb}}_{\alpha\beta}$:

$$\begin{aligned} \tau^{\text{nb}}_{\alpha\beta}\left(\{\rho_{\text{cell}}\},T\right) &= \frac{1}{V_{\mathscr{R}}} \sum_{\gamma=1}^{3} \mathbb{F}_{\alpha\gamma} \left\{ \frac{\partial}{\partial \mathbb{F}_{\beta\gamma}} \left[\sum_{k\,\in\,\text{cells}} V^{\text{acc}}_{\text{cell},k} a_{\text{vol}}\left(\rho_{\text{cell},k},T\right) \right] \right\} \\ &= \frac{1}{V_{\mathscr{R}}} \sum_{\gamma=1}^{3} \mathbb{F}_{\alpha\gamma} \sum_{k\,\in\,\text{cells}} \left[\frac{\partial V^{\text{acc}}_{\text{cell},k}}{\partial \mathbb{F}_{\beta\gamma}} a_{\text{vol}}\left(\rho_{\text{cell},k},T\right) \right] \\ &+ \frac{1}{V_{\mathscr{R}}} \sum_{\gamma=1}^{3} \mathbb{F}_{\alpha\gamma} \sum_{k\,\in\,\text{cells}} \left[V^{\text{acc}}_{\text{cell},k} \frac{\partial a_{\text{vol}}\left(\rho_{\text{cell},k},T\right)}{\partial \mathbb{F}_{\beta\gamma}} \right] \\ &= \frac{1}{V_{\mathscr{R}}} \sum_{k\,\in\,\text{cells}} a_{\text{vol}}\left(\rho_{\text{cell},k},T\right) \sum_{\gamma=1}^{3} \mathbb{F}_{\alpha\gamma} \frac{\partial V^{\text{acc}}_{\text{cell},k}}{\partial \mathbb{F}_{\beta\gamma}} \end{aligned}$$

$$
\begin{aligned}
&+ \frac{1}{V_{\mathscr{R}}} \sum_{k \,\in\, \text{cells}} V_{\text{cell},k}^{\text{acc}} \sum_{\gamma=1}^{3} \mathbb{F}_{\alpha\gamma} \frac{\partial a_{\text{vol}}\left(\rho_{\text{cell},k}, T\right)}{\partial \mathbb{F}_{\beta\gamma}} \\
&= \frac{1}{V_{\mathscr{R}}} \sum_{k \,\in\, \text{cells}} a_{\text{vol}}\left(\rho_{\text{cell},k}, T\right) \sum_{\gamma=1}^{3} \mathbb{F}_{\alpha\gamma} \frac{\partial V_{\text{cell},k}^{\text{acc}}}{\partial \mathbb{F}_{\beta\gamma}} \\
&+ \frac{1}{V_{\mathscr{R}}} \sum_{k \,\in\, \text{cells}} V_{\text{cell},k}^{\text{acc}} \sum_{\gamma=1}^{3} \mathbb{F}_{\alpha\gamma} \frac{\partial a_{\text{vol}}\left(\rho_{\text{cell},k}, T\right)}{\partial \rho_{\text{cell},k}} \frac{\partial \rho_{\text{cell},k}}{\partial \mathbb{F}_{\beta\gamma}} \\
&= \frac{1}{V_{\mathscr{R}}} \sum_{k \,\in\, \text{cells}} a_{\text{vol}}\left(\rho_{\text{cell},k}, T\right) \sum_{\gamma=1}^{3} \mathbb{F}_{\alpha\gamma} \frac{\partial V_{\text{cell},k}^{\text{acc}}}{\partial \mathbb{F}_{\beta\gamma}} \\
&- \frac{1}{V_{\mathscr{R}}} \sum_{k \,\in\, \text{cells}} \rho_{\text{cell},k} \frac{\partial a_{\text{vol}}\left(\rho_{\text{cell},k}, T\right)}{\partial \rho_{\text{cell},k}} \sum_{\gamma=1}^{3} \mathbb{F}_{\alpha\gamma} \frac{\partial V_{\text{cell},k}^{\text{acc}}}{\partial \mathbb{F}_{\beta\gamma}} \\
&= \frac{1}{V_{\mathscr{R}}} \sum_{k \,\in\, \text{cells}} \Bigg[a_{\text{vol}}\left(\rho_{\text{cell},k}, T\right) \\
&- \rho_{\text{cell},k} \frac{\partial a_{\text{vol}}\left(\rho_{\text{cell},k}, T\right)}{\partial \rho_{\text{cell},k}} \Bigg] \sum_{\gamma=1}^{3} \mathbb{F}_{\alpha\gamma} \frac{\partial V_{\text{cell},k}^{\text{acc}}}{\partial \mathbb{F}_{\beta\gamma}}
\end{aligned}
\tag{5.28}
$$

where $a_{\text{vol}}\left(\rho_{\text{cell},k}, T\right)$ is the nonbonded Helmholtz energy density in cell k. The term in brackets is the negative of the pressure, $-p\left(\rho_{\text{cell},k}, T\right)$ as that is predicted by the equation of state (eq 2.129) under given density $\rho_{\text{cell},k}$ and temperature, T. At this point we have to calculate the derivatives expressing the variation of the volume of a cell with respect to an element of the deformation gradient tensor, $\partial V_{\text{cell},k}^{\text{acc}} / \partial \mathbb{F}_{\beta\gamma}$.

At this point we restrict ourselves to the case of a pure polymer. The determinant of the deformation gradient tensor is the ratio of volumes or densities of the deformed and initial configurations, eq 2.34 on page 22:

$$
\det\left(\mathbb{F}\right) = \frac{V'}{V_{\mathscr{R}}} = \frac{V_{\text{cell},k}^{\text{acc}\;\prime}}{V_{\text{cell},k}^{\text{acc}}} = \frac{\rho}{\rho'} = \frac{\rho_{\text{cell},k}}{\rho'_{\text{cell},k}} \tag{5.29}
$$

where the use of primes denotes the deformed configuration. If nanoparticles exist in the system, attention should be paid to the cells intersecting nanoparticles. The derivative of the determinant of $\mathbb{F}$ with respect to the tensor $\mathbb{F}$ itself is calculated by the following equation:[334]

$$
\frac{\partial\left(\det\left(\mathbb{F}\right)\right)}{\partial \mathbb{F}} = \det\left(\mathbb{F}\right) \left(\mathbb{F}^{-1}\right)^{\mathrm{T}} \tag{5.30}
$$

Finally, the nonbonded contribution to the stress tensor, substituting the above terms in eq 5.28

is:

$$\begin{aligned}\tau^{\mathrm{nb}}_{\alpha\beta}\left(\{\rho_{\mathrm{cell}}\},T\right) &= -\frac{1}{V_{\mathscr{R}}}\sum_{k\,\in\,\mathrm{cells}} p\left(\rho_{\mathrm{cell},k},T\right)\sum_{\gamma=1}^{3}\mathbb{F}_{\alpha\gamma}\frac{\partial V^{\mathrm{acc}}_{\mathrm{cell},k}}{\partial \mathbb{F}_{\beta\gamma}} \\ &= -\frac{1}{V_{\mathscr{R}}}\sum_{k\,\in\,\mathrm{cells}} p\left(\rho_{\mathrm{cell},k},T\right)\sum_{\gamma=1}^{3}\mathbb{F}_{\alpha\gamma}\frac{\partial V^{\mathrm{acc}}_{\mathrm{cell},k}}{\partial \det\left(\mathbb{F}\right)}\frac{\partial\left(\det\left(\mathbb{F}\right)\right)}{\partial \mathbb{F}_{\beta\gamma}} \\ &= -\delta_{\alpha\beta}\frac{1}{V_{\mathscr{R}}}\sum_{k\,\in\,\mathrm{cells}} p\left(\rho_{\mathrm{cell},k},T\right)V^{\mathrm{acc}}_{\mathrm{cell},k} \end{aligned} \tag{5.31}$$

where all volumes, $V_{\mathscr{R}}$ and $V^{\mathrm{acc}}_{\mathrm{cell},k}$ refer to the undeformed (reference) state of the system. Eq 5.31 could be fully anticipated. The contribution of the equation of state to the stress tensor of the system is limited to the diagonal components and its magnitude is the negative of the weighted average pressure over the cells of the grid, with volumes $V^{\mathrm{acc}}_{\mathrm{cell},k}$ being the weights multiplying the individual contributions. Please note the similarity with eq 3.12 on page 91.

5.2.4 Generation of Initial Configurations

Initial configurations for the linear melt are obtained by FTiMC equilibration of a coarse-grained melt, wherein chains are represented as freely jointed sequences of Kuhn segments subject to a coarse-grained Helfand Hamiltonian which prevents the density from departing from its mean value anywhere in the system (please consult Chapter 4).[176,327] The coarse-graining from the freely jointed chain model to the bead-spring model involves placement of beads at regular intervals along the contour of the chains obtained after the MC equilibration. As already discussed in the previous section, at the new (coarser, mesoscopic) level of description, the polymer is envisioned as a network of strands connecting internal nodal points and end points. The effects of entanglements are introduced by slip springs between chains. Slip-springs can either be placed randomly at the initial configuration, or they can be allowed to be created, following the kMC scheme described below. The number of entanglements (slip-springs) is chosen so as to be consistent with the molar mass between entanglements, M_{e}, of the polymer under consideration.

Starting from a well equilibrated configuration $\mathscr{R}$, obtained from a FTiMC simulation, we determine the box size and shape for which the Gibbs energy function:[179]

$$G\left(T,\boldsymbol{\tau}\right) = A\left(\{\mathbf{r}_{ij}\},\{\rho\left(\mathbf{r},T\right)\},T\right) - V_{\mathscr{R}}\frac{1}{3}\mathrm{Tr}\left(\boldsymbol{\tau}\right) - V_{\mathscr{R}}\sum_{\alpha\beta}\tau_{\alpha\beta}\epsilon_{\alpha\beta} \tag{5.32}$$

becomes minimal under the given, externally imposed T and $\boldsymbol{\tau}$. The presence of any symmetry element in the stress tensor reduces the number of minimization parameters, and in the special case where only hydrostatic pressure is applied on the system, the sum of the last two terms in eq 5.32 is equivalent to $-pV$, letting the volume V of the deformed configuration be the only parameter for the Gibbs energy minimization. In that case, the volume is expressed as $V = V_{\mathscr{R}}\left(1 + \epsilon_{xx} + \epsilon_{yy} + \epsilon_{zz}\right)$. The Gibbs energy function, eq 5.32, is, of course, valid only for small deformations away from the reference state. In our case, we let the system relax under atmospheric hydrostatic pressure, starting from an equilibrated configuration at the average density for the temperature under consideration.

5.2.5 Brownian Dynamics

When simulating a system of coarse-grained particles, some degrees of freedom are treated explicitly, whereas other are represented only by their stochastic influence on the former ones. In our model the effect of the surrounding melt on the motion of the coarse-grained beads is mimicked by introducing a stochastic force plus a frictional force into the equations of motion of the beads. When the stochastic force contains no correlations in space or time, one obtains the simplest form of stochastic dynamics, called BD.[81,335,336] The theory of Brownian motion was developed to describe the dynamic behavior of particles whose mass and size are much larger than those of the host medium particles. In this case the position Langevin equation becomes (please refer to page 54):

$$\mathbf{v}_i\left(t\right) = \frac{1}{\zeta_i}\mathbf{F}_i\left(\left\{\mathbf{r}_i\left(t\right)\right\}\right) + \frac{1}{\zeta_i}\boldsymbol{\mathcal{F}}_i\left(t\right) \tag{2.156}$$

The systematic force $\mathbf{F}_i\left(t\right)$ is the explicit mutual force between the N particles and $\boldsymbol{\mathcal{F}}_i\left(t\right)$ represents the effect of the medium on the particles. Each particle is characterized by its mass m_i and the friction coefficient ζ_i, measured in kg/s. The systematic force, $\mathbf{F}_i$, is to be derived from the free energy following eqs 5.3 and eq 5.13:

$$\mathbf{F}_i\left(\left\{\mathbf{r}_i\left(t\right)\right\}\right) = -\nabla_{\mathbf{r}_i(t)}A\left(\left\{\mathbf{r}_{ij}\left(t\right)\right\}, \left\{\rho\left(\mathbf{r}, t\right)\right\}, T\right) \tag{5.33}$$

with the expression of the Helmholtz energy as given in eq 5.1. The stochastic force $\boldsymbol{\mathcal{F}}_i$ is assumed to be stationary, Markovian and Gaussian with zero mean and to have no correlation with prior velocities nor with the systematic force. For large values of $(\zeta_i/m_i)\Delta t$ in the diffusive regime, when the friction is so strong that the velocities relax within Δt, the BD algorithm of van Gunsteren and Berendsen,[129] eq 2.157 can be used:

$$r_{i,\alpha}\left(t_n+\Delta t\right)=r_{i,\alpha}\left(t_n\right)+\frac{1}{\zeta_i}\left[F_{i,\alpha}\left(t_n\right)\Delta t+\frac{1}{2}\dot{F}_{i,\alpha}\left(t_n\right)\left(\left(\Delta t\right)^2\right)\right]+\mathcal{R}_{i,\alpha}\left(\Delta t\right) \tag{2.157}$$

where the random variable $\mathcal{R}_{i,\alpha,n}\left(\Delta t\right)$ is sampled from a Gausssian distribution with zero mean and width:

$$\left\langle\mathcal{R}_{i,\alpha}^2\left(\Delta t\right)\right\rangle=\frac{2k_{\mathrm{B}}T_{\mathrm{ref}}}{\zeta_i}\Delta t \tag{2.158}$$

5.2.6 Slip-spring Kinetic Monte Carlo

5.2.6/i General formulation

Chain slippage corresponds to hopping of a slip-spring along the contour of the chains it connects, without actual displacements of their beads. The ends of the slip-spring connect beads a_0 and b_0 along chains a and b (see Figure 5.2). In order to develop a formalism of elementary events of slip-spring hopping, creation or destruction, we need expressions for the rate of slippage along the chain backbone. We extract the diffusivity of the slip-springs following the work of Terzis et al.[326] The self-diffusion along the chain contour is described by the Rouse model (Section 2.3.4 page 36). This model addresses the dynamics of polymers in unentangled melts. A polymer chain is represented by a set of beads connected by harmonic springs. The dynamics is modeled as a Brownian motion of these tethered beads, the environment of a chain being represented as a continuum (viscous medium), ignoring all excluded volume and hydrodynamic interactions. In this model the self-diffusivity of the center of mass of the polymer is related to the friction coefficient ζ_i of a bead by eq 2.107 (page 40):

$$D_{\mathrm{cm}}^{\mathrm{Rouse}}=\frac{k_{\mathrm{B}}T}{\left(N+1\right)\zeta} \tag{2.107}$$

with $(N+1)$ being the number of beads per chain. In the picture we invoke in our slip-spring model, the center of mass diffusivity along the contour is related to the rate of slip-spring jumps across beads (by distance $N_{\mathrm{Kuhns/bead}}b_{\mathrm{K}}^2$) in each direction by:

$$D_{\mathrm{cm}}^{\mathrm{Rouse}}=k_{\mathrm{diff}}\frac{N_{\mathrm{Kuhns/bead}}b_{\mathrm{K}}^2}{N+1}=\nu_{\mathrm{diff}}\frac{N_{\mathrm{Kuhns/bead}}b_{\mathrm{K}}^2}{N+1}\exp\left(\frac{A_0}{k_{\mathrm{B}}T}\right) \tag{5.34}$$

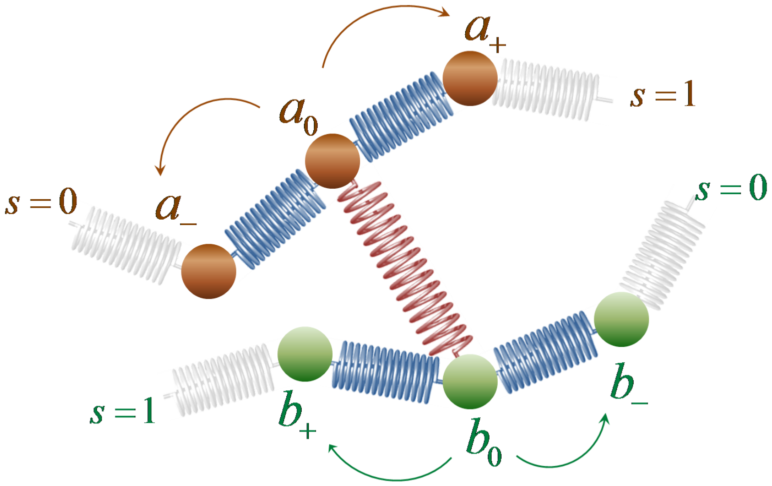

Figure 5.2: Illustration of the "hopping" scheme of slip-springs along the chain contour, by switching the beads the spring is attached to.

where we have introduced k_{diff} as the rate of diffusion of a Rouse bead along the chain, which is not a very useful quantity. Hence, we derive the following expression for ν_{diff}:

$$\nu_{\text{diff}} = \frac{k_{\text{B}}T}{N_{\text{Kuhns/bead}} b_{\text{K}}^2 \zeta} \exp\left(-\frac{A_0}{k_{\text{B}}T}\right) \tag{5.35}$$

where A_0 is a free energy per slip-spring in the melt at equilibrium, which establishes a baseline for measuring free energies, and ζ the friction coefficient of an individual bead, measured in kg/s. We should note here that ζ is the same friction coefficient used by the BD simulations, eq 2.157. It can be calculated from temperature-dependent expressions for the viscosity based on experiment, or from analyses of the temperature-dependent chain self-diffusivity and Rouse time based on atomistic molecular dynamics simulations of unentangled melts.[337] We will elaborate more on this, later.

An individual jump of one end of a slip-spring along the chain backbone, e.g. from bead a_0 to bead a_+, takes place with rate:

$$k_{\text{hopping}} = \nu_0 \exp\left(-\frac{A^{\ddagger}_{\mathscr{O}\to\mathscr{N}} - A_{a_0-b_0}}{k_{\text{B}}T}\right) = k_{\text{diff}} \exp\left(\frac{A_{a_0-b_0} - A_0}{k_{\text{B}}T}\right)$$

or more conveniently:

$$k_{\text{hopping}} = \nu_{\text{diff}} \exp\left(\frac{A_{a_0-b_0}}{k_{\text{B}}T}\right) \tag{5.36}$$

conforming to a Transition State Theory (TST) picture of the slippage along the backbone as an infrequent event, which involves a transition from state $\mathscr{O} \equiv a_0 \wedge b_0$ to state $\mathscr{N} \equiv a_+ \wedge b_0$

Table 5.1: Transition probabilities of a slip-spring both ends of which can hop along the chain

Slip-spring end	Transition	Rate	Probability in a time step of Δt
a_0	$a_0 \rightarrow a_-$	$k_{a_0 \rightarrow a_-} = \nu_{\text{diff}} \exp\left(\frac{A_{a_0-b_0}}{k_{\text{B}}T}\right)$	$p_{a_0 \rightarrow a_-} = k_{a_0 \rightarrow a_-} \Delta t$
	$a_0 \rightarrow a_+$	$k_{a_0 \rightarrow a_+} = \nu_{\text{diff}} \exp\left(\frac{A_{a_0-b_0}}{k_{\text{B}}T}\right)$	$p_{a_0 \rightarrow a_+} = k_{a_0 \rightarrow a_+} \Delta t$
b_0	$b_0 \rightarrow b_-$	$k_{b_0 \rightarrow b_-} = \nu_{\text{diff}} \exp\left(\frac{A_{a_0-b_0}}{k_{\text{B}}T}\right)$	$p_{b_0 \rightarrow b_-} = k_{b_0 \rightarrow b_-} \Delta t$
	$b_0 \rightarrow b_+$	$k_{b_0 \rightarrow b_+} = \nu_{\text{diff}} \exp\left(\frac{A_{a_0-b_0}}{k_{\text{B}}T}\right)$	$p_{b_0 \rightarrow b_+} = k_{b_0 \rightarrow b_+} \Delta t$

over a free energy barrier, $A^{\ddagger}_{\mathscr{O} \rightarrow \mathscr{N}}$. We use the logical conjunction operator "$\wedge$" to denote the connectivity of the system. In the final expression, the rate of hopping, k_{hopping}, depends directly on the energy of the initial state of the slip-spring, $A_{a_0-b_0}$, while the dependence on the height of the free energy at the barrier (i.e. $A^{\ddagger}_{\mathscr{O} \rightarrow \mathscr{N}}$) has been absorbed into the pre-exponential factor ν_{diff}. As depicted in Figure 5.2, in the case considered none of the nearest neighbor beads of the ends of the chain is a chain end. Double jumps (e.g. $a_0 \rightarrow a_+$ and $b_0 \rightarrow b_+$) are disallowed, which may not be too bad an approximation for small timesteps, Δt. Thus, the ends of the slip-spring can hop independently with the probabilities given in Table 5.1.

5.2.6/ii Slip-spring hopping along the chain contour in the presence of a chain end

The ends of the slip-spring connect beads a_0 and b_0 as those are depicted in Figure 5.3. One of the beads connected by the slip-spring (e.g. b_0) is a chain end. One end of the slip spring can hop along the chain, while the second can either hop moving away from the chain end or be destroyed. The possible transitions and the associated probabilities are reported in Table 5.2. The rate of destruction of a slip-spring is equal to the rate of hopping along the chain. This assumption keeps the necessary adjustable parameters to an absolute minimum. Through the intrinsic dynamics of the system, it is possible for a slip-spring end to leave its chain. This process mimics the disentanglement at the chain ends and the process of constraint release (CR). The process of slip-spring destruction is introduced in the model in order to represent the chain disentanglement, as that is envisioned by the polymer tube theories.

5.2.6/iii Creation of a slip-spring connecting a chain end with an internal bead of another chain

At each step of the kMC hopping simulation, every free end of the system can randomly create a new slip-spring with an internal bead of a neighboring chain. We consider the case illustrated in Figure 5.4. The chain end "a" searches for candidate mates to be paired, excluding other chain ends and beads lying outside a sphere of prescribed radius, α_{attempt}. The rate for the

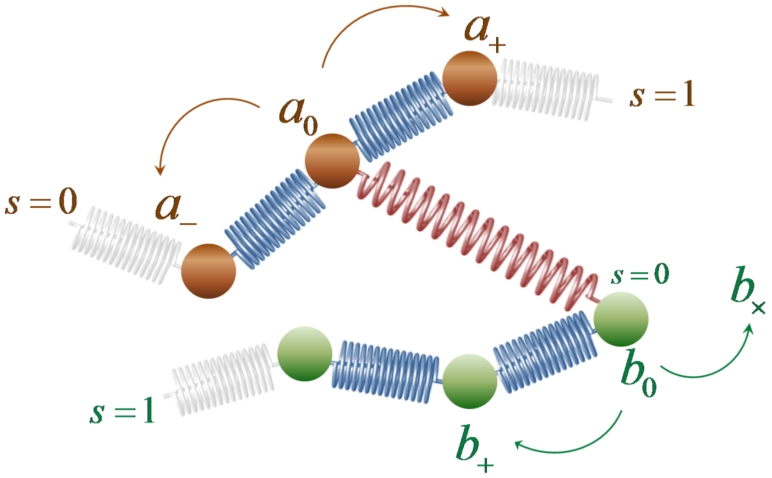

Figure 5.3: Illustration of the “hopping” scheme of slip-springs along the chain contour, in the case a destruction event can take place.

Table 5.2: Transition probabilities of a slip-spring whose one end can hop away from the chain (be destroyed)

Slip-spring end	Transition	Rate	Probability in a time step of Δt
a_0	$a_0 \to a_-$	$k_{a_0 \to a_-} = \nu_{\text{diff}} \exp\left(\frac{A_{a_0-b_0}}{k_{\text{B}}T}\right)$	$p_{a_0 \to a_-} = k_{a_0 \to a_-} \Delta t$
	$a_0 \to a_+$	$k_{a_0 \to a_+} = \nu_{\text{diff}} \exp\left(\frac{A_{a_0-b_0}}{k_{\text{B}}T}\right)$	$p_{a_0 \to a_+} = k_{a_0 \to a_+} \Delta t$
b_0	$b_0 \to \times$	$k_{b_0 \to b_\times} = \nu_{\text{diff}} \exp\left(\frac{A_{a_0-b_0}}{k_{\text{B}}T}\right)$	$p_{b_0 \to b_\times} = k_{b_0 \to b_\times} \Delta t$
	$b_0 \to b_+$	$k_{b_0 \to b_+} = \nu_{\text{diff}} \exp\left(\frac{A_{a_0-b_0}}{k_{\text{B}}T}\right)$	$p_{b_0 \to b_+} = k_{b_0 \to b_+} \Delta t$

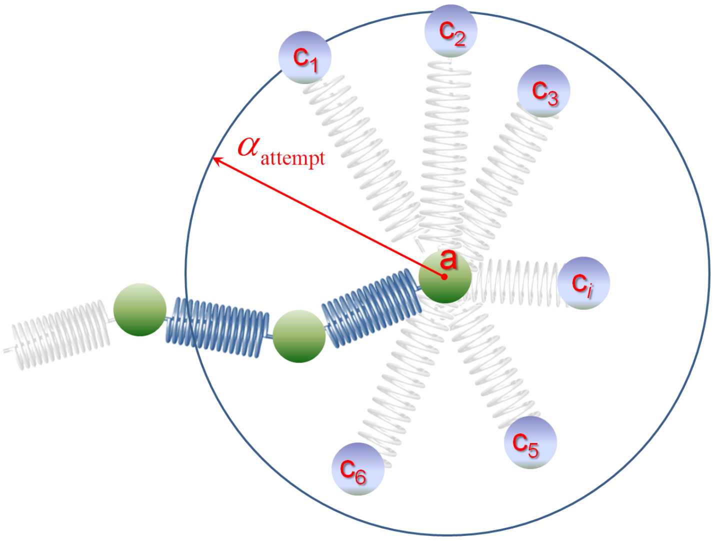

Figure 5.4: Illustration of the slip-spring creation process

creation of a new slip-spring is closely related to the probability of pairing the end "a" with one of its candidate mates, i, which lies inside a sphere of prescribed radius, α_{attempt}. The rate constant of this process is:

$$k_{\text{creation}} = \nu_{\text{formation}} n_{\text{cands}} \frac{\exp\left(-\frac{A_{a\wedge c_i}}{k_{\text{B}}T}\right)}{\sum_{j=1}^{n_{\text{cands}}} \exp\left(-\frac{A_{a\wedge c_j}}{k_{\text{B}}T}\right)} \tag{5.37}$$

where we have used $a \wedge c_i$ to denote the pairing of chain end a with a candidate internal bead i. The probability of achieving a connection of the above kind in a time step Δt:

$$p_{a\wedge c_i} = k_{a\wedge c_i} \Delta t \tag{5.38}$$

while the probability of not creating a new slip-spring is:

$$p_{a\wedge\emptyset} = 1 - \sum_{j=1}^{n_{\text{cands}}} p_{a\wedge c_j} \tag{5.39}$$

The definition of the probability of not creating a new slip-spring, $p_{a\wedge\emptyset}$, implies that the more crowded chain ends are the more probable to create a slip-spring. The number of neighbors around a chain end can be tuned via the radius of the sphere within which the search takes place, α_{attempt}. A good estimate of α_{attempt} is given by the tube diameter, a_{pp} of the polymer.

5.2.7 Simulation Details

The systems considered were cis-1,4 polyisoprene (natural rubber) melts. All simulations were carried out in the canonical statistical ensemble, at the temperature of $T = 413$K, where rheological measurements are available.[174] The simulation box was cubic with varying edge length from 30 nm to 100 nm.

5.2.7/i Equation of state parameters

We have used the parameters of the Sanchez-Lacombe equation of state, given by Rudolf et al.[333] who have conducted pVT measurements on several polymers in isothermal conditions, above their glass transition temperature. These authors suggest $p^* = 383.0$ MPa, $T^* = 631.2$ K and $\rho^* = 0.961$ g/cm^3 for molten polyisoprene of $M = 2594$ g/mol. Based on these values, the density of polyisoprene at $T = 300$ K is estimated as $\rho(300\text{ K}) = 0.908$ g/cm^3.

5.2.7/ii Kuhn length parametrization

The mean squared end-to-end distance of a PI chain can be either expressed in terms of the number of isoprene units or Kuhn lengths:

$$\left\langle R_{\mathrm{e},0}^{2}\right\rangle = C_{\infty} 4 N_{\mathrm{monomers}} l^{2} = N_{\mathrm{Kuhn}} b^{2} \tag{5.40}$$

where C_{∞} is the characteristic ratio of PI, l is the average carbon-carbon bond length for isoprene and b is the Kuhn length of polyisoprene. The factor of 4 is required because each isoprene contains four backbone bonds. Using Mark's[338] values for C_{∞} and l of 4.7 and 0.1485 nm, respectively, we obtain $b = 0.958$ nm and 2.21 isoprene units per Kuhn length.[339] The effective length of an isoprene unit has been shown to have a slight temperature dependence,[340] however, we ignore this effect in our model. Each bead in our representation consists of $n_{\mathrm{Kuhns/bead}} = 10$ PI Kuhn segments. Thus, its mass is $m_{\mathrm{bead}} = 1506$ g/mol and its characteristic mean-square end-to-end distance (if considered as a random walk) should be $\left(n_{\mathrm{Kuhns/bead}} b^{2}\right) = 9.1776 \times 10^{-18}\ \mathrm{m}^{2}$.

Fetters et al.[174] have estimated the entanglement molecular weight of polyisoprene (PI), M_{e} to be $5430\ \mathrm{g/mol}$. Based on the chain discretization we have introduced above, the average distance between the slip-springs should be roughly four coarse-grained beads.

5.2.7/iii Friction coefficient

Klopffer et al.[341] have characterized the rheological behavior of a series of polybutadienes and polyisoprenes over a wide range of temperatures. The viscoelastic coefficients resulting from the time-temperature superposition principle were determined. A Rouse theory modified for undiluted polymers was used to calculate the monomeric friction coefficient, ζ_0. The monomeric friction coefficient, ζ_0, characterizes the resistance encountered by a monomer unit moving through its surroundings. It was concluded that, within experimental error, a single set of Williams - Landel - Ferry (WLF) parameters[205] at T_{g} was adequate to characterize the relaxation dynamics irrespective of the vinyl content of the polybutadienes and polyisoprenes. These authors proposed that the variation of the monomeric friction coefficient with temperature can be given by:

$$\log \zeta_0 (T) = \log \zeta_{\infty} + \frac{C_1^{\mathrm{g}} C_2^{\mathrm{g}}}{T - T_{\mathrm{g}} + C_2^{\mathrm{g}}} \tag{5.41}$$

with the parameters $C_1^{\mathrm{g}} = 13.5 \pm 0.2$, $C_2^{\mathrm{g}} = 45 \pm 3$ K, $\log \zeta_{\infty} = -10.4$ dyn s cm^{-1} and $T_{\mathrm{g}} = 211.15$ K. At a temperature of 298 K, $\zeta_0(298\,\mathrm{K}) = 1.61 \times 10^{-6}$ dyn s cm^{-1}, while at a temperature of 413 K, $\zeta_0(413\,\mathrm{K}) = 1.1508 \times 10^{-11}\ \mathrm{kg/s}$

If we think the friction coefficient as being proportional to the mass of the entity it refers to, we can estimate the friction coefficient of our coarse-grained beads as:

$$\zeta_{\text{bead}} = \frac{m_{\text{bead}}}{m_{\text{monomer}}}\zeta_0 \tag{5.42}$$

where $m_{\text{monomer}} = 68.12$ g/mol refers to the molar mass of a PI monomer. The friction coefficient of a coarse-grained bead, at the temperature of 413 K is:

$$\zeta_{\text{bead}} = 2.54 \times 10^{-10}\frac{\text{kg}}{\text{s}} \tag{5.43}$$

Doxastakis et al.[207,342] have estimated the self-diffusion coefficient of unentangled PI chains consisted of 115 carbon atoms, at $T = 413$ K to be:

$$D_{\text{C}_{115}} = 4.4 \times 10^{-11}\ \frac{\text{m}^2}{\text{s}} \tag{5.44}$$

The length of these chains corresponds to 23 monomers (or 11 PI Kuhn segments). If we use the Rouse model[88] to predict the diffusivity of these chains, based the parameters we have chosen above, that would be:

$$D_{\text{Rouse,C}_{115}} = \frac{k_B T}{N_{\text{monomers}}\zeta_0} = 2.15 \times 10^{-11}\ \frac{\text{m}^2}{\text{s}} \tag{5.45}$$

where N_{monomers} is the chain length measured in monomers and ζ_0 the monomeric friction coefficient. Our estimation of the self-diffusivity of Rouse chains, based on the model parameters we have introduced coheres with what Doxastakis et al. have measured both experimentally and by all-atom MD simulations.

5.3 Results and Discussion

5.3.1 Structural Features

We start by examining the structure of the melt chains at the level of individual strands, where we refer to a *strand* as the distance between successive beads along the contour of a chain. The distribution of the length of the strands (entropic springs) that connect the beads along the contour of the chains is depicted in Figure 5.5. The entropic springs along the chain are considered Gaussian with an unperturbed length which equals total length of the Kuhn segments adsorbed by a coarse-grained bead. The conformational features, at least at the strand level, continue to be respected during the BD simulation. Moreover, the distribution of strand lengths during the

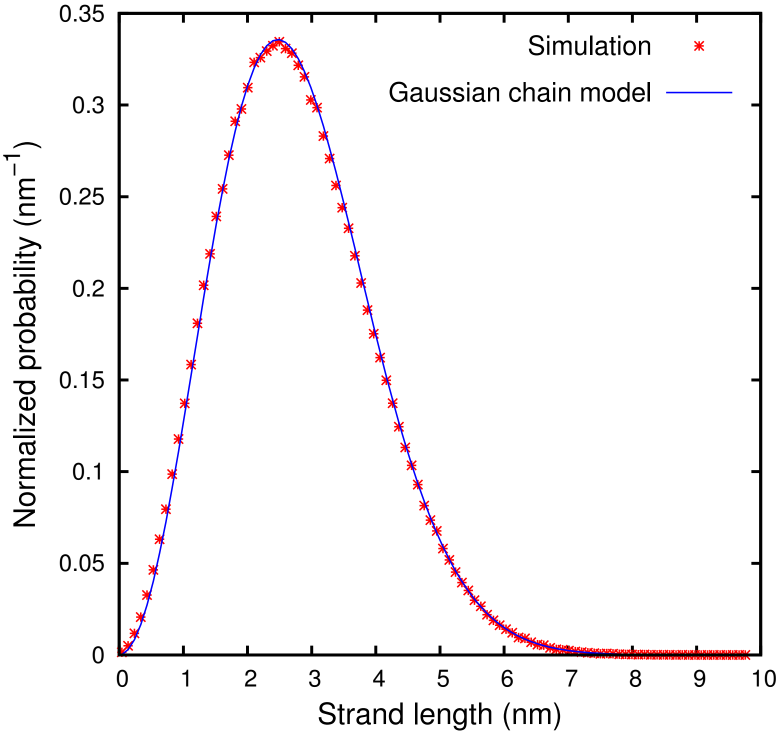

Figure 5.5: Distribution of the length of the strands along the contour of the chain. The term *strand* refers to the distance between successive beads along the same chain.

simulation coincides with a Gaussian distribution centered at the unperturbed strand length, as is theoretically expected. Our simulation scheme seems to produce trajectories of the system consistent with the imposed free energy function.

In Figure 5.6 we examine the distribution of slip-spring lengths. Slip-springs represent entanglements of a chain with its surrounding chains. The polymer tube model considers a tube formed around the primitive path of the chain, which fluctuates in time. Recent simulations have shown that the probability of finding segments of the neighboring chains inside the tube of the chain under consideration is Gaussian.[343] This is also the case in our simulations. The use of Gaussian entropic springs for describing the free energy of the slip-springs results in a Gaussian distribution of slip-spring lengths, conforming to the picture obtained by more detailed simulations and theoretical arguments. Again, the distribution obtained by the simulation is in favorable agreement with the one expected.

5.3.2 Dynamics

Figure 5.7 shows results for the time dependence of the mean-square displacements, $g_i\left(t\right)$ (eq 2.110, page 40) and $g_{\mathrm{cm}}\left(t\right)$ (eq 2.105, 39) for an unentangled melt. As can be seen, the mean-square center-of-mass displacement, $g_{\mathrm{cm}}\left(t\right)$, remains linear all times; this means the

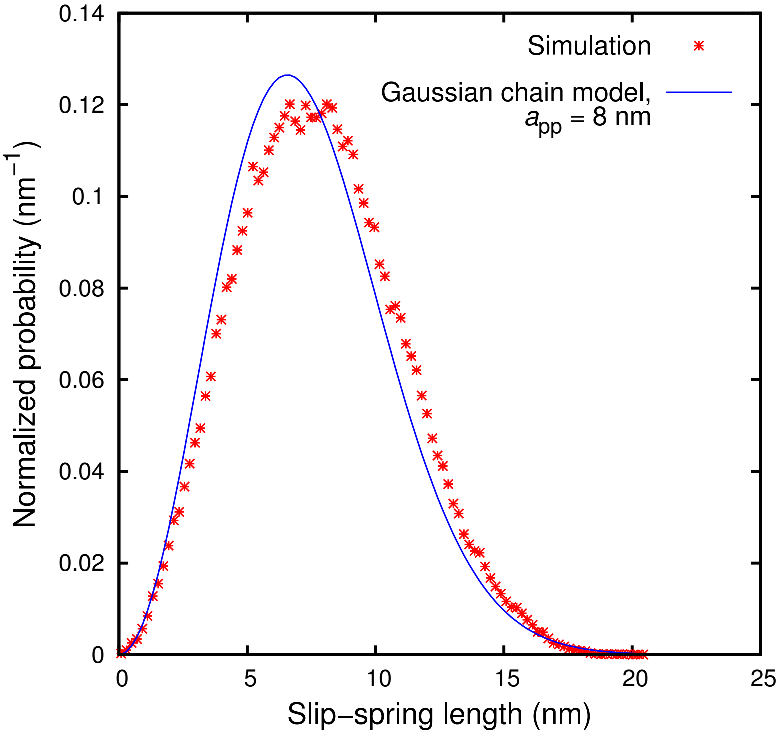

Figure 5.6: Distribution of the length of the slip-springs connecting beads belonging to different chains. In our network description, slip-springs represent entanglements between neighboring chains.

intermolecular forces between polymers are too weak to affect diffusive behavior and play a minor role compared to the bonded interactions. The beads mean-squared displacements, $g_i(t)$, exhibit a subdiffusive behavior that arises from chain connectivity, and is characterized by a power law of the form $g_i(t) \sim t^{1/2}$. After an initial relaxation time where a change in $g_i(t)$ occurs, a regular diffusive regime is entered, where $g_i(t) \sim t$. This sequence of scaling trends is predicted by the Rouse theory (subsection 2.3.4, page 41). The limiting behavior of the chains' center-of-mass displacement can yield an estimate of the diffusivity of the chains:

$$\lim_{t \to \infty} g_{\mathrm{cm}}(t) = 6 D_{\mathrm{cm}} t \tag{5.46}$$

which has been found in excellent agreement with the predicted diffusivity by all-atom MD simulations of PI chains of the same molecular weight by Doxastakis et al.[342] The introduction of non-bonded interactions does not seem to affect the scaling laws of the unentangled melt.

Figure 5.8 shows results for the mean-square displacements, $g_i(t)$ and $g_{\mathrm{cm}}(t)$, as a function of time, obtained from the simulation of a 50 kg/mol PI melt with slip-springs present. It can be seen that at short times the bead's mean-square displacement, $g_i(t)$, shows a scaling regime with a power law $t^{1/2}$; at intermediate times, a regime with a power law $t^{1/4}$ appears; eventually

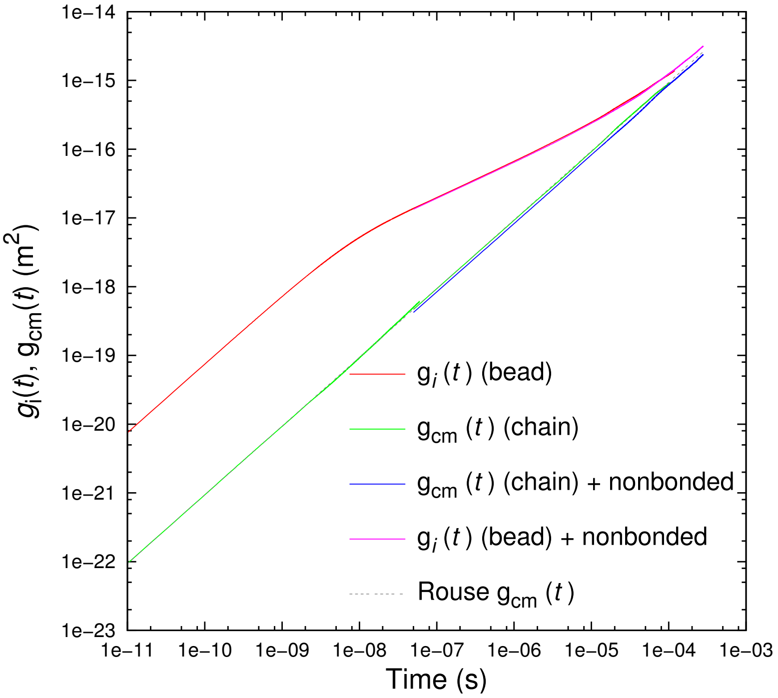

Figure 5.7: Time evolution of the mean-square displacements of the beads ($g_i\left(t\right)$) and center of mass of the chains ($g_{\text{cm}}\left(t\right)$) for $M = 50$ kg/mol in the absence of slip-springs. In $g_i\left(t\right)$, a regime with $t^{1/2}$ scaling can be seen, in agreement with the Rouse model.

we observe a crossover to regular diffusion at long times. The mean-square displacement of the chain center-of-mass, $g_{\text{cm}}\left(t\right)$, also exhibits subdiffusive behavior at intermediate times, with a scaling behavior $t^{1/2}$, as predicted by the tube model; at long times, regular diffusion is achieved. From the long time behavior of $g_{\text{cm}}\left(t\right)$, we can estimate the longest relaxation time, τ_{d}. Despite the fact that the scaling regions are not accurately discerned in our results, the scaling of polymer melts, as expected by the tube theory, is observed.

5.3.3 Rheology

Linear rheological properties can be characterized through the shear relaxation modulus, $G\left(t\right)$, as that was defined in eq 2.40:

$$\tau_{xy}\left(t\right) = \gamma G\left(t\right) \tag{2.40}$$

with γ being a small shear deformation and xy two orthogonal axes. In computer simulations, the most convenient way of evaluating $G(t)$ is by using the fluctuation-dissipation theorem (section 2.4.3/i on page 53):[91]

$$G\left(t\right) = \frac{V}{k_{\text{B}}T}\left\langle \tau_{\alpha\beta}\left(t_0 + t\right)\tau_{\alpha\beta}\left(t_0\right)\right\rangle \tag{5.47}$$

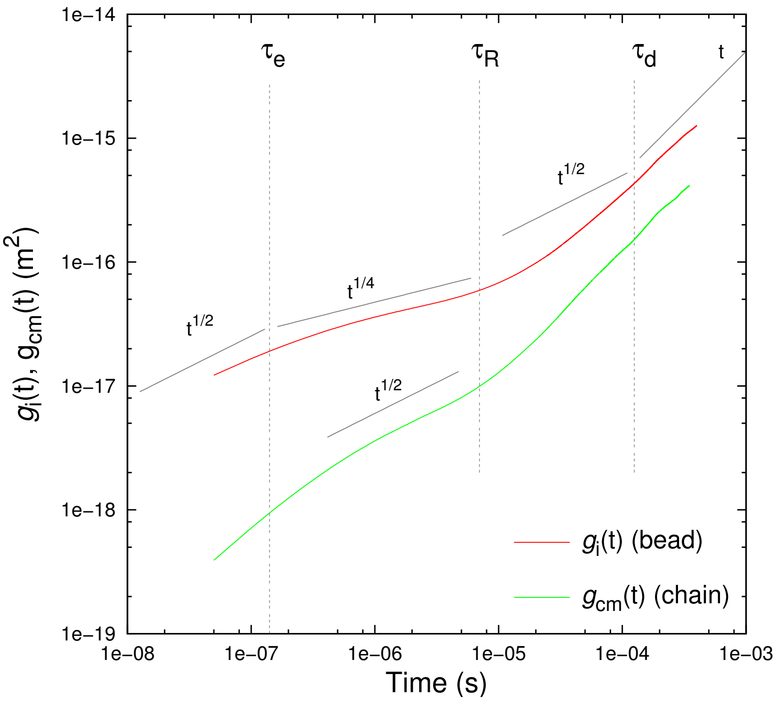

Figure 5.8: Time evolution of the mean-square displacements of the beads ($g_i\,(t)$) and center of mass of the chains ($g_{\text{cm}}\,(t)$) for $M = 50$ kg/mol. The chains are entangled (slip-springs are present). The scaling of both functions is in good agreement with the tube model predictions (Figure 2.3 on page 44).

where $\alpha\beta$ any two orthogonal directions. However, the stress autocorrelation function (acf) is notoriously difficult to calculate due to huge fluctuations at early times (caused by bond vibrations). In order to improve accuracy we average $\langle\tau_{\alpha\beta}\,(t_0+t)\,\tau_{\alpha\beta}\,(t_0)\rangle$ over all possible ways to select a pair of perpendicular axes α and β.[91] The result is:

$$G\,(t) = \frac{V}{5k_{\text{B}}T}\begin{bmatrix}\langle\tau_{xy}\,(t_0+t)\,\tau_{xy}\,(t_0)\rangle\\ +\langle\tau_{xz}\,(t_0+t)\,\tau_{xz}\,(t_0)\rangle\\ +\langle\tau_{yz}\,(t_0+t)\,\tau_{yz}\,(t_0)\rangle\end{bmatrix} + \frac{V}{30k_{\text{B}}T}\begin{bmatrix}\langle\mathcal{N}_{xy}\,(t_0+t)\,\mathcal{N}_{xy}\,(t_0)\rangle\\ +\langle\mathcal{N}_{xz}\,(t_0+t)\,\mathcal{N}_{xz}\,(t_0)\rangle\\ +\langle\mathcal{N}_{yz}\,(t_0+t)\,\mathcal{N}_{yz}\,(t_0)\rangle\end{bmatrix} \tag{5.48}$$

where $\mathcal{N}_{\alpha\beta} = \tau_{\alpha\alpha} - \tau_{\beta\beta}$. We compute the time correlation functions in eq 5.48 by using the multiple-tau correlator algorithm of Ramírez et al.[344] The shear viscosity, η, can be computed from the stress relaxation function through a Green-Kubo relation:

$$\eta = \int_0^\infty G_{\alpha\beta}(t)\mathrm{d}t \tag{5.49}$$

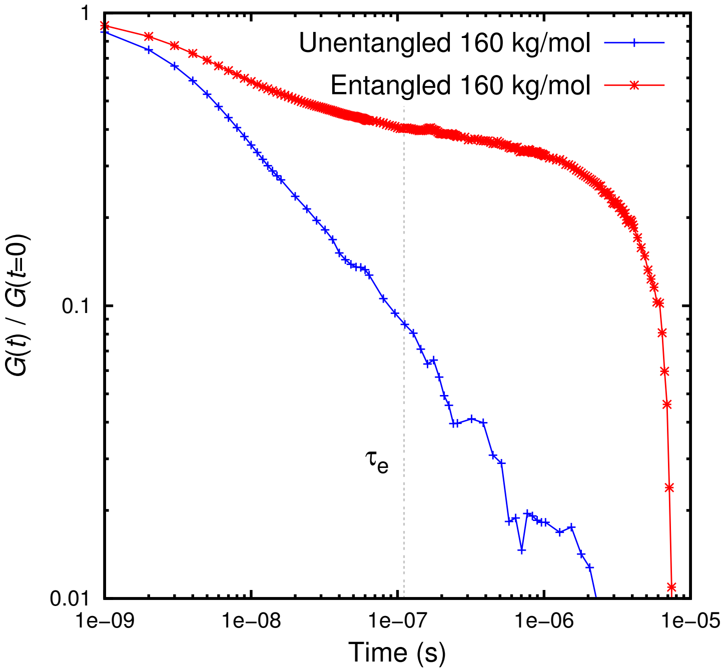

Figure 5.9: Temporal evolution of the shear relaxation modulus, $G\left(t\right)$, for a PI melt of 160 kg/mol in the absence and presence of slip-springs which represent entanglements between different chains.

Our results for the average stress relaxation function, as defined in eq 5.48 are shown in Figure 5.9. The long time behavior of the stress autocorrelation function arises from the Rouse like dynamics of the single chain. In particular, the intermediate time scale behavior of the stress acf is consistent with the Rouse model scaling, $G(t) \sim t^{-1/2}$, while the long time decay is exponential, with a time constant characterizing the longest stress relaxation time in the system. It is clear that the longest relaxation time from the stress autocorrelation function follows the same power law scaling with N as the end-to-end vector relaxation time. In the presence of slip-springs, a plateau starts to appear; this indicates that the viscoelastic character of polymer melts is captured by our model.

5.4 Summary and Conclusions

The first steps towards a consistent coarse-grained model capable of reproducing the rhelogical properties of (nanocomposite) polymer melts have been presented. The methodology and the corresponding computer code have been developed for the case of a pure polymer melt. Chains are modeled as sequences of beads, each bead encompassing approximately 10 Kuhn segments. The Helmholtz energy of the system is written as a sum of three contributions: entropy springs, representing the entropic elasticity of chain strands between beads; slip-springs, representing entanglements; and non-bonded interactions. The Helmholtz energy of non-bonded interactions is estimated by invoking an arbitrary equation of state and is computed as a functional of the local density by passing an orthogonal grid through the simulation box. Slip-springs are envisioned as connecting nodes on different polymer chains. Equations for a stochastic description of the dynamics are derived from the coarse-grained Helmholtz energy function. All beads execute Brownian motion in the high friction limit. The ends of the slip-springs execute thermally activated hops between adjacent beads along chain backbones, these hops being tracked by kMC simulation. In addition, creation/destruction processes are included for the slip-springs. A slip spring is destroyed when one of its ends slips past the free end of a polymer chain. A new slip spring is formed when a chain end captures a bead of another chain lying within a certain radius from it, according to a prescribed rate constant. Parameters needed in the model are derived from experimental volumetric and melt viscosity data or from atomistic molecular dynamics simulations. Initial configurations for the network are obtained from FTiMC simulations of linear melts. Tests of the simulation code on molten linear (non-crosslinked) cis-1,4 polyisprene of high molar mass at equilibrium have given satisfactory results for the mean square displacement of beads and for the shear relaxation modulus. The ultimate goal of this effort is the model to be applied to pure and nanocomposite rubbers. A way of cross-linking FTiMC configurations is presented in Appendix B. The incorporation of the dispersed nanoparticles in the model will be based on our work at the FTiMC level.

6 Main Conclusions and Innovations

In this work, through the use of appropriately designed molecular simulation techniques, three main accomplishments have been brought to completion. First, by conducting Molecular Dynamics (MD) simulations of a well equilibrated polystyrene (PS) - C_{60} system, we obtained critical insight into its local segmental dynamics and stresses. Then, we accessed the scaling features of grafted polymer layers by utilizing a novel Monte Carlo (MC) methodology based on ideas from polymer mean-field theory. That level served as a stepping stone for moving to entangled polymer simulations via a Brownian Dynamics (BD) - kinetic Monte Carlo (kMC) scheme based on the tube theory, where entangled melt rheology has been predicted. The main contribution of this thesis was to build up a bottom-up modeling hierarchy capable of providing fundamental understanding and answers to specific nanocomposite design problems, and explore the relations between the several modeling levels within it. In the following we briefly present the innovations brought by the dissertation at three levels: methodology, physical insight, and computational tools.

6.1 Methodological Advances

- In addition to the “atomic virial” formulation of Theodorou et al.,[134] two more *stress tensor definitions* have been used in order to calculate stresses from molecular simulations. The first one, based on the derivative of the Helmholtz enegy with respect to the strain, allows clear mathematical treatment of three- and four-body potentials as well as conservative fields (Appendix A). The second one, based on the deformation gradient tensor, proved very efficient in the case of spatial discretization schemes, as the one described in Chapter 5 and Appendix C.

- A rigorous and efficient *reverse mapping* scheme for coarse grained (CG) PS has been developed, which provides atomistic configurations with conformational characteristics in excellent agreement with experimental measurements. Previous efforts resulted in unrealistic polymer configurations. Moreover, we consider it as *true reverse mapping* because the positions of the coarse-grained sites are kept constant, during a procedure involving local MC moves and energy minimizations, ensuring that the atomistic configuration shares exactly the same features as the CG one, at length scales larger than the monomer size.

- Derivation of an *integrated potential between a point and a spherical shell* on the grounds of Hamaker's theory. Despite the fact that expressions for point-point, point-sphere and sphere-sphere integrations have already appeared in the literature, it was the first time for a point-spherical shell integrated potential to be reported.

- Quite a long time after the pioneering work of Theodorou and Suter,[218] *atomic and local stresses* have been calculated for polymer melts and glasses. The contribution of this thesis consists in deriving the necessary expressions for arbitrary three- and four-body potentials and estimating the atomic volume by a Voronoi tessellation of the simulation domain.

- Quantification of nanoparticle-induced *confinement* by employing the *volume of the Voronoi cells* as a measure of it. Many-particle influence on dynamics and stress distributions has been studied.

- Formulation of a *MC simulation approach inspired by polymer mean field theory*, capable of capturing structural features at length scales in the order of hundreds of nanometers. Polymer chains are represented as random walks and Hamaker integrated potentials are used for describing polymer-particle and particle-particle interactions. The parameterization of the coarse-grained model is based directly on the atomistic force fields without the need of introducing additional parameters.

- Derivation of a *closed form expression* for the scattering of freely jointed chains by combining and extending previous works.[81,287,288] That expression was incorporated in a Pedersen-like[293] model in order to analyze Small Angle Neutron Scattering (SANS) spectra of the grafted polymer brushes.

- Development of an *equation of state - based slip-spring model* capable of describing the dynamics of (entangled) polymer melts. The parameterization of the model can be based on atomistic simulations and an arbitrary Equation of State (EoS) can be incorporated.

- Development of a *kMC scheme* for capturing the *tube motion* of the chains in entangled environments. The mechanisms of reptation, contour-length fluctuation (CLF) and constraint release (CR) have been incorporated.
- Well-equilibrated initial configurations for entangled slip-spring polymer melt simulations have been obtained by Field Theory-inspired Monte Carlo (FTiMC) simulations. Moreover, crosslinked initial configurations can be obtained by following the procedure described in Appendix B.

6.2 Physical Insight Obtained

By using the methodologies described above we have extended our understanding of materials in the following ways:

- *PS chain conformations* obtained through CG MC simulations were equilibrated at all length scales and found to be in excellent agreement with available experimental evidence (Figures 3.1 and 3.2 on page 70).
- *No effect of the dispersion of C_{60}s* has been observed at the *chain conformations* of PS chains.
- Our simulation results generally indicate that the *addition of C_{60}s to PS* leads to *slower segmental dynamics* (as estimated by characteristic times extracted from the decay of orientational time-autocorrelation functions of suitably chosen vectors).
- The overall *mean-square displacement of backbone atoms* is found to be *smaller in the presence of fullerenes*, than in bulk PS (Figure 3.12 on page 87).
- Atoms moving in *smaller (more confined) Voronoi cells* exhibit *faster motion* than the atoms moving inside larger Voronoi cells. If this is correlated with the *increased rotational diffusion of fullerenes*, as the volume of the Voronoi cell becomes smaller, can drive us to envision fullerenes as *nanoscopic millstones* that force the polymeric chains to translationally diffuse.
- The *dynamic heterogeneity* caused by the addition of fullerenes exhibits *strong temperature dependence*, getting larger as the temperature is lowered.
- *Coordination numbers* and *atomic volumes* of atoms in polymer melts and glasses have been calculated via a Voronoi tessellation of the simulation domain. That was an in-

termediate step in calculating atomic stresses, where the volume of an atom should be defined in order to convert virial into stress (eq 3.11 on page 90).

- *Atomic stresses* in the *melt* and *glassy* state have been calculated. Each united atom is characterized by a *distribution of atomic stresses* whose shape and position reflect its chemical nature, connectivity, and geometric disposition within the system.
- *Local stresses* have been obtained by the summation of atomic contributions from atoms lying inside a control volume and their dependence on the observation length-scale has been studied. Hydrostatic pressure can be calculated from arbitrarily small control volumes, while von Mises shear stress has been found to scale as the inverse square root of the volume of the material used for the calculation.
- By *increasing the particle grafting density*, the brush of grafted chains undergoes a phase transition from its stretched to its collapsed form, in agreement to scaling theories[244] and MD simulations.[247] The phase transition has been attributed to the *autophobic dewetting of the brush by the melt.*
- *Increasing the brush chain length leads to thicker grafted brushes*, which improve the miscibility of nanoparticles with the homopolymer matrix, in agreement with Self Consistent Field (SCF) studies.[242]
- The density distributions around a nanoparticle seem to *depend only on grafting density and grafted chain length*, especially when the matrix chain length is equal to or longer than the grafted chain length. *"Wet-to-dry"* conformational transition[260] *has not been observed*. Our prediction was later validated by experimental studies.[345]
- The *scaling of polymeric layers grafted to nanoparticles* can be well described by the model proposed by *Daoud and Cotton*[232] for star-shaped polymers. The brush thickness scales with the *square root of the grafted chain length* and the *fourth root of the grafted density*.
- *Single chain and corona SANS scattering spectra* for chains grafted to nanoparticles have been estimated from simulations for the first time.
- At the single chain level, grafted chains *deviate strongly from their random walk statistics*, especially for *high surface coverage and molar mass*.
- The *corona structure factors* for 13-nm-radius grafted particles dispersed in different molar mass matrices have been *validated against SANS measurements* of Chevigny et al.[260]

6.3 Computational Tools

In the framework of the present thesis the following computer codes have been developed:

- *MC builder*[346] capable of building polymeric chains of arbitrary geometry in *heavily confined environments*, based on the quasi-Metropolis scheme of Theodorou and Suter.[165] In case the insertion of a new monomer fails, a local energy minimization is undertaken in order to drive the insertion to the most energetically favorable positions.
- *Configurationally biased reverse mapping* of CG PS to the atomistic level. This F77 code can restore atomistic details of CG PS configurations. With little effort it can also be extended to other molecular architectures.
- *FTiMC code for the generation and equilibration of polymer matrix nanocomposites* using molecular characteristics and thermodynamic information as input. It is coupled to the analytical algorithm of Dodd and Theodorou[263] for the estimation of free volume. Moroever, it is self-contained with the only input being the molecular characteristics (Kuhn length, molecular weight), the isothermal compressibility and the Hamaker constants of the polymer and the particles.
- *Random-crosslinking of FTiMC configurations* C++ source code (Appendix B). The code can disperse random crosslinks in the presence of nanoparticles, taking periodic boundary conditions into account. It can be easily generalized to arbitrary molecular architectures.
- *EoS-based BD slip-spring simulation* C++ source code. The code can track the dynamics of slip-springs along the chain contour via a kinetic MC scheme. It can be easily extended and has been thoroughly documented.
- *Post-processing scripts for trajectories generated by the LAMMPS* application in Python, for hydrogen reconstruction, for studying structure (local density, SANS and X-ray spectra) and dynamics (bond/torsional autocorrelation functions, dynamic structure factor, local dynamics) of polymer melts and glasses.
- *Generic and easily extensible* C++ source code for *post-processing molecular simulation trajectories*. This code employs an abstract data model for the representation of molecular entities, allowing atomic-level and local calculations by using various discretization schemes. The user can interact by a specially designed scripting language. The incorporation of new features requires minimum effort due to the intrinsic object-oriented design

of the code which has been based on standard graph algorithms and lexical parsing techniques.

and the following ones have been extended:

- Polyethylene connectivity-altering MC F77 code. The original code has been developed by Theodorou, Boone, Mavrantzas and Karayiannis. Our contribution is limited to creating C interfaces and initial CUDA routines (used for a successful Academic Partnership proposal to nVIDIA) which were then extended and implemented in polyethylene simulations by A. Morphis.
- CG PS connectivity-altering MC F77 code. Spyriouni[32] has modified the above PE connectivity-altering MC code in order to simulate CG PS instead of PE. We have extended this code with the capability of simulating nanocomposite materials (incorporating spherical nanoparticles interacting via sphere/sphere, sphere/shell, shell/shell Hamaker potentials), non-periodic and confined systems.
- The Large-scale Atomic/Molecular Massively Parallel Simulator (LAMMPS) MD simulation application has been extended with the necessary routines for fully supporting the united-atom forcefield of PS.[177]

6.4 Side Projects

In order to address the main challenges of the PhD thesis, several other problems have been resolved:

- A method has been formulated, based on combining self-consistent field theory with dynamically corrected transition state theory, for estimating the rates of adsorption and desorption of end-constrained chains (e.g., by cross-links or entanglements) from a polymer melt onto a solid substrate.[347] This method has been tested on a polyethylene/graphite system, where it was parameterized based on atomistically detailed molecular simulations. For short-chain melts, which can still be addressed by molecular dynamics simulations with reasonable computational resources, this SCF/TST approach gives predictions of the adsorption and desorption rate constants which are gratifyingly close to molecular dynamics estimates.
- The generation of well-equilibrated atomistic configurations of polymer systems is a prerequisite for the reliable prediction of their properties through molecular and multiscale modeling. We have managed to integrate the unprecedented computational power

of graphics processing unit (GPU) computing into a MC scheme enabling equilibration of polymeric melts and polymer-matrix nanocomposite systems at large length scales. Our strategy for parallelizing MC codes for use with nVIDIA GPUs supporting CUDA involves concurrent calculation of the bonded interactions at the central processing unit (CPU) and non-bonded interactions at the GPU. Well equilibrated MC configurations have been used to predict the structure and thermodynamic properties of long-chain PE and PS melts. Both MC and MD simulations have been accelerated by at least an order of magnitude by exploiting nVIDIA Fermi architecture GPUs. This has made feasible the atomistic simulation of polymer systems of molar mass up to 400 kg/mol consisting of hundreds of thousands of interacting atoms on a modern computer server node.

7 Research Outlook

The mathematical formulation, the computer codes developed, as well as the selection of input parameters to all simulation levels were carried out in a rigorous and versatile way, ensuring their applicability to a wide class of problems. Special attention has been paid to linking the individual levels of modeling in a consistent way. Below we summarize some interesting potential applications, which are very relevant to the ones studied in the present thesis.

7.1 PS Coarse-Graining - Reverse Mapping - Atomistic MD

Based on the methods developed for the atomistic simulation of polystyrene (PS), several other problems can be addressed:

- *Elastic constants* for both pure and nanocomposite polymer glasses can be immediately calculated from atomistic Molecular Dynamics (MD) trajectories, based on a stress fluctuation formalism,[137] and the second-order strain derivatives, already derived in Appendix A. The first results on the estimation of the elastic constants of an argon crystal are highly promising and the necessary methodology and computer code for extending the study to polymer glasses has been fully developed. Moreover, atomic level elastic constants can be defined, through a rigorous geometric framework. Based on atomic level elastic constants, local elastic constants can be defined by summing individual atomic contributions.

- *Spatial and temporal stress correlations* in polymer melts and glasses. We start from the Green-Kubo expression that relates viscosity to the time-integral of the macroscopic shear stress correlation function and we decompose it into correlation functions between atomic-level stresses, extending previous work by Levashov et al. in the field of metallic melts[348–350] and crystals.[351] The concept of the atomic-level stresses allows the macroscopic stress-stress correlation function in the Green-Kubo relation to be expressed in terms of the space- and time-correlations arising among the atomic-level stresses.

7.2 Field Theory-inspired Monte Carlo Simulations

Based on the Field Theory-inspired Monte Carlo (FTiMC) methodology, a broad range of materials (pure and composite) can be addressed, by simply providing as an input to the method the melt compressibility and the Kuhn length of the polymer. Among the limitless possibilities, the following classes of materials exhibit special interest:

- *Block copolymers* for use in directed self-assembly (DSA). DSA is one of the most promising techniques to sustain the miniaturization of integrated circuits and to boost the performance predicted by Moore's law. It combines top-down photolithography for creation of guiding patterns with engineered new materials and processes to facilitate cost effective bottom-up techniques for pattern density multiplication and defect rectification.[352]
- *Binary blends of linear polymer with well-separated molecular weights*. FTiMC can provide well equilibrated initial configurations of systems consisting of two kinds of polymer chains with very different chain lengths. Slip-spring simulations of these systems can provide insight into the constraint release (CR) and dynamic tube dilation processes.[330,331]

7.3 EOS-based Slip Spring Model for Polymer Dynamics

The methodology and tools developed based on the slip-spring model introduced in Chapter 5 can be used for predicting the rheology of arbitrary polymer melts. The input parameters, either for the molecular characteristics of the system, or for the equation of state involved, can be extracted from experimental findings. Initial configurations can be obtained by FTiMC simulations. Possibly interesting case studies would include:

- *Nanoparticle filled melts and elastomers*. We are currently in the process of adding the capability of simulating polymer melts with dispersed spherical particles. The free energy function has been extended by two additional terms describing the polymer-nanoparticle and nanoparticle-nanoparticle interactions. The kinetic Monte Carlo scheme will be enriched by events of adsorption/desorption of nodal points on the surface of the particles, by employing a suitable model for the estimation of the rates.[347]
- *Binary blends of linear polymer with well-separated molecular weights*. In connection to

the interesting case studies for the FTiMC approach, the rheology of blends of polymers with extremely different molecular weights is of paramount importance, both in terms of fundamental understanding and industrial applications.

Appendices

A Strain Derivatives of the Potential Energy

We consider a potential energy function, $\mathcal{V}$, which can be written as:

$$\begin{aligned}\mathcal{V} = &\sum_{(i,j)} \mathcal{V}_{\text{bond}}\left(r_{ij}\right) + \sum_{(i,j,k)} \mathcal{V}_{\text{angle}}\left(\theta_{ijk}\right) \\ &+ \sum_{(i,j,k,l)} \mathcal{V}_{\text{torsion}}\left(\phi_{ijkl}\right) + \sum_{(i,j)} \mathcal{V}_{\text{nb}}\left(r_{ij}\right) + \mathcal{V}_{\text{long}}\end{aligned} \tag{A.1}$$

which is a sum of contributions of bond stretching potentials, $\mathcal{V}_{\text{bond}}\left(r_{ij}\right)$, between connected atoms, bond bending potentials, $\mathcal{V}_{\text{angle}}\left(\theta_{ijk}\right)$, involving three (not necessarily consecutive atoms), torsional potentials $\mathcal{V}_{\text{torsion}}\left(\phi_{ijkl}\right)$ involving four arbitrary (not necessarily connected with bonds) atoms, pairwise additive nonbonded interactions, $\mathcal{V}_{\text{nb}}\left(r_{ij}\right)$ and long-range corrections, $\mathcal{V}_{\text{long}}$. The summations extend over the relevant sets of tuples, $\{(\dots)\}$, where (i,j) are pairs of i and j, (i,j,k) are triads of i, j and k, etc. The description we employ here, which is based on sets of bonds, angles, torsion angles and pairs of atoms interacting through non-bonded interactions, allows for special rules e.g. between neighboring atoms to exist.

The Cartesian coordinates of the atoms are denoted by lowercase latin characters with one index, e.g. $\mathbf{r}_i, \mathbf{r}_j$, while the separation vectors with lowercase latin characters with two indices, e.g. $\mathbf{r}_{ij}$. It holds that $\mathbf{r}_{ij} = \mathbf{r}_j - \mathbf{r}_i$ and $r_{ij} = \|\mathbf{r}_{ij}\|$.

At constant temperature T the stress tensor, $\tau_{\alpha\beta}$, is given in terms of the Helmholtz energy by eq 2.161 on page 58:[353]

$$\tau_{\alpha\beta} = \frac{1}{V_{\mathscr{R}}} \left.\frac{\partial A}{\partial \epsilon_{\alpha\beta}}\right)_{T,\epsilon_{[\alpha\beta]}} \tag{A.2}$$

which in the NVT ensemble is cast in eq 2.170 on page 59:

$$\tau_{\alpha\beta} = \left\langle \sigma^{\mathcal{V}}_{\alpha\beta} \right\rangle_{NVT} - \rho k_{\text{B}} T \delta_{\alpha\beta} \tag{A.3}$$

where

$$\sigma^{\mathcal{V}}_{\alpha\beta} = \frac{1}{V_{\mathscr{R}}} \left.\frac{\partial \mathcal{V}}{\partial \epsilon_{\alpha\beta}}\right)_{T,\epsilon_{[\alpha\beta]}} \tag{A.4}$$

with ρ being the number density and the brackets denoting the NVT ensemble average.

The isothermal stiffness tensor, $C_{\alpha\beta\gamma\delta}$ is given in terms of the Helmholtz energy by:[354]

$$C_{\alpha\beta\gamma\delta} = \frac{1}{V_{\mathscr{R}}} \frac{\partial^2 A}{\partial \epsilon_{\alpha\beta} \partial \epsilon_{\gamma\delta}} \tag{A.5}$$

Differentiating the free energy twice with respect to the strain gives:[140,353]

$$C_{\alpha\beta\gamma\delta} = C^{\mathcal{V}}_{\alpha\beta\gamma\delta} + C^{\mathcal{F}}_{\alpha\beta\gamma\delta} + C^{\mathcal{K}}_{\alpha\beta\gamma\delta} \tag{A.6}$$

where

$$C^{\mathcal{V}}_{\alpha\beta\gamma\delta} = \frac{1}{V_{\mathscr{R}}} \left\langle \frac{\partial^2 \mathcal{V}}{\partial \epsilon_{\alpha\beta} \partial \epsilon_{\gamma\delta}} \right\rangle \tag{A.7}$$

$$C^{\mathcal{F}}_{\alpha\beta\gamma\delta} = -\frac{V_{\mathscr{R}}}{k_{\mathrm{B}}T} \left[\left\langle \sigma^{\mathcal{V}}_{\alpha\beta} \sigma^{\mathcal{V}}_{\gamma\delta} \right\rangle - \left\langle \sigma^{\mathcal{V}}_{\alpha\beta} \right\rangle \left\langle \sigma^{\mathcal{V}}_{\gamma\delta} \right\rangle \right] \tag{A.8}$$

and

$$C^{\mathcal{K}}_{\alpha\beta\gamma\delta} = 2\rho k_{\mathrm{B}} T \left(\delta_{\alpha\gamma}\delta_{\beta\delta} + \delta_{\alpha\delta}\delta_{\beta\gamma} \right) \tag{A.9}$$

The first term in eq A.6 is the so-called Born term and is related to zero temperature elastic constants. The second term is the stress fluctuation term and accounts for the finite temperature effects. The last term in eq A.6 is the ideal gas contribution and is related to the derivatives of the volume with respect to strain tensor. Typically, only the first two terms contribute significantly to the elastic constants. The Born term describes the contribution to the elastic moduli resulting from a uniform displacement of all particles provoked by a macroscopically imposed homegeneous deformation. The assumption of such an affine displacement at all length scales is not necessarily justified. At the molecular scale, nonaffine particle motion can decrease the free energy and lead to a further contribution to the elastic moduli. This contribution is accounted for by the stress-fluctuation term.

By construction, the stress-fluctuation formalism is a thermodynamic approach; it can be applied to the equilibrium crystal, but also to the equilibrium liquid. For an equilibrium liquid the shear and bulk moduli can be determined from the stress-fluctuation formalism by following the calculations of Zwanzig and Mountain.[355] For the shear modulus one finds $G = 0$, as it must be for a liquid, while the result for the bulk modulus gives back an expression known from the literature (e.g. eq 2.79 from ref 198). For the polymer glasses studied here, the averages in eqs A.3 and A.6 are not equilibrium averages. A polymeric glass is not in thermodynamic equilibrium is not in thermodynamic equilibrium and does not have access to all of configuration space. Thermal motion consists predominantly of solid-like vibrations of atoms around their equilibrium positions and mechanical response to small deformations is adequately described by linear elasticity.[179]

Although the stress-fluctuation formula for the elasticity tensor has several advantages, its use has been limited by the difficulty in evaluating the Born term for complex atomic potentials.[356,357] For many potentials, multibody interactions such as bending and torsion make the use of stress fluctuation formula unattractive. Exact expressions for the Born term for potentials that include bending and torsional contributions were derived by van Workum et al.[358] From eqs A.3 and A.6 we can compute the stress and elasticity tensor for any given potential energy function, $\mathcal{V}$, given an equilibrium trajectory of the system.

A.1 Strain Derivatives of Two-body Potentials

A.1.1 Bond Stretching Potential

The contribution of the bond stretching potential, $\mathcal{V}_{\text{bond}}(r_{ji})$ to the box stress tensor is:

$$\sigma_{\alpha\beta}^{\mathcal{V},\text{bond}} = \frac{1}{V}\sum_{(i,j)} \frac{\partial \mathcal{V}_{\text{bond}}\left(r_{ij}\right)}{\partial r_{ij}} \frac{\partial r_{ij}}{\partial \epsilon_{\alpha\beta}} \tag{A.10}$$

where the (i, j) stands for a bond connecting the pair of atoms i and j and $\{(i, j)\}$ denotes the set of all bonds present in the system. The partial derivative of the norm of the bond vector with respect to the strain is:

$$\frac{\partial r_{ij}}{\partial \epsilon_{\alpha\beta}} = \frac{r_{ij,\alpha} r_{ij,\beta}}{r_{ij}} \tag{A.11}$$

The Born contribution to the elasticity tensor is:

$$\begin{aligned} C_{\alpha\beta\gamma\delta}^{\mathcal{V},\text{bond}} &= \frac{1}{V}\sum_{(i,j)} \frac{\partial^2 \mathcal{V}_{\text{bond}}\left(r_{ij}\right)}{\partial \epsilon_{\alpha\beta}\partial \epsilon_{\gamma\delta}} \\ &= \frac{1}{V}\sum_{(i,j)} \left[\frac{\partial^2 \mathcal{V}_{\text{bond}}(r_{ij})}{\partial r_{ij}^2} - \frac{1}{r_{ij}}\frac{\partial \mathcal{V}_{\text{bond}}(r_{ij})}{\partial r_{ij}}\right] \frac{r_{ij,\alpha} r_{ij,\beta} r_{ij,\gamma} r_{ij,\delta}}{r_{ij}^2} \end{aligned} \tag{A.12}$$

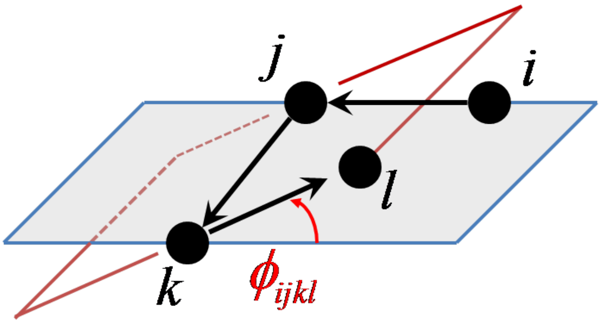

Figure A.1: Vectors defining the bond angle θ_{ijk} and torsion angle ϕ_{ijkl}.

A.1.2 Pairwise Additive Non-bonded Potential

The contribution of the pairwise additive non-bonded potential, $\mathcal{V}_{\text{nb}}(r_{ij})$ to stress tensor $\sigma_{\alpha\beta}^{\mathcal{V},\text{nb}}$ tensor is:

$$\sigma_{\alpha\beta}^{\mathcal{V},\text{nb}} = \frac{1}{V}\sum_{(i,j)} \frac{\partial \mathcal{V}_{\text{nb}}\left(r_{ij}\right)}{\partial \epsilon_{\alpha\beta}} = \frac{1}{V}\sum_{(i,j)} \frac{\partial \mathcal{V}_{\text{nb}}\left(r_{ij}\right)}{\partial r_{ij}} \frac{\partial r_{ij}}{\partial \epsilon_{\alpha\beta}} \tag{A.13}$$

where the derivative $\partial r_{ij}/\partial \epsilon_{\alpha\beta}$ is given by eq A.11.

The contribution of the pairwise additive non-bonded interactions to the Born term of the elasticity tensor is:

$$\begin{aligned} C_{\alpha\beta\gamma\delta}^{\mathcal{V},\text{nb}} &= \frac{1}{V}\sum_{(i,j)} \frac{\partial^2 \mathcal{V}_{\text{nb}}\left(r_{ij}\right)}{\partial \epsilon_{\alpha\beta}\partial \epsilon_{\gamma\delta}} \\ &= \frac{1}{V}\sum_{(i,j)} \left[\frac{\partial^2 \mathcal{V}_{\text{nb}}(r_{ij})}{\partial r_{ij}^2} - \frac{1}{r_{ij}}\frac{\partial \mathcal{V}_{\text{nb}}(r_{ij})}{\partial r_{ij}}\right] \frac{r_{ij,\alpha} r_{ij,\beta} r_{ij,\gamma} r_{ij,\delta}}{r_{ij}^2} \end{aligned} \tag{A.14}$$

A.2 Strain Derivatives of Three-body Potentials

We consider the angle formed between three consecutive atoms i, j and k as:

$$\theta_{ijk} = \arccos\left(\frac{\mathbf{r}_{ji}\cdot\mathbf{r}_{jk}}{\|\mathbf{r}_{ji}\|\,\|\mathbf{r}_{jk}\|}\right) \tag{A.15}$$

where $\mathbf{r}_{ji} = \mathbf{r}_i - \mathbf{r}_j$ and $\mathbf{r}_{jk} = \mathbf{r}_k - \mathbf{r}_j$. We consider the vector $\mathbf{r}_{ji}$ instead of $\mathbf{r}_{ij}$ so as the bond vectors start from the same origin, which facilitates the calculation of first- and second-order derivatives.

The contribution of the three-body angle potential, $\mathcal{V}_{\text{angle}}\left(\theta_{ijk}\right)$ to the stress tensor is:

$$\sigma_{\alpha\beta}^{\mathcal{V},\text{angle}} = \frac{1}{V}\sum_{\theta_{ijk}} \frac{\partial \mathcal{V}_{\text{angle}}\left(\theta_{ijk}\right)}{\partial \cos\theta_{ijk}} \frac{\partial \cos\left(\theta_{ijk}\right)}{\partial \epsilon_{\alpha\beta}} \tag{A.16}$$

where the derivative of $\cos\left(\theta_{ijk}\right)$ with respect to the strain $\epsilon_{\alpha\beta}$ is given as:[358,359]

$$\frac{\partial \cos\left(\theta_{ijk}\right)}{\partial \epsilon_{\alpha\beta}} = \left(\frac{r_{jk,\alpha}r_{ji,\beta} + r_{ji,\alpha}r_{jk,\beta}}{\|\mathbf{r}_{ji} \cdot \mathbf{r}_{jk}\|} - \frac{r_{ji,\alpha}r_{ji,\beta}}{r_{ji}^2} - \frac{r_{jk,\alpha}r_{jk,\beta}}{r_{jk}^2}\right)\cos\left(\theta_{ijk}\right) \tag{A.17}$$

The contribution of the angle potential to the elasticity tensor of the box is:

$$\begin{aligned} C_{\alpha\beta\gamma\delta}^{\mathcal{V},\text{angle}} &= \frac{1}{V}\sum_{\theta_{ijk}} \frac{\partial^2 \mathcal{V}_{\text{angle}}\left(\theta_{ijk}\right)}{\partial \epsilon_{\alpha\beta}\partial \epsilon_{\gamma\delta}} \\ &= \frac{1}{V}\sum_{\theta_{ijk}} \left[\frac{\partial^2 \mathcal{V}_{\text{angle}}}{\partial \cos^2\left(\theta_{ijk}\right)}\frac{\partial \cos\left(\theta_{ijk}\right)}{\partial \epsilon_{\alpha\beta}}\frac{\partial \cos\left(\theta_{ijk}\right)}{\partial \epsilon_{\gamma\delta}} + \frac{\partial \mathcal{V}_{\text{angle}}}{\partial \cos\left(\theta_{ijk}\right)}\frac{\partial^2 \cos\left(\theta_{ijk}\right)}{\partial \epsilon_{\alpha\beta}\partial \epsilon_{\gamma\delta}}\right] \end{aligned} \tag{A.18}$$

with the second derivative of $\cos\left(\theta_{ijk}\right)$ with respect to the strain being:

$$\frac{\partial^2 \cos\left(\theta_{ijk}\right)}{\partial \epsilon_{\alpha\beta}\partial \epsilon_{\gamma\delta}} = \cos\left(\theta_{ijk}\right)\frac{\partial^2 \ln\left[\cos\left(\theta_{ijk}\right)\right]}{\partial \epsilon_{\alpha\beta}\partial \epsilon_{\gamma\delta}} + \frac{1}{\cos\left(\theta_{ijk}\right)}\frac{\partial \cos\left(\theta_{ijk}\right)}{\partial \epsilon_{\alpha\beta}}\frac{\partial \cos\left(\theta_{ijk}\right)}{\partial \epsilon_{\gamma\delta}} \tag{A.19}$$

where the first right-hand term of the last relation is equal to:

$$\begin{aligned} \frac{\partial^2 \ln\left[\cos\left(\theta_{ijk}\right)\right]}{\partial \epsilon_{\alpha\beta}\partial \epsilon_{\gamma\delta}} &= 2\left(\frac{r_{ji,\alpha}\, r_{ji,\beta}\, r_{ji,\gamma}\, r_{ji,\delta}}{\|\mathbf{r}_{ji}\|^4} + \frac{r_{jk,\alpha}\, r_{jk,\beta}\, r_{jk,\gamma}\, r_{jk,\delta}}{\|\mathbf{r}_{jk}\|^4}\right) \\ &\quad - \frac{\left(r_{jk,\alpha}\, r_{ji,\beta} + r_{ji,\alpha}\, r_{jk,\beta}\right)\left(r_{jk,\gamma}\, r_{ji,\delta} + r_{ji,\gamma}\, r_{jk,\delta}\right)}{\|\mathbf{r}_{ji} \cdot \mathbf{r}_{jk}\|^2} \end{aligned} \tag{A.20}$$

A.3 Strain Derivatives of Four-body Potentials

Torsional potentials commonly contain terms that include the cosine of the dihedral angle formed by four consecutive atoms:

$$\cos\left(\phi_{ijkl}\right) = \frac{\mathbf{r}_{ij} \times \mathbf{r}_{jk}}{\|\mathbf{r}_{ij} \times \mathbf{r}_{jk}\|} \cdot \frac{\mathbf{r}_{jk} \times \mathbf{r}_{kl}}{\|\mathbf{r}_{jk} \times \mathbf{r}_{kl}\|} \tag{A.21}$$

The first derivative of a torsional potential with respect to the strain is given as:

$$\sigma_{\alpha\beta}^{\mathcal{V},\text{torsion}} = \frac{1}{V}\sum_{\phi_{ijkl}} \frac{\partial \mathcal{V}_{\text{torsion}}}{\partial \cos\left(\phi_{ijkl}\right)}\frac{\partial \cos\left(\phi_{ijkl}\right)}{\partial \epsilon_{\alpha\beta}} \tag{A.22}$$

For clarity, the substitution $\mathbf{m} = \mathbf{r}_{ij} \times \mathbf{r}_{jk}$ and $\mathbf{n} = \mathbf{r}_{jk} \times \mathbf{r}_{kl}$ is made, so that:

$$\cos\left(\phi_{ijkl}\right) = \frac{\mathbf{m} \cdot \mathbf{n}}{mn} \tag{A.23}$$

Following Van Workum et al.,[358] the first and the second strain derivative of the cosine of the torsion angle ϕ_{ijkl} can be written as:

$$\frac{\partial \cos\left(\phi_{ijkl}\right)}{\partial \epsilon_{\alpha\beta}} = \frac{\cos\left(\phi_{ijkl}\right)}{2}\left[\frac{2}{(\mathbf{m}\cdot\mathbf{n})}\frac{\partial\left(\mathbf{m}\cdot\mathbf{n}\right)}{\partial \epsilon_{\alpha\beta}} - \frac{1}{m^2}\frac{\partial\left(m^2\right)}{\partial \epsilon_{\alpha\beta}} - \frac{1}{n^2}\frac{\partial\left(n^2\right)}{\partial \epsilon_{\alpha\beta}}\right] \tag{A.24}$$

where:

$$\begin{aligned}\frac{\partial\left(\mathbf{m}\cdot\mathbf{n}\right)}{\partial \epsilon_{\alpha\beta}} &= \left(\mathbf{r}_{ij}\cdot\mathbf{r}_{jk}\right)\left(r_{jk,\alpha}\, r_{kl,\beta} + r_{kl,\alpha}\, r_{jk,\beta}\right)\\ &+ \left(\mathbf{r}_{jk}\cdot\mathbf{r}_{kl}\right)\left(r_{ij,\alpha}\, r_{jk,\beta} + r_{jk,\alpha}\, r_{ij,\beta}\right)\\ &- \left(\mathbf{r}_{ij}\cdot\mathbf{r}_{kl}\right)\left(r_{jk,\alpha}\, r_{jk,\beta} + r_{jk,\alpha}\, r_{jk,\beta}\right)\\ &- \left(\mathbf{r}_{jk}\cdot\mathbf{r}_{jk}\right)\left(r_{ij,\alpha}\, r_{kl,\beta} + r_{kl,\alpha}\, r_{ij,\beta}\right)\end{aligned} \tag{A.25}$$

$$\begin{aligned}\frac{\partial\left(m^2\right)}{\partial \epsilon_{\alpha\beta}} = 2\big[&\left(\mathbf{r}_{jk}\cdot\mathbf{r}_{jk}\right) r_{ij,\alpha} r_{ij,\beta}\\ &+ \left(\mathbf{r}_{ij}\cdot\mathbf{r}_{ij}\right) r_{jk,\alpha} r_{jk,\beta}\\ &- \left(\mathbf{r}_{ij}\cdot\mathbf{r}_{jk}\right)\left(r_{ij,\alpha} r_{jk,\beta} + r_{jk,\alpha} r_{ij,\beta}\right)\big]\end{aligned} \tag{A.26}$$

$$\begin{aligned}\frac{\partial\left(n^2\right)}{\partial \epsilon_{\alpha\beta}} = 2\big[&\left(\mathbf{r}_{jk}\cdot\mathbf{r}_{jk}\right) r_{kl,\alpha} r_{kl,\beta}\\ &+ \left(\mathbf{r}_{kl}\cdot\mathbf{r}_{kl}\right) r_{jk,\alpha} r_{jk,\beta}\\ &- \left(\mathbf{r}_{kl}\cdot\mathbf{r}_{jk}\right)\left(r_{kl,\alpha} r_{jk,\beta} + r_{jk,\alpha} r_{kl,\beta}\right)\big]\end{aligned} \tag{A.27}$$

The contribution of the torsional potential to the Born term of the elasticity tensor of the box is:

$$\begin{aligned}
C_{\alpha\beta\gamma\delta}^{\mathcal{V},\text{torsion}} &= \frac{1}{V}\sum_{\phi_{ijkl}} \frac{\partial^2 \mathcal{V}_{torsion}\left(\phi_{ijkl}\right)}{\partial\epsilon_{\alpha\beta}\partial\epsilon_{\gamma\delta}} \\
&= \frac{1}{V}\sum_{\phi_{ijkl}} \left[\frac{\partial^2 \mathcal{V}_{\text{torsion}}}{\partial\left(\cos\left(\phi_{ijkl}\right)\right)^2} \frac{\partial \cos\left(\phi_{ijkl}\right)}{\partial\epsilon_{\alpha\beta}} \frac{\partial \cos\left(\phi_{ijkl}\right)}{\partial\epsilon_{\gamma\delta}} \right. \\
&\qquad \left. + \frac{\partial \mathcal{V}_{\text{torsion}}}{\partial \cos\left(\phi_{ijkl}\right)} \frac{\partial^2 \cos\left(\phi_{ijkl}\right)}{\partial\epsilon_{\alpha\beta}\partial\epsilon_{\gamma\delta}} \right]
\end{aligned} \tag{A.28}$$

The second derivative of $\cos\left(\phi_{ijkl}\right)$ with respect to the strain is given as:

$$\begin{aligned}
\frac{2}{\cos\phi_{ijkl}} \frac{\partial^2 \cos\left(\phi_{ijkl}\right)}{\partial\epsilon_{\alpha\beta}\epsilon\gamma\delta} = &- \frac{4}{\left(\mathbf{m}\cdot\mathbf{n}\right)^2} \frac{\partial\left(\mathbf{m}\cdot\mathbf{n}\right)}{\partial\epsilon_{\alpha\beta}} \frac{\partial\left(\mathbf{m}\cdot\mathbf{n}\right)}{\partial\epsilon_{\gamma\delta}} + \frac{2}{\left(\mathbf{m}\cdot\mathbf{n}\right)} \frac{\partial^2\left(\mathbf{m}\cdot\mathbf{n}\right)}{\partial\epsilon_{\alpha\beta}\epsilon_{\gamma\delta}} \\
&+ \frac{1}{m^4} \frac{\partial\left(m^2\right)}{\partial\epsilon_{\alpha\beta}} \frac{\partial\left(m^2\right)}{\partial\epsilon_{\gamma\delta}} - \frac{1}{m^2} \frac{\partial^2\left(m^2\right)}{\partial\epsilon_{\alpha\beta}\partial\epsilon_{\gamma\delta}} \\
&+ \frac{1}{n^4} \frac{\partial\left(n^2\right)}{\partial\epsilon_{\alpha\beta}} \frac{\partial\left(n^2\right)}{\partial\epsilon_{\gamma\delta}} - \frac{1}{n^2} \frac{\partial^2\left(n^2\right)}{\partial\epsilon_{\alpha\beta}\partial\epsilon_{\gamma\delta}}
\end{aligned} \tag{A.29}$$

where:

$$\begin{aligned}
\frac{\partial^2\left(\mathbf{m}\cdot\mathbf{n}\right)}{\partial\epsilon_{\alpha\beta}\partial\epsilon_{\gamma\delta}} &= \left(r_{ij,\alpha}\, r_{jk,\beta} + r_{jk,\alpha}\, r_{ij,\beta}\right)\left(r_{kl,\gamma}\, r_{jk,\delta} + r_{jk,\gamma}\, r_{kl,\delta}\right) \\
&+ \left(r_{kl,\alpha}\, r_{jk,\beta} + r_{jk,\alpha}\, r_{kl,\beta}\right)\left(r_{ij,\gamma}\, r_{jk,\delta} + r_{jk,\gamma}\, r_{ij,\delta}\right) \\
&- \left(r_{ij,\alpha}\, r_{kl,\beta} + r_{kl,\alpha}\, r_{ij,\beta}\right)\left(r_{jk,\gamma}\, r_{jk,\delta} + r_{jk,\gamma}\, r_{jk,\delta}\right) \\
&- \left(r_{jk,\alpha}\, r_{jk,\beta} + r_{jk,\alpha}\, r_{jk,\beta}\right)\left(r_{ij,\gamma}\, r_{kl,\delta} + r_{kl,\gamma}\, r_{ij,\delta}\right)
\end{aligned} \tag{A.30}$$

$$\begin{aligned}
\frac{\partial^2\left(m^2\right)}{\partial\epsilon_{\alpha\beta}\partial\epsilon_{\gamma\delta}} &= 4\left(r_{ij,\alpha}\, r_{ij,\beta}\, r_{jk,\gamma}\, r_{jk,\delta} + r_{jk,\alpha}\, r_{jk,\beta}\, r_{ij,\gamma}\, r_{ij,\delta}\right) \\
&- 2\left(r_{ij,\alpha}\, r_{jk,\beta} + r_{jk,\alpha}\, r_{ij,\beta}\right)\left(r_{ij,\gamma}\, r_{jk,\delta} + r_{jk,\gamma}\, r_{ij,\delta}\right)
\end{aligned} \tag{A.31}$$

$$\begin{aligned}
\frac{\partial^2\left(n^2\right)}{\partial\epsilon_{\alpha\beta}\partial\epsilon_{\gamma\delta}} &= 4\left(r_{kl,\alpha}\, r_{kl,\beta}\, r_{jk,\gamma}\, r_{jk,\delta} + r_{jk,\alpha}\, r_{jk,\beta}\, r_{kl,\gamma}\, r_{kl,\delta}\right) \\
&- 2\left(r_{kl,\alpha}\, r_{jk,\beta} + r_{jk,\alpha}\, r_{kl,\beta}\right)\left(r_{kl,\gamma}\, r_{jk,\delta} + r_{jk,\gamma}\, r_{kl,\delta}\right)
\end{aligned} \tag{A.32}$$

A.4 Long-range Contributions

A.4.1 Ewald Summation of Non-bonded Interactions

In the following, we consider a system of N atoms, in a simulation box of volume $V = L_x L_y L_z$, which are thought to interact via a 12-6 Lennard-Jones potential of the form:

$$\mathcal{V}_{ij}\left(r_{ij}\right) = 4\epsilon_{ij}\left[\left(\frac{\sigma_{ij}}{r_{ij}}\right)^{12} - \left(\frac{\sigma_{ij}}{r_{ij}}\right)^{6}\right] \tag{A.33}$$

where ϵ_{ij} is the depth of the potential well, σ_{ij} is the finite distance at which the interatomic potential is zero and r_{ij} is the distance between the particles. We are mainly interested in applying long-range summation to the attractive r^{-6} term, since the repulsive r^{-12} term can be neglected, particularly as r becomes large.

Following Nijboer and de Wette[360] and Williams,[361] we choose the converge function $\phi_{\text{d}}(r)$ as

$$\phi_{\text{d}}(r) = \frac{1}{\Gamma(m/2)}\int_{r^2/\eta^2}^{\infty} t^{m/2-1}e^{-t}\text{d}t \tag{A.34}$$

Then, Karasawa and Goddard,[362] have derived expressions for the dispersion part of energy, force, stress and elasticity tensors using Ewald summations.

For the energy, they have found:

$$\begin{aligned}\mathcal{V}_{\text{6,long}} &= \frac{1}{2\eta^6}\sum_{L,i,j} B_{ij}\left(a^{-6} + a^{-4} + \frac{1}{2}a^{-2}\right)e^{-a^2} \\ &+ \frac{\pi^{3/2}}{24V}\sum_{\mathbf{k}} k^3\left[\pi^{1/2}\text{erfc}\left(b\right) + \left(\frac{1}{2b^3} - \frac{1}{b}\right)e^{-b^2}\right]\sum_{ij} B_{ij}\cos\left[\mathbf{k}\cdot\left(\mathbf{r}_i - \mathbf{r}_j\right)\right] \\ &+ \frac{\pi^{3/2}}{6V\eta^3}\sum_{i,j} B_{ij} - \frac{1}{12\eta^6}\sum_{i} B_{ii}\end{aligned} \tag{A.35}$$

where $b = \frac{1}{2}h\eta$, $a = \left\|\mathbf{r}_i - \mathbf{r}_j - \mathbf{r}_L\right\|/\eta$, $k = \|\mathbf{k}\|$, $\mathbf{k}$ is the reciprocal lattice vector, the dispersion constant is $B_{ij} = 4\epsilon_{ij}\sigma_{ij}^6$ and the parameter $\mathbf{r}_L$ represents the lattice translation vector. The parameter η (with units of length) represents the range of interactions handled in the reciprocal vector; for a given value of r, the larger the value of η, the more interactions are included in the reciprocal space sum. The first term contribution to the energy sums over lattices L and particles i and j. The third term arises from $\mathbf{k} = 0$ in the second term, while the fourth term is from exclusion of $i = j$ terms when $L = 0$.

It is convenient to replace the first term of Eq. (A.35) with:

$$\sum_{L,i,j} B_{ij}\left(a^{-6}+a^{-4}+\frac{1}{2}a^{-2}\right)e^{-a^{2}} = \frac{1}{\eta^{6}}\sum_{L}\sum_{j>i} B_{ij}a^{-2}e^{-a^{2}}\left(a^{-4}+a^{-2}+\frac{1}{2}\right) + \frac{1}{2\eta^{6}}\sum_{L}\left[a_L^{-2}e^{-a_L^{2}}\left(a_L^{-4}+a_L^{-2}+\frac{1}{2}\right)\sum_{i} B_{ii}\right] \tag{A.36}$$

where $a_L = \|\mathbf{r}_L\|/\eta$.

If we assume for simplicity than only one kind of interaction sites is present in the system, or that we can apply geometric mixing of dispersion constants, it trivially holds that

$$-B_{ij} = \sqrt{B_{ii}B_{jj}} \tag{A.37}$$

which allows us to express the structure factor as:

$$\sum_{i,j} B_{ij}\cos\left[\mathbf{k}\cdot\left(\mathbf{r}_i-\mathbf{r}_j\right)\right] = -\left[\sum_{i}\left(|B_{ii}|\right)^{1/2}\cos\left(\mathbf{k}\cdot\mathbf{r}_i\right)\right]^{2} - \left[\sum_{i}\left(|B_{ii}|\right)^{1/2}\sin\left(\mathbf{k}\cdot\mathbf{r}_i\right)\right]^{2} \tag{A.38}$$

In the case of arithmetic mixing of dispersion constants, in't Veld et al.[363] have derived the necessary expressions for the structure factor.

The stress tensor,

$$\sigma_{\alpha\beta}^{\mathcal{V},\text{long}} = \frac{1}{V_{\mathscr{R}}}\frac{\partial\mathcal{V}_{6,\text{long}}}{\partial\epsilon_{\alpha\beta}} \tag{A.39}$$

with the derivative appearing in the right-hand side being given by:[362]

$$\begin{aligned}\frac{\partial\mathcal{V}_{6,\text{long}}}{\partial\epsilon_{\alpha\beta}} = {} & \frac{1}{2\eta^{8}}\sum_{L}\sum_{ij} B_{ij}\left(6a^{-8}+6a^{-6}+3a^{-4}+a^{-2}\right)e^{-a^{2}}\times \\ & \left(\mathbf{r}_i-\mathbf{r}_j-\mathbf{r}_L\right)_{\alpha}\cdot\left(\mathbf{r}_i-\mathbf{r}_j-\mathbf{r}_L\right)_{\beta} \\ & + \frac{\pi^{3/2}}{24V}\sum_{\mathbf{k}}\sum_{ij} B_{ij}\cos\left[\mathbf{k}\cdot\left(\mathbf{r}_i-\mathbf{r}_j\right)\right]\times \\ & \left\{k^{3}\left[\pi^{1/2}\text{erfc}\left(b\right)+\left(\frac{1}{2b^{3}}-\frac{1}{b}\right)e^{-b^{2}}\right]\delta_{\alpha\beta}+3k\left(\pi^{1/2}\text{erfc}\left(b\right)-\frac{e^{-b^{2}}}{b}\right)\mathbf{k}_{\alpha}\mathbf{k}_{\beta}\right\} \\ & + \frac{\pi^{3/2}}{6\eta^{3}V}\sum_{ij} B_{ij}\delta_{\alpha\beta}\end{aligned} \tag{A.40}$$

where it can be observed that terms other than the one corresponding to the real space, contribute only to the normal stresses, $\sigma_{\alpha\alpha}$.

The second derivative of $\mathcal{V}_{6,\text{long}}$ with respect to $\epsilon_{\alpha\alpha}$ has the form:

$$\begin{aligned}\frac{\partial^2\mathcal{V}_{6,\text{long}}}{\partial\epsilon_{\alpha\alpha}^2} =& -\frac{1}{2\eta^8}\sum_{L,i,j} B_{ij}\left[F'\frac{1}{a\eta^2}\left(\mathbf{r}_i-\mathbf{r}_j-\mathbf{r}_L\right)_\alpha^4 + 2F\left(\mathbf{r}_i-\mathbf{r}_j-\mathbf{r}_L\right)_\alpha^2\right] \\ &+ \frac{\pi^{3/2}}{24V}\sum_{\mathbf{k}}\sum_{ij} B_{ij}\cos\left[\mathbf{k}\cdot\left(\mathbf{r}_i-\mathbf{r}_j\right)\right]\left[\frac{1}{2}\eta^2\mathbf{k}_\alpha^4 H' + 4H\mathbf{k}_\alpha^2 + G\right] \\ &+ \frac{\pi^{3/2}}{6\eta^3 V}\sum_{ij} B_i j \end{aligned} \tag{A.41}$$

while the second derivative of $\mathcal{V}_{6,\text{long}}$ with respect to $\epsilon_{\alpha\beta}$ is given by:

$$\begin{aligned}\frac{\partial^2\mathcal{V}_{6,\text{long}}}{\partial\epsilon_{\alpha\beta}^2} =& -\frac{1}{2\eta^8}\sum_{L,i,j} B_{ij}\left[F'\frac{1}{a\eta^2}\left(\mathbf{r}_i-\mathbf{r}_j-\mathbf{r}_L\right)_\alpha^2\left(\mathbf{r}_i-\mathbf{r}_j-\mathbf{r}_L\right)_\beta^2\right] \\ &+ \frac{\pi^{3/2}}{24V}\sum_{\mathbf{k}}\sum_{ij} B_{ij}\cos\left[\mathbf{k}\cdot\left(\mathbf{r}_i-\mathbf{r}_j\right)\right]\left[\frac{1}{2}\eta^2\mathbf{k}_\alpha^2\mathbf{k}_\beta^2 H' + H\left(\mathbf{k}_\alpha^2+\mathbf{k}_\beta^2\right) + G\right] \\ &+ \frac{\pi^{3/2}}{6\eta^3 V}\sum_{ij} B_{ij} \end{aligned} \tag{A.42}$$

where

$$F = \left(6a^{-8}+6a^{-6}+3a^{-4}+a^{-2}\right)e^{-a^2} \tag{A.43}$$

$$G = \frac{8b^3}{\eta^3}\left[\pi^{1/2}\text{erfc}\left(b\right) + \left(\frac{1}{2b^3}-\frac{1}{b}\right)e^{-b^2}\right] \tag{A.44}$$

$$H = \frac{6b}{\eta}\left(\pi^{1/2}\text{erfc}\left(b\right) - \frac{e^{-b^2}}{b}\right) \tag{A.45}$$

and

$$F' = \frac{\mathrm{d}F}{\mathrm{d}a} \tag{A.46}$$

$$H' = \frac{\mathrm{d}H}{\mathrm{d}b^2} \tag{A.47}$$

respectively.

A.4.2 Treatment of Excluded Interactions

It is usual, in polymer simulation to choose to consider non-bonded interactions only for atoms lying in different chains, or across the same parent image of the chain three or four bonds apart. At this point, we restate Eq. (A.35), taking into account Eq. (A.36) since this will facilitate in subtracting excluded interactions. The energy of the system, can be expressed as:

$$\begin{aligned}\mathcal{V}_{6,\text{long}} &= \frac{1}{\eta^6}\sum_L\sum_{j>i} B_{ij} a^{-2} e^{-a^2}\left(a^{-4}+a^{-2}+\frac{1}{2}\right)\\ &+ \frac{1}{2\eta^6}\sum_L\left[a_L^{-2}e^{-a_L^2}\left(a_L^{-4}+a_L^{-2}+\frac{1}{2}\right)\sum_i B_{ii}\right]\\ &+ \frac{\pi^{3/2}}{24V}\sum_{\mathbf{h}\neq\mathbf{0}} h^3\left[\pi^{1/2}\text{erfc}\left(b\right)+\left(\frac{1}{2b^3}-\frac{1}{b}\right)e^{-b^2}\right]\sum_{ij} B_{ij}\cos\left[\mathbf{h}\cdot\left(\mathbf{r}_i-\mathbf{r}_j\right)\right]\\ &+ \frac{\pi^{3/2}}{6V\eta^3}\sum_{i,j} B_{ij} - \frac{1}{12\eta^6}\sum_i B_{ii} \end{aligned} \tag{A.48}$$

We assume that we should exclude a finite set of united-atom pairs, (i', j'), all lying in the primary simulation box, $\mathbf{r}_L = \mathbf{0}$. We allow atoms belonging to different images of the same parent chain interact with each other. Also, we consider that the effect of images of these (i', j') pairs lying far apart the primary simulation box is screened, so we can ignore it. Based on these assumptions, a finite range energy contribution, $\mathcal{V}_{6,\text{excl}}$, should be subtracted from Eq. (A.48) in order to compensate for the exclusion rules affecting the primary simulation box:

$$\mathcal{V}_{6,\text{excl}} = \frac{1}{\eta^6}\sum_{(i',j')} B_{i'j'} a_0^{-2} e^{-a_0^2}\left(a_0^{-4}+a_0^{-2}+\frac{1}{2}\right) \tag{A.49}$$

where $a_0 = \left\|\mathbf{r}_{j'}^{\text{min.im.}(i')} - \mathbf{r}_{i'}\right\|/\eta$ defined as a in Eq. (A.35) for $\mathbf{r}_L = 0$. In the calculation of a_0, minimum image condition should be taken into account. Except the first term of the Eq. (A.48) which sums in the real space, the other terms are left unaffected by the introduction of excluded pairs.

Finally, the Ewald sum of long-range dispersion forces, in the presence of an exclusion list of interactions, (i', j'), takes the form:

$$\begin{aligned}\mathcal{V}_{6,\text{long/excl}} = {} & \frac{1}{\eta^6}\sum_L \sum_{j>i} B_{ij} a^{-2} e^{-a^2}\left(a^{-4} + a^{-2} + \frac{1}{2}\right) \\ & - \frac{1}{\eta^6}\sum_{(i',j')} B_{i'j'} a_0^{-2} e^{-a_0^2}\left(a_0^{-4} + a_0^{-2} + \frac{1}{2}\right) \\ & + \frac{1}{2\eta^6}\sum_L \left[a_L^{-2} e^{-a_L^2}\left(a_L^{-4} + a_L^{-2} + \frac{1}{2}\right)\sum_i B_{ii}\right] \\ & + \frac{\pi^{3/2}}{24V}\sum_{\mathbf{h}\neq\mathbf{0}} h^3\left[\pi^{1/2}\text{erfc}\left(b\right) + \left(\frac{1}{2b^3} - \frac{1}{b}\right)e^{-b^2}\right]\sum_{ij} B_{ij}\cos\left[\mathbf{h}\cdot\left(\mathbf{r}_i - \mathbf{r}_j\right)\right] \\ & + \frac{\pi^{3/2}}{6V\eta^3}\left[\sum_{i,j} B_{ij} - \sum_{(i',j')} B_{i'j'}\right] - \frac{1}{12\eta^6}\sum_i B_{ii} \qquad \text{(A.50)}\end{aligned}$$

B Random Linking of FTiMC configurations

Our starting points for the creation of randomly crosslinked polymer networks are equilibrated configurations obtained from Field Theory-inspired Monte Carlo (FTiMC) simulations. In order to investigate the statistical properties of random cross-linking, we have cross-linked our polymeric melts as follows. For each melt configuration, N_{links} cross-links are placed at random in the simulation box; thus, the average number of *unique* crosslinks per chain is $\bar{N}_{\text{c}} = N_{\text{links}}/n$, where n stands for the number of chains present in the simulation box and N_{c} stands for the links per chain (two links are shared between two chains, thus the average number of crosslinks per chain is $2\bar{N}_{\text{c}}$). For every crosslink, we locate the nodal points of the Kuhn segments that are closest to it (Figure B.1). All these nodal points are enumerated and sorted on the basis of their distance from the considered crosslink. Then, successive attempts are made, starting from the nodal points closest to the crosslink, in order to pair these points to the crosslinking point. During this procedure one can choose whether only intermolecular pairs (nodal points belonging to different chains) or all possible pairs are going to be linked to the crosslink. The computer code developed can handle both cases. For a completely random cross-linking process, as occurs in irradiation cross-linking, two monomers are linked together without regard to whether they belong to the same chain or not. However, for rubber elasticity, it is important to know more about such self-connections, which are usually accounted as inactive for elasticity, even though they form loops that contribute to the elastic density.

The bridging of points to the crosslink can be done randomly, requiring that the new configuration of the system be as close as possible to the starting non-crosslinked configuration. Special care is taken in order to avoid multiple cross-linking of the same nodal points. In order to prevent an artificially strong coupling along the chain, nodal points separated by one or two Kuhn segments along the same chain are excluded from forming a connection. This cross-linking procedure is repeated until the desired number of cross-links is added to the system. The methodology follows earlier work by Grest and Kremer on more detailed model systems.[364]

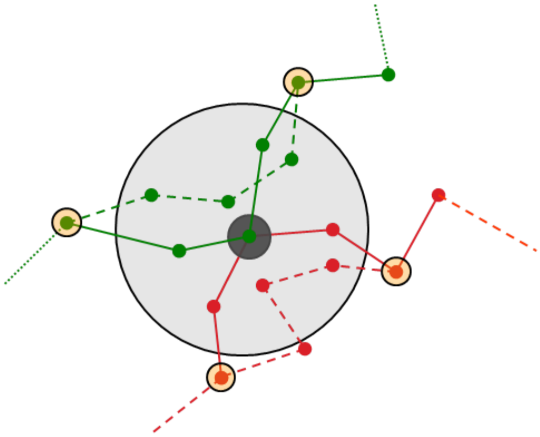

Figure B.1: Schematic of the cross-linking procedure. Final configuration is drawn with continuous lines, while initial Kuhn segments are drawn with dashed lines.

The procedure undertaken tries to mimic irradiation cross-linking. Here it is considered as an adequate representation of e.g. chemical crosslinking via sulphur bridges in cis-1,4 polyisoprene. In contrast to more detailed approaches to irradiation cross-linking, we do not allow chain scission.[365]

The starting point for cross-linking are well equilibrated FTiMC pure polyisoprene configurations. The cross-linked configurations are produced by imposing $\bar{N}_{\mathrm{c}} = 0.5$ to 20 unique links per chain. The initial FTiMC configuration consists of chains with molar mass of $M_{\mathrm{w}} = 42$ kg/mol (corresponds to 294 Kuhn segments), so the upper limit ($\bar{N}_{\mathrm{c}} = 20$) corresponds to 6 % w/w sulphur content assuming 4-atom long sulphur bridges, on average.

For an ideal random cross-linking, the individual connections can be treated as statistically independent events. Thus, the distribution of the number of cross-links per chain, $P\left(N_{\mathrm{c}}\right)$, should be Gaussian, centered around the average number of cross-links per chain. Since each connection that is added to the system connects two different nodal points, the average number of cross-links per chain is $2\bar{N}_{\mathrm{c}}$. In Figure B.2 the distribution of crosslinks per chain is shown, for purely intermolecular cross-linking of a system of 42 kg/mol polyisoprene chains, for six values of $\bar{N}_{\mathrm{c}}$. In Figure B.3 we present the same distribution normalized by the mean $2\bar{N}_{\mathrm{c}}$. The results peak around $\bar{N}_{\mathrm{c}}$, as expected. It is apparent from the data that, as $\bar{N}_{\mathrm{c}}$ increases, the distribution becomes more symmetric. The distributions of crosslinks per chain obtained by our random linking algorithm are in excellent agreement with those obtained by Grest and Kremer (Figure 1 of ref 364).

Next we consider the distribution $P_{\mathrm{L}}\left(L_{\mathrm{c}}\right)$ of strand lengths L_{c} between two cross-links (Figure B.4). For a completely random process the distribution is expected to be a simple

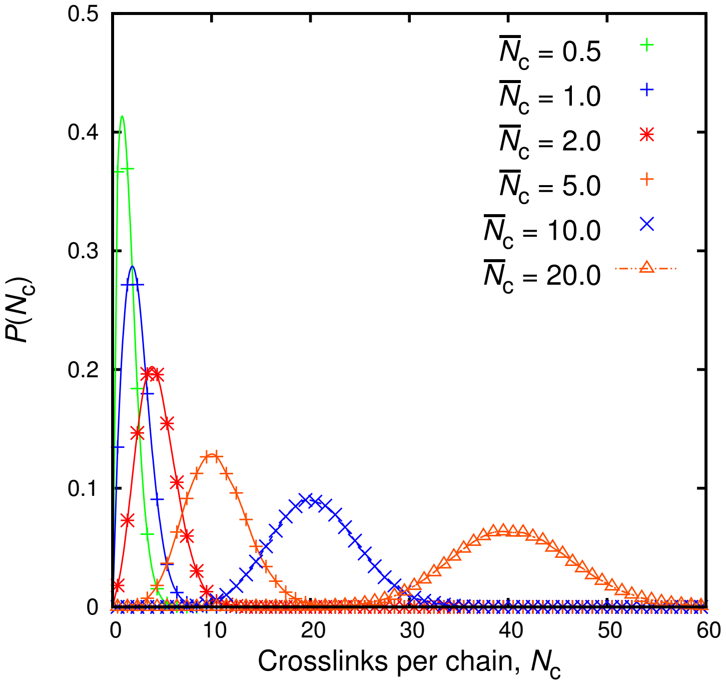

Figure B.2: Distribution of crosslinks per chain, N_c, for FTiMC polyisoprene chains of 42 kg/mol molar mass.

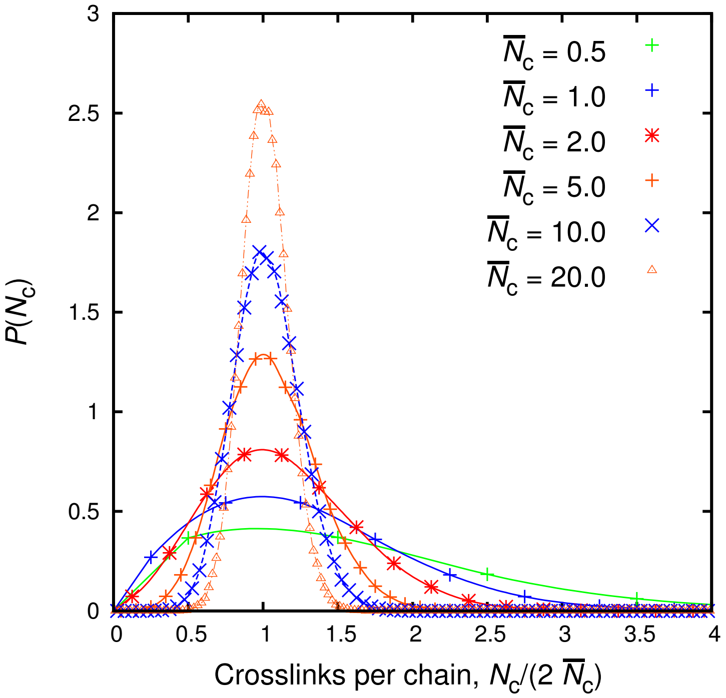

Figure B.3: Distribution of crosslinks per chain, N_c, for FTiMC polyisoprene chains of 42 kg/-mol molar mass. The distributions are normalized by the average number of unique crosslinks per chain, $\bar{N}_c$.

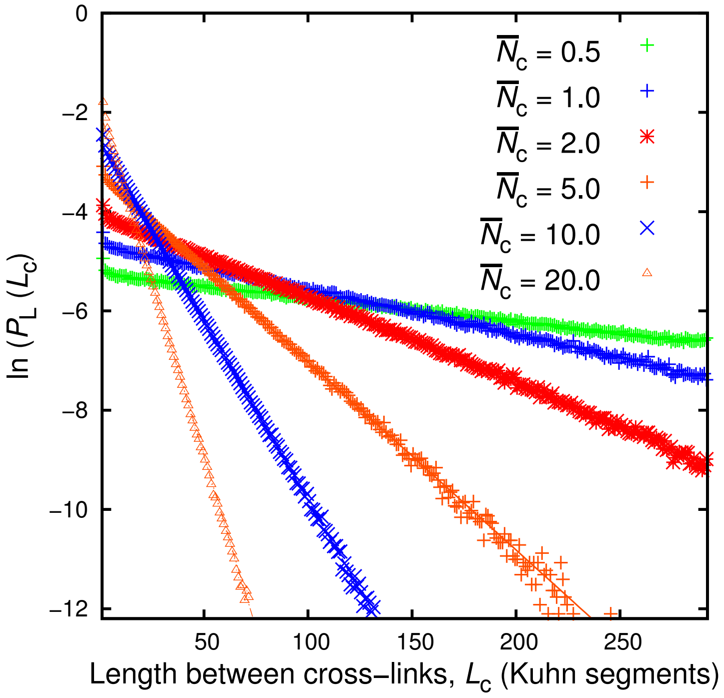

Figure B.4: Semilogarithmic plot of the distribution of the length between cross-links, $P_{\mathrm{L}}\left(L_{\mathrm{c}}\right)$, for several values of $\bar{N}_{\mathrm{c}}$.

exponential with a decay length L_{c}^{*}:

$$P_{\mathrm{L}}\left(L_{\mathrm{c}}\right) \propto \exp\left(-\frac{L}{L_{\mathrm{c}}^{*}}\right) \quad . \tag{B.1}$$

The decay length, L_{c}^{*}, is proportional to the average length between crosslinks, $\langle L_{\mathrm{c}}\rangle$. We should note that this length can only be defined when there are at least two crosslinks on a chain. The distributions of length between crosslinks are in favorable agreement with those obtained by Grest and Kremer (Figure 2 of ref 364).

C Discrete Nonbonded Interactions Scheme for Slip-Spring Simulations

The simplest option for relating the positions and masses of the beads to ρ_{cell} is to envision each bead i as a cube containing mass m_i, of edge length h_i, centered at position $\mathbf{r}_i = (x_i, y_i, z_i)$, as shown in Figure C.1. The cell dimensions along the x, y and z directions will be denoted as l_x, l_y, and l_z, respectively. We will focus on a cell extending between $x_{\text{cell}} - l_x$ and x_{cell} along the x-direction, between $y_{\text{cell}} - l_y$ and y_{cell} along the y-direction, and between $z_{\text{cell}} - l_z$ and z_{cell} along the z-direction. In the regular grid considered, if $(0, 0, 0)$ is taken as one of the grid points, x_{cell}, y_{cell}, and z_{cell} will be integer multiples of l_x, l_y and l_z, respectively. In the following, we assume that $h_i < \min(l_x, l_y, l_z)$.

The mass contributed by the node to the cell is:

$$m_{i,\text{cell}} = m_i \frac{V_{\text{cube } i \cap \text{cell}}}{V_{\text{cube } i}} \tag{C.1}$$

with $V_{\text{cube } i \cap \text{cell}}$ being the volume of the intersection of cube i, associated with bead i, and the considered cell, while $V_{\text{cube } i} = h_i^3$ is the volume of cube i.

Under the condition $h_i < \min(l_x, l_y, l_z)$, $V_{\text{cube } i \cap \text{cell}}$ is obtainable as:

$$\begin{aligned} V_{\text{cube } i \cap \text{cell}} = &\max\left\{\left[\min\left(x_i + \frac{h_i}{2}, x_{\text{cell}}\right) - \max\left(x_i - \frac{h_i}{2}, x_{\text{cell}} - l_x\right)\right], 0\right\} \\ &\times \max\left\{\left[\min\left(y_i + \frac{h_i}{2}, y_{\text{cell}}\right) - \max\left(y_i - \frac{h_i}{2}, y_{\text{cell}} - l_y\right)\right], 0\right\} \\ &\times \max\left\{\left[\min\left(z_i + \frac{h_i}{2}, z_{\text{cell}}\right) - \max\left(z_i - \frac{h_i}{2}, z_{\text{cell}} - l_z\right)\right], 0\right\} \end{aligned} \tag{C.2}$$

As defined by eq C.2, $V_{\text{cube } i \cap \text{cell}}$ is a linear function of the bead coordinates. Clearly, if cube i lies entirely within the cell, $V_{\text{cube } i \cap \text{cell}} = V_{\text{cube } i}$ and, consequently, $m_{i,\text{cell}} = m_i$. If however, the borders of the cube i intersect the borders of the considered cell, then node i will contribute

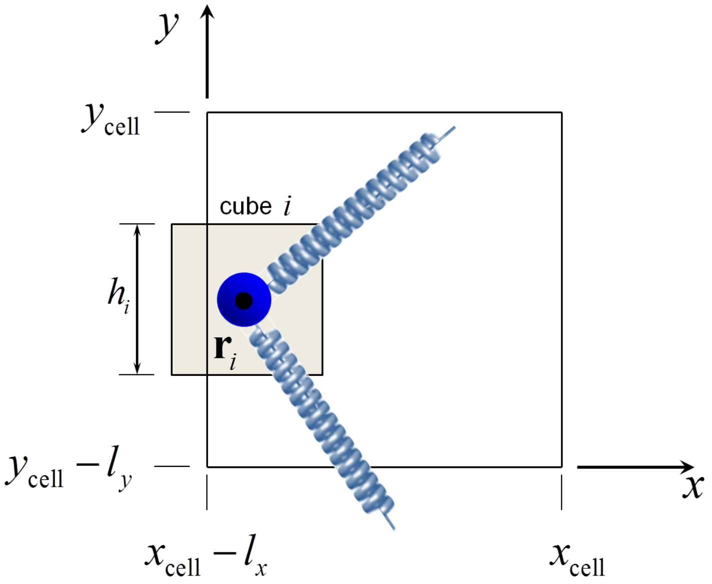

Figure C.1: Schematic representation of a grid cell and a nodal point with its surrounding cube.

a mass $m_{i,\text{cell}} < m_i$ to the cell. The total mass contributed by bead i to all cells in which it participates will always be m_i.

The density ρ_{cell} in the considered cell is estimated as:

$$\rho_{\text{cell}} = \frac{1}{V_{\text{cell}}^{\text{acc}}} \sum_i m_{i,\text{cell}} \tag{C.3}$$

Clearly, only beads i whose cubes have a nonzero overlap with the considered cell will contribute to the summation of eq C.3. The position vectors $\mathbf{r}_i$ of these nodal points will necessarily lie within the considered cell or its immediate neighbors.

The precise conditions for cube i to have common points with the considered cell are:

$$\begin{aligned} x_{\text{cell}} - l_x < x_i + \frac{h_i}{2} < x_{\text{cell}} + h_i \\ y_{\text{cell}} - l_y < y_i + \frac{h_i}{2} < y_{\text{cell}} + h_i \\ z_{\text{cell}} - l_z < z_i + \frac{h_i}{2} < z_{\text{cell}} + h_i \end{aligned} \tag{A4}$$

According to the above approach, the force on node i due to nonbonded interactions is:

$$\mathbf{F}_i = -\nabla_{\mathbf{r}_i} A_{\text{nb}} = - \sum_{\text{cells} \cap \text{cube } i} V_{\text{cell}}^{\text{acc}} \left. \frac{\partial a_{\text{vol}}(\rho, T)}{\partial \rho} \right|_{\rho = \rho_{\text{cell}}} \nabla_{\mathbf{r}_i} \rho_{\text{cell}} \tag{C.4}$$

From eqs C.1, C.2 and C.3 one can obtain the components of $\nabla_{\mathbf{r}_i}\rho_{\text{cell}}$. Along the x direction,

$$\frac{\partial}{\partial x_i}\rho_{\text{cell}} = \begin{cases} 0 & \text{if } x_i \leq x_{\text{cell}} - l_x - \dfrac{h_i}{2} \\ \dfrac{m_i}{V_{\text{cell}}^{\text{acc}}} \dfrac{V_{\text{cube } i \cap \text{cell}}}{V_{\text{cube } i}} \dfrac{1}{x_i + \frac{h_i}{2} - x_{\text{cell}} + l_x} & \text{if } x_{\text{cell}} - l_x - \dfrac{h_i}{2} < x_i < x_{\text{cell}} - l_x + \dfrac{h_i}{2} \\ 0 & \text{if } x_{\text{cell}} - l_x + \dfrac{h_i}{2} \leq x_i \leq x_{\text{cell}} - \dfrac{h_i}{2} \\ -\dfrac{m_i}{V_{\text{cell}}^{\text{acc}}} \dfrac{V_{\text{cube } i \cap \text{cell}}}{V_{\text{cube } i}} \dfrac{1}{x_{\text{cell}} - x_i + \frac{h_i}{2}} & \text{if } x_{\text{cell}} - \dfrac{h_i}{2} < x_i < x_{\text{cell}} + \dfrac{h_i}{2} \\ 0 & \text{if } x_i \geq x_{\text{cell}} + \dfrac{h_i}{2} \end{cases} \tag{C.5}$$

and similarly for $\partial\rho_{\text{cell}}/\partial y_i$ and $\partial\rho_{\text{cell}}/\partial z_i$

The derivatives are bounded but not continuous. To make them continuous, an extension of the “smearing scheme” for beads which uses a uniform density distribution for the contribution of each bead would be required.

Two nodes whose cubes lie entirely within a cell experience the same nonbonded force (zero). This is not true, however, of nodes whose cubes intersect cell borders.

The edge length of the cube assigned to node i, h_i, can be set approximately equal to the root mean square end-to-end distance of the strands assigned to a node:

$$h_i = \left(\frac{m_i}{m_{\text{K}}}\, b_{\text{K}}^2\right)^{1/2} \tag{C.6}$$

where m_{K} and b_{K} are the mass and the length of a Kuhn segment of the polymer under consideration.

References

[1] Kumar, S. K.; Krishnamoorti, R. “Nanocomposites: Structure, Phase Behavior, and Properties”. *Annu. Rev. Chem. Biomol. Eng.* **2010**, *1*, 37–58.

[2] Balazs, A. C.; Emrick, T.; Russell, T. P. “Nanoparticle Polymer Composites: Where Two Small Worlds Meet”. *Science* **2006**, *314*, 1107–1110.

[3] Goodyear, C. “Verfahren zur Fabrication von Gegenständen aus Kautschuk und Guttapercha in Verbindung mit anderen Stoffen”. *Polytech. J.* **1856**, *139*, 376–390.

[4] Baekeland, L. H. “Bakelite, a New Composition of Matter. Its Synthesis, Constitution and Uses”. *Sci. Am.* **1909**, *68 (Suppl. 1768)*, 322 – 323.

[5] Baekeland, L. H. “Bakelite, a New Composition. - II Its Synthesis, Constitution and Uses”. *Sci. Am.* **1909**, *68 (Suppl. 1769)*, 342 – 343.

[6] Baekeland, L. H. “Uses of Bakelite. Its Electrical and Electrochemical Application”. *Sci. Am.* **1910**, *69 (Suppl. 1774)*, 11 – 11.

[7] Baekeland, L. H. “Uses of Bakelite. II Its Electrical and Electrochemical Application”. *Sci. Am.* **1910**, *69 (Suppl. 1775)*, 30 – 32.

[8] Usuki, A.; Kojima, Y.; Kawasumi, M.; Okada, A.; Fukushima, Y.; Kurauchi, T.; Kamigaito, O. “Synthesis of nylon 6-clay hybrid”. *J. Mater. Res.* **1993**, *8*, 1179–1184.

[9] Kojima, Y.; Usuki, A.; Kawasumi, M.; Okada, A.; Fukushima, Y.; Kurauchi, T.; Kamigaito, O. “Mechanical properties of nylon 6-clay hybrid”. *J. Mater. Res.* **1993**, *8*, 1185–1189.

[10] Bansal, A.; Yang, H.; Li, C.; Benicewicz, B. C.; Kumar, S. K.; Schadler, L. S. “Controlling the thermomechanical properties of polymer nanocomposites by tailoring the polymer–particle interface”. *J. Polym. Sci., Part B: Polym. Phys.* **2006**, *44*, 2944–2950.

[11] Lee, J. Y.; Buxton, G. A.; Balazs, A. C. “Using nanoparticles to create self-healing composites”. *J. Chem. Phys.* **2004**, *121*, 5531–5540.

[12] Bockstaller, M. R.; Thomas, E. L. “Proximity Effects in Self-Organized Binary Particle - Block Copolymer Blends”. *Phys. Rev. Lett.* **2004**, *93*, 166106.

[13] Si, M.; Araki, T.; Ade, H.; Kilcoyne, A. L. D.; Fisher, R.; Sokolov, J. C.; Rafailovich, M. H. “Compatibilizing Bulk Polymer Blends by Using Organoclays”. *Macromolecules* **2006**, *39*, 4793–4801.

[14] Stratford, K.; Adhikari, R.; Pagonabarraga, I.; Desplat, J.-C.; Cates, M. E. “Colloidal Jamming at Interfaces: A Route to Fluid-Bicontinuous Gels”. *Science* **2005**, *309*, 2198–2201.

[15] Jayaraman, A.; Schweizer, K. S. “Effective Interactions, Structure, and Phase Behavior of Lightly Tethered Nanoparticles in Polymer Melts”. *Macromolecules* **2008**, *41*, 9430–9438.

[16] Kumar, S. K.; Jouault, N.; Benicewicz, B.; Neely, T. “Nanocomposites with Polymer Grafted Nanoparticles”. *Macromolecules* **2013**, *46*, 3199–3214.

[17] Theodorou, D. N. “Hierarchical modelling of polymeric materials”. *Chem. Eng. Sci.* **2007**, *62*, 5697 – 5714.

[18] Theodorou, D. N. “Understanding and predicting structure–property relations in polymeric materials through molecular simulations”. *Mol. Phys.* **2004**, *102*, 147–166.

[19] Anogiannakis, S. D.; Tzoumanekas, C.; Theodorou, D. N. “Microscopic Description of Entanglements in Polyethylene Networks and Melts: Strong, Weak, Pairwise, and Collective Attributes”. *Macromolecules* **2012**, *45*, 9475–9492.

[20] Allegra, G.; Raos, G.; Vacatello, M. “Theories and simulations of polymer-based nanocomposites: From chain statistics to reinforcement”. *Prog. Polym. Sci.* **2008**, *33*, 683 – 731.

[21] Edwards, S. F.; Vilgis, T. A. “The tube model theory of rubber elasticity”. *Rep. Prog. Phys.* **1988**, *51*, 243.

[22] Dodd, L.; Boone, T.; Theodorou, D. “A concerted rotation algorithm for atomistic Monte Carlo simulation of polymer melts and glasses”. *Mol. Phys.* **1993**, *78*, 961–996.

[23] Siepmann, J. I.; Frenkel, D. “Configurational bias Monte Carlo: a new sampling scheme for flexible chains”. *Mol. Phys.* **1992**, *75*, 59–70.

[24] de Pablo, J. J.; Laso, M.; Suter, U. W. “Simulation of polyethylene above and below the melting point”. *J. Chem. Phys* **1992**, *96*, 2395–2403.

[25] Uhlherr, A. “Monte Carlo Conformational Sampling of the Internal Degrees of Freedom of Chain Molecules”. *Macromolecules* **2000**, *33*, 1351–1360.

[26] Pant, P. V. K.; Theodorou, D. N. “Variable Connectivity Method for the Atomistic Monte Carlo Simulation of Polydisperse Polymer Melts”. *Macromolecules* **1995**, *28*, 7224–7234.

[27] Mavrantzas, V. G.; Boone, T. D.; Zervopoulou, E.; Theodorou, D. N. “End-Bridging Monte Carlo: A Fast Algorithm for Atomistic Simulation of Condensed Phases of Long Polymer Chains”. *Macromolecules* **1999**, *32*, 5072–5096.

[28] Karayiannis, N. C.; Mavrantzas, V. G.; Theodorou, D. N. “A Novel Monte Carlo Scheme for the Rapid Equilibration of Atomistic Model Polymer Systems of Precisely Defined Molecular Architecture”. *Phys. Rev. Lett.* **2002**, *88*, 105503.

[29] Karayiannis, N. C.; Giannousaki, A. E.; Mavrantzas, V. G.; Theodorou, D. N. "Atomistic Monte Carlo simulation of strictly monodisperse long polyethylene melts through a generalized chain bridging algorithm". *J. Chem. Phys.* **2002**, *117*, 5465–5479.

[30] Doxastakis, M.; Mavrantzas, V. G.; Theodorou, D. N. "Atomistic Monte Carlo simulation of cis-1,4 polyisoprene melts. I. Single temperature end-bridging Monte Carlo simulations". *J. Chem. Phys.* **2001**, *115*, 11339–11351.

[31] Doxastakis, M.; Mavrantzas, V. G.; Theodorou, D. N. "Atomistic Monte Carlo simulation of cis-1,4 polyisoprene melts. II. Parallel tempering end-bridging Monte Carlo simulations". *J. Chem. Phys.* **2001**, *115*, 11352–11361.

[32] Spyriouni, T.; Tzoumanekas, C.; Theodorou, D.; Müller-Plathe, F.; Milano, G. "Coarse-Grained and Reverse-Mapped United-Atom Simulations of Long-Chain Atactic Polystyrene Melts: Structure, Thermodynamic Properties, Chain Conformation, and Entanglements". *Macromolecules* **2007**, *40*, 3876–3885.

[33] Milano, G.; Müller-Plathe, F. "Mapping Atomistic Simulations to Mesoscopic Models: A Systematic Coarse-Graining Procedure for Vinyl Polymer Chains". *J. Phys. Chem. B* **2005**, *109*, 18609–18619.

[34] Fredrickson, G. *"The Equilibrium Theory of Inhomogeneous Polymers"*; International Series of Monographs on Physics; Oxford University Press Oxford, 2013.

[35] Laradji, M.; Guo, H.; Zuckermann, M. J. "Off-lattice Monte Carlo simulation of polymer brushes in good solvents". *Phys. Rev. E* **1994**, *49*, 3199–3206.

[36] Daoulas, K. C.; Müller, M. "Single chain in mean field simulations: Quasi-instantaneous field approximation and quantitative comparison with Monte Carlo simulations". *J. Chem. Phys.* **2006**, *125*, 184904.

[37] Detcheverry, F. A.; Kang, H.; Daoulas, K. C.; Müller, M.; Nealey, P. F.; de Pablo, J. J. "Monte Carlo Simulations of a Coarse Grain Model for Block Copolymers and Nanocomposites". *Macromolecules* **2008**, *41*, 4989–5001.

[38] Detcheverry, F. m. c.; Pike, D.; Nealey, P.; Müller, M.; de Pablo, J. "Monte Carlo Simulation of Coarse Grain Polymeric Systems". *Phys. Rev. Lett.* **2009**, *102*, 197801.

[39] Öttinger, H. C. *"Beyond Equilibrium Thermodynamics"*; Wiley, 2005.

[40] Vaia, R. A.; Wagner, H. D. "Framework for nanocomposites". *Mater. Today* **2004**, *7*, 32 – 37.

[41] Ediger, M. D.; Angell, C. A.; Nagel, S. R. "Supercooled Liquids and Glasses". *J. Phys. Chem.* **1996**, *100*, 13200–13212.

[42] Angell, C. A. "Formation of Glasses from Liquids and Biopolymers". *Science* **1995**, *267*, 1924–1935.

[43] Rittigstein, P.; Priestley, R. D.; Broadbelt, L. J.; Torkelson, J. M. "Model polymer nanocomposites provide an understanding of confinement effects in real nanocomposites". *Nat. Mater.* *6*, 278 – 282.

[44] Ash, B.; Schadler, L.; Siegel, R. "Glass transition behavior of alumina/polymethylmethacrylate nanocomposites". *Mater. Lett.* **2002**, *55*, 83 – 87.

[45] Bershtein, V. A.; Egorova, L. M.; Yakushev, P. N.; Pissis, P.; Sysel, P.; Brozova, L. "Molecular dynamics in nanostructured polyimide–silica hybrid materials and their thermal stability". *J. Polym. Sci., Part B: Polym. Phys.* **2002**, *40*, 1056–1069.

[46] Klonos, P.; Panagopoulou, A.; Bokobza, L.; Kyritsis, A.; Peoglos, V.; Pissis, P. "Comparative studies on effects of silica and titania nanoparticles on crystallization and complex segmental dynamics in poly(dimethylsiloxane)". *Polymer* **2010**, *51*, 5490 – 5499.

[47] Chen, K. H.; Yang, S. M. "Synthesis of epoxy–montmorillonite nanocomposite". *J. Appl. Polym. Sci.* **2002**, *86*, 414–421.

[48] Liu, X.; Wu, Q. "PP/clay nanocomposites prepared by grafting-melt intercalation". *Polymer* **2001**, *42*, 10013 – 10019.

[49] Fragiadakis, D.; Pissis, P.; Bokobza, L. "Glass transition and molecular dynamics in poly(dimethylsiloxane)/silica nanocomposites". *Polymer* **2005**, *46*, 6001 – 6008.

[50] Tao, P.; Viswanath, A.; Schadler, L. S.; Benicewicz, B. C.; Siegel, R. W. "Preparation and Optical Properties of Indium Tin Oxide/Epoxy Nanocomposites with Polyglycidyl Methacrylate Grafted Nanoparticles". *ACS Appl. Mater. Interfaces* **2011**, *3*, 3638–3645, PMID: 21823657.

[51] Srivastava, S.; Agarwal, P.; Archer, L. A. "Tethered Nanoparticle–Polymer Composites: Phase Stability and Curvature". *Langmuir* **2012**, *28*, 6276–6281.

[52] Harton, S. E.; Kumar, S. K. "Mean-field theoretical analysis of brush-coated nanoparticle dispersion in polymer matrices". *J. Polym. Sci., Part B: Polym. Phys.* **2008**, *46*, 351–358.

[53] Corbierre, M. K.; Cameron, N. S.; Sutton, M.; Laaziri, K.; Lennox, R. B. "Gold Nanoparticle/Polymer Nanocomposites: Dispersion of Nanoparticles as a Function of Capping Agent Molecular Weight and Grafting Density". *Langmuir* **2005**, *21*, 6063–6072.

[54] Lan, Q.; Francis, L. F.; Bates, F. S. "Silica nanoparticle dispersions in homopolymer versus block copolymer". *J. Polym. Sci., Part B: Polym. Phys.* **2007**, *45*, 2284–2299.

[55] Glogowski, E.; Tangirala, R.; Russell, T. P.; Emrick, T. "Functionalization of nanoparticles for dispersion in polymers and assembly in fluids". *J. Polym. Sci., Part A: Polym. Chem.* **2006**, *44*, 5076–5086.

[56] Krishnamoorti, R. "Strategies for Dispersing Nanoparticles in Polymers". *MRS Bull.* **2007**, *32*, 341–347.

[57] Tsubokawa, N. “Surface Grafting of Polymers onto Nanoparticles in a Solvent-Free Dry-System and Applications of Polymer-grafted Nanoparticles as Novel Functional Hybrid Materials”. *Polym. J. (Tokyo, Jpn.)* **2007**, *39*, 983 – 1000.

[58] Goel, V.; Chatterjee, T.; Bombalski, L.; Yurekli, K.; Matyjaszewski, K.; Krishnamoorti, R. “Viscoelastic properties of silica-grafted poly(styrene–acrylonitrile) nanocomposites”. *J. Polym. Sci., Part B: Polym. Phys.* **2006**, *44*, 2014–2023.

[59] Schadler, L. S.; Kumar, S. K.; Benicewicz, B. C.; Lewis, S. L.; Harton, S. E. “Designed Interfaces in Polymer Nanocomposites: A Fundamental Viewpoint”. *MRS Bull.* **2007**, *32*, 335–340.

[60] Iacovella, C. R.; Horsch, M. A.; Glotzer, S. C. “Local ordering of polymer-tethered nanospheres and nanorods and the stabilization of the double gyroid phase”. *J. Chem. Phys.* **2008**, *129*, 044902.

[61] Meli, L.; Arceo, A.; Green, P. F. “Control of the entropic interactions and phase behavior of athermal nanoparticle/homopolymer thin film mixtures”. *Soft Matter* **2009**, *5*, 533–537.

[62] Zhao, L.; Li, Y.-G.; Zhong, C. “Integral equation theory study on the phase separation in star polymer nanocomposite melts”. *J. Chem. Phys.* **2007**, *127*, 154909.

[63] Xu, C.; Ohno, K.; Ladmiral, V.; Composto, R. J. “Dispersion of polymer-grafted magnetic nanoparticles in homopolymers and block copolymers”. *Polymer* **2008**, *49*, 3568 – 3577.

[64] Wang, M.-J. “Effect of Polymer-Filler and Filler-Filler Interactions on Dynamic Properties of Filled Vulcanizates”. *Rubber Chem. Technol.* **1998**, *71*, 520 – 589.

[65] Payne, A. R. “The dynamic properties of carbon black-loaded natural rubber vulcanizates. Part I”. *J. Appl. Polym. Sci.* **1962**, *6*, 57–63.

[66] Mullins, L. “Softening of Rubber by Deformation”. *Rubber Chem. Technol.* **1969**, *42*, 339 – 362.

[67] Reichl, L. *“A Modern Course in Statistical Physics”*; Wiley, 2009.

[68] Goldstein, H. *“Classical Mechanics”*; Addison-Wesley series in physics; Addison-Wesley Publishing Company, 1980.

[69] Boltzmann, L. “Ueber die mechanischen Analogien des zweiten Hauptsatzes der Thermodynamik”. *J. Reine Angew. Math.* **1887**, *1887*, 201–212.

[70] Born, M.; Oppenheimer, R. “Zur Quantentheorie der Molekeln”. *Ann. Phys. (Berlin, Ger.)* **1927**, *389*, 457–484.

[71] Chandler, D. *“Introduction to Modern Statistical Mechanics”*; Oxford University Press, 1987.

[72] Landau, L.; Lifshitz, E. *“Statistical Physics”*; Elsevier Science, 1996; Vol. 5.

[73] Fung, Y. *"A First Course in Continuum Mechanics: For Physical and Biological Engineers and Scientists"*; Tsinghua University Press, 1994.

[74] Weiner, J. *"Statistical Mechanics of Elasticity"*; Wiley-Interscience, 1983.

[75] Hencky, H. "Über die Form des Elastizitätgesetzes bei ideal elastischen Stoffen". *Zeitschrift für Technische Physik* **1928**, *9*, 214–247.

[76] Rees, D. *"Basic Engineering Plasticity: An Introduction with Engineering and Manufacturing Applications"*; Elsevier Science, 2006.

[77] Barnes, H.; Hutton, J.; Walters, K. *"An Introduction to Rheology"*; Annals of Discrete Mathematics; Elsevier, 1989.

[78] Flory, P. *"Principles of Polymer Chemistry"*; Cornell University Press, 1953.

[79] Gedde, U. *"Polymer Physics"*; Springer, 1995.

[80] Theodorou, D. N.; Suter, U. W. "Shape of unperturbed linear polymers: polypropylene". *Macromolecules* **1985**, *18*, 1206–1214.

[81] Chandrasekhar, S. "Stochastic Problems in Physics and Astronomy". *Rev. Mod. Phys.* **1943**, *15*, 1–89.

[82] Rayleigh, L. "XXXI. On the problem of random vibrations, and of random flights in one, two, or three dimensions". *Philos. Mag. (1798-1977)* **1919**, *37*, 321–347.

[83] Rayleigh, L. *"Scientific Papers"*; Cambridge Library Collection, 2009; Vol. 6; p 604.

[84] Treloar, L. R. G. "The statistical length of long-chain molecules". *Trans. Faraday Soc.* **1946**, *42*, 77–82.

[85] Hughes, B. *"Random Walks and Random Environments: Random walks"*; Clarendon Press, 1995; Vol. 1.

[86] Rubinstein, M.; Colby, R. *"Polymer Physics"*; Oxford University Press, 2003.

[87] Kuhn, W. "Über die Gestalt fadenförmiger Moleküle in Lösungen *(On the state of polymers in solution)*". *Kolloid-Z.* **1934**, *68*, 2–15.

[88] Rouse, P. E. "A Theory of the Linear Viscoelastic Properties of Dilute Solutions of Coiling Polymers". *J. Chem. Phys.* **1953**, *21*, 1272–1280.

[89] Doi, M.; Edwards, S. *"The Theory of Polymer Dynamics"*; The International Series of Monographs on Physics Series; Clarendon Press, 1988.

[90] Zimm, B. H. "Dynamics of Polymer Molecules in Dilute Solution: Viscoelasticity, Flow Birefringence and Dielectric Loss". *J. Chem. Phys.* **1956**, *24*, 269–278.

[91] Likhtman, A. In *Polymer Science: A Comprehensive Reference*; Matyjaszewski, K., Möller, M., Eds.; Elsevier: Amsterdam, 2012; pp 133 – 179.

[92] Doi, M. *“Soft Matter Physics”*; Oxford University Press Oxford, 2013.

[93] de Gennes, P. G. “Reptation of a Polymer Chain in the Presence of Fixed Obstacles”. *J. Chem. Phys.* **1971**, *55*, 572–579.

[94] Doi, M.; Edwards, S. F. “Dynamics of concentrated polymer systems. Part 1.-Brownian motion in the equilibrium state”. *J. Chem. Soc., Faraday Trans. 2* **1978**, *74*, 1789–1801.

[95] Doi, M.; Edwards, S. F. “Dynamics of concentrated polymer systems. Part 2.-Molecular motion under flow”. *J. Chem. Soc., Faraday Trans. 2* **1978**, *74*, 1802–1817.

[96] Doi, M.; Edwards, S. F. “Dynamics of concentrated polymer systems. Part 3.-The constitutive equation”. *J. Chem. Soc., Faraday Trans. 2* **1978**, *74*, 1818–1832.

[97] Doi, M.; Edwards, S. F. “Dynamics of concentrated polymer systems. Part 4.-Rheological properties”. *J. Chem. Soc., Faraday Trans. 2* **1979**, *75*, 38–54.

[98] Ebert, U.; Schäfer, L.; Baumgärtner, A. “Segment Motion in the Reptation Model of Polymer Dynamics. I. Analytical Investigation”. *J. Stat. Phys.* **1998**, *90*, 1325–1373.

[99] Baumgärtner, A.; Ebert, U.; Schäfer, L. “Segment Motion in the Reptation Model of Polymer Dynamics. II. Simulations”. *J. Stat. Phys.* **1998**, *90*, 1375–1400.

[100] Masubuchi, Y. “Simulating the Flow of Entangled Polymers”. *Annu. Rev. Chem. Biomol. Eng.* **2014**, *5*, 11–33.

[101] Schieber, J. D.; Andreev, M. “Entangled Polymer Dynamics in Equilibrium and Flow Modeled Through Slip Links”. *Annu. Rev. Chem. Biomol. Eng.* **2014**, *5*, 367–381.

[102] Doi, M. “Explanation for the 3.4-power law for viscosity of polymeric liquids on the basis of the tube model”. *J. Polym. Sci., Polym. Phys. Ed.* **1983**, *21*, 667–684.

[103] Milner, S. T.; McLeish, T. C. B. “Reptation and Contour-Length Fluctuations in Melts of Linear Polymers”. *Phys. Rev. Lett.* **1998**, *81*, 725–728.

[104] Likhtman, A. E.; McLeish, T. C. B. “Quantitative Theory for Linear Dynamics of Linear Entangled Polymers”. *Macromolecules* **2002**, *35*, 6332–6343.

[105] Tsenoglou, C. “Molecular weight polydispersity effects on the viscoelasticity of entangled linear polymers”. *Macromolecules* **1991**, *24*, 1762–1767.

[106] des Cloizeaux, J. “Double Reptation vs. Simple Reptation in Polymer Melts”. *Europhys. Lett.* **1988**, *5*, 437.

[107] Graessley, W. *“Synthesis and Degradation Rheology and Extrusion”*; Adv. Polym. Sci.; Springer Berlin Heidelberg, 1982; Vol. 47; pp 67–117.

[108] Marrucci, G. “Relaxation by reptation and tube enlargement: A model for polydisperse polymers”. *J. Polym. Sci., Polym. Phys. Ed.* **1985**, *23*, 159–177.

[109] Hatsopoulos, G. N.; Keenan, J. H. *“Principles of General Thermodynamics”*; Wiley, 1965.

[110] Sanchez, I. C.; Lacombe, R. H. “An elementary molecular theory of classical fluids. Pure fluids”. *J. Phys. Chem.* **1976**, *80*, 2352–2362.

[111] Cown, J. “Some general features of T_g-M relations for oligomers and amorphous polymers”. *Eur. Polym. J.* **1975**, *11*, 297 – 300.

[112] Allen, P.; Tildesley, D. *“Computer Simulation of Liquids”*; Oxford Science Publ; Clarendon Press, 1989.

[113] Verlet, L. “Computer ’Experiments’ on Classical Fluids. I. Thermodynamical Properties of Lennard-Jones Molecules”. *Phys. Rev.* **1967**, *159*, 98–103.

[114] Swope, W. C.; Andersen, H. C.; Berens, P. H.; Wilson, K. R. “A computer simulation method for the calculation of equilibrium constants for the formation of physical clusters of molecules: Application to small water clusters”. *J. Chem. Phys.* **1982**, *76*, 637–649.

[115] Metropolis, N.; Rosenbluth, A. W.; Rosenbluth, M. N.; Teller, A. H.; Teller, E. “Equation of State Calculations by Fast Computing Machines”. *J. Chem. Phys.* **1953**, *21*, 1087–1092.

[116] Pangali, C.; Rao, M.; Berne, B. “On a novel Monte Carlo scheme for simulating water and aqueous solutions”. *Chem. Phys. Lett.* **1978**, *55*, 413 – 417.

[117] Langevin, P. “Sur la théorie de mouvement Brownien”. *C.R. Acad. Sci. Paris* **1908**, *146*, 530–533.

[118] Lemons, D. S.; Gythiel, A. “Paul Langevin’s 1908 paper “On the Theory of Brownian Motion” [“Sur la théorie du mouvement Brownien,” C. R. Acad. Sci. (Paris) 146, 530–533 (1908)]”. *Am. J. Phys.* **1997**, *65*, 1079–1081.

[119] van Gunsteren, W.; Berendsen, H.; Rullmann, J. “Stochastic dynamics for molecules with constraints”. *Mol. Phys.* **1981**, *44*, 69–95.

[120] Hütter, M.; Öttinger, H. C. “Fluctuation-dissipation theorem, kinetic stochastic integral and efficient simulations”. *J. Chem. Soc., Faraday Trans.* **1998**, *94*, 1403–1405.

[121] Einstein, A. “Über die von der molekularkinetischen Theorie der Wärme geforderte Bewegung von in ruhenden Flüssigkeiten suspendierten Teilchen”. *Ann. Phys. (Leipzig)* **1905**, *17*, 549–560.

[122] Nyquist, H. “Thermal Agitation of Electric Charge in Conductors”. *Phys. Rev.* **1928**, *32*, 110–113.

[123] Callen, H. B.; Welton, T. A. “Irreversibility and Generalized Noise”. *Phys. Rev.* **1951**, *83*, 34–40.

[124] Kubo, R.; Toda, M.; Hashitsume, N. *“Statistical Physics II”*; Springer Berlin Heidelberg, 1991.

[125] Zwanzig, R. “Ensemble Method in the Theory of Irreversibility”. *J. Chem. Phys.* **1960**, *33*, 1338–1341.

[126] Zwanzig, R. “Memory Effects in Irreversible Thermodynamics”. *Phys. Rev.* **1961**, *124*, 983–992.

[127] Mori, H. “Transport, Collective Motion, and Brownian Motion”. *Prog. Theor. Phys.* **1965**, *33*, 423–455.

[128] Mori, H. “A Continued-Fraction Representation of the Time-Correlation Functions”. *Prog. Theor. Phys.* **1965**, *34*, 399–416.

[129] van Gunsteren, W.; Berendsen, H. “Algorithms for brownian dynamics”. *Mol. Phys.* **1982**, *45*, 637–647.

[130] Van Gunsteren, W. F.; Berendsen, H. J. C. “A Leap-frog Algorithm for Stochastic Dynamics”. *Mol. Simul.* **1988**, *1*, 173–185.

[131] Rossky, P. J.; Doll, J. D.; Friedman, H. L. “Brownian dynamics as smart Monte Carlo simulation”. *J. Chem. Phys.* **1978**, *69*, 4628–4633.

[132] Clausius, R. “XVI. On a mechanical theorem applicable to heat”. *Philos. Mag. (1798-1977)* **1870**, *40*, 122–127.

[133] Clausius, R. “I. On different forms of the virial”. *Philos. Mag. (1798-1977)* **1874**, *48*, 1–11.

[134] Theodorou, D. N.; Boone, T. D.; Dodd, L. R.; Mansfield, K. F. “Stress tensor in model polymer systems with periodic boundaries”. *Macromol. Theory Simul.* **1993**, *2*, 191–238.

[135] Nye, J. *“Physical Properties of Crystals: Their Representation by Tensors and Matrices”*; Oxford science publications; Clarendon Press, 1985.

[136] Born, M.; Huang, K. *“Dynamical Theory of Crystal Lattices”*; Oxford classic texts in the physical sciences; Clarendon Press, 1998.

[137] Lutsko, J. F. “Stress and elastic constants in anisotropic solids: Molecular dynamics techniques”. *J. Appl. Phys.* **1988**, *64*, 1152–1154.

[138] Lutsko, J. F. “Generalized expressions for the calculation of elastic constants by computer simulation”. *J. Appl. Phys.* **1989**, *65*, 2991–2997.

[139] Ray, J. R.; Rahman, A. “Statistical ensembles and molecular dynamics studies of anisotropic solids”. *J. Chem. Phys.* **1984**, *80*, 4423–4428.

[140] Van Workum, K.; Yoshimoto, K.; de Pablo, J. J.; Douglas, J. F. “Isothermal stress and elasticity tensors for ions and point dipoles using Ewald summations”. *Phys. Rev. E* **2005**, *71*, 061102.

[141] Lustig, S. R.; Shay, R. M.; Caruthers, J. M. “Thermodynamic constitutive equations for materials with memory on a material time scale”. *J. Rheol.* **1996**, *40*, 69–106.

[142] Mavrantzas, V. G.; Theodorou, D. N. “Atomistic Simulation of Polymer Melt Elasticity: Calculation of the Free Energy of an Oriented Polymer Melt”. *Macromolecules* **1998**, *31*, 6310–6332.

[143] Einstein, A. “Eine neue Bestimmung der Moleküldimensionen”. *Ann. Phys.* **1906**, *324*, 289–306.

[144] Einstein, A. “Berichtigung zu meiner Arbeit: “Eine neue Bestimmung der Moleküldimensionen””. *Ann. Phys.* **1911**, *339*, 591–592.

[145] Mackay, M. E.; Dao, T. T.; Tuteja, A.; Ho, D. L.; Van Horn, B.; Kim, H.-C.; Hawker, C. J. “Nanoscale effects leading to non-Einstein-like decrease in viscosity”. *Nat. Mater.* **2003**, *2*, 762–766.

[146] Tuteja, A.; Mackay, M. E.; Hawker, C. J.; Van Horn, B. “Effect of Ideal, Organic Nanoparticles on the Flow Properties of Linear Polymers: Non-Einstein-like Behavior”. *Macromolecules* **2005**, *38*, 8000–8011.

[147] Tuteja, A.; Duxbury, P. M.; Mackay, M. E. “Multifunctional Nanocomposites with Reduced Viscosity”. *Macromolecules* **2007**, *40*, 9427–9434.

[148] Kropka, J. M.; Garcia Sakai, V.; Green, P. F. “Local Polymer Dynamics in Polymer−C60 Mixtures”. *Nano Lett.* **2008**, *8*, 1061–1065.

[149] Sanz, A.; Ruppel, M.; Douglas, J. F.; Cabral, J. T. “Plasticization effect of C_{60} on the fast dynamics of polystyrene and related polymers: an incoherent neutron scattering study”. *J. Phys.: Condens. Matter* **2008**, *20*, 104209.

[150] Wong, H. C.; Sanz, A.; Douglas, J. F.; Cabral, J. T. “Glass formation and stability of polystyrene - fullerene nanocomposites”. *J. Mol. Liq.* **2010**, *153*, 79 – 87.

[151] Vacatello, M. “Monte Carlo Simulations of Polymer Melts Filled with Solid Nanoparticles”. *Macromolecules* **2001**, *34*, 1946–1952.

[152] Desai, T.; Keblinski, P.; Kumar, S. K. “Molecular dynamics simulations of polymer transport in nanocomposites”. *J. Chem. Phys.* **2005**, *122*, 134910.

[153] Smith, G. D.; Bedrov, D.; Li, L.; Byutner, O. “A molecular dynamics simulation study of the viscoelastic properties of polymer nanocomposites”. *J. Chem. Phys.* **2002**, *117*, 9478–9489.

[154] Smith, G. D.; Bedrov, D.; Borodin, O. “Structural Relaxation and Dynamic Heterogeneity in a Polymer Melt at Attractive Surfaces”. *Phys. Rev. Lett.* **2003**, *90*, 226103.

[155] Ndoro, T. V. M.; Böhm, M. C.; Müller-Plathe, F. “Interface and Interphase Dynamics of Polystyrene Chains near Grafted and Ungrafted Silica Nanoparticles”. *Macromolecules* **2012**, *45*, 171–179.

[156] Toepperwein, G. N.; Karayiannis, N. C.; Riggleman, R. A.; Kröger, M.; de Pablo, J. J. “Influence of Nanorod Inclusions on Structure and Primitive Path Network of Polymer Nanocomposites at Equilibrium and Under Deformation”. *Macromolecules* **2011**, *44*, 1034–1045.

[157] Li, Y.; Kröger, M.; Liu, W. K. “Nanoparticle Effect on the Dynamics of Polymer Chains and Their Entanglement Network”. *Phys. Rev. Lett.* **2012**, *109*, 118001.

[158] Li, Y.; Kröger, M.; Liu, W. K. “Nanoparticle Geometrical Effect on Structure, Dynamics and Anisotropic Viscosity of Polyethylene Nanocomposites”. *Macromolecules* **2012**, *45*, 2099–2112.

[159] Milano, G.; Müller-Plathe, F. “Mapping Atomistic Simulations to Mesoscopic Models: A Systematic Coarse-Graining Procedure for Vinyl Polymer Chains”. *J. Phys. Chem. B* **2005**, *109*, 18609–18619.

[160] Dünweg, B.; Kremer, K. “Molecular dynamics simulation of a polymer chain in solution”. *J. Chem. Phys.* **1993**, *99*, 6983–6997.

[161] Hamaker, H. “The London- van der Waals attraction between spherical particles”. *Physica(Amsterdam)* **1937**, *IV*, 1058.

[162] Girifalco, L. A. “Molecular properties of fullerene in the gas and solid phases”. *J. Phys. Chem.* **1992**, *96*, 858–861.

[163] Müller, M.; Steinmüller, B.; Daoulas, K. C.; Ramirez-Hernandez, A.; de Pablo, J. J. “Polymer-solid contacts described by soft, coarse-grained models”. *Phys. Chem. Chem. Phys.* **2011**, *13*, 10491–10502.

[164] Mondello, M.; Yang, H.-J.; Furuya, H.; Roe, R.-J. “Molecular Dynamics Simulation of Atactic Polystyrene. 1. Comparison with X-ray Scattering Data”. *Macromolecules* **1994**, *27*, 3566–3574.

[165] Theodorou, D. N.; Suter, U. W. “Detailed molecular structure of a vinyl polymer glass”. *Macromolecules* **1985**, *18*, 1467–1478.

[166] Sato, H.; Tanaka, Y.; Hatada, K. “13C NMR analysis of polystyrene by means of model compounds”. *Makromol. Chem., Rapid Commun.* **1982**, *3*, 181–185.

[167] Kawamura, T.; Uryu, T.; Matsuzaki, K. “Reinvestigation of the stereoregularity of polystyrene by 100 MHz 13 C NMR spectroscopy”. *Makromol. Chem., Rapid Commun.* **1982**, *3*, 661–665.

[168] Sato, H.; Tanaka, Y.; Hatada, K. “C-13 NMR analysis of polystyrene from low-molecular-weight model compounds”. *J. Polym. Sci., Polym. Phys. Ed.* **1983**, *21*, 1667–1674.

[169] Nelder, J. A.; Mead, R. “A Simplex Method for Function Minimization”. *The Computer Journal* **1965**, *7*, 308–313.

[170] Plimpton, S. “Fast Parallel Algorithms for Short-Range Molecular Dynamics”. *J. Comp. Phys.* **1995**, *117*, 1 – 19.

[171] Polak, E., Ed. *“Computational Methods in Optimization: A Unified Approach”*; Mathematics in Science and Engineering; Elsevier, 1971; Vol. 77.

[172] Ribière, G. “Note sur la convergence de methodes de directions conjuguées”. *Revue Française d' Informatique et de Recherche Opérationnelle* **1969**, *16*, 35–43.

[173] Auhl, R.; Everaers, R.; Grest, G. S.; Kremer, K.; Plimpton, S. J. “Equilibration of long chain polymer melts in computer simulations”. *J. Chem. Phys.* **2003**, *119*, 12718–12728.

[174] Fetters, L. J.; Lohse, D. J.; Richter, D.; Witten, T. A.; Zirkel, A. “Connection between Polymer Molecular Weight, Density, Chain Dimensions, and Melt Viscoelastic Properties”. *Macromolecules* **1994**, *27*, 4639–4647.

[175] Cotton, J. P.; Decker, D.; Benoit, H.; Farnoux, B.; Higgins, J.; Jannink, G.; Ober, R.; Picot, C.; des Cloizeaux, J. “Conformation of Polymer Chain in the Bulk”. *Macromolecules* **1974**, *7*, 863–872.

[176] Vogiatzis, G. G.; Voyiatzis, E.; Theodorou, D. N. “Monte Carlo simulations of a coarse grained model for an athermal all-polystyrene nanocomposite system”. *Eur. Polym. J.* **2011**, *47*, 699 – 712.

[177] Lyulin, A. V.; Michels, M. A. J. “Molecular Dynamics Simulation of Bulk Atactic Polystyrene in the Vicinity of Tg”. *Macromolecules* **2002**, *35*, 1463–1472.

[178] Destree, M.; Laupretre, F.; Lyulin, A.; Ryckaert, J.-P. “Local dynamics of isotactic and syndiotactic polypropylene in solution”. *J. Chem. Phys.* **2000**, *112*, 9632–9644.

[179] Lempesis, N.; Vogiatzis, G. G.; Boulougouris, G. C.; van Breemen, L. C.; Hütter, M.; Theodorou, D. N. “Tracking a glassy polymer on its energy landscape in the course of elastic deformation”. *Mol. Phys.* **2013**, *111*, 3430–3441.

[180] Mayo, S. L.; Olafson, B. D.; Goddard, W. A. “DREIDING: a generic force field for molecular simulations”. *J. Phys. Chem.* **1990**, *94*, 8897–8909.

[181] Monticelli, L. “On Atomistic and Coarse-Grained Models for C60 Fullerene”. *J. Chem. Theory Comput.* **2012**, *8*, 1370–1378.

[182] Flory, P. J.; Sundararajan, P. R.; DeBolt, L. C. “Configurational statistics of vinyl polymer chains”. *J. Am. Chem. Soc.* **1974**, *96*, 5015–5024.

[183] Humphrey, W.; Dalke, A.; Schulten, K. “VMD: Visual molecular dynamics”. *J. Mol. Graphics* **1996**, *14*, 33 – 38.

[184] Nocedal, J.; Wright, S. *“Numerical Optimization”*, 2nd ed.; Springer series in operations research and financial engineering; Springer, 2006.

[185] Bristow, G. M.; Watson, W. F. “Cohesive energy densities of polymers. Part 2.-Cohesive energy densities from viscosity measurements”. *Trans. Faraday Soc.* **1958**, *54*, 1742–1747.

[186] Robyr, P.; Tomaselli, M.; Grob-Pisano, C.; Meier, B. H.; Ernst, R. R.; Suter, U. W. “Characterization of Local Order in Atactic Polystyrene Using Two-Dimensional Nuclear Magnetic Resonance and Atomistic Simulations”. *Macromolecules* **1995**, *28*, 5320–5324.

[187] Robyr, P.; Gan, Z.; Suter, U. W. “Conformation of Racemo and Meso Dyads in Glassy Polystyrenes from 13C Polarization-Transfer NMR”. *Macromolecules* **1998**, *31*, 8918–8923.

[188] Robyr, P.; Müller, M.; Suter, U. W. “Atomistic Simulations of Glassy Polystyrenes with Realistic Chain Conformations”. *Macromolecules* **1999**, *32*, 8681–8684.

[189] Rapold, R. F.; Suter, U. W.; Theodorou, D. N. “Static atomistic modelling of the structure and ring dynamics of bulk amorphous polystyrene”. *Macromol. Theory Simul.* **1994**, *3*, 19–43.

[190] Rapold, R. F.; Suter, U. W. “Conformational characteristics of polystyrene”. *Macromol. Theory Simul.* **1994**, *3*, 1–17.

[191] Dunbar, M.; Novak, B.; Schmidt-Rohr, K. “Trans content in atactic polystyrene estimated by double-quantum solid-state NMR”. *Solid State Nucl. Magn. Reson.* **1998**, *12*, 119 – 137.

[192] Williams, A. D.; Flory, P. J. “Stereochemical equilibrium and configurational statistics in polystyrene and its oligomers”. *J. Am. Chem. Soc.* **1969**, *91*, 3111–3118.

[193] Fujiwara, Y.; Flory, P. J. “Pentad Conformations in Vinyl Polymers and the Nuclear Magnetic Resonance Spectrum of Methine Protons in Polystyrene”. *Macromolecules* **1970**, *3*, 43–49.

[194] Ghanbari, A.; Böhm, M. C.; Müller-Plathe, F. “A Simple Reverse Mapping Procedure for Coarse-Grained Polymer Models with Rigid Side Groups”. *Macromolecules* **2011**, *44*, 5520–5526.

[195] Yoon, D. Y.; Sundararajan, P. R.; Flory, P. J. “Conformational Characteristics of Polystyrene”. *Macromolecules* **1975**, *8*, 776–783.

[196] Shinoda, W.; Shiga, M.; Mikami, M. “Rapid estimation of elastic constants by molecular dynamics simulation under constant stress”. *Phys. Rev. B* **2004**, *69*, 134103.

[197] Tuckerman, M. E.; Alejandre, J.; López-Rendón, R.; Jochim, A. L.; Martyna, G. J. “A Liouville-operator derived measure-preserving integrator for molecular dynamics simulations in the isothermal–isobaric ensemble”. *J. Phys. A: Math. Gen.* **2006**, *39*, 5629.

[198] Allen, P.; Tildesley, D. *“Computer Simulation of Liquids”*; Oxford University Press: USA, 1989.

[199] Nosé, S. “A molecular dynamics method for simulations in the canonical ensemble”. *Mol. Phys.* **1984**, *52*, 255–268.

[200] Ahumada, O.; Theodorou, D. N.; Triolo, A.; Arrighi, V.; Karatasos, C.; Ryckaert, J.-P. “Segmental Dynamics of Atactic Polypropylene As Revealed by Molecular Simulations and Quasielastic Neutron Scattering”. *Macromolecules* **2002**, *35*, 7110–7124.

[201] Kohlrausch, R. “Theorie des elektrischen Rückstandes in der Leidener Flasche”. *Ann. Phys. (Berlin, Ger.)* **1854**, *167*, 56–82.

[202] Williams, G.; Watts, D. C. “Non-symmetrical dielectric relaxation behaviour arising from a simple empirical decay function”. *Trans. Faraday Soc.* **1970**, *66*, 80–85.

[203] Logotheti, G. E.; Theodorou, D. N. “Segmental and Chain Dynamics of Isotactic Polypropylene Melts”. *Macromolecules* **2007**, *40*, 2235–2245.

[204] Harmandaris, V. A.; Floudas, G.; Kremer, K. “Temperature and Pressure Dependence of Polystyrene Dynamics through Molecular Dynamics Simulations and Experiments”. *Macromolecules* **2011**, *44*, 393–402.

[205] Williams, M. L.; Landel, R. F.; Ferry, J. D. “The Temperature Dependence of Relaxation Mechanisms in Amorphous Polymers and Other Glass-forming Liquids”. *J. Am. Chem. Soc.* **1955**, *77*, 3701–3707.

[206] Smith, G. D.; Yoon, D. Y.; Wade, C. G.; O’Leary, D.; Chen, A.; Jaffe, R. L. “Dynamics of poly(oxyethylene) melts: Comparison of 13C nuclear magnetic resonance spin-lattice relaxation and dielectric relaxation as determined from simulations and experiments”. *J. Chem. Phys.* **1997**, *106*, 3798–3805.

[207] Doxastakis, M.; Theodorou, D. N.; Fytas, G.; Kremer, F.; Faller, R.; Müller-Plathe, F.; Hadjichristidis, N. “Chain and local dynamics of polyisoprene as probed by experiments and computer simulations”. *J. Chem. Phys.* **2003**, *119*, 6883–6894.

[208] Hintermeyer, J.; Herrmann, A.; Kahlau, R.; Goiceanu, C.; Rössler, E. A. “Molecular Weight Dependence of Glassy Dynamics in Linear Polymers Revisited”. *Macromolecules* **2008**, *41*, 9335–9344.

[209] Kumar, S. K.; Colby, R. H.; Anastasiadis, S. H.; Fytas, G. “Concentration fluctuation induced dynamic heterogeneities in polymer blends”. *J. Chem. Phys.* **1996**, *105*, 3777–3788.

[210] He, Y.; Lutz, T. R.; Ediger, M. D.; Ayyagari, C.; Bedrov, D.; Smith, G. D. “NMR Experiments and Molecular Dynamics Simulations of the Segmental Dynamics of Polystyrene”. *Macromolecules* **2004**, *37*, 5032–5039.

[211] Spiess, H.; Sillescu, H. “Solid echoes in the slow-motion region”. *J. Magn. Reson. (1969-1992)* **1981**, *42*, 381 – 389.

[212] Starr, F. W.; Sastry, S.; Douglas, J. F.; Glotzer, S. C. “What Do We Learn from the Local Geometry of Glass-Forming Liquids?”. *Phys. Rev. Lett.* **2002**, *89*, 125501.

[213] Rycroft, C. H. “VORO++: A three-dimensional Voronoi cell library in C++”. *Chaos* **2009**, *19*, 041111.

[214] Rycroft, C. H.; Grest, G. S.; Landry, J. W.; Bazant, M. Z. “Analysis of granular flow in a pebble-bed nuclear reactor”. *Phys. Rev. E* **2006**, *74*, 021306.

[215] Harmandaris, V. A.; Doxastakis, M.; Mavrantzas, V. G.; Theodorou, D. N. “Detailed molecular dynamics simulation of the self-diffusion of n-alkane and cis-1,4 polyisoprene oligomer melts”. *J. Chem. Phys.* **2002**, *116*, 436–446.

[216] Harmandaris, V. A.; Mavrantzas, V. G.; Theodorou, D. N.; Kröger, M.; Ramírez, J.; Öttinger, H. C.; Vlassopoulos, D. “Crossover from the Rouse to the Entangled Polymer Melt Regime: Signals from Long, Detailed Atomistic Molecular Dynamics Simulations, Supported by Rheological Experiments”. *Macromolecules* **2003**, *36*, 1376–1387.

[217] Egami, T.; Maeda, K.; Vitek, V. “Structural defects in amorphous solids A computer simulation study”. *Philos. Mag. A* **1980**, *41*, 883–901.

[218] Theodorou, D. N.; Suter, U. W. “Local structure and the mechanism of response to elastic deformation in a glassy polymer”. *Macromolecules* **1986**, *19*, 379–387.

[219] Thompson, A. P.; Plimpton, S. J.; Mattson, W. “General formulation of pressure and stress tensor for arbitrary many-body interaction potentials under periodic boundary conditions”. *J. Chem. Phys.* **2009**, *131*, 154107.

[220] Cohen, M. H.; Turnbull, D. “Molecular Transport in Liquids and Glasses”. *J. Chem. Phys.* **1959**, *31*, 1164–1169.

[221] Dammert, R. M.; Maunu, S. L.; Maurer, F. H. J.; Neelov, I. M.; Niemelä, S.; Sundholm, F.; Wästlund, C. “Free Volume and Tacticity in Polystyrenes”. *Macromolecules* **1999**, *32*, 1930–1938.

[222] Srolovitz, D.; Maeda, K.; Vitek, V.; Egami, T. “Structural defects in amorphous solids Statistical analysis of a computer model”. *Philos. Mag. A* **1981**, *44*, 847–866.

[223] Yoshimoto, K.; Jain, T. S.; Workum, K. V.; Nealey, P. F.; de Pablo, J. J. “Mechanical Heterogeneities in Model Polymer Glasses at Small Length Scales”. *Phys. Rev. Lett.* **2004**, *93*, 175501.

[224] MacNeill, D.; Rottler, J. “From macroscopic yield criteria to atomic stresses in polymer glasses”. *Phys. Rev. E* **2010**, *81*, 011804.

[225] Argon, A. “Plastic deformation in metallic glasses”. *Acta Metall.* **1979**, *27*, 47 – 58.

[226] Egami, T.,; Maed, K.,; Srolovitz, D.,; Vitek, V., “Local Atomic Structure of Amorphous Metals”. *J. Phys. Colloques* **1980**, *41*, C8–272–C8–275.

[227] Srolovitz, D.; Egami, T.; Vitek, V. “Radial distribution function and structural relaxation in amorphous solids”. *Phys. Rev. B* **1981**, *24*, 6936–6944.

[228] Sunday, D.; Ilavsky, J.; Green, D. L. “A Phase Diagram for Polymer-Grafted Nanoparticles in Homopolymer Matrices”. *Macromolecules* **2012**, *45*, 4007–4011.

[229] Hasegawa, R.; Aoki, Y.; Doi, M. “Optimum Graft Density for Dispersing Particles in Polymer Melts”. *Macromolecules* **1996**, *29*, 6656–6662.

[230] Akcora, P.; Liu, H.; Kumar, S. K.; Moll, J.; Li, Y.; Benicewicz, B. C.; Schadler, L. S.; Acehan, D.; Panagiotopoulos, A. Z.; Pryamitsyn, V.; Ganesan, V.; Ilavsky, J.; Thiyagarajan, P.; Colby, R. H.; Douglas, J. F. “Anisotropic self-assembly of spherical polymer-grafted nanoparticles”. *Nat. Mater.* **2009**, *8*, 354–359.

[231] de Gennes, P. G. “Conformations of Polymers Attached to an Interface”. *Macromolecules* **1980**, *13*, 1069–1075.

[232] Alexander, S., “Adsorption of chain molecules with a polar head a scaling description”. *J. Phys. France* **1977**, *38*, 983–987.

[233] Aubouy, M.; Fredrickson, G. H.; Pincus, P.; Raphaeel, E. “End-Tethered Chains in Polymeric Matrixes”. *Macromolecules* **1995**, *28*, 2979–2981.

[234] Cosgrove, T.; Heath, T.; Van Lent, B.; Leermakers, F.; Scheutjens, J. “Configuration of terminally attached chains at the solid/solvent interface: self-consistent field theory and a Monte Carlo model”. *Macromolecules* **1987**, *20*, 1692–1696.

[235] Milner, S. T.; Witten, T. A.; Cates, M. E. “Theory of the grafted polymer brush”. *Macromolecules* **1988**, *21*, 2610–2619.

[236] Zhulina, E. B.; Birshtein, T. M.; Borisov, O. V. “Theory of Ionizable Polymer Brushes”. *Macromolecules* **1995**, *28*, 1491–1499.

[237] Ferreira, P. G.; Ajdari, A.; Leibler, L. “Scaling Law for Entropic Effects at Interfaces between Grafted Layers and Polymer Melts”. *Macromolecules* **1998**, *31*, 3994–4003.

[238] Reiter, G.; Auroy, P.; Auvray, L. “Instabilities of Thin Polymer Films on Layers of Chemically Identical Grafted Molecules”. *Macromolecules* **1996**, *29*, 2150–2157.

[239] Grest, G. S. “Grafted polymer brushes in polymeric matrices”. *J. Chem. Phys.* **1996**, *105*, 5532–5541.

[240] Maas, J. H.; Fleer, G. J.; Leermakers, F. A. M.; Cohen Stuart, M. A. “Wetting of a Polymer Brush by a Chemically Identical Polymer Melt: Phase Diagram and Film Stability”. *Langmuir* **2002**, *18*, 8871–8880.

[241] Matsen, M. W.; Gardiner, J. M. “Autophobic dewetting of homopolymer on a brush and entropic attraction between opposing brushes in a homopolymer matrix”. *J. Chem. Phys.* **2001**, *115*, 2794–2804.

[242] Wijmans, C. M.; Zhulina, E. B. “Polymer brushes at curved surfaces”. *Macromolecules* **1993**, *26*, 7214–7224.

[243] Ball, R. C.; Marko, J. F.; Milner, S. T.; Witten, T. A. “Polymers grafted to a convex surface”. *Macromolecules* **1991**, *24*, 693–703.

[244] Borukhov, I.; Leibler, L. “Enthalpic Stabilization of Brush-Coated Particles in a Polymer Melt”. *Macromolecules* **2002**, *35*, 5171–5182.

[245] Daoud, M.; Cotton, J. “Star shaped polymers : a model for the conformation and its concentration dependence”. *J. Phys. France* **1982**, *43*, 531–538.

[246] Peters, B. L.; Lane, J. M. D.; Ismail, A. E.; Grest, G. S. “Fully Atomistic Simulations of the Response of Silica Nanoparticle Coatings to Alkane Solvents”. *Langmuir* **2012**, *28*, 17443–17449.

[247] Kalb, J.; Dukes, D.; Kumar, S. K.; Hoy, R. S.; Grest, G. S. “End grafted polymer nanoparticles in a polymeric matrix: Effect of coverage and curvature”. *Soft Matter* **2011**, *7*, 1418–1425.

[248] Meng, D.; Kumar, S. K.; D. Lane, J. M.; Grest, G. S. “Effective interactions between grafted nanoparticles in a polymer matrix”. *Soft Matter* **2012**, *8*, 5002–5010.

[249] Kremer, K.; Grest, G. S.; Carmesin, I. “Crossover from Rouse to Reptation Dynamics: A Molecular-Dynamics Simulation”. *Phys. Rev. Lett.* **1988**, *61*, 566–569.

[250] Hooper, J. B.; Schweizer, K. S. “Theory of Phase Separation in Polymer Nanocomposites”. *Macromolecules* **2006**, *39*, 5133–5142.

[251] Surve, M.; Pryamitsyn, V.; Ganesan, V. “Nanoparticles in Solutions of Adsorbing Polymers: Pair Interactions, Percolation, and Phase Behavior”. *Langmuir* **2006**, *22*, 969–981.

[252] Ganesan, V.; Khounlavong, L.; Pryamitsyn, V. “Equilibrium characteristics of semiflexible polymer solutions near probe particles”. *Phys. Rev. E* **2008**, *78*, 051804.

[253] Lo Verso, F.; Yelash, L.; Egorov, S. A.; Binder, K. “Effect of the solvent quality on the structural rearrangement of spherical brushes: coarse-grained models”. *Soft Matter* **2012**, *8*, 4185–4196.

[254] Kritikos, G.; Terzis, A. F. “Variable density self consistent field study on bounded polymer layer around spherical nanoparticles”. *Eur. Polym. J.* **2013**, *49*, 613 – 629.

[255] Sides, S. W.; Kim, B. J.; Kramer, E. J.; Fredrickson, G. H. “Hybrid Particle-Field Simulations of Polymer Nanocomposites”. *Phys. Rev. Lett.* **2006**, *96*, 250601.

[256] Soga, K. G.; Guo, H.; Zuckermann, M. J. “Polymer Brushes in a Poor Solvent”. *Europhys. Lett.* **1995**, *29*, 531.

[257] Stoykovich, M. P.; Daoulas, K. C.; Müller, M.; Kang, H.; de Pablo, J. J.; Nealey, P. F. “Remediation of Line Edge Roughness in Chemical Nanopatterns by the Directed Assembly of Overlying Block Copolymer Films”. *Macromolecules* **2010**, *43*, 2334–2342.

[258] Striolo, A.; Egorov, S. A. “Steric stabilization of spherical colloidal particles: Implicit and explicit solvent”. *J. Chem. Phys.* **2007**, *126*, 014902.

[259] Dukes, D.; Li, Y.; Lewis, S.; Benicewicz, B.; Schadler, L.; Kumar, S. K. “Conformational Transitions of Spherical Polymer Brushes: Synthesis, Characterization, and Theory”. *Macromolecules* **2010**, *43*, 1564–1570.

[260] Chevigny, C.; Jestin, J.; Gigmes, D.; Schweins, R.; Di-Cola, E.; Dalmas, F.; Bertin, D.; Boué, F. “‘Wet-to-Dry’ Conformational Transition of Polymer Layers Grafted to Nanoparticles in Nanocomposite”. *Macromolecules* **2010**, *43*, 4833–4837.

[261] Chevigny, C.; Dalmas, F.; Di Cola, E.; Gigmes, D.; Bertin, D.; Boué, F.; Jestin, J. “Polymer-Grafted-Nanoparticles Nanocomposites: Dispersion, Grafted Chain Conformation, and Rheological Behavior”. *Macromolecules* **2011**, *44*, 122–133.

[262] Wang, Q.; Yin, Y. "Fast off-lattice Monte Carlo simulations with "soft" repulsive potentials". *J. Chem. Phys.* **2009**, *130*, 104903.

[263] Dodd, L. R.; Theodorou, D. N. "Analytical treatment of the volume and surface area of molecules formed by an arbitrary collection of unequal spheres intersected by planes". *Mol. Phys.* **1991**, *72*, 1313–1345.

[264] Helfand, E.; Tagami, Y. "Theory of the Interface between Immiscible Polymers. II". *J. Chem. Phys.* **1972**, *56*, 3592–3601.

[265] Everaers, R.; Ejtehadi, M. R. "Interaction potentials for soft and hard ellipsoids". *Phys. Rev. E* **2003**, *67*, 041710.

[266] Brodka, A.; Zerda, T. W. "Properties of liquid acetone in silica pores: Molecular dynamics simulation". *J. Chem. Phys.* **1996**, *104*, 6319–6326.

[267] Bijsterbosch, B. "Preparation and characterization of detergent-free monodisperse polystyrene latices of small particle size". *Colloid Polym. Sci.* **1978**, *256*, 343–349.

[268] Tsaur, S.-L.; Fitch, R. M. "Preparation and properties of polystyrene model colloids: II. Effect of surface charge density on coagulation behavior". *J. Colloid Interface Sci.* **1987**, *115*, 463 – 471.

[269] Bergström, L. "Hamaker constants of inorganic materials". *Adv. Colloid Interface Sci.* **1997**, *70*, 125 – 169.

[270] Hiemenz, P. C. *"Principles of colloid and surface chemistry"*, 2nd ed.; Dekker, 1977.

[271] Wall, F. T.; Mandel, F. "Macromolecular dimensions obtained by an efficient Monte Carlo method without sample attrition". *J. Chem. Phys.* **1975**, *63*, 4592–4595.

[272] Lal, M. " 'Monte Carlo' computer simulation of chain molecules. I". *Mol. Phys.* **1969**, *17*, 57–64.

[273] Chevigny, C.; Gigmes, D.; Bertin, D.; Jestin, J.; Boue, F. "Polystyrene grafting from silica nanoparticles via nitroxide-mediated polymerization (NMP): synthesis and SANS analysis with the contrast variation method". *Soft Matter* **2009**, *5*, 3741–3753.

[274] Meyer, M. "The Microscopic Structure of Polymer Grafted Nanoparticles". Ph.D. thesis, Westfälischen Wilhelms-Universität Münster, 2012.

[275] Jiang, X.; Zhao, B.; Zhong, G.; Jin, N.; Horton, J. M.; Zhu, L.; Hafner, R. S.; Lodge, T. P. "Microphase Separation of High Grafting Density Asymmetric Mixed Homopolymer Brushes on Silica Particles". *Macromolecules* **2010**, *43*, 8209–8217.

[276] Hocker, H.; Blake, G. J.; Flory, P. J. "Equation-of-state parameters for polystyrene". *Trans. Faraday Soc.* **1971**, *67*, 2251–2257.

[277] Milner, S. T. "Polymer Brushes". *Science* **1991**, *251*, 905–914.

[278] Ndoro, T. V. M.; Voyiatzis, E.; Ghanbari, A.; Theodorou, D. N.; Böhm, M. C.; Müller-Plathe, F. “Interface of Grafted and Ungrafted Silica Nanoparticles with a Polystyrene Matrix: Atomistic Molecular Dynamics Simulations”. *Macromolecules* **2011**, *44*, 2316–2327.

[279] Ohno, K.; Morinaga, T.; Takeno, S.; Tsujii, Y.; Fukuda, T. “Suspensions of Silica Particles Grafted with Concentrated Polymer Brush: Effects of Graft Chain Length on Brush Layer Thickness and Colloidal Crystallization”. *Macromolecules* **2007**, *40*, 9143–9150.

[280] Ghanbari, A.; Ndoro, T. V. M.; Leroy, F.; Rahimi, M.; Böhm, M. C.; Müller-Plathe, F. “Interphase Structure in Silica–Polystyrene Nanocomposites: A Coarse-Grained Molecular Dynamics Study”. *Macromolecules* **2012**, *45*, 572–584.

[281] Green, P. F. “The structure of chain end-grafted nanoparticle/homopolymer nanocomposites”. *Soft Matter* **2011**, *7*, 7914–7926.

[282] Egorov, S. A.; Binder, K. “Effect of solvent quality on the dispersibility of polymer-grafted spherical nanoparticles in polymer solutions”. *J. Chem. Phys.* **2012**, *137*, 094901.

[283] Trombly, D. M.; Ganesan, V. “Curvature effects upon interactions of polymer-grafted nanoparticles in chemically identical polymer matrices”. *J. Chem. Phys.* **2010**, *133*, 154904.

[284] Dan, N.; Tirrell, M. “Polymers tethered to curves interfaces: a self-consistent-field analysis”. *Macromolecules* **1992**, *25*, 2890–2895.

[285] Steel, R. G. D.; Torrie, J. H. *“Principles and procedures of statistics”*; McGraw-Hill, 1960.

[286] Jouault, N.; Dalmas, F.; Said, S.; Di Cola, E.; Schweins, R.; Jestin, J.; Boué, F. “Direct Measurement of Polymer Chain Conformation in Well-Controlled Model Nanocomposites by Combining SANS and SAXS”. *Macromolecules* **2010**, *43*, 9881–9891.

[287] Daniels, H. E. “XXI.—The Statistical Theory of Stiff Chains”. *Proc. - R. Soc. Edinburgh, Sect. A: Math. Phys. Sci.* **1952**, *63*, 290–311.

[288] Burchard, W.; Kajiwara, K. “The Statistics of Stiff Chain Molecules. I. The Particle Scattering Factor”. *Proc. R. Soc. London, Ser. A* **1970**, *316*, 185–199.

[289] Grest, G. S.; Kremer, K.; Witten, T. A. “Structure of many arm star polymers: a molecular dynamics simulation”. *Macromolecules* **1987**, *20*, 1376–1383.

[290] Catmull, E.; Rom, R. In *Computer aided geometric design*; Barnhill, R., Riesenfeld, R., Eds.; Academic Press, 1974.

[291] Higgins, J. S.; Benoît, H. C. *“Polymers and Neutron Scattering”*; Oxford series on neutron scattering in condensed matter; Clarendon Press, 1994.

[292] Pedersen, J. S.; Gerstenberg, M. C. “Scattering Form Factor of Block Copolymer Micelles”. *Macromolecules* **1996**, *29*, 1363–1365.

[293] Pedersen, J. S. “Structure factors effects in small-angle scattering from block copolymer micelles and star polymers”. *J.Chem.Phys.* **2001**, *114*, 2839–2846.

[294] Förster, S.; Wenz, E.; Lindner, P. “Density Profile of Spherical Polymer Brushes”. *Phys. Rev. Lett.* **1996**, *77*, 95–98.

[295] Edwards, S. F. “The statistical mechanics of polymerized material”. *Proc. Phys. Soc.* **1967**, *92*, 9.

[296] De Gennes, P. *“Scaling Concepts in Polymer Physics”*; Cornell University Press, 1979.

[297] Graessley, W. W.; Pearson, D. S. “Stress–strain behavior in polymer networks containing nonlocalized junctions”. *J. Chem. Phys.* **1977**, *66*, 3363–3370.

[298] Ball, R.; Doi, M.; Edwards, S.; Warner, M. “Elasticity of entangled networks”. *Polymer* **1981**, *22*, 1010 – 1018.

[299] Edwards, S.; Vilgis, T. “The effect of entanglements in rubber elasticity”. *Polymer* **1986**, *27*, 483 – 492.

[300] Hua, C. C.; Schieber, J. D. “Segment connectivity, chain-length breathing, segmental stretch, and constraint release in reptation models. I. Theory and single-step strain predictions”. *J. Chem. Phys.* **1998**, *109*, 10018–10027.

[301] Hua, C. C.; Schieber, J. D.; Venerus, D. C. “Segment connectivity, chain-length breathing, segmental stretch, and constraint release in reptation models. II. Double-step strain predictions”. *J. Chem. Phys.* **1998**, *109*, 10028–10032.

[302] Rubinstein, M.; Panyukov, S. “Elasticity of Polymer Networks”. *Macromolecules* **2002**, *35*, 6670–6686.

[303] Indei, T.; Schieber, J.; Takimoto, J.-i. “Effects of fluctuations of cross-linking points on viscoelastic properties of associating polymer networks”. *Rheol. Acta* **2012**, *51*, 1021–1039.

[304] Shanbhag, S.; Larson, R. G.; Takimoto, J.; Doi, M. “Deviations from Dynamic Dilution in the Terminal Relaxation of Star Polymers”. *Phys. Rev. Lett.* **2001**, *87*, 195502.

[305] Doi, M.; Takimoto, J.-i. “Molecular modelling of entanglement”. *Philos. Trans. R. Soc., A* **2003**, *361*, 641–652.

[306] Likhtman, A. E. “Single-Chain Slip-Link Model of Entangled Polymers: Simultaneous Description of Neutron Spin−Echo, Rheology, and Diffusion”. *Macromolecules* **2005**, *38*, 6128–6139.

[307] Masubuchi, Y.; Takimoto, J.-I.; Koyama, K.; Ianniruberto, G.; Marrucci, G.; Greco, F. “Brownian simulations of a network of reptating primitive chains”. *J. Chem. Phys.* **2001**, *115*, 4387–4394.

[308] Masubuchi, Y.; Ianniruberto, G.; Greco, F.; Marrucci, G. “Entanglement molecular weight and frequency response of sliplink networks”. *J. Chem. Phys.* **2003**, *119*, 6925–6930.

[309] Masubuchi, Y.; Ianniruberto, G.; Greco, F.; Marrucci, G. “Molecular simulations of the long-time behaviour of entangled polymeric liquids by the primitive chain network model”. *Modell. Simul. Mater. Sci. Eng.* **2004**, *12*, S91.

[310] Masubuchi, Y.; Ianniruberto, G.; Greco, F.; Marrucci, G. “Quantitative comparison of primitive chain network simulations with literature data of linear viscoelasticity for polymer melts”. *J. Non-Newtonian Fluid Mech.* **2008**, *149*, 87 – 92.

[311] Yaoita, T.; Isaki, T.; Masubuchi, Y.; Watanabe, H.; Ianniruberto, G.; Greco, F.; Marrucci, G. “Highly entangled polymer primitive chain network simulations based on dynamic tube dilation”. *J. Chem. Phys.* **2004**, *121*, 12650–12654.

[312] Masubuchi, Y.; Ianniruberto, G.; Greco, F.; Marrucci, G. “Primitive chain network simulations for branched polymers”. *Rheol. Acta* **2006**, *46*, 297–303.

[313] Yaoita, T.; Isaki, T.; Masubuchi, Y.; Watanabe, H.; Ianniruberto, G.; Greco, F.; Marrucci, G. “Statics, linear, and nonlinear dynamics of entangled polystyrene melts simulated through the primitive chain network model”. *J. Chem. Phys.* **2008**, *128*.

[314] Yaoita, T.; Isaki, T.; Masubuchi, Y.; Watanabe, H.; Ianniruberto, G.; Marrucci, G. “Primitive Chain Network Simulation of Elongational Flows of Entangled Linear Chains: Role of Finite Chain Extensibility”. *Macromolecules* **2011**, *44*, 9675–9682.

[315] Yaoita, T.; Isaki, T.; Masubuchi, Y.; Watanabe, H.; Ianniruberto, G.; Marrucci, G. “Primitive Chain Network Simulation of Elongational Flows of Entangled Linear Chains: Stretch/Orientation-induced Reduction of Monomeric Friction”. *Macromolecules* **2012**, *45*, 2773–2782.

[316] Masubuchi, Y.; Watanabe, H.; Ianniruberto, G.; Greco, F.; Marrucci, G. “Comparison among Slip-Link Simulations of Bidisperse Linear Polymer Melts”. *Macromolecules* **2008**, *41*, 8275–8280.

[317] Masubuchi, Y.; Ianniruberto, G.; Greco, F.; Marrucci, G. “Primitive chain network model for block copolymers”. *J. Non-Cryst. Solids* **2006**, *352*, 5001 – 5007.

[318] Okuda, S.; Inoue, Y.; Masubuchi, Y.; Uneyama, T.; Hojo, M. “Wall boundary model for primitive chain network simulations”. *J. Chem. Phys.* **2009**, *130*, 214907.

[319] Chappa, V. C.; Morse, D. C.; Zippelius, A.; Müller, M. “Translationally Invariant Slip-Spring Model for Entangled Polymer Dynamics”. *Phys. Rev. Lett.* **2012**, *109*, 148302.

[320] Ramirez-Hernandez, A.; Muller, M.; de Pablo, J. J. “Theoretically informed entangled polymer simulations: linear and non-linear rheology of melts”. *Soft Matter* **2013**, *9*, 2030–2036.

[321] Ramŕez-Hernández, A.; Detcheverry, F. A.; Peters, B. L.; Chappa, V. C.; Schweizer, K. S.; Müller, M.; de Pablo, J. J. “Dynamical Simulations of Coarse Grain Polymeric Systems: Rouse and Entangled Dynamics”. *Macromolecules* **2013**, *46*, 6287–6299.

[322] Uneyama, T.; Masubuchi, Y. “Multi-chain slip-spring model for entangled polymer dynamics”. *J. Chem. Phys.* **2012**, *137*, 154902.

[323] Langeloth, M.; Masubuchi, Y.; Böhm, M. C.; Müller-Plathe, F. “Recovering the reptation dynamics of polymer melts in dissipative particle dynamics simulations via slip-springs”. *J. Chem. Phys.* **2013**, *138*.

[324] Terzis, A. F.; Theodorou, D. N.; Stroeks, A. “Entanglement Network of the Polypropylene/Polyamide Interface. 1. Self-Consistent Field Model”. *Macromolecules* **2000**, *33*, 1385–1396.

[325] Terzis, A. F.; Theodorou, D. N.; Stroeks, A. “Entanglement Network of the Polypropylene/Polyamide Interface. 2. Network Generation”. *Macromolecules* **2000**, *33*, 1397–1410.

[326] Terzis, A. F.; Theodorou, D. N.; Stroeks, A. “Entanglement Network of the Polypropylene/Polyamide Interface. 3. Deformation to Fracture”. *Macromolecules* **2002**, *35*, 508–521.

[327] Vogiatzis, G. G.; Theodorou, D. N. “Structure of Polymer Layers Grafted to Nanoparticles in Silica–Polystyrene Nanocomposites”. *Macromolecules* **2013**, *46*, 4670–4683.

[328] Watanabe, H.; Kotaka, T. “Viscoelastic properties and relaxation mechanisms of binary blends of narrow molecular weight distribution polystyrenes”. *Macromolecules* **1984**, *17*, 2316–2325.

[329] Wang, S.; von Meerwall, E. D.; Wang, S.-Q.; Halasa, A.; Hsu, W.-L.; Zhou, J. P.; Quirk, R. P. “Diffusion and Rheology of Binary Polymer Mixtures”. *Macromolecules* **2004**, *37*, 1641–1651.

[330] Wang, Z.; Larson, R. G. “Constraint Release in Entangled Binary Blends of Linear Polymers: A Molecular Dynamics Study”. *Macromolecules* **2008**, *41*, 4945–4960.

[331] van Ruymbeke, E.; Shchetnikava, V.; Matsumiya, Y.; Watanabe, H. “Dynamic Dilution Effect in Binary Blends of Linear Polymers with Well-Separated Molecular Weights”. *Macromolecules* **2014**, *47*, 7653–7665.

[332] B. Fischel, L.; Newman, J.; N. Theodorou, D. “Segment density of a block copolymer chain tethered at both ends”. *J. Chem. Soc., Faraday Trans.* **1997**, *93*, 4355–4370.

[333] Rudolf, B.; Schneider, H.; Cantow, H.-J. “Pressure-volume-temperature behaviour of molten polymers”. *Polym. Bull. (Heidelberg, Ger.)* **1995**, *34*, 109–116.

[334] Carlson, D. E.; Hoger, A. “On the derivatives of the principal invariants of a second-order tensor”. *Journal of Elasticity* **1986**, *16*, 221–224.

[335] Ermak, D. L.; Yeh, Y. “Equilibrium electrostatic effects on the behavior of polyions in solution: polyion-mobile ion interaction”. *Chem. Phys. Lett.* **1974**, *24*, 243 – 248.

[336] Ermak, D. L.; McCammon, J. A. “Brownian dynamics with hydrodynamic interactions”. *J. Chem. Phys.* **1978**, *69*, 1352–1360.

[337] Harmandaris, V. A.; Mavrantzas, V. G.; Theodorou, D. N. “Atomistic Molecular Dynamics Simulation of Polydisperse Linear Polyethylene Melts”. *Macromolecules* **1998**, *31*, 7934–7943.

[338] Mark, J. E. “Random-Coil Configurations of cis-1,4-Polybutadiene and cis-1,4-Polyisoprene. Theoretical Interpretation”. *J. Am. Chem. Soc.* **1966**, *88*, 4354–4359.

[339] Hanson, D. E. “The distributions of chain lengths in a crosslinked polyisoprene network”. *J. Chem. Phys.* **2011**, *134*, 064906.

[340] Hanson, D. E.; Martin, R. L. “Quantum chemistry and molecular dynamics studies of the entropic elasticity of localized molecular kinks in polyisoprene chains”. *J. Chem. Phys.* **2010**, *133*, 084903.

[341] Klopffer, M.-H.; Bokobza, L.; Monnerie, L. “Effect of vinyl content on the viscoelastic properties of polybutadienes and polyisoprenes - monomeric friction coefficient ”. *Polymer* **1998**, *39*, 3445 – 3449.

[342] Doxastakis, M.; Kitsiou, M.; Fytas, G.; Theodorou, D. N.; Hadjichristidis, N.; Meier, G.; Frick, B. “Component segmental mobilities in an athermal polymer blend: Quasielastic incoherent neutron scattering versus simulation”. *J. Chem. Phys.* **2000**, *112*, 8687–8694.

[343] Qin, J.; Milner, S. T. “Tubes, Topology, and Polymer Entanglement”. *Macromolecules* **2014**, *47*, 6077–6085.

[344] Ramírez, J.; Sukumaran, S. K.; Vorselaars, B.; Likhtman, A. E. “Efficient on the fly calculation of time correlation functions in computer simulations”. *J. Chem. Phys.* **2010**, *133*, 154103.

[345] Hore, M. J. A.; Ford, J.; Ohno, K.; Composto, R. J.; Hammouda, B. “Direct Measurements of Polymer Brush Conformation Using Small-Angle Neutron Scattering (SANS) from Highly Grafted Iron Oxide Nanoparticles in Homopolymer Melts”. *Macromolecules* **2013**, *46*, 9341–9348.

[346] Vogiatzis, G. G.; Theodorou, D. N. “Local Segmental Dynamics and Stresses in Polystyrene - C_{60} Mixtures”. *Macromolecules* **2014**, *47*, 387–404.

[347] Theodorou, D. N.; Vogiatzis, G. G.; Kritikos, G. “Self-Consistent-Field Study of Adsorption and Desorption Kinetics of Polyethylene Melts on Graphite and Comparison with Atomistic Simulations”. *Macromolecules* **2014**, *47*, 6964–6981.

[348] Levashov, V. A.; Morris, J. R.; Egami, T. “Viscosity, Shear Waves, and Atomic-Level Stress-Stress Correlations”. *Phys. Rev. Lett.* **2011**, *106*, 115703.

[349] Levashov, V. A.; Morris, J. R.; Egami, T. “The origin of viscosity as seen through atomic level stress correlation function”. *J. Chem. Phys.* **2013**, *138*, 044507.

[350] Levashov, V. A. “Dependence of the atomic level Green-Kubo stress correlation function on wavevector and frequency: Molecular dynamics results from a model liquid”. *J. Chem. Phys.* **2014**, *141*, 124502.

[351] Levashov, V. A. “Understanding the atomic-level Green-Kubo stress correlation function for a liquid through phonons in a model crystal”. *Phys. Rev. B* **2014**, *90*, 174205.

[352] Li, W.; Nealey, P. F.; de Pablo, J. J.; Müller, M. “Defect Removal in the Course of Directed Self-Assembly is Facilitated in the Vicinity of the Order-Disorder Transition”. *Phys. Rev. Lett.* **2014**, *113*, 168301.

[353] Ray, J. R. “Fluctuations and thermodynamic properties of anisotropic solids”. *J. Appl. Phys.* **1982**, *53*, 6441–6443.

[354] Theodorou, D. N.; Suter, U. W. “Atomistic modeling of mechanical properties of polymeric glasses”. *Macromolecules* **1986**, *19*, 139–154.

[355] Zwanzig, R.; Mountain, R. D. “High□Frequency Elastic Moduli of Simple Fluids”. *J. Chem. Phys.* **1965**, *43*, 4464–4471.

[356] Gusev, A. A.; Zehnder, M. M.; Suter, U. W. “Fluctuation formula for elastic constants”. *Phys. Rev. B* **1996**, *54*, 1–4.

[357] Karimi, M.; Yates, H.; Ray, J. R.; Kaplan, T.; Mostoller, M. “Elastic constants of silicon using Monte Carlo simulations”. *Phys. Rev. B* **1998**, *58*, 6019–6025.

[358] Van Workum, K.; Gao, G.; Schall, J. D.; Harrison, J. A. “Expressions for the stress and elasticity tensors for angle-dependent potentials”. *J. Chem. Phys.* **2006**, *125*, 144506.

[359] Voyiatzis, E. “Mechanical properties and elastic constants of atomistic systems through the stress-fluctuation formalism”. *Comput. Phys. Commun.* **2013**, *184*, 27 – 33.

[360] Nijboer, B.; Wette, F. D. “On the calculation of lattice sums”. *Physica* **1957**, *23*, 309 – 321.

[361] Williams, D. E. “Accelerated convergence of crystal-lattice potential sums”. *Acta Crystallogr., Sect. A: Cryst. Phys., Diffr., Theor. Gen. Crystallogr.* **1971**, *27*, 452–455.

[362] Karasawa, N.; Goddard, W. A. “Acceleration of convergence for lattice sums”. *J. Phys. Chem.* **1989**, *93*, 7320–7327.

[363] in ’t Veld, P. J.; Ismail, A. E.; Grest, G. S. “Application of Ewald summations to long-range dispersion forces”. *J. Chem. Phys.* **2007**, *127*, 144711.

[364] Grest, G. S.; Kremer, K. “Statistical properties of random cross-linked rubbers”. *Macromolecules* **1990**, *23*, 4994–5000.

[365] Shy, L. Y.; Eichinger, B. E. “Computer simulations of radiation-cured networks”. *Macromolecules* **1986**, *19*, 2787–2793.

Index

Curriculum Vitae

Georgios Grigorios Vogiatzis

Ph.D. Candidate
Department of Materials Science and Engineering
School of Chemical Engineering
National Technical University of Athens
9 Heroon Polytechniou Street, Zografou Campus, GR-157 80 Athens, Greece
Tel. (+30) 210 772 3216, Cell (+30) 697 2452859
E-mail: gvog@chemeng.ntua.gr

Personal Data

Born 4 July, 1987 in Athens, Greece
Single

Research interests

Computer modeling of matter
Polymer science and engineering
High Performance Computing
Parallel programming for multicore, cluster and heterogeneous systems

Education

2010 - today **Ph.D. Candidate, National Technical University of Athens, Greece.**

- ◇ School of Chemical Engineering

2010–2012 **Master of Science, National Technical University of Athens, 2012, Greece.**

- ◇ School of Applied Mathematical and Physical Science
- ◇ Inter-Departmental Postgraduate Programme: "Microsystems and nano-devices"
- ◇ *Academic Degree:* Master of Science, *Grade:* 9.17 / 10.0
- ◇ *Thesis:* Segmental Dynamics in Polystyrene - C_{60} mixtures
- ◇ *Thesis Advisor:* Prof. Doros N. Theodorou

2005–2010 **Diploma, National Technical University of Athens, 2010, Greece.**

- ◇ School of Chemical Engineering
- ◇ *Academic Degree:* Diploma in Chemical Engineering, *Grade:* 8.53 / 10.0
- ◇ *Thesis:* Structure prediction of polymer nanocomposites from Self Consistent Field Theory
- ◇ *Thesis Advisor:* Prof. Doros N. Theodorou

Honors and Awards

2011 - 2014	Doctoral Scholarship of the Alexander S. Onassis Public Benefit Foundation
2012	Best poster award, 9th Hellenic Polymer Society Conference, Thessaloniki, Greece.
2010	Thomaides awards for scientific contributions, National Technical University of Athens, Greece
2010	Thomaides award for the Best Diploma Thesis of the National Technical University of Athens for the year of 2010
2010	Best Diploma Thesis of the School of Chemical Engineering, National Technical University of Athens, Greece.
2010	Best Diploma Thesis of the Department of Materials Science and Engineering of School of Chemical Engineering, National Technical University of Athens, Greece.

Experience

2010 - today Member of the Technical Chamber of Greece (Reg. No. 125328)

2009 HPC Europa 2 Transnational Access Visit N. 175
- 20 July - 31 August, 2009
- CINECA Consortio Interuniversitario, via Magnanelli 6/3, 40033 Casalechio di Reno, Bologna, Italy
- Development of a highly parallel Monte Carlo code for the study of polymer matrix nanocomposites

Professional Development

2012 Programming and Tuning Massively Parallel Systems (PUMPS) Summer School 2012
- 2-6 July, 2012
- Barcelona Supercomputing Centre (BSC), Barcelona, Spain
- Advanced course and hands-on experience in developing applications software for many-core processors, such as general purpose graphics processing units (GPUs).

2008 Autodesk AutoCAD 2009 2D Certification
- September 2008 - November 2008
- Loulakis S.A. Autodesk Authorized Certification Center, Athens, Greece
- 2D design using Autodek AutoCAD.

2008 2nd Workshop on Drug Design
- March 2008 - June 2008
- Institute of Biology, Medicinal Chemistry and Biotechnology, National Hellenic Research Foundation, Athens, Greece
- Training on rational drug design through Molecular Modeling, NMR and X-ray techniques.

Co-supervision

2010 - 2011 MSc Thesis student: *Andreas Morphis*
- “Computationally efficient molecular simulations of polymeric melts”
- School of Chemical Engineering, National Technical University of Athens

2011 - 2012 MSc Thesis student: *Ioulia Tzouvadaki*
- “Mesoscopic simulations of polymer matrix nanocomposites”
- School of Chemical Engineering, National Technical University of Athens

2012 - 2013 Diploma Thesis student: *Ioannis Petsagkourakis*
- “Monte Carlo simulations of a graphite polyethylene nanocomposite”
- School of Chemical Engineering, National Technical University of Athens

2012 - 2013 MSc Thesis student: *Xrysa Charitoglou*
- “Self Consistent Field study of a graphite polyethylene nanocomposite”
- School of Chemical Engineering, National Technical University of Athens

2012 - 2014 Diploma Thesis student: *Andreas Gavrielides*
- “Monte Carlo simulation of polystyrene epimerization”
- School of Chemical Engineering, National Technical University of Athens

2013 - 2014 Diploma Thesis student: *Ariadni Boziki*
- “Monte Carlo simulations of a PE/graphite system”
- School of Chemical Engineering, National Technical University of Athens

Languages

Greek	Mother tongue
English	Fluent (C2: Certificates of Proficiency in English from the University of Cambridge and the University of Michigan)
German	Elementary

Technical skills

Languages	Fortran 77, 90/95, 2003, C, C++, Python, Perl, Haskell, Prolog
Paradigms	MPI, openMP, nVIDIA CUDA
Platforms	CentOS cluster administration
Tools	LaTeX, doxygen, Texinfo

Personal Interests

Music	Playing the violin and the piano. Degrees in: Harmony and Counterpoint
Chess	2004 and 2005 Pan-Athenian School Chess Championships Awards
Software development	Member of the Novell Developer Communities

A. Publications *(as of January 10, 2015)*

h-index: **3**, total citations*: **27**
(data: Scopus, Web of Science, Researcher ID: D-7825-2014)

A1 Vogiatzis, G. G.; Voyiatzis, E.; Theodorou, D. N. "Monte Carlo simulations of a coarse grained model for an athermal all-polystyrene nanocomposite system" *Eur. Polym. J* **2011**, *47*, 699 –712.
[2013 Impact Factor: 3.242, Times cited*: **20**]
[arXiv: http://arxiv.org/abs/1401.3364]

A2 Vogiatzis, G. G.; Theodorou, D. N. "Structure of Polymer Layers Grafted to Nanoparticles in Silica - Polystyrene Nanocomposites" *Macromolecules* **2013**, *46*, 4670–4683.
[2013 Impact Factor: 5.927, Times cited*: **4**]
[arXiv: http://arxiv.org/abs/1401.4001]

A3 Lempesis, N.; Vogiatzis, G. G.; Boulougouris, G. C.; Breemen, L. C. van; Hütter, M.; Theodorou, D. N. "Tracking a glassy polymer on its energy landscape in the course of elastic deformation" *Mol. Phys.* **2013**, *111*, 3430–3441.
[2013 Impact Factor: 1.642, Times cited*: **0**]

A4 Vogiatzis, G. G.; Theodorou, D. N. "Local Segmental Dynamics and Stresses in Polystyrene - C_{60} Mixtures" *Macromolecules* **2014**, *47*, 387–404.
[2013 Impact Factor: 5.927, Times cited*: **3**]
[arXiv: http://arxiv.org/abs/1401.4314]

A5 Theodorou, D. N.; Vogiatzis, G. G.; Kritikos, G. "Self-Consistent-Field Study of Adsorption and Desorption Kinetics of Polyethylene Melts on Graphite and Comparison with Atomistic Simulations" *Macromolecules* **2014**, *47*, 6964–6981.
[2013 Impact Factor: 5.927, Times cited*: **0**]

* excluding self-citations from all authors

B. Invited talks *(as of December 18, 2014)*

B1 *Vogiatzis, G. G.*; Megariotis, G.; Tzoumanekas, C.; Theodorou, D. N. "Polymer network simulations at a mesoscopic level", *FEMS EUROMAT 2013 European Congress and Exhibition on Advanced Materials and Processes*, Hotel Barceló Renacimiento, Sevilla, Spain, 8 - 13 September, 2013.

C. International conference proceedings *(as of December 18, 2014)*

C1 *Vogiatzis, G. G.*; Voyiatzis, E.; Theodorou, D. N. "Parallel Monte Carlo Simulations of a Coarse Grain Model for Polymer Nanocomposites", *Poster presented during HPC-Europa2 Transnational Access Meeting 2010*, Helsinki, Finland, 15-17 June, 2010.

C2 *Vogiatzis, G. G.*; Voyiatzis, E.; Theodorou, D. N. "Accelerating Monte Carlo Simulations using Graphics Processing Units", *in Proceedings of the 7th GRACM International Congress on Computational Mechanics*, Athens, 30 June - 2 July, 2011.

C3 Vogiatzis, G. G.; Voyiatzis, E.; Mathioudakis, I.; *Theodorou, D. N.* "Multiscale modelling of polymer-matrix nanocomposites", *CECAM Workshop: Coarse-Graining Strategies and Methodologies for Polymeric and Biomolecular Assemblies*, CFCAM-RA Centre Blaise Pascal, Lyon, France, 5-8 July, 2011.

C4 Morphis, A. D.; *Vogiatzis, G.G.*; Theodorou, D. N. "Accelerating molecular simulations of polymers using Graphics Processing Units", *Poster presented during Programming and Tuning Massively Parallel Systems summer school (PUMPS)*, Barcelona Supercomputing Centre (BSC), Barcelona, Spain, 2-6 July, 2012.

C5 Vogiatzis, G. G.; Voyiatzis, E.; *Theodorou, D. N.* "Multiscale Modeling of Polymer-Matrix Nanocomposites" *Polym. Prepr. (Am. Chem. Soc., Div. Polym. Chem.)* **2012**, *53*, 19-23 August, 2012, 64–65.

C6 *Vogiatzis, G. G.*; Theodorou, D. N. "Chain Conformations in Polymer Nanocomposites: A Field Theory-Inspired Monte Carlo Simulation Approach", *in Proceedings of the XI International Conference on Nanostructured Materials*, Rhodes, Greece, 26-31 August, 2012.

C7 Vogiatzis, G. G.; *Theodorou, D. N.* "Multiscale Simulations of Polymer-Matrix Nanocomposites", *in Proceedings of the 6th International Conference on Multiscale Materials Modeling*, Biopolis, Singapore, 15-19 October, 2012.

C8 Vogiatzis, G. G.; *Theodorou, D. N.* "Chain Conformations in Polymer Nanocomposites: A Field Theory-Inspired Monte Carlo Simulation Approach", *in Proceedings of the 2012 Annual Meeting of the American Institute of Chemical Engineers*, Pittsburgh, PA, USA, 28 October - 2 November, 2012.

C9 Vogiatzis, G. G.; *Theodorou, D. N.* "Multiscale Simulations of Macromolecular Conformation and Dynamics in Polymer-Matrix Nanocomposites", *Macromolecules in Constrained Environments*, École de Physique des Houches, France, 24 - 29 March, 2013.

C10 *Vogiatzis, G. G.*; Megariotis, G.; Theodorou, D. N. "Multiscale Simulations of of Polymer-Matrix Nanocomposites", *in Proceedings of the 10th International Conference on Nanosciences and Nanotechnologies*, Porto Palace Conference Centre and Hotel, Thessaloniki, Greece, 9 - 12 July, 2013.

C11 Vogiatzis, G. G.; Megariotis, G.; *Theodorou, D. N.* "Atomistic and coarse-grained simulations of polymer-matrix nanocomposites", *CECAM Workshop: Coarse-graining multi-component soft matter systems: equilibrium and dynamics*, Johannes-Gutenberg Universität, Mainz, Germany, 21 - 23 August, 2013.

C12 Vogiatzis, G. G.; Megariotis, G.; *Theodorou, D. N.* "Coarse-graining and multiscale simulations of polymer-matrix nanocomposites", *in Proceedings of the 246th ACS National Meeting - Division of Physical Chemistry*, Indianapolis, IN, USA, 8 - 12 September 2013, pp 64–65.

C13 Mathioudakis, I. G.; Vogiatzis, G. G.; *Theodorou, D. N.* "Molecular modeling of polymer nanocomposites at multiple length scales", *in Proceedings of the 11th International Conference on Nanosciences and Nanotechnologies*, Porto Palace Conference Centre and Hotel, Thessaloniki, Greece, 8 - 11 July, 2014.

C14 *Delhorme, M.*; Lempesis, N.; Vogiatzis, G. G.; Boulougouris, G. C.; Breemen, L. C. A. van; Hütter, M.; Theodorou, D. N. “Tracking a glassy polymer on its energy landscape in the course of small time-dependent deformations”, *in Proceedings of the 7th International Conference on Multiscale Materials Modeling*, Berkeley, California USA, 6-10 October, 2014.

D. National conference proceedings *(as of December 18, 2014)*

D1 *Vogiatzis, G. G.*; Voyiatzis, E.; Theodorou, D. N. “Coarse-grained Monte Carlo simulations of polymer nanocomposites”, *Proceedings of the 8th Panhellenic Scientific Conference in Chemical Engineering*, Thessaloniki, Greece, 26-28 May, 2011.

D2 *Vogiatzis, G. G.*; Theodorou, D. N. “Local Polymer Dynamics in Polystyrene - C_{60} Mixtures”, *Poster presented during the 9th Hellenic Polymer Society Conference*, Thessaloniki, Greece, 29 November - 1 December, 2012.

D3 Vogiatzis, G. G.; *Theodorou, D. N.* “Multiscale modelling of polymer-matrix nanocomposites”, *in Proceedings of the 9th Hellenic Polymer Society Conference*, Thessaloniki, Greece, 29 November - 1 December, 2012.

D4 *Mathioudakis, I. G.*; Vogiatzis, G. G.; Theodorou, D. N. “Multiscale Modeling of Polymer-Matrix Nanocomposites”, *in Proceedings of the 9th Panhellenic Scientific Conference in Chemical Engineering*, Athens, Greece, 23-25 May, 2013.

D5 *Mathioudakis, I. G.*; Vogiatzis, G. G.; Theodorou, D. N. “Molecular simulation of polymer nanocomposites at multiple length scales”, *in Proceedings of the XXIX Panhellenic Connference of Solid State Physics and Materials Science*, Athens, Greece, 22-25 September, 2013.

D6 *Vogiatzis, G. G.*; Megariotis, G.; Theodorou, D. N. “Multiscale modeling of polymer-matrix nanocomposites: structure and dynamics at multiple length scales”, *in Proceedings of the 10th Hellenic Polymer Society Conference*, Patras, Greece, 4 - 6 December, 2014.

D7 Lempesis, N.; Vogiatzis, G. G.; Boulougouris, G.; *Theodorou, D. N.* “Energy landscape analysis of polymer glasses”, *in Proceedings of the 10th Hellenic Polymer Society Conference*, Patras, Greece, 4 - 6 December, 2014.

D8 *Mathioudakis, I. G.*; Vogiatzis, G. G.; Theodorou, D. N. “Molecular simulation of polymer nanocomposites at multiple length scales”, *in Proceedings of the 10th Hellenic Polymer Society Conference*, Patras, Greece, 4 - 6 December, 2014.